Réponse acoustique non-linéaire de métamatériaux compacts soumis à des niveaux d'excitation sonore élevés, modélisation par une approche masse-ressort

par

Maël LOPEZ

THÈSE PAR ARTICLES PRÉSENTÉE À L'ÉCOLE DE TECHNOLOGIE SUPÉRIEURE COMME EXIGENCE PARTIELLE À L'OBTENTION DU DOCTORAT EN GÉNIE
Ph.D.

MONTRÉAL, LE MERCREDI 16 OCTOBRE 2024

ÉCOLE DE TECHNOLOGIE SUPÉRIEURE
UNIVERSITÉ DU QUÉBEC

PRÉSENTATION DU JURY

CETTE THÈSE A ÉTÉ ÉVALUÉE

PAR UN JURY COMPOSÉ DE:

M. Thomas Dupont, directeur de thèse
Département de génie mécanique à l'École de Technologie Supérieure, Canada

M. Raymond Panneton, codirecteur
Département de génie mécanique à l'Université de Sherbrooke, Canada

M. Jean-Philippe Roberge, président du jury
Département de génie des systèmes à l'École de Technologie Supérieure, Canada

M. Olivier Doutres, membre du jury
Département de génie mécanique à l'École de Technologie Supérieure, Canada

M. Morvan Ouisse, examinateur externe
SUPMICROTECH, Université de Franche Comté, CNRS, Institut FEMTO-ST, France

ELLE A FAIT L'OBJET D'UNE SOUTENANCE DEVANT JURY ET PUBLIC

LE MERCREDI 25 SEPTEMBRE 2024

À L'ÉCOLE DE TECHNOLOGIE SUPÉRIEURE

REMERCIEMENTS

Mes remerciements s'adressent en premier lieu à mon directeur de thèse Thomas Dupont pour cette opportunité de doctorat qu'il m'a offerte, pour son encadrement et la confiance qu'il m'a octroyée. Également, ils vont à mon à codirecteur Raymond Panneton qui a été (est) une référence tant sur le point scientifique qu'humain pour moi. Ce fut un plaisir d'échanger et d'apprendre auprès d'eux tout au long de mon doctorat. Je tiens aussi à remercier Tenon Charly Kone et Alla Eddine Benchikh Lehocine qui se sont joint en cours de route de ce projet. Leur aide a été inestimable sur la fin de cette thèse. Aussi, je remercie ma famille, mes ami·e·s et mes colocataires de France de m'avoir soutenu dans cette aventure qu'est la thèse. Je tiens à chaleureusement remercier toutes les personnes qui ont fait des années passées au Canada des moments de bonheur. Cette aventure a commencé par de belles rencontres au sein du laboratoire, Maxime P., Lucie, Alexandre, Magdeleine, Julien et Solenn. Dans ces remerciements, je tiens en particulier à remercier des personnes qui ont été là depuis le début de mon doctorat. Lucie qui a commencé son doctorat en même temps que moi et avec qui nous avons bien pipeletté durant ces années. Et également Gauthier, avec qui j'ai pris notamment plaisir à échanger et collaborer avec, je trouve, une belle intelligence. Et aux personnes qui sont arrivées par la suite, notamment à Maxime et nos belles virées faites ensemble. Je remercie toutes les personnes qui sont passées par le groupe de recherche du GRAM (étudiant·e·s, professeur·e·s, personnel de l'IRSST) lors de ces dernières années et avec qui j'ai passé de très beaux moments. Aussi, merci pour ces instants informels : lunchs, pauses-café/thé, viennoiseries ou encore autour d'une bière. Je ne pourrai citer tout le monde. Merci à la petite équipe sportive du laboratoire, Kevin, Stanislas et Quentin. Et aussi à Bastien, Clément C., Clément N., Hugo S.G., Kevin C., Laurianne, Loïc, Lucas, Marion, Michel, Robin, Simon P., Tigran, Thomas P. et Valentin pour les différents moments de bonne humeur partagés ensemble.

J'ai eu la chance de m'impliquer à travers divers clubs et évènements en parallèle de mon doctorat. La musique tient une place très importante dans ma vie. Je suis heureux d'avoir pu continuer de partager ma passion avec d'autres musicien·e·s que je remercie chaleureusement. En particulier, toutes les personnes qui jouées dans l'orchestre et le capitaine de ce club Valentin

P.. Je ne peux oublier de remercie les membres du trio Maëlys et William. Des moments et des expériences formidables passés ensemble et avec qui je suis parti à l'exploration des paysages québécois. Merci encore à Maëlys, pour m'avoir soutenu et fait garder le moral lors de cette fin de thèse ! Merci à Rémy de m'avoir gentiment invité à rejoindre le Comité des Jeux de Société et aux différents membres de ce club Clément P., François, Marie et Victoria. Finalement, mes dernières pensées vont à toutes les belles rencontres que j'ai pu faire au Québec, Arthur, Gabriel, Hugo B., Léa, Parpou, Robert, Simon C., Tania, Thomas F et Tom.

Réponse acoustique non-linéaire de métamatériaux compacts soumis à des niveaux d'excitation sonore élevés, modélisation par une approche masse-ressort

Maël LOPEZ

RÉSUMÉ

L'absorption des ondes acoustiques basses fréquences par des matériaux compacts est un challenge. En effet, les matériaux conventionnels poreux (ex. : mousses) et les résonateurs (ex. : plaque perforée suivie d'une cavité) nécessitent des épaisseurs importantes, de l'ordre de grandeur de la longueur d'onde à traiter. Les volumes disponibles pour les matériaux acoustiques sont souvent restreints, comme par exemple dans les carénages de rotors de queue arrière d'hélicoptère. Pour ce type de problème, les matériaux structurés résonants sont des solutions intéressantes. Ils sont efficaces pour des longueurs d'onde de bien plus grandes dimensions que leur épaisseur. Cependant, ils sont sensibles aux niveaux d'excitation sonore. L'objectif principal de cette thèse porte sur l'analyse du comportement et le développement de matériaux structurés compacts pour le traitement acoustique des basses fréquences, soumis à des niveaux d'excitation sonore faibles à élevés. Pour répondre à cet objectif, les résultats de la thèse sont présentés dans quatre chapitres dont trois sont des articles scientifiques. Le premier article porte sur l'étude du comportement de matériaux structurés pour des niveaux d'excitation acoustiques faibles (<110 dB). Le matériau structuré proposé est constitué d'un réseau périodique de pores d'air espacés de résonateurs d'Helmholtz annulaires. Pour analyser son comportement, un modèle masse-ressort (analogie mécanoacoustique) a été développé. La solution du problème aux valeurs propres a permis de déterminer les fréquences des modes (fréquences des pics d'absorption) et leurs déformées. Ce modèle se compare bien aux résultats expérimentaux et issus de simulations numériques (éléments finis). Le deuxième article s'intéresse aux pertes ajoutées par les forts niveaux acoustiques pour un matériau de référence comprenant un réseau compact de plaques perforées. Une estimation de ces pertes a été déterminée en étudiant la résistivité au passage de l'air sur un matériau composé d'un réseau périodique de pores d'air espacés de cavités fines. Une étude par mécanique des fluides numérique a permis de montrer que les pertes dominent dans le premier pore et d'estimer un coefficient associé à ces pertes. Dans le troisième article, le modèle masse-ressort a été adapté à partir du paramètre de Forchheimer pour prédire l'absorption acoustique d'un matériau de référence sous forts niveaux. Le modèle a été validé avec des mesures pour des niveaux sonores allant jusqu'à 140 dB. Le dernier chapitre traite du comportement non-linéaire des trous noirs acoustiques : réseau de pores d'air à section décroissante espacés de cavités annulaires fines. Le modèle masse-ressort a été adapté à cette géométrie et validé par des mesures. La sensibilité aux forts niveaux d'excitation sonore a été analysée pour différents profils de décroissance de la section du pore.

Mots-clés: métamatériaux acoustiques, absorption basse-fréquence, forts niveaux de pression sonore, modèle masse-ressort, réponse acoustique non-linéaire

Nonlinear acoustic response of compact metamaterials under high sound pressure levels, modelled by a mass-spring approach

Maël LOPEZ

ABSTRACT

The absorption of sound at low frequencies by compact materials remains a challenge. Conventional porous materials (e.g. : foams) and resonators (e.g. : perforated plate backed by cavity) require significant thicknesses, of the order of magnitude of the wavelength to be treated. The volumes available for acoustic solutions are often limited, as in the case of helicopter tail rotor fairings. For this type of problem, resonant structured materials are interesting solutions. They are effective at wavelengths far greater than their thickness. However, they are sensitive to their environment, particularly to sound excitation levels. The main objective of this thesis is to analyze the behavior and develop compact structured materials for acoustic treatment of sound at low frequencies, subjected to low to high levels of sound excitation. To meet this objective, the results of the thesis are presented in four chapters, three of which are scientific papers. The first paper focuses on the study of the behavior of structured materials for low acoustic excitation levels (<110 dB). The proposed structured material consists of a periodic array of air pores spaced by annular Helmholtz resonators. To analyze its behavior, a mass-spring model was developed. By solving the eigenvalue problem, mode frequencies (absorption peak frequencies) and deformations were determined. This model compares well with experimental and numerical (finite element) simulation results. The second paper looks at the losses added by high acoustic levels in the reference material composed of a compact array of perforated plates. An estimate of these losses was determined by studying the resistivity to air flow over a material composed of a periodic array of air pores spaced by thin air cavities. A computational fluid dynamics study showed that losses dominate in the first pore and estimated a coefficient associated with these losses. In the third paper, the mass-spring model was adapted from the Forchheimer parameter to predict the sound absorption of the reference material at high levels. The model is validated with measurements at sound levels up to 140 dB. The last chapter is interested in the non-linear behavior of acoustic black holes : compact array of air pores with decreasing cross-section along the material thickness spaced by thin air cavities. The mass-spring model has been adapted to this geometry and validated by measurements. Sensitivity to high sound excitation levels was analyzed for different profiles of decreasing pore cross-section.

Keywords: acoustic metamaterials, low frequency sound absorption, high sound pressure levels, mass-spring model, acoustic non-linear response

TABLE DES MATIÈRES

LISTE DES TABLEAUX

LISTE DES FIGURES

LISTE DES ABRÉVIATIONS, SIGLES ET ACRONYMES

ABH	*Acoustic black hole*
AHR	*Annular Helmholtz Resonator*
ARM	*Airflow Resistivity Meter*
CFD	*Computational Fluid Dynamics*
CPU	*Central Processing Unit*
CRASH-UdeS	Centre de Recherche acoustique-signal-humain de l'Université de Sherbrooke
CS	*Closely Cpaced*
DE	*Dead-End*
FEM	*Finite Element Method*
ICAR	Infrastructure commune en acoustique pour la recherche
JCA	Johnson-Champoux-Allard
MS	*Mass-Spring*
NRC	Conseil national de recherches Canada
OA	*Open Area*
PUC	*Periodic Unit Cell*
SPL	*Sound Pressure Level*
SPP	*single-perforation plate*
TL	*Transmission Loss*
TMM	*Transfer Matrix Method*
TVA	*Thermoviscous-Acoustic*

LISTE DES SYMBOLES ET UNITÉS DE MESURE

s	seconde
Hz	hertz (avec préfixe k pour kilo)
m	mètre (avec préfixe m pour milli)
Pa	pascal
dB	décibel
kg	kilogramme

INTRODUCTION

Les nuisances sonores font partie intégrante de notre quotidien, elles sont généralement issues des transports, activités industrielles ou de loisir. Les milieux bruyants ont de nombreux impacts sur les populations qui les côtoient (santé et inconfort) et les personnes qui y travaillent (santé et sécurité au travail). L'exposition des populations aux environnements bruyants peut engendrer des problèmes à court terme (perturbation du sommeil, problème de concentration, problème de communication...), moyen terme (stress, fatigue, perte de performance scolaire...), long terme (problème cardiovasculaire, problème d'audition...). Au Québec, c'est un-million-cent-vingt-cinq-mille personnes qui ont été exposées à des bruits environnementaux à « fort dérangement » entre 2014 et 2015 (Lebel, Martin & Dubé, 2019). Le coût social lié au bruit représenterait six-cent-soixante-dix-neuf-millions de dollars par an au Québec (Martin, Deshaies & Poulin, 2016). D'un autre côté, la réduction du bruit peut être un argument commercial important (ex. : vente d'avions d'affaires, de voitures ou d'électroménagers silencieux). Pour améliorer ces environnements ou minimiser les problèmes liés au bruit dans nos sociétés, différentes actions peuvent être mises en place à la source de bruit (équilibrage par exemple), sur les chemins de transferts ou sur les individus (temps d'exposition, protections auditives pour la santé et sécurité au travail). Une des actions importantes pour la réduction du bruit est donc l'action sur les chemins de transferts aériens par des traitements acoustiques. Dans le secteur des transports par exemple, le bruit produit par un moteur ou un rotor de queue doit être atténué avant qu'il ne se propage dans l'environnement. Des traitements acoustiques sont alors installés en aval de la source de bruit. Parmi ces traitements, des solutions conventionnelles peuvent être communément employées telles que les matériaux poreux (ex. : mousses) et les résonateurs (ex. : plaque perforée suivie d'une cavité). Cependant, les solutions conventionnelles nécessitent des épaisseurs et volumes importants pour être efficaces en basses fréquences (épaisseur de l'ordre de grandeur du quart ou demi de la longueur d'onde à traiter). Dans le cas d'applications industrielles, le volume peut être restreint et l'ajout de masse doit être limité (notamment pour réduire la consommation d'énergie et réduire l'empreinte environnementale dans le secteur des transports). Cependant, des sources sonores basses fréquences sont présentes comme dans les nacelles d'avion ou le carénage de rotor de queue d'hélicoptère (Pongratz & Redmann, 2016). Par ailleurs, ces environnements peuvent présenter de forts niveaux de pression acoustique et vibratoire, de l'écoulement ou des gradients de température. Ces conditions extrêmes peuvent venir modifier le comportement acoustique du traitement. Une bonne compréhension des différents phénomènes est alors requise pour proposer un matériau acoustique performant dans un volume restreint et pour des environnements pouvant être extrêmes.

Pour répondre à cet enjeu, une nouvelle famille de matériaux a été proposée : les matériaux structurés. La définition proposée dans le cadre de cette thèse est la suivante : un matériau structuré est un système dont la géométrie est arrangée pour améliorer un ou plusieurs indices de performance acoustiques (ex. : coefficient d'absorption ou indice de pertes par transmission), pour une plage de fréquences et un volume donnés. Ces matériaux permettent notamment le traitement acoustique des sons à basses fréquences à des épaisseurs et/ou volumes bien inférieurs à ceux requis par les solutions conventionnelles.

Dans les familles des matériaux structurés, qui seront présentées plus en détail dans la revue de littérature, les matériaux à compressibilité effective augmentée permettent une réduction des sons à basses fréquences tout en restant compacts et pouvant s'intégrer dans des environnements pouvant être extrêmes. Dans cette catégorie de matériau, Dupont, Leclaire, Panneton & Umnova (2018) ont proposé un matériau structuré composé d'un pore principal, le résonateur principal, auquel est ajouté un réseau périodique de cavités fines annulaires. Le matériau est appelé absorbeur à réseau de cavité fine ou « *multi-pancakes* ». L'effet de l'ajout d'un réseau périodique est équivalent à un ralentissement des ondes acoustiques dans le pore principal dû à l'augmentation de la compressibilité effective. Lorsque le matériau est placé sur mur rigide, plusieurs pics d'absorption sont présents. Ces pics sont à des fréquences correspondant à de grandes longueurs d’onde alors que le matériau reste de petite dimension. Cependant, plusieurs questions restent en suspens. Quelles sont les paramètres géométriques les plus influant sur les fréquences des phénomènes caractéristiques de ces matériaux (premières fréquences des pics d’absorption, fréquences de bande interdites par exemple) ? Est-il possible d’obtenir un matériau efficace en terme d’absorption pour des fréquences encore plus basses sans augmenter le volume ?

Par ailleurs, le nombre d’études portant sur le comportement des matériaux structurés sous conditions extrêmes est relativement peu important, comme les forts niveaux d’excitation acoustique (Brooke, Umnova, Leclaire & Dupont, 2020) ou la présence d’écoulement (Aurégan, Farooqui & Groby, 2016). Concernant les forts niveaux d’excitation, plusieurs points sont encore à traiter. Comment quantifier plus précisément les pertes ajoutées par les forts niveaux d’excitation acoustique ? Comment prendre en compte ces pertes dans les modèles acoustiques ? Quel est l’impact des forts niveaux sur un réseau composé d’une multitude d’éléments périodiques et pseudo-périodiques ?

Ainsi, cette thèse propose le développement de matériaux structurés compacts et l’analyse de leur comportement acoustique en basses fréquences pour des niveaux d’excitation acoustique faibles à élevés.

Cette thèse est une thèse par articles. Le manuscrit de thèse est organisé en plusieurs chapitres, les chapitres 3 à 5 sont des articles scientifiques. Le chapitre 1 présente une revue de littérature qui comporte deux parties. Dans la première partie, différents matériaux structurés résonants sont rapportés pour le traitement (en absorption et en isolation) des sons à basses fréquences. La deuxième partie est consacrée aux effets des forts niveaux d’excitation acoustique sur le comportement acoustique des matériaux acoustiques. À la suite, une analyse critique de la revue de littérature est présentée. Elle permet de justifier les objectifs et méthodes présentés dans le chapitre 2. Un plan détaillé des prochains chapitres est également établi. Le chapitre 3 présente un nouveau concept de matériau structuré et un modèle basé sur une analogie masse-ressort en régime linéaire. Ce nouvel outil permet d'aider à la compréhension des phénomènes physiques. Le chapitre 4 s'intéresse à la caractérisation et la quantification des pertes engendrées notamment par les forts niveaux acoustiques par une approche de mécanique des fluides numérique (CFD). Dans le chapitre 5, à partir des coefficients de pertes obtenus au chapitre 4, le modèle masse-ressort (présenté dans le chapitre 3) est adapté pour modéliser et analyser la réponse acoustique d'un matériau structuré périodique résonant sous forts niveaux d'excitation acoustique. Le chapitre 6 correspond à une application du modèle masse-ressort qui est utilisé pour prédire et analyser le comportement des trous noirs acoustiques (profils décroissants de la section du pore principal) sous forts niveaux d'excitation acoustique.

CHAPITRE 1

REVUE DE LITTÉRATURE

Dans le but de réduire les nuisances sonores, des matériaux acoustiques conventionnels sont utilisés dans différents contextes, ex. : transport, énergie, bâtiment. Les matériaux acoustiques peuvent être utilisés selon plusieurs configurations, comme en transmission (réduction de l'amplitude de l'onde transmise) ou en absorption sur fond rigide (réduction de l'amplitude de l'onde réfléchie, l'amplitude de l'onde transmise est ici supposée nulle). Indépendemment de ces configurations, les matériaux acoustiques sont constitués de plusieurs familles. La première regroupe les matériaux passifs (ex. : granuleux, poreux et fibreux) qui dissipent l'énergie d'une onde sonore incidente sous forme de chaleur due à des effets de cisaillement au niveau des couches limites (effets visqueux) ou d'échange de chaleur au sein du fluide (effets thermiques) (Allard & Atalla, 2009a). Ces matériaux ont une efficacité sur une bande de fréquence large, mais requièrent des épaisseurs importantes pour réduire les sons à basses fréquences (de l'ordre de grandeur du quart de la longueur d'onde). Une deuxième famille est celle des matériaux réactifs (ex. : résonateurs quart-d'onde et d'Helmholtz (Helmholtz & Ellis, 1895)). L'amplitude de l'onde sonore incidente est réduite par interférence destructive avec des ondes produites par le résonateur à la résonance. Ces matériaux sont efficaces pour des fréquences de résonance du matériau : c.-à-d. quand de grandes oscillations de pression, déplacement ou vitesse sont présentes au sein de la structure du matériau ou du fluide pour un matériau rigide. Les dimensions (épaisseur et/ou volume) des matériaux réactifs conventionnels peuvent être plus petites que celles des matériaux passifs pour réduire un même son. Cependant, leurs dimensions restent encore proches de la longueur d'onde à la première résonance et leur efficacité est pour la plupart concentrée sur ou autour de la première fréquence de résonance.

Les matériaux structurés sont des solutions qui font l'objet de recherches récentes (Jiménez, Umnova & Groby, 2021). Le terme « métamatériau » est également souvent utilisé pour décrire cette famille de matériaux. Actuellement, la communauté scientifique n'a pas trouvé de consensus concernant les définitions de ces terminologies (Panneton, 2023). De plus, le terme « métamatériau » est parfois utilisé pour qualifier un matériau dont l'épaisseur est bien inférieure à la plus grande longueur d'onde des ondes qu'ils atténuent. Il est alors confondu avec le terme « *subwavelength material* » (matériau à épaisseur très petite devant la longueur d'onde). Dans le cas de cette thèse, des définitions distinctes sont proposées pour « matériau structuré » et « métamatériau ». Ces définitions sont discutées pour tenter de parvenir à une meilleure précision des terminologies utilisées.

Un matériau structuré est un système dont la géométrie est arrangée pour améliorer un ou plusieurs indices de performance acoustiques (ex. : coefficient d'absorption ou indice de pertes par transmission), pour une plage de fréquence donnée. Ces matériaux permettent notamment le traitement acoustique des sons à basses fréquences à des épaisseurs ou volumes bien inférieurs à ceux requis par les matériaux conventionnels. Le critère de longueur d'onde à la première résonance du matériau sur l'épaisseur du matériau est particulièrement utilisé pour décrire l'efficacité de ces dispositifs à basses fréquences.

Dans le cadre de cette définition, les métamatériaux sont inclus dans la famille des matériaux structurés. Le préfixe tiré du grec « meta » fait référence au changement et peut se traduire par « au-delà » (Merriam-Webster, 2024). En effet, un métamatériau est un système dont la géométrie de sa structure est arrangée de telle sorte à obtenir des propriétés acoustiques « au-delà » de celles des matériaux « conventionnels ». Les grandeurs physiques peuvent être alors impactées, telles que la masse volumique effective ou le module de compressibilité effectif (la grandeur inverse est souvent utilisée : *Bulk modulus* ou module d'élasticité isostatique). Le terme de propriétés acoustiques effectives est alors employé pour désigner le changement opéré dans le matériau. La modification de ces propriétés acoustiques effectives permet notamment de rendre invisible d'un point de vue acoustique un matériau (Cummer & Schurig, 2007; Zigoneanu, Popa & Cummer, 2014), d'avoir un indice de réfraction négatif (Fok & Zhang, 2011; Park & Lee, 2019) ou d'obtenir une célérité effective diminuée (Leclaire, Umnova, Dupont & Panneton, 2015; Groby, Huang, Lardeau & Aurégan, 2015a). Une des conséquences de la modification des paramètres effectifs est que certains métamatériaux permettent d'absorber ou isoler des ondes qui ont des longueurs bien plus grandes que leurs dimensions géométriques.

Une classification de plusieurs matériaux structurés est présentée par la figure 1.1.

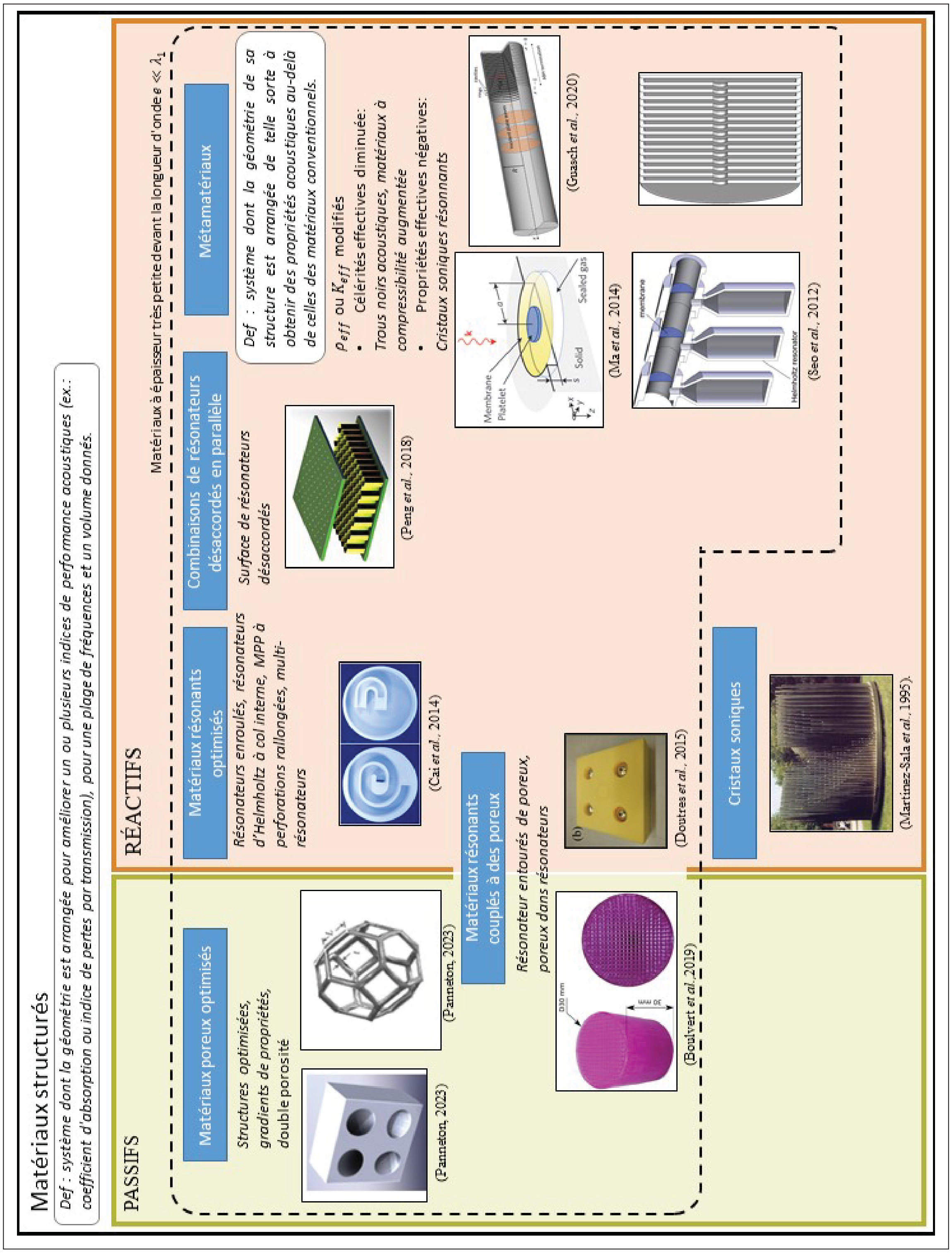

Figure 1.1 Classification des matériaux structurés

Dans de nombreux cas d'applications industrielles, le volume est souvent restreint et les conditions présentes peuvent être extrêmes (présence de fortes humidités, températures, écoulements et vibrations). Les matériaux dont la structure est robuste sont alors préférés. Ainsi, cette thèse s'intéresse aux matériaux structurés résonants dont l'épaisseur est très petite devant la longueur d'onde à la résonance. Ces matériaux font l'objet de la présente revue de littérature. Cette dernière est organisée en deux sections. La section 1.1 présente des catégories des matériaux structurés résonants soumis à de faibles niveaux d'excitation sonore. Les effets des forts niveaux d'excitation acoustique sur le comportement acoustique des matériaux perforés et des matériaux poreux à squelettes rigides sont présentés dans la section 1.2.

1.1 Matériaux structurés résonants

Différentes catégories de matériaux structurés résonants pour le traitement acoustique de son de basses fréquences sont présentées. La section 1.1.1 présente les matériaux résonants conventionnels à géométrie modifiée. Les combinaisons de résonateurs désaccordés en parallèle sont présentées dans la section 1.1.2. Les matériaux structurés composés de membranes et de films avec masses sont rapportés dans la section 1.1.3. La section 1.1.4 présente des matériaux structurés combinant des résonateurs et des matériaux poreux. La section 1.1.5 est consacrée aux cristaux soniques résonants. Les matériaux à compressibilité effective augmentée sont présentés dans la section 1.1.6. La section 1.1.7 présente les trous noirs acoustiques.

1.1.1 Résonateurs à géométrie modifiée

Les résonateurs conventionnels peuvent être modifiés dans le but de les rendre davantage compacts tout en maintenant une fréquence de résonance dans les basses fréquences. Les résonateurs quart-d'onde peuvent être enroulés (Cai, Guo, Hu & Yang, 2014), représenté par la figure 1.2(a). Dans le cas des résonateurs d'Helmholtz, une solution est de placer le col à l'intérieur de la cavité (Cai *et al.*, 2014; Huang *et al.*, 2019; Duan, Yu, Xu, Xin & Lu, 2020; Chen, Lee & Park, 2020), comme illustré par la figure 1.2. En approximation à basse fréquence (grande longueur devant les dimensions du matériau), un résonateur d'Helmholtz peut être représenté par un système masse-ressort (Rayleigh, 1896). Le col peut être représenté par une masse et la cavité par une raideur. Dans le cas du matériau de Huang *et al.* (2019), la fréquence et la valeur du coefficient d'absorption du matériau sont quasiment inchangées pour le col à l'extérieur de la cavité ou à l'intérieur, voir figure 1.2(b). En effet, la masse est identique pour les deux configurations tandis que le volume de la cavité est légèrement diminué. La fréquence de résonance est alors peu altérée, alors que l'épaisseur du dispositif est réduite. Cai *et al.* (2014) mettent en avant un ratio de longueur d'onde à la première résonance sur épaisseur $\lambda_1/e = 50$ pour le résonateur quart-d'onde enroulé ($e = 17.3$ mm) et $\lambda_1/e = 102$ pour le résonateur d'Helmholtz modifié ($e = 13.3$ mm). Huang *et al.* (2019) obtiennent un $\lambda_1/e = 50$ pour une épaisseur totale de 50 mm. Cependant, le critère λ_1/e prend en compte seulement l'épaisseur et non le volume (ce critère est discuté plus en détail dans la section 1.1.6). La forme des cols des résonateurs d'Helmholtz peut être modifiée pour obtenir une absorption à des fréquences plus basses ou une largeur de bande de fréquence à mi-hauteur plus grande (Park, 2013; Mercier, Marigo & Maurel, 2017; Duan *et al.*, 2020).

De façon similaire aux résonateurs d'Helmholtz à un col et une cavité, Simon (2018) a proposé de modifier des plaques perforées suivies d'une cavité. Les perforations sont rallongées avec des tubes positionnés à l'intérieur de la cavité. La figure 1.2(c) montre un schéma du matériau.

Les matériaux structurés mentionnés précédemment ont une seule fréquence de résonance en basses fréquences. Doria (1995) proposa un résonateur d'Helmholtz à deux degrés de liberté en série (col-cavité-col-cavité). Ce système possède alors deux fréquences de résonances. Par la suite, ce système a été mis en œuvre pour de silencieux et nommé « *Dual Helmholtz Resonator* » (Xu, Selamet & Kim, 2010). Pour les résonateurs d'Helmholtz, le principe a été étendu à trois degrés de liberté (Guan & Jiao, 2012) et même *N* degrés de liberté (Al Jahdali & Wu, 2018). Pour minimiser l'encombrement, les cols peuvent également être placés à l'intérieur de la cavité (Guo, Fang, Jiang & Zhang, 2020; Duan *et al.*, 2021; Simon & Sebbane, 2021). Cependant, les longueurs d'onde correspondant aux fréquences de résonance ne sont pas toujours inférieures à l'épaisseur du matériau.

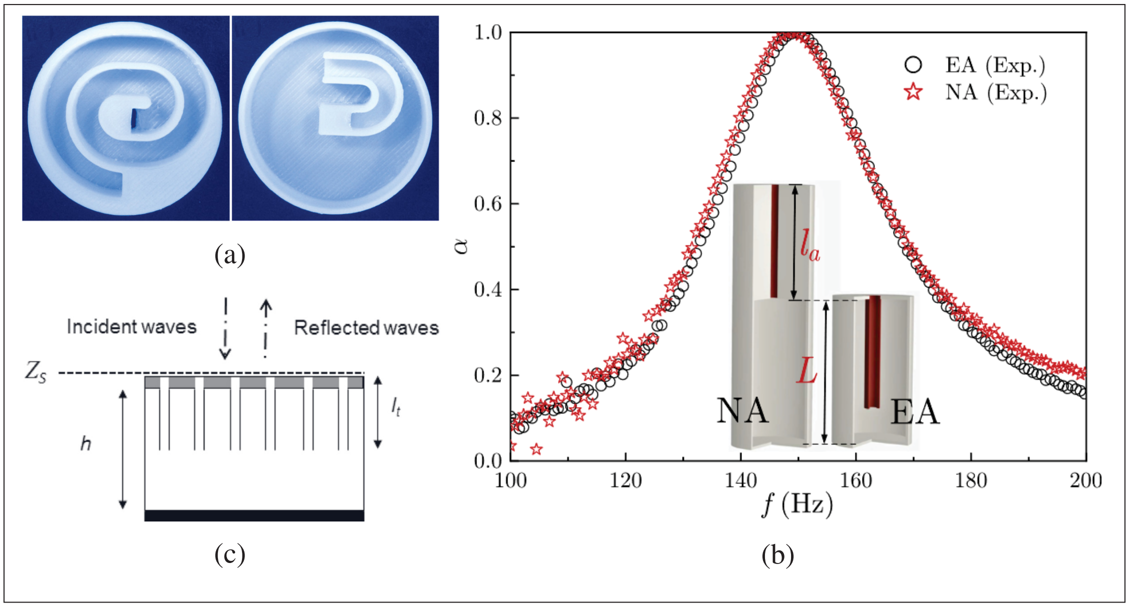

Figure 1.2 Représentation de résonateurs à géométrie modifiée. (a) Résonateurs quart d'onde et d'Helmholtz enroulés. Tiré de Cai *et al.* (2014). (b) Absorptions et schémas d'un résonateur d'Helmholtz conventionnel (noté NA) et avec col à l'intérieur de la cavité (EA). Tiré de Huang *et al.* (2019). (c) Schéma de plaques perforées connecté à des tubes. Tiré de Simon (2018)

1.1.2 Combinaison de résonateurs désaccordés en parallèle

Dans le but d'obtenir une efficacité sur une bande de fréquence plus large, plusieurs résonateurs désaccordés (fréquences de résonance des résonateurs légèrement différentes) peuvent être combinés dans une cellule périodique élémentaire. En modifiant les propriétés de ces matériaux, un couplage entre les différentes résonances peut être obtenu.

Zhao, Wang, Wen, Lam & Umnova (2018) ont étudié une combinaison de résonateurs d'Helmholtz désaccordés positionnés en parallèle. Les résonateurs d'Helmholtz étaient composés de deux fentes débouchant sur deux cavités, voir la figure 1.3(a). Lorsque les deux résonateurs ont des fréquences de résonances proches, un couplage s'opère : l'absorption des deux résonateurs couplés est meilleure que leur absorption individuelle, comme illustrée par la figure 1.3(b). L'absorption va alors dépendre des paramètres géométriques de chacun des résonateurs et de la distance entre les fentes. Le système est dit couplé critiquement lorsque le coefficient d'absorption tend vers 100 % pour les deux fréquences des résonateurs. Dans le cas du matériau présenté par Zhao *et al.* (2018), la largeur de bande de fréquence est limitée, car seulement deux résonateurs sont utilisés. Par conséquent en augmentant le nombre de résonateurs la largeur de la bande de fréquence va également augmenter (Peng, Ji & Jing, 2018). La figure 1.3(c) représente un matériau avec une cellule périodique élémentaire composée de neuf résonateurs d'Helmholtz désaccordés. La courbe du coefficient d'absorption de ce matériau est représentée par la figure 1.3(d).

Des combinaisons de résonateurs à géométrie modifiée (section 1.1.1) désaccordés mis en parallèle ont également été proposées. La cellule périodique élémentaire peut être composée de résonateurs quart-d'onde enroulés désaccordés (Zhang & Hu, 2016) (voir figure 1.3(e)), de résonateurs d'Helmholtz à plusieurs degrés de liberté désaccordés Liu *et al.* (2019), des résonateurs d'Helmholtz ou des plaques perforées dont les cols sont rallongés dans la cavité à un degré de liberté désaccordés (Guo *et al.*, 2020; Guo, Fang, Jiang & Zhang, 2021a; Guo, Zhou, Fang & Zhang, 2021d) ou plusieurs (Guo *et al.*, 2021c; Guo, Fang, Qu, Liu & Zhang, 2021b).

1.1.3 Membranes et films avec masses

Les membranes et films avec masses sont utilisés pour des problèmes d'isolation sonore (au travers du matériau) ou d'absorption sur mur rigide (sans transmission). Les matériaux structurés composés d'une membrane et d'une masse furent proposés par Yang, Mei, Yang, Chan & Sheng (2008) pour des problématiques d'isolation sonore. Généralement, ces matériaux sont composés d'une cellule périodique élémentaire qui est reproduite dans deux dimensions de l'espace.

Les prochaines sections s'intéressent à ces matériaux pour les problématiques d'isolation, section 1.1.3.1, et d'absorption sur mur rigide section 1.1.3.2.

1.1.3.1 Membranes et films avec masses pour l'isolation

Ces structures sont de faible épaisseur devant la longueur d'onde et ont fait l'objet d'autres études. Un moyen de rendre ces dispositifs efficaces sur une plus grande plage de fréquence

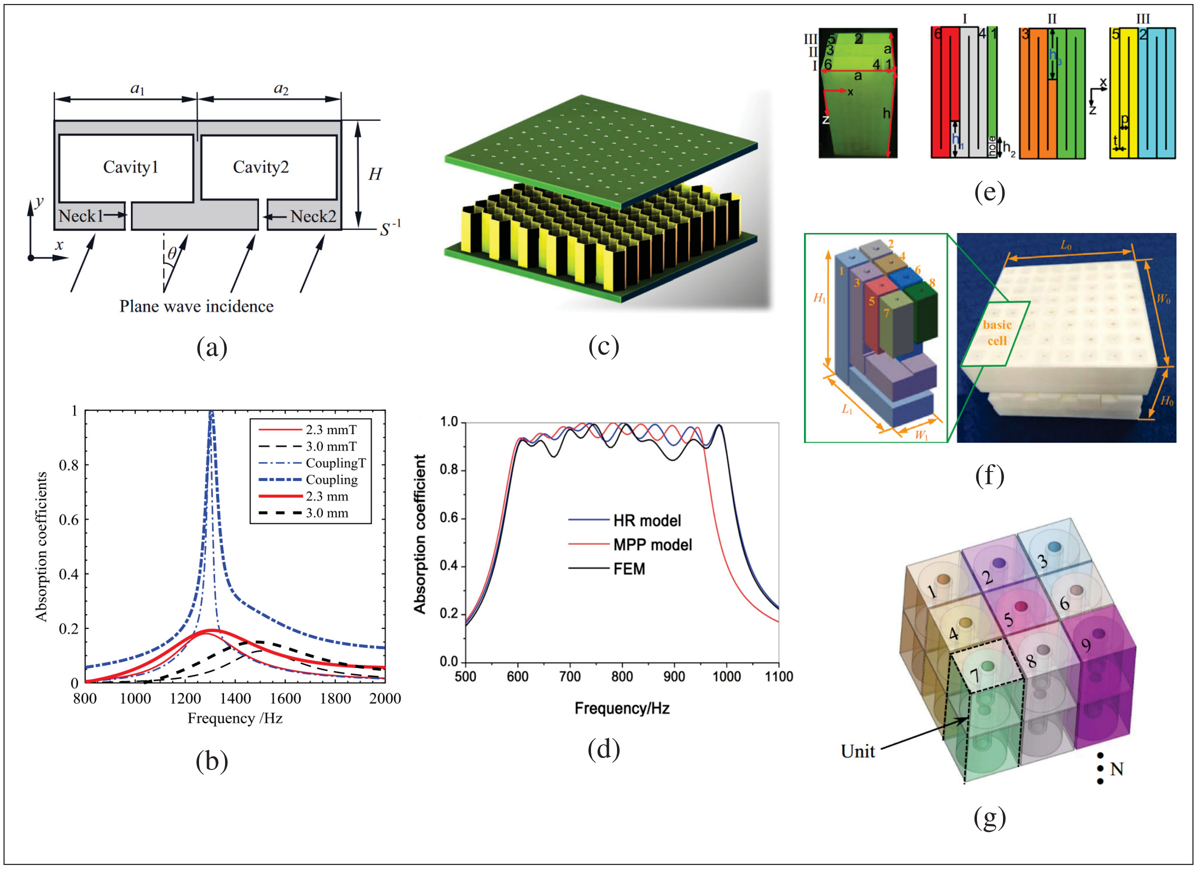

Figure 1.3 (a) Schéma du matériau composé de deux fentes avec cavités et (b) coefficient d'absorption en incidence normale pour différentes largeurs de fente du matériau (2.3 et 3 mm). Le « T » indique les résultats obtenus théoriquement, les autres sont issus de simulations numériques. (a) et (b) sont tirés de Zhao *et al.* (2018). (c) Représentation d'une structure à nid d'abeille couverte d'une plaque perforée. (d) Coefficient d'absorption en incidence normale de l'échantillon. Tiré de Peng *et al.* (2018). (e) Photo et vues en coupe d'un échantillon d'un matériau absorbant labyrinthe 3D. Tiré de Zhang & Hu (2016). (f) Photo d'un échantillon composée de résonateurs d'Helmholtz à plusieurs degrés de libertés et zoom sur la cellule périodique élémentaire. Tiré de Liu *et al.* (2019). (g) Schéma de la cellule périodique élémentaire d'un matériau composé de neuf résonateurs d'Helmholtz à deux degrés de liberté et à cols rallongés dans les cavités. Tirée de Guo *et al.* (2021c)

est de mettre plusieurs systèmes de membrane avec masse légèrement désaccordés à la suite (multicouches) (Yang, Dai, Chan, Ma & Sheng, 2010). Une autre manière est d'utiliser plusieurs masses dans une cellule périodique élémentaire (Mei *et al.*, 2012; Leblanc & Lavie, 2017; Lu, Yu, Lau, Khoo & Cui, 2020).

Une variante de ces solutions est l'utilisation de films à la place des membranes appelée « Plate-type Acoustic Metamaterial »(Ang, Koh & Lee, 2018; Langfeldt & Gleine, 2019a,b, 2020). Une photo de ce type de matériau est montrée par la figure 1.4(a). Dans cette variante, la cellule unitaire n'a pas besoin d'être maintenue par un cadre, ce qui rend l'ensemble du matériau plus léger (Langfeldt & Gleine, 2020). De façon similaire aux matériaux structurés composés de membranes avec masses, la largeur de bande de fréquence peut être augmentée en réalisant un multicouche ou en positionnant plusieurs masses dans une cellule périodique élémentaire (Langfeldt & Gleine, 2019b, 2020).

Pour améliorer l'isolation sonore d'une plaque, des résonateurs masse-ressort (Xiao, Wen & Wen, 2012) ou des matériaux poro-élastique peuvent être ajoutés Li, Dauchez & Nennig (2023a).

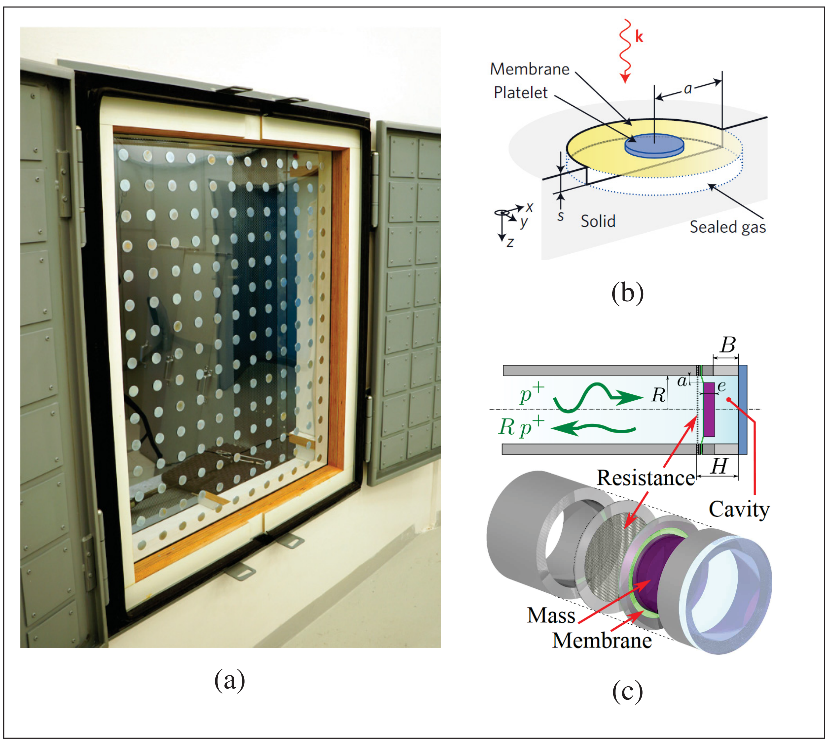

Figure 1.4 (a) Photo d'un échantillon et du dispositif expérimental d'un matériau composé d'un film (transparent) avec plusieurs masses identiques (disques blanc). Tirée de Langfeldt & Gleine (2020). (b) et (c) schémas de matériaux composés de membranes avec masses. (b) Tiré de Ma *et al.* (2014). (c) Tiré de Aurégan (2018)

1.1.3.2 Membranes et films avec masses pour l'absorption sur mur rigide

Pour améliorer l'absorption sur mur rigide des structures composées de membranes avec masses, Ma *et al.* (2014) les ont couplées avec une cavité remplie d'un gaz. Le gaz emprisonné est de l'hexafluorure de soufre pour obtenir une résonance à des fréquences plus basses. La figure 1.4(b) représente le matériau qu'ils ont étudié. Un pic d'absorption est observé pour une résonance hybride de la cavité et du système masse plus membrane. Les auteurs ont mesuré un coefficient d'absorption en incidence normale du système proche de 99 % à 152 Hz alors que la structure n'a qu'une épaisseur de 17 mm ($\lambda_1/e = 133$). La fréquence de résonance dépend fortement de la tension de la membrane (surface de la masse plus petite que celle de la membrane, voir figure 1.4(b)). Pour s'affranchir de cette contrainte et obtenir un matériau plus robuste, Aurégan (2018) a étudié un matériau où la surface de la masse est proche de celle de la membrane, voir le schéma représenté par la figure 1.4(c). Un écran résistif est utilisé pour obtenir une absorption parfaite. La tension de la membrane a peu d'impact sur la fréquence de résonance de la structure étudiée. Un coefficient d'absorption supérieur à 99 % à 112 Hz est rapporté pour un rapport $\lambda_1/e = 201$ (l'épaisseur totale est de 16 mm). Cependant en basses fréquences ces matériaux n'ont qu'une seule fréquence de résonance et la largeur du pic à mi-hauteur est très faible, de l'ordre de 2 Hz pour les matériaux présentés dans ce paragraphe.

1.1.4 Matériaux résonants couplés avec des matériaux passifs

Les matériaux présentés précédemment sont efficaces (en particulier en basses fréquences) sur une bande de fréquences plus ou moins large. Pour élargir la bande de fréquence, ces matériaux peuvent être couplés avec des matériaux passifs conventionnels (comme des mousses et fibreux). Les matériaux poreux sont plus adaptés pour dissiper l'énergie acoustique en moyennes et hautes fréquences (efficace à partir de $\lambda_1/e \approx 4$ pour configuration sur mur rigide). Une première solution possible est d'inclure des résonateurs à structure rigide dans un matériau poreux (Doutres, Atalla & Osman, 2015; Kone, Ghinet, Panneton, Dupont & Grewal, 2021a; Zhu, Lau, Lu & Jeon, 2019; Lagarrigue, Groby, Tournat, Dazel & Umnova, 2013; Groby *et al.*, 2015b). Un exemple est représenté sur les figures 1.5(a)-(b). Une autre solution possible est de créer des inclusions d'air dans un matériau poreux. Ces inclusions peuvent résonner et absorber le son (Nori & Venegas, 2017; Zieliński *et al.*, 2024), voir un exemple de ce type de matériau en figure 1.5(c). En fonction de la perméabilité du matériau poreux, l'inclusion d'air faite dans un matériau poreux peut résonner à une fréquence plus basse comparée à la même inclusion d'air usinée dans une matière rigide.

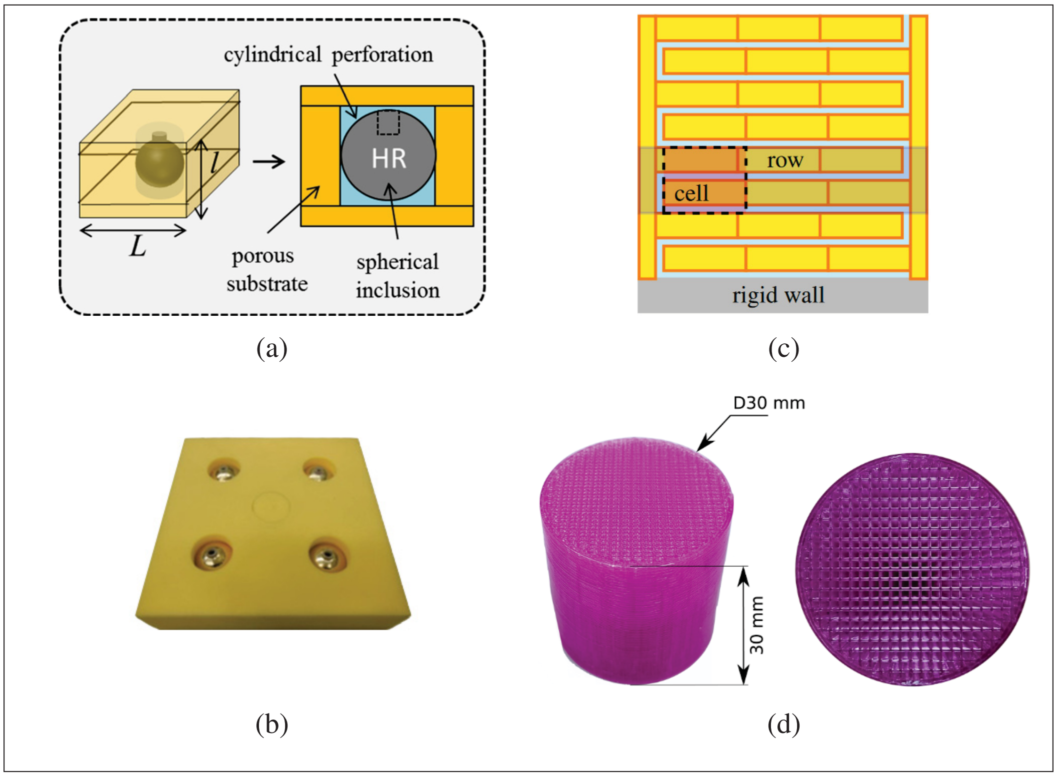

Figure 1.5 (a) Schéma d'une cellule périodique élémentaire et (b)) photo d'un matériau composé de résonateurs d'Helmholtz (boules de Noël) couplé avec un matériau poreux. Adaptées avec autorisation de Doutres *et al.* (2015). (c) schéma d'un résonateur quart-d'onde à tortuosité augmentée dans un matériaux poreux (ici en jaune). Tirée de Zieliński *et al.* (2024). (d) Photo d'un matériau poreux par impression 3D. Tirée de Boulvert *et al.* (2019)

Pour obtenir une efficacité sur une bande de fréquence plus large ou augmenter les pertes d'un matériau résonant, les matériaux poreux peuvent être intégrés dans des résonateurs (Gao, Wu, Lu & Zhong, 2021). Boulvert *et al.* (2019) se sont intéressés à l'impression 3D de matériaux poreux, le matériau est représenté par la figure 1.5(d). En optimisant les paramètres caractéristiques du matériau poreux, ils ont réussi à décaler la fréquence d'absorption vers des fréquences légèrement plus basses. Ce type de solution peut être couplé avec des résonateurs quart-d'onde torsadés pour obtenir une absorption en plus basses fréquences (Boulvert *et al.*, 2022).

Les matériaux poreux sont également présents pour des problématiques de transmission. Ils peuvent être intégrés dans les doubles parois. Dans le cas des matériaux avec film et membrane, l'ajout d'un matériau poreux permet d'améliorer l'atténuation globale du matériau. Notamment aux fréquences de résonances (fréquences pour lesquelles le son est fortement transmis dans une configuration sans poreux) (Langfeldt & Gleine, 2019b).

1.1.5 Cristaux soniques résonants

Des phénomènes de bandes interdites apparaissent dans les structures périodiques (appelés aussi cristaux soniques). Les bandes interdites sont des plages de fréquences pour lesquelles le son ne se propage pas dans le matériau (la réflexion tend à être totale, ainsi la transmission tend à être nulle). Dans un réseau de Bragg, l'apparition des bandes interdites provient du phénomène de diffraction (diffraction de Bragg) engendré par la structure périodique. Ce phénomène a été observé expérimentalement en acoustique en premier par Martínez-Sala *et al.* (1995). La structure étudiée était constituée de cylindres métalliques périodiques, illustrée par la figure 1.6(a). Pour ces structures, une chute du coefficient de transmission est observée pour les sons dont la demi-longueur d'onde est égale à l'espacement entre les éléments périodiques.

Dans le cas de réseau périodique de résonateurs ou cristaux soniques résonants, des effets de bande interdite apparaissent proches de la résonance des résonateurs. Ces phénomènes peuvent s'expliquer à partir des paramètres effectifs (comme masse volumique effective ou module de compressibilité effectif) qui peuvent devenir négatifs dans la bande interdite pour ces structures. La masse volumique effective est modifiée dans le cas de réseau périodique 1D de membranes (Lee, Park, Seo, Wang & Kim, 2009a), le schéma du matériau est donné par la figure 1.6(b). Le module de compressibilité est modifié dans le cas d'un guide d'onde avec un réseau de résonateur affleurant (Lee, Park, Seo, Wang & Kim, 2009b; Fang *et al.*, 2006), le schéma du matériau est donné par la figure 1.6(c). Seo *et al.* (2012) ont proposé de combiner des réseaux périodiques de membranes et de résonateurs affleurants, le matériau est représenté par la figure 1.6(d). Les auteurs ont obtenu des bandes de fréquence où la masse volumique ou/et le module de compressibilité d'effectifs deviennent négatifs, correspondant à plusieurs bandes de fréquences interdites.

Dans le cas de la propagation d'onde dans un conduit, Wang & Mak (2012) ont étudié l'atténuation apportée par une répétition de résonateurs identiques. En faisant coïncider la fréquence de résonance du résonateur avec la fréquence centrale de Bragg (qui dépend de la distance entre deux résonateurs), ils ont montré que l'atténuation est sur une bande de fréquence plus large. Cependant, ces types de solutions ne sont pas adaptés pour la problématique, car ils demandent une distance entre les éléments périodiques égale à la demi-longueur d'onde.

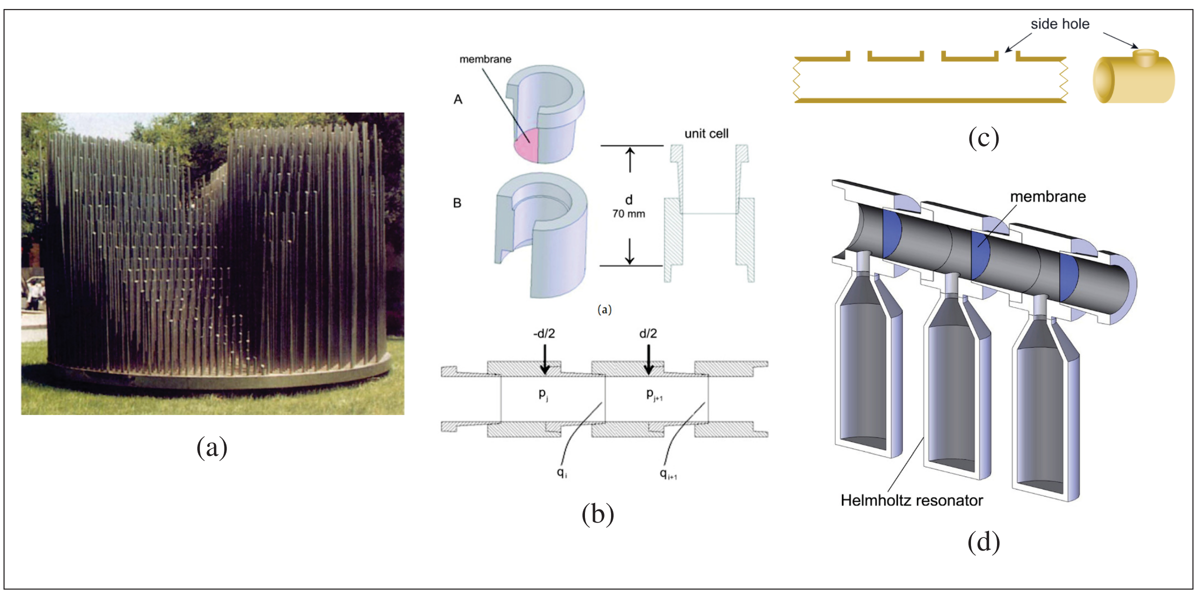

Figure 1.6 (a) Photo de la sculpture étudiée par Martínez-Sala *et al.* (1995). Tirée de Martínez-Sala *et al.* (1995). (1995). (b) Schéma d'un réseau périodique 1D de membrane. Tiré de Lee *et al.* (2009a). (c) Schémas d'un réseau périodique de trous latéraux. Tiré de Lee *et al.* (2009b). (d) Schéma d'un réseau périodique 1D de membrane couplé d'un réseau de résonateur d'Helmholtz. Tirée de Seo *et al.* (2012)

1.1.6 Matériaux à compressibilité effective augmentée

Les matériaux à compressibilité effective augmentée sont composés d'un pore principal qui peut être un résonateur quart d'onde ou demi-onde (en fonction des conditions aux limites). Sur ce pore principal, un réseau périodique de résonateurs est ajouté. À cause de la périodicité, ces matériaux présentent des bandes interdites (voir section 1.1.5). Cependant, une autre propriété de la périodicité est utilisée dans ces matériaux. Dans un guide d'onde, l'ajout d'un réseau périodique de résonateurs vient augmenter la compressibilité effective en basses fréquences (Leclaire *et al.*, 2015). La célérité effective du son dans le pore principal est alors diminuée. Les fréquences de résonance du pore principal sont alors décalées vers les basses fréquences sans que la longueur du pore soit augmentée. Cette famille de matériaux est aussi appelée « *slow sound material* » (Groby *et al.*, 2015a).

Dans le cas où les matériaux à compressibilité effective augmentée sont placés sur un fond rigide (aucune transmission), le matériau est composé d'un résonateur quart d'onde (pore principal), auquel est connecté un réseau latéral de résonateurs. Différents types de résonateurs latéraux ont été étudiés. D'abord des résonateurs quart-d'onde ont été utilisés (Leclaire *et al.*, 2015; Groby *et al.*, 2015a; Groby, Pommier & Aurégan, 2016), représentés par la figure 1.7(a). Des recherches se sont intéressées à l'utilisation de résonateurs d'Helmholtz (Jiménez, Huang, Romero-García, Pagneux & Groby, 2016; Jiménez, Groby, Pagneux & Romero-García, 2017b), illustrées par la figure 1.7(b). Dupont *et al.* (2018) se sont basés sur l'approximation basses fréquences de la fréquence de résonance des matériaux à compressibilité effective (la fréquence de résonance est proportionnelle au volume des résonateurs latéraux) pour proposer un matériau avec un réseau de cavités annulaires fines appelées « pancakes ». Le matériau est nommé dans ce document matériau à compressibilité effective augmentée composé d'un réseau de résonateurs *pancakes*. La figure 1.7(c) est une vue en coupe de la géométrie étudiée par Dupont *et al.* (2018). La figure 1.7(d) représente une courbe d'absorption pour un matériau à compressibilité effective augmentée composé d'un réseau de résonateurs *pancakes* (Dupont *et al.*, 2018). Pour ces matériaux d'épaisseur de 31 mm, plusieurs pics d'absorption sont observés en basses fréquences. Pour le premier pic d'absorption, les résultats des modèles sont en accord avec ceux des mesures expérimentales. Mais les résultats diffèrent pour les pics d'absorption plus élevés. L'hypothèse principale avancée pour expliquer cette différence concerne la fabrication du matériau par impression 3D (qui peut induire des imprécisions sur les dimensions et les formes de la géométrie ainsi que des effets de la vibration des parois) et l'hypothèse de propagation en onde plane dans tout le matériau pour le modèle analytique. Les différents modèles montrent qu'avec l'augmentation de la fréquence les pics d'absorption sont plus rapprochés en fréquence. Le nombre de pics d'absorption dépend du nombre de résonateurs latéraux. Un effet de bande de fréquence large est présent en moyennes fréquences, mais avec une amplitude du coefficient d'absorption faible. Pour des fréquences plus élevées, le coefficient d'absorption chute vers zéro. Cette chute du coefficient d'absorption correspond à l'apparition d'une bande interdite (Jiménez *et al.*, 2016; Dupont *et al.*, 2018). La bande interdite apparaît à une fréquence proche de la fréquence de résonance du résonateur latéral (cavité *pancake* annulaire dans le cas du matériau de Dupont *et al.* (2018)).

Les matériaux à compressibilité effective augmentée permettent d'obtenir plusieurs pics d'absorption pour des ratios λ/e grands, notamment pour le premier pic d'absorption. Bien que ces matériaux soient similaires, différents ratios de λ_1/e pour le premier pic d'absorption sont rapportés dans le tableau 1.1. Le critère λ_1/e reste à nuancer. Comme énoncé auparavant, ce critère ne prend pas en compte le volume d'occupation des échantillons de matériaux. Dans cette idée, un autre critère est proposé dans ce manuscrit : $\lambda_1/\sqrt[3]{V_{cell}}$. Les valeurs obtenues par ce dernier critère pour différents échantillons de matériaux à compressibilité effective augmentée sont rapportées dans le tableau 1.1. L'échantillon optimisé proposé par Jiménez *et al.* (2016) montre une valeur très élevée de λ_1/e. L'échantillon a été optimisé selon ce critère et il possède qu'une seule fréquence de résonance (la géométrie possède un seul résonateur d'Helmholtz latéral). Même si cet échantillon est peu épais, le volume a été augmenté selon les autres directions (largeur et hauteur) pour obtenir une absorption à des fréquences plus basses. Dans ce sens, cet échantillon présente une valeur de $\lambda_1/\sqrt[3]{V_{cell}}$ similaire aux autres échantillons de matériaux à compressibilité effective augmentée composés d'un réseau de résonateurs d'Helmholtz. De façon similaire, l'échantillon étudié par Brooke *et al.* (2020) présente un meilleur ratio λ_1/e que

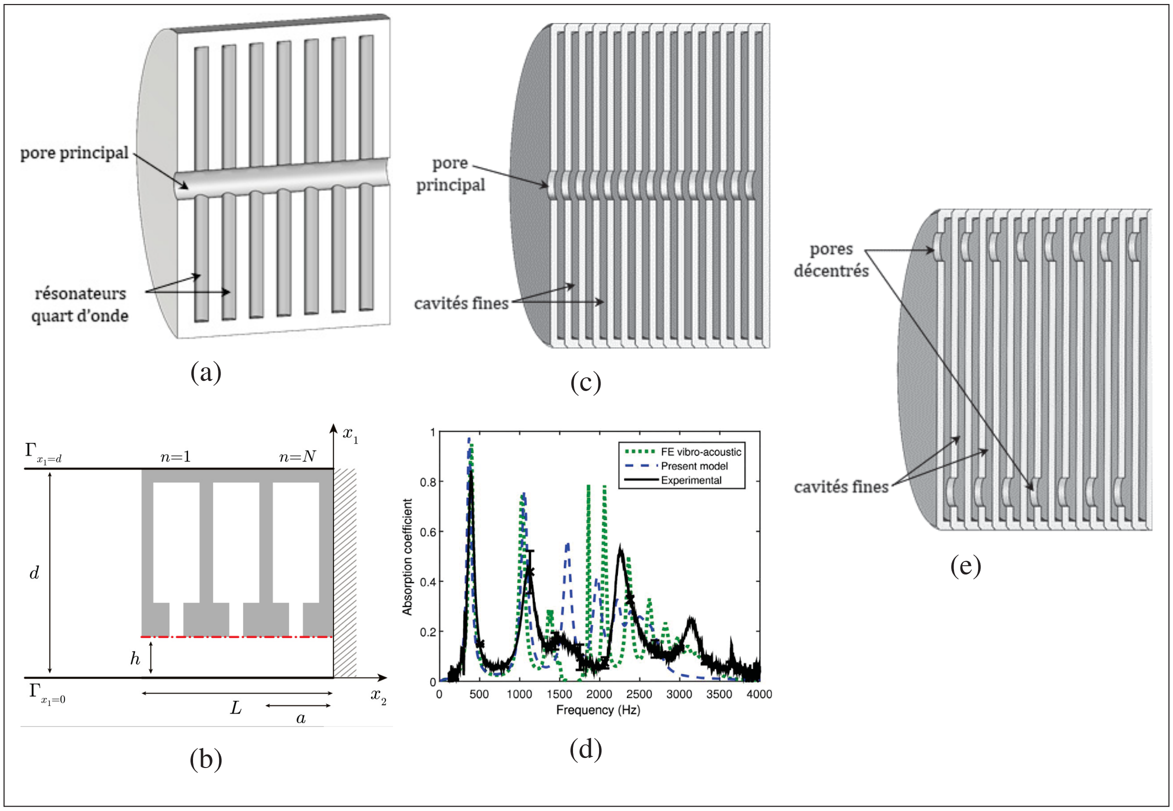

Figure 1.7 (a) Schéma d'un matériau à compressibilité effective augmentée composé de plusieurs quart-d'onde connectés à un tube (ouverte-fermée). (b) Schéma d'un matériau à compressibilité effective augmentée composé de trois résonateurs d'Helmholtz connectés à une fente (ouverte-fermée). Tiré de Jiménez *et al.* (2016). (c) Vue en coupe et (d) courbe d'absorption d'un matériau à compressibilité effective augmentée composé de quinze résonateurs *pancakes* (Dupont *et al.*, 2018). (d) Tiré de Dupont *et al.* (2018). (e) Schéma d'un matériau à compressibilité effective augmentée composé de quinze résonateurs *pancakes* dont les pores sont décentrés

celui proposé par Dupont *et al.* (2018). À même épaisseur, le volume est plus élevé dans le cas de l'échantillon étudié par Brooke *et al.* (2020). Les deux échantillons présentent des valeurs de $\lambda_1/\sqrt[3]{V_{cell}}$ quasiment identiques.

Des formules analytiques des différentes fréquences caractéristiques de ces matériaux (fréquences de résonance et début de bande interdite par exemple) seraient intéressantes notamment pour proposer des matériaux plus performants en basses fréquences.

Tableau 1.1 Comparaison des fréquences du premier pic d'absorption, de différents critères d'efficacité en basse fréquence et des dimensions géométriques (épaisseur e et volume de la cellule périodique élémentaire V_{cell}) de différents matériaux à compressibilité effective augmentée

Type de résonateur latéral	Article	f_1 (Hz)	e (mm)	V (mm^3)	$\frac{\lambda_1}{e_{cell}}$ (-)	$\frac{\lambda_1}{\sqrt[3]{V_{cell}}}$ (-)
quart-d'onde	(Groby *et al.*, 2015a)	590	42	74088	14	13.7
quart-d'onde	(Groby *et al.*, 2016)	645	30	105840	17.7	11.1
Helmholtz	(Jiménez *et al.*, 2016)	275	36	30240	34.5	39.7
Helmholtz	(Jiménez *et al.*, 2016)	338.5	11	18029	88	38.3
Helmholtz	(Jiménez *et al.*, 2017b)	250	57.2	163592	24	24.9
Helmholtz	(Jiménez *et al.*, 2017b)	290	65.3	71068	18	28.3
pancakes	(Dupont *et al.*, 2018)	400	31	48084	26.4	23.4
pancakes	(Brooke *et al.*, 2020)	231	30	235619	49.0	23.8
pancakes	(Kone *et al.*, 2021b)	210	44.5	69055	36.4	39.5
pancakes décentrés	(Kone *et al.*, 2021b)	185	44.5	69055	41.3	44.8

Dans le but d'obtenir une absorption sur une plus grande bande de fréquence en basses fréquences, Groby *et al.* (2016) ont proposé d'utiliser une combinaison de résonateurs désaccordés en parallèle. La cellule périodique élémentaire est composée de trois résonateurs à compressibilité effective augmentée. Kone *et al.* (2021b) ont pris comme point de départ un matériau à compressibilité effective augmentée composé d'un réseau de résonateurs *pancakes* dont ils ont décentré les pores reliant les cavités. La tortuosité globale du matériau est augmentée, ce qui a pour conséquence d'obtenir une absorption à des fréquences plus basses par rapport au même matériau avec un pore principal droit (de l'ordre de 30 Hz pour le premier pic d'absorption pour les matériaux étudiés par Kone *et al.* (2021b), voir tableau 1.1.).

Une application différente des matériaux à compressibilité effective augmentée vise à diminuer la transmission d'onde acoustique qui se propage au travers du pore principal. Le matériau est composé d'un pore principal ouvert de part et d'autre du matériau. Le pore principal est un résonateur demi-onde (ouvert-ouvert). La figure 1.8(a) représente un schéma de ce type de matériau. Les réseaux de résonateurs d'Helmholtz sont majoritairement utilisés pour cette application Jiménez, Romero-García, Pagneux & Groby (2017c); Romero-García *et al.* (2020). Ces matériaux sont utilisés pour réduire à la fois la réflexion et la transmission. À la résonance demi-onde (et multiple), les coefficients de réflexion et de transmission tendent à être nuls. Pour une réflexion et une transmission parfaitement nulles (théoriquement), une cellule périodique élémentaire composée d'un seul résonateur à compressibilité effective augmentée ne suffit pas (Romero-García *et al.*, 2020). Pour les matériaux symétriques, une résonance symétrique (ex. : résonance d'une demi-longueur d'onde) et asymétrique (ex. : résonance d'une longueur d'onde) doivent avoir lieu à des fréquences proches. Dans ce cas, la cellule périodique élémentaire est composée de deux résonateurs à compressibilité effective augmentée dont l'un possède un résonateur d'Helmholtz latéral et le second deux résonateurs latéraux. Un schéma est donné par la figure 1.8(b).

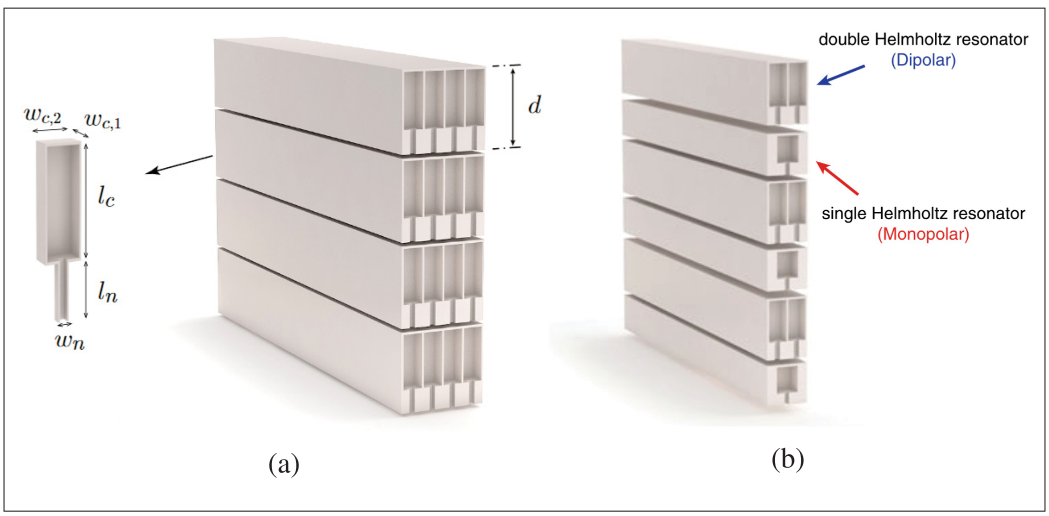

Figure 1.8 (a) Schéma d'un matériau à compressibilité effective augmentée composé de quatre résonateurs d'Helmholtz connectés à une fente (ouverte-ouverte). Tiré de Jiménez *et al.* (2017c). (b) Schéma d'une combinaison de deux résonateurs à compressibilité effective augmentée proposé par Romero-García *et al.* (2020). Tiré de Jiménez *et al.* (2021)

1.1.7 Trous noirs acoustiques

Les trous noirs acoustiques sont des structures qui « piègent » les ondes vibratoires ou acoustiques grâce à leur forme géométrique (profil) qui évolue avec l'épaisseur. Pour les ondes vibratoires, ces dispositifs ont été proposés en premier temps pour diminuer la réflexion de l'onde à la terminaison d'une structure finie (Pelat, Gautier, Conlon & Semperlotti, 2020). Cela s'explique par une augmentation de l'amplitude de l'onde mécanique (acoustique ou vibratoire) et une diminution locale de sa célérité. Théoriquement, la réflexion pourrait être nulle si l'épaisseur diminuait progressivement jusqu'à zéro. Dans le cas des ondes acoustiques, le dispositif proposé est composé d'une succession de cavités espacées par des anneaux rigides (plaque à une perforation) dont la section de l'anneau décroît (Guasch, Arnela & Sánchez-Martín, 2017; Guasch, Sánchez-Martín & Ghilardi, 2020). La figure 1.9(a) représente un schéma d'un trou noir acoustique. L'absorption de ce type de matériau est sur une bande de fréquence large, cependant elle n'est pas basses fréquences (longueur d'onde à la première résonance proche de l'épaisseur du matériau). Jiménez, Romero-Garcia, Pagneux & Groby (2017a) ont proposé un matériau similaire à un trou noir acoustique. La cellule périodique élémentaire est composée d'un pore principal à largeur décroissante avec un réseau de résonateurs d'Helmholtz différents, représenté par la figure 1.9(b). En optimisant la géométrie, les longueurs d'onde traitées peuvent être de bien plus grandes dimensions que l'épaisseur. Même si la géométrie s'apparente à un trou noir, la diminution de la célérité effective selon le profil du matériau n'a pas été mise en évidence. Le matériau est efficace aux résonances des résonateurs d'Helmholtz. Jiménez *et al.* (2017a) ont mis en évidence l'impact des dimensions des pores reliant les résonateurs d'Helmholtz sur le couplage de la réponse acoustique.

Le nombre d'études concernant les trous noirs acoustiques pour « piéger » les ondes acoustiques est en plein essor (Bednarik & Cervenka, 2024; Yu, Mi, Zhai & Cheng, 2023; Serra, Guasch, Arnela & Miralles, 2023; Chua, Li, Yu & Zhai, 2023; Sheng, He, Pueh Lee & Ding, 2024; Peng *et al.*, 2024; Deng, Guasch & Ghilardi, 2024; Zhang *et al.*, 2024; Chen *et al.*, 2024; Hruška, Groby & Bednařík, 2024). Pour les différencier des trous noirs utilisés en vibration, ces matériaux sont également appelés trous noirs soniques (*sonic black holes*). D'autres études se sont intéressées à des trous noirs acoustiques avec pertes en utilisant des cavités fines, résonateurs *pancakes* (Umnova, Brooke, Leclaire & Dupont, 2023; Bezançon *et al.*, 2024). En utilisant des cavités fines, les effets visco-thermiques augmentent dans les cavités. Dans leurs matériaux,

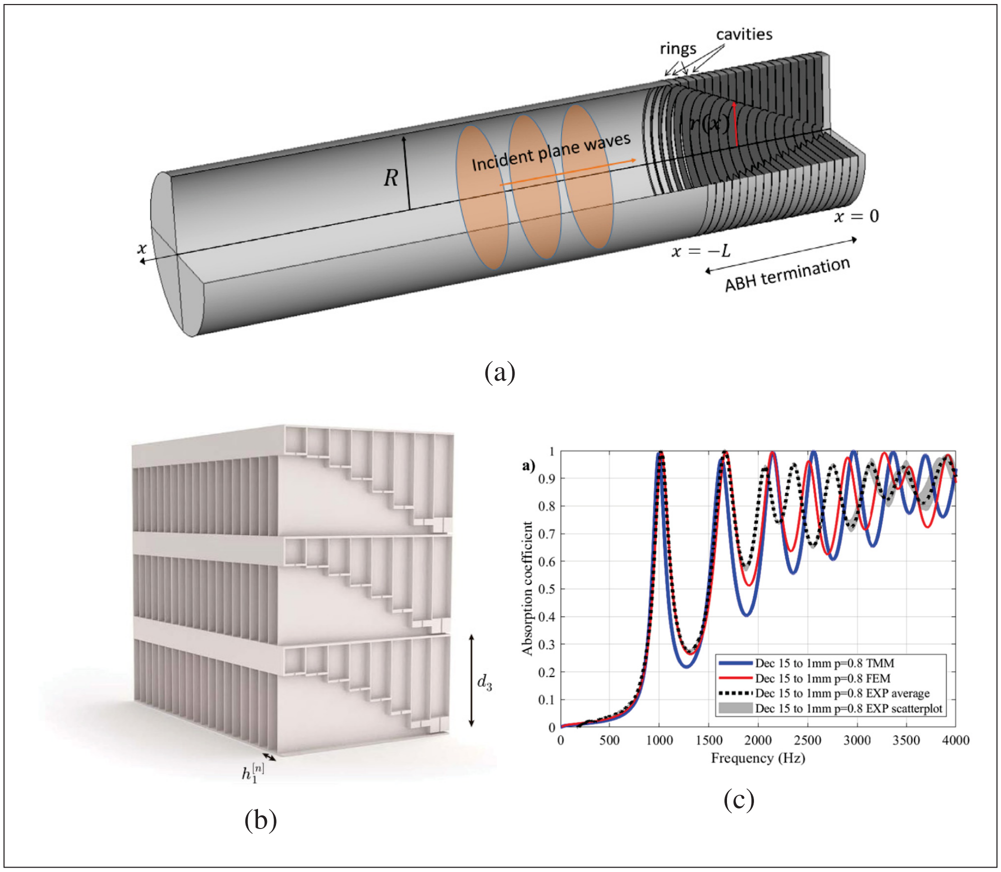

Figure 1.9 (a) Schéma d'un tube d'impédance associé à un trou noir acoustique. Tiré de Guasch *et al.* (2020). (b) Schéma d'un matériau à gradient de propriété géométrique : réseaux de résonateurs d'Helmholtz relié à un pore principal dont la largeur décroît. Tiré de Jiménez *et al.* (2017a). (c) Absorption d'un trou noir sonique à cavités fines. Tiré de Bezançon *et al.* (2024)

la porosité de surface (rapport de la section du premier pore et de la section extérieure de l'échantillon) est de taille bien inférieure à la section du tube, ce qui permet de décaler l'efficacité des trous noirs vers les basses fréquences. La courbe d'absorption pour un échantillon est représentée par la figure 1.9(c). Ces solutions sont efficaces en basses fréquences, Umnova *et al.* (2023) ont rapporté un échantillon avec un premier pic d'absorption avec un rapport $\lambda_1/e = 14$. Elles présentent également un coefficient d'absorption moyen élevé sur une bande de fréquence large en moyennes fréquences, c.-à-d. pour fréquences proches ou supérieures au quart de la longueur d'onde $\lambda/e = 4$ (à noter qu'à volume équivalent les trous noirs acoustiques possèdent une première fréquence de résonance plus élevée qu'un matériau périodique à compressibilité effective augmentée, mais la largeur de bande d'efficacité est plus grande (Bezançon *et al.*, 2024)).

1.2 Comportements acoustiques des matériaux sous fort niveau d'excitation acoustique

1.2.1 Matériaux poreux à squelette rigide

Dans le cas des matériaux poreux à squelettes rigides, l'atténuation d'une onde acoustique peut dépendre du niveau d'excitation acoustique (dépendamment de sa porosité et de sa résistivité au passage de l'air) . Les effets de dissipation ajoutés par l'augmentation du niveau d'excitation acoustique sont davantage liés à des effets visqueux et non à des effets thermiques (Kuntz & Blackstock, 1987; Wilson, McIntosh & Lambert, 1988; McIntosh & Lambert, 1990). Sous faible niveau d'excitation acoustique, la résistivité au passage de l'air est constante, en accord avec la loi de Darcy. Ils peuvent être considérés par une loi linéaire pour la résistivité au passage de l'air (loi de Darcy-Forchheimer) (Kuntz & Blackstock, 1987; Wilson *et al.*, 1988; McIntosh & Lambert, 1990; Lambert & McIntosh, 1990; Aurégan & Pachebat, 1999; Umnova, Attenborough, Shin & Cummings, 2004). Les effets dissipatifs ajoutés par les forts niveaux d'excitation acoustique dépendent de la vitesse acoustique dans le matériau et sont associés à des effets inertiels.

1.2.2 Matériaux perforés

Différentes études se sont intéressées au comportement non-linéaire engendré par les forts niveaux d'excitation acoustique sur une perforation. Ingård & Labate (1950) ont mis en évidence le lien entre les pertes dues aux effets de circulation du fluide et les pertes acoustiques. Avec l'augmentation du niveau d'excitation acoustique, des jets et des vortex en forme d'anneau se forment en alternance de part et d'autre de l'orifice. Une photo des vortex est donnée par la figure 1.10(a). Au niveau des jets et des vortex, l'énergie de l'onde acoustique se transforme en énergie cinétique (dissipation visqueuse) (Ingård & Labate, 1950; Cummings, 1984). Par la suite, Ingard & Ising (1967) ont mesuré simultanément la pression par un microphone et la vitesse particulaire au niveau d'une perforation à l'aide d'un fil chaud. Ils ont montré qu'à des niveaux d'excitation acoustique faibles, la relation entre la pression et la vitesse particulaire est linéaire. Lorsque le niveau d'excitation acoustique augmente, la relation entre la pression et la vitesse tend vers une loi quadratique. Ce qui revient à dire que la résistance acoustique (partie réelle de l'impédance de surface) d'une perforation n'est plus constante, mais croît linéairement avec la vitesse particulaire (c.-à-d. avec le niveau d'excitation acoustique). Ingard & Ising (1967) ont observé que la réactance acoustique de la perforation (partie imaginaire de l'impédance de surface) est moins impactée par les forts niveaux d'excitation acoustique, mais diminue avec l'augmentation du niveau de l'excitation. Cela peut être interprété comme une diminution de la correction de longueur du rayonnement acoustique à l'embouchure due à la formation des jets et vortex. Ce qui a pour conséquence un décalage de la résonance vers les hautes fréquences des systèmes composés de plaques perforées suivies d'une cavité. Différents modèles ont été proposés pour prendre en compte l'augmentation de la résistance acoustique et/ou la diminution de la correction de longueur du rayonnement acoustique à l'embouchure pour les plaques micro-perforées couplées avec des cavités d'air (Melling, 1973; Guess, 1975; Cummings, 1984; Maa, 1994; Tayong, Dupont & Leclaire, 2010; Laly, Atalla & Meslioui, 2018) et les résonateurs d'Helmholtz (Achilleos, Richoux & Theocharis, 2016). Laly *et al.* (2018) modélise la plaque micro-perforée par la méthode des fluides équivalents (Allard & Atalla, 2009a). Les forts niveaux d'excitation acoustique sont pris en compte dans l'expression de la résistivité en ajoutant un terme qui dépend notamment de la vitesse acoustique dans la perforation et d'un coefficient de décharge. Ainsi cette expression est similaire à la loi de Darcy-Forchheimer dans les matériaux poreux.

1.2.3 Matériaux structurés

Plusieurs études analysent le comportement acoustique de matériaux structurés sous forts niveaux. Simon (2018) a mesuré la réponse de plaque perforée avec des cols rallongés dans la cavité

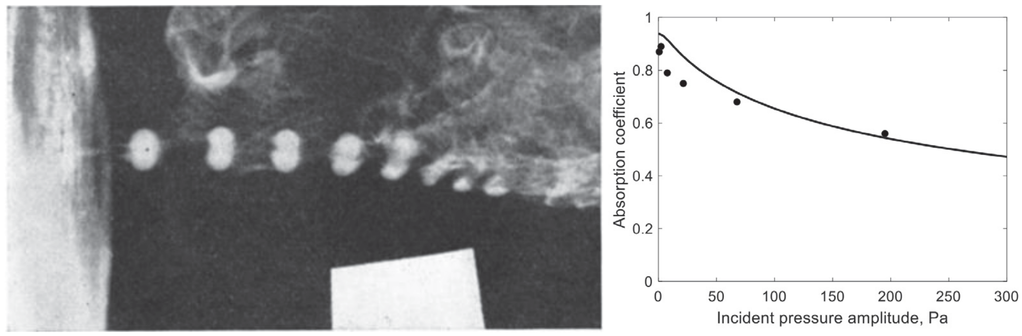

(a) (b)

Figure 1.10 (a) Photo d'anneaux de vortex à la sortie d'un orifice pour une excitation sous forts niveaux. Tirée de Ingård & Labate (1950). (b) Évolution du coefficient d'absorption d'un échantillon d'un matériau à compressibilité effective augmentée composé d'un réseau de résonateurs *pancakes* pour différentes amplitudes de pression acoustique. La courbe en trait plein correspond aux résultats issus du modèle et les points sont des mesures expérimentales. Tirée de Brooke *et al.* (2020)

(voir figure 1.2(c)). Cet allongement permet de réduire la formation de vortex (ratio longueur sur rayon des cols supérieur à 28 pour les matériaux de l'étude). Le coefficient d'absorption varie moins avec le niveau d'excitation acoustique. Zhu, Qu, Gao & Meng (2022) ont étudié par éléments finis le comportement sous forts niveaux d'excitation acoustique de résonateurs d'Helmholtz à col structuré (col en dent de scie). Lors de l'ajout d'une grande rugosité dans le col, le matériau présente une sensibilité aux forts niveaux d'excitation acoustique plus faible.

Brooke *et al.* (2020) ont réalisé une première étude sur les matériaux à compressibilité effective augmentée à réseau de résonateurs *pancakes* sous forts niveaux d'excitation acoustique. Dans leur approche, le matériau est considéré comme homogène et est modélisé de façon similaire à un matériau poreux à squelette rigide. À partir de la mesure de la résistivité au passage de l'air à vitesse élevée, le paramètre de Forchheimer a été déterminé pour les différents échantillons étudiés. Le modèle a été validé avec des mesures du coefficient d'absorption du premier pic pour différents niveaux d'excitation acoustique, représenté par la figure 1.10(b). Par la suite, sur un autre matériau à compressibilité effective augmentée, Zhu, Gao, Dai, Qu & Meng (2023) ont utilisé une loi empirique pour déterminer le paramètre de Forchheimer (Zinn, 1970).

Ces chercheurs se sont seulement intéressés au premier pic d'absorption du matériau. Les résultats obtenus sont en adéquation avec des résultats obtenus par éléments finis et mesures expérimentales sous forts niveaux d'excitation acoustique.

1.3 Analyse de la revue de littérature

La revue de littérature qui a été présentée est sélective. Cette revue sera complétée dans les introductions de chaque article présenté dans ce manuscrit, notamment concernant les modèles théoriques et approches expérimentales.

Plusieurs familles de matériaux structurés pour la réduction en absorption sur mur rigide et/ou en transmission des sons à basses fréquences ont été présentées dans la section 1.1. Dans le but de répondre à la problématique de cette thèse, le matériau d'intérêt doit-être peu épais et/ou volumineux (c.-à-d. avec des critères λ_1/e et/ou $\lambda_1/\sqrt[3]{V_cell}$ élevés), robuste et adapté pour des environnements extrêmes (forts niveaux d'excitation acoustique et vibratoire, écoulement, forts taux d'humidité) présents par exemple dans les carénages de rotors de queue d'hélicoptère. Les membranes avec masses peuvent présenter des valeurs très élevées de λ_1/e et $\lambda_1/\sqrt[3]{V_cell}$, cependant ils semblent moins appropriés et moins robustes (tension de la membrane à conserver) pour être appliqués dans des environnements extrêmes. Les résonateurs à géométrie modifiée et les matériaux à compressibilité effective augmentée sont intéressants pour obtenir une absorption à basses fréquences. Ces deux familles de matériaux présentent des ratios λ_1/e et $\lambda_1/\sqrt[3]{V_cell}$ élevés. Les matériaux à compressibilité effective augmentée ont l'avantage de pouvoir présenter plusieurs pics d'absorption à des longueurs d'onde inférieures à l'épaisseur du matériau. En particulier, les matériaux à compressibilité effective augmentée à réseau de cavités *pancakes* semblent intéressants, voir la figure 1.7(c). Ces matériaux sont à la fois robustes et compacts (grands ratios λ_1/e) (Brooke *et al.*, 2020). Dans cette famille, les matériaux proposés par Dupont *et al.* (2018) permettent d'obtenir des ratios λ_1/e pouvant aller jusqu'à 49 et des ratios $\lambda_1/\sqrt[3]{V_cell}$ pouvant aller jusqu'à 44.8 (voir tableau 1.1). Par conséquent, ils semblent pertinents pour répondre à la problématique de cette thèse. De plus en faisant varier le profil des rayons des pores de ces matériaux, une absorption sur une bande de fréquence large peut être obtenue (voir section 1.1.7). Sous faible niveau d'excitation acoustique, plusieurs points restent à approfondir, notamment concernant la compréhension et l'analyse des effets physiques responsables de l'absorption acoustique et de l'affaiblissement dans la configuration en transmission de ces matériaux. Comment modifier la géométrie des matériaux à compressibilité effective augmentée à réseau de cavités *pancakes* pour obtenir une efficacité d'absorption à des fréquences encore plus basses sans augmenter le volume ? Quelles sont les expressions analytiques des différentes fréquences caractéristiques (premières fréquences de résonance, fréquences de bande interdites par exemple) de ces matériaux ? Quel est le comportement (déformées de la pression acoustique) du matériau aux fréquences de résonance et aux fréquences de bande interdites ? Est-il possible de développer un modèle simple et pratique pour améliorer la compréhension des phénomènes physiques responsables de l'absorption de ces matériaux ? Comment fabriquer des matériaux plus efficaces et le plus fidèle possible aux géométries et aux hypothèses (squelette rigide) des modèles ?

D'un autre côté, peu d'études ont porté sur le comportement non-linéaire des matériaux à compressibilité effective augmentée : Brooke *et al.* (2020) et Zhu *et al.* (2023) dans le cas des forts niveaux d'excitation et Aurégan *et al.* (2016) lors de la présence d'écoulement. Pour prendre en compte les pertes dues à l'augmentation du niveau d'excitation acoustique, Brooke *et al.* (2020) ont mesuré la résistivité au passage de l'air sur l'ensemble du matériau. Ce qui suppose que la résistivité est constante dans le matériau. Cette hypothèse est valable pour de faible écoulement (correspondant aux pertes pour de faibles niveaux d'excitation acoustique). Mais, est-ce que cette hypothèse est vérifiée pour des vitesses d'écoulement plus élevées (correspondant aux pertes pour de forts niveaux d'excitation acoustique) ? Est-ce qu'une approche locale permettrait d'améliorer la précision des modèles sous forts niveaux d'excitation acoustique ? Par ailleurs, Brooke *et al.* (2020) n'ont pas tenu compte de l'influence du niveau d'excitation acoustique sur la correction de longueur contrairement à ce qui est fait pour les plaques perforées. En effet, la validation expérimentale a été effectuée à une seule fréquence autour de la fréquence de résonance, ce qui rend difficile la validation de cette hypothèse. Est-il possible de prendre en compte les effets non-linéaires d'un point de vue local, dans le but d'améliorer la précision des modèles ?

Les trous noirs acoustiques compacts permettent une absorption sur une bande de fréquence large sous faible niveau d'excitation acoustique. Ces solutions pourraient être mises en place dans des applications industrielles où de forts niveaux d'excitation acoustique seraient présents. Dans ces conditions, quel est l'impact des forts niveaux d'excitation acoustique dans les trous noirs acoustiques compacts ?

CHAPITRE 2

OBJECTIFS ET ORGANISATION DU DOCUMENT

2.1 Objectifs

L'objectif principal de cette thèse est le développement de matériaux structurés compacts pour l'absorption acoustique des basses fréquences et l'analyse de leurs réponses acoustiques à des niveaux d'excitation sonore faibles à élevés.

Le premier sous-objectif est l'analyse du comportement et le développement de matériaux structurés périodiques pour le traitement acoustique des basses fréquences dans le domaine linéaire : niveau d'excitation acoustique faible.

Le deuxième sous-objectif est la prise en compte des effets non-linéaires, forts niveaux d'excitation acoustique, et l'analyse du comportement acoustique de matériaux structurés périodiques dans le domaine non-linéaire.

Le troisième sous-objectif porte sur l'analyse du comportement et le développement de matériaux structurés large bande dans les domaines linéaire et non-linéaire avec une application aux trous noirs acoustiques.

2.2 Organisation du document

Le manuscrit de doctorat suit une structure d'une thèse par article. Trois articles en anglais ont été soumis ou publiés dans des revues spécialisées et sont intégrés comme des chapitres dans le présent manuscrit. Le chapitre 6 est présenté comme un article, il correspond à un quatrième article qui n'a pas encore été soumis au moment de la finalisation du manuscrit et est en relecture par les coauteurs. Les différents chapitres du manuscrit visent à répondre à la problématique principale et aux sous-objectifs énoncés précédemment. De l'objectif principal, trois sous-objectifs sont proposés.

Le chapitre 3 répond au premier sous-objectif. Un concept de géométrie de matériaux structurés périodiques est proposé pour le traitement des basses fréquences. Un modèle analytique est développé pour modéliser et analyser le comportement acoustique de ce matériau structuré dans le domaine linéaire. Ce modèle se base sur une analogie masse-ressort. Des approches par éléments finis permettent la vérification du modèle. Des prototypes sont usinés en aluminium dans le but de limiter les imprécisions géométriques et les effets vibratoires. Des mesures (tube d'impédance acoustique) sur ces prototypes sont effectuées à des niveaux d'excitation acoustique faibles, ce qui a permis de valider le modèle analytique pour deux types de configuration : en absorption sur fond rigide et en transmission. Un complément est ajouté à la suite de l'article dans lequel le matériau structuré proposé est comparé à un matériau à compressibilité effective augmentée à réseau de cavités *pancakes* à même volume.

Les chapitres 4 et 5 traitent du deuxième sous-objectif. Les effets acoustiques (effets de circulation du fluide, augmentation des pertes visqueuses) en régime non-linéaire sont complexes. Ces effets sont étudiés pour un matériau à compressibilité effective augmentée à réseau de cavités *pancakes*. En effet, une étude a déjà été menée pour ce matériau sous forts niveaux d'excitation acoustique (Brooke *et al.*, 2020) et certains points restent à approfondir (voir section 1.3). L'augmentation des pertes visqueuses dues aux forts niveaux d'excitation acoustique pour un matériau structuré perforé peut être modélisée à partir de la résistivité au passage de l'air, notamment à l'aide du coefficient de Forchheimer (voir section 1.2). Des simulations numériques (*Computational Fluid Dynamics, CFD*) et des mesures au résistivimètre sont réalisées pour déterminer le coefficient de Forchheimer suivant la loi de Darcy-Forchheimer. Une étude paramétrique est proposée à l'aide des simulations numériques sur l'impact du nombre de cellules périodiques élémentaires. Le coefficient est déterminé pour le matériau au complet (approche globale) et au niveau de chaque pore (approche locale). L'approche locale montre que l'augmentation de la résistivité au passage de l'air avec la vitesse du flux d'air n'est pas constante dans le matériau. La résistivité au passage de l'air du premier pore domine par rapport à celles des autres pores. Les résultats du chapitre 4 sont mis en application dans le chapitre 5 pour prendre en considération les forts niveaux d'excitation acoustique des matériaux à compressibilité effective augmentée composés d'un réseau de résonateurs *pancakes*. Pour cela, le modèle masse-ressort (présenté dans le chapitre 3) est adapté en prenant en compte le coefficient de Forchheimer par une approche globale et une approche locale (déterminé dans le chapitre 4). Les prédictions du modèle masse-ressort dans le cas des approches globale et locale du coefficient de Forchheimer sont comparées à des mesures en tube d'impédance pour des niveaux d'excitation acoustique allant jusqu'à 140 dB. Deux études paramétriques sont menées sur le nombre de cellules périodiques élémentaires (suivant l'épaisseur) et sur la taille du diamètre des perforations. Le modèle masse-ressort est employé pour analyser la transition entre le régime linéaire et non-linéaire. Un complément à l'article est présenté dans un article de conférence rapporté dans l'annexe VII. Dans cette annexe, le modèle masse-ressort est comparé à des résultats issus de simulations numériques (éléments finis) sous forts niveaux d'excitation sonore. Le champ de vitesse acoustique est obtenu à partir des simulations numériques. Le modèle numérique permet de visualiser la formation de jet et d'anneaux pour les matériaux à compressibilité effective augmentée composés d'un réseau de résonateurs *pancakes* lors de l'augmentation du niveau d'excitation acoustique incident. Le travail présenté dans ces chapitres est le fruit d'une collaboration avec Tenon Charly Kone (NRC) et Alla Eddine Benchickh Le Hocine (CRASH-UdeS) qui ont développé les outils de modélisation de mécaniques des fluides numériques.

Le chapitre 6 traite du troisième sous-objectif. Le format de ce chapitre est celui d'un article. La dernière version est proposée dans le manuscrit. Umnova *et al.* (2023) et Bezançon *et al.* (2024) ont étudié des trous noirs acoustiques une variation décroissante du profil des perforations des matériaux à compressibilité effective augmentée composé d'un réseau de résonateurs *pancakes*. Ce type de géométrie permet d'obtenir une absorption large bande en moyennes et basses fréquences. Dans le but d'analyser le comportement de ce matériau structuré sous forts niveaux d'excitation acoustique, le modèle masse-ressort est adapté. Des mesures sont réalisées en tube d'impédance acoustique pour des niveaux d'excitation acoustique élevés pour valider le modèle. Les réponses acoustiques pour différents profils de décroissance sont comparées et analysées. Cet article est issu d'une collaboration avec Gauthier Bezançon (doctorant au laboratoire ICAR).

CHAPITRE 3

MASS-SPRING MODEL FOR ACOUSTIC METAMATERIALS CONSISTING OF A COMPACT LINEAR PERIODIC ARRAY OF DEAD-END RESONATORS

Maël Lopez[1] , Thomas Dupont[1] , Raymond Panneton[2]

[1] Département de Génie Mécanique, École de Technologie Supérieure,
1100 Notre-Dame Ouest, Montréal, Québec, Canada H3C 1K3
[2] CRASH-UdeS, Department of Mechanical Engineering, Université de Sherbrooke,
2500 boul. de l'Université, Sherbrooke, Québec, J1K 2R1, Canada

Article publié dans « Journal of the Acoustical Society of America » en janvier 2024.

3.1 Abstract

This paper presents a mass-spring model to predict the normal incidence acoustic response of a metamaterial composed of a compact linear periodic array of dead-end resonators. The dead-end resonators considered are ring-shaped Helmholtz resonators. The model is based on a mass-spring analogy and considers the thermoviscous losses in the metamaterial following an effective fluid approach. A matrix equation of acoustic motion is derived for the finite case of N-periodic arrays. Under external excitation, its direct solution predicts the sound absorption coefficient and transmission loss. Under the homogeneous case, the solution of its associated eigenvalue problem predicts the acoustic eigenfrequencies and mode shapes. The dispersion relation is also solved to predict the beginning of the first stopband, and a low frequency approximation allows developing a formula to estimate the first eigenfrequency. The results show that the system with N degrees-of-freedom has three stopbands over the frequency range studied, with zero sound absorption and transmission. The model also helps to understand how

the acoustic dissipation, at a given resonant frequency, is affected by the position of the acoustic velocity nodes (eigenmodes) in the geometry of the metamaterial. Prototypes are designed, manufactured, and tested in an impedance tube to validate the model.

3.2 Introduction

Conventional acoustic materials, such as porous materials and resonators, are sometimes not suitable for noise mitigation at low frequencies. Indeed, at these frequencies, they may require a significant thickness to obtain good acoustic properties (sound absorption and/or sound transmission loss). Research is moving towards new solutions such as subwavelength acoustic metamaterials. When properly engineered, subwavelength acoustic metamaterials have good acoustic properties at small thickness-to-wavelength ratios; generally smaller than 1/10, even 1/100, against 1/5 for conventional materials. Different types of acoustic metamaterials exist such as membrane-type (Ma *et al.*, 2014), structured resonators (Cai & Mak, 2018; Huang *et al.*, 2019; Zhang & Hu, 2016), surface arrangements (Zhang & Hu, 2016; Liu *et al.*, 2019; Peng *et al.*, 2018) or dead-end (DE) periodic structures (Leclaire *et al.*, 2015; Groby *et al.*, 2015a). DE structures are composed of a main pore with a periodic arrangement of lateral resonators. The periodic arrangement of DE is responsible for the effective increase in air compressibility in the main pore (Leclaire *et al.*, 2015). Due to this increase, the effective celerity is decreased as well as the resonance frequencies of the material. Following this principle, these materials are also known as "slow sound materials" (Groby *et al.*, 2015a).

The first studies of these periodic DE materials focused on straight quarter-wavelength resonators as the DE structures (Leclaire *et al.*, 2015; Groby *et al.*, 2015a, 2016). Also, side branch Helmholtz resonators were used as DE resonators (Jiménez *et al.*, 2016, 2017c). In another way, Dupont *et al.* (2018) proposed the use of ring-shaped cavities around the main pore as DE resonators. Such a resonator is the equivalent of an axisymmetric quarter-wavelength resonator. It will be called hereafter a quarter-wavelength annular resonator. Linear periodic arrangements of these DE resonators were the subject of other studies: Brooke *et al.* (2020) investigated the nonlinear response of these materials at high sound pressure level, while numerical modelling was done to effectively consider thermoviscous losses in the metamaterial (Kone *et al.*, 2021b).

In this paper, a variant of the ring-shaped quarter-wavelength annular resonator is studied. It is an annular (or ring-shaped) Helmholtz resonator (AHR). It is formed by an annular neck connected to an annular cavity. Therefore, the whole material is composed of a compact linear periodic array of AHR along a main central cylindrical pore. This metamaterial will be called multi-AHR.

To study periodic DE materials, the transfer matrix method is commonly used (Leclaire *et al.*, 2015; Jiménez *et al.*, 2016, 2017c; Dupont *et al.*, 2018). However, that method does not allow a simple visualization of the phenomena involved, nor does it allow the making of a detailed analysis of the eigenfrequencies and mode shapes. For this purpose, a mass-spring model, based on a mechanical analogy, is proposed. Mass-spring models are largely used in acoustics to describe Helmholtz resonators with 1 or more degrees of freedom (Cai & Mak, 2018; Al Jahdali & Wu, 2018; Duan *et al.*, 2021; Guan & Jiao, 2012; Xu *et al.*, 2010). Periodic mass-spring systems are similar to one-dimensional monatomic harmonic crystals that have been studied for a long time (Ashcroft & Mermin, 1976). The aim of this article is to show that previous works on this topic can be transposed to acoustic DE structures with a view of studying their propagation behaviors, their dispersion relations, their stopbands, and their natural frequencies and mode shapes. Moreover, a simple formula is derived from the mass-spring analogy to predict the first eigenvalue of the studied metamaterial. Finally, an original mapping of the mass displacement according to the frequencies and the position of the masses is proposed to analyze the complexity of the acoustic phenomena (propagation of the sound, resonances, stopbands, and modes) underlying the metamaterial.

The present paper is organized as follows. In section 3.3, the studied geometry is presented. Section 3.4 presents the model to determine the surface acoustic impedance of an AHR. In section 3.5, the complete mass-spring model of the metamaterial is presented. It is shown how this model can be transposed to a global transfer matrix. Also, the non-dissipative eigenvalue problem is presented, and a simple expression for the first natural frequency is derived. Section 3.6 presents the validation of the developed model against experimental impedance tube tests and predictions obtained by another modeling method. Then the sound propagation through the metamaterial is studied. Note that some of the developments presented below were presented in the form of a conference paper (Lopez, Dupont & Panneton, 2022).

3.3 Materials

The proposed metamaterial is composed of a compact linear array of periodic unit cell (PUC), see figure 3.1(a). A PUC is composed of a pore ①, a junction ②, and a DE resonator (here an AHR, neck ③ and cavity ④). Figure 3.1(b) shows a photo of the manufactured axisymmetric multi-AHR sample. For the experimental part, the samples of the proposed metamaterial is composed of several stackable elements which have been manufactured in aluminum 6061-T6. A 0.45 mm chamfer is present on the contour of the cells to facilitate their assembly and reduce acoustic leaks. The geometry has been designed so that the aluminum plate between cavities ④ is 1 mm thick. Note that the first and last circular pores are shorter than the inner pores. The length of the first and last pores is l_{end} = 1.5 mm. The length of the inner pores is l_p = 2 mm. The radius of all the pores (viewed as the central main pore) is r_p = 2 mm. The neck of an AHR starts at r_p and ends at r_n = 3 mm with an annular neck thickness of h_n = 1 mm. The AHR cavity ends at radius r_c = 21 mm and its thickness is h_c = 2 mm. The number of cells is N=10, for a total length of 31 mm. The sample radius is r_{sample} = 22.22 mm. The geometric parameters of the sample are summarized in table 3.1.

Table 3.1 Dimensions of the main parameters of multi-annular Helmholtz resonators sample

Geometric parameters	l_{end}	l_p	r_p	r_n	h_n	r_c	h_c	r_{sample}
Sample (mm)	1.5	1	2	3	1	21	2	22.22

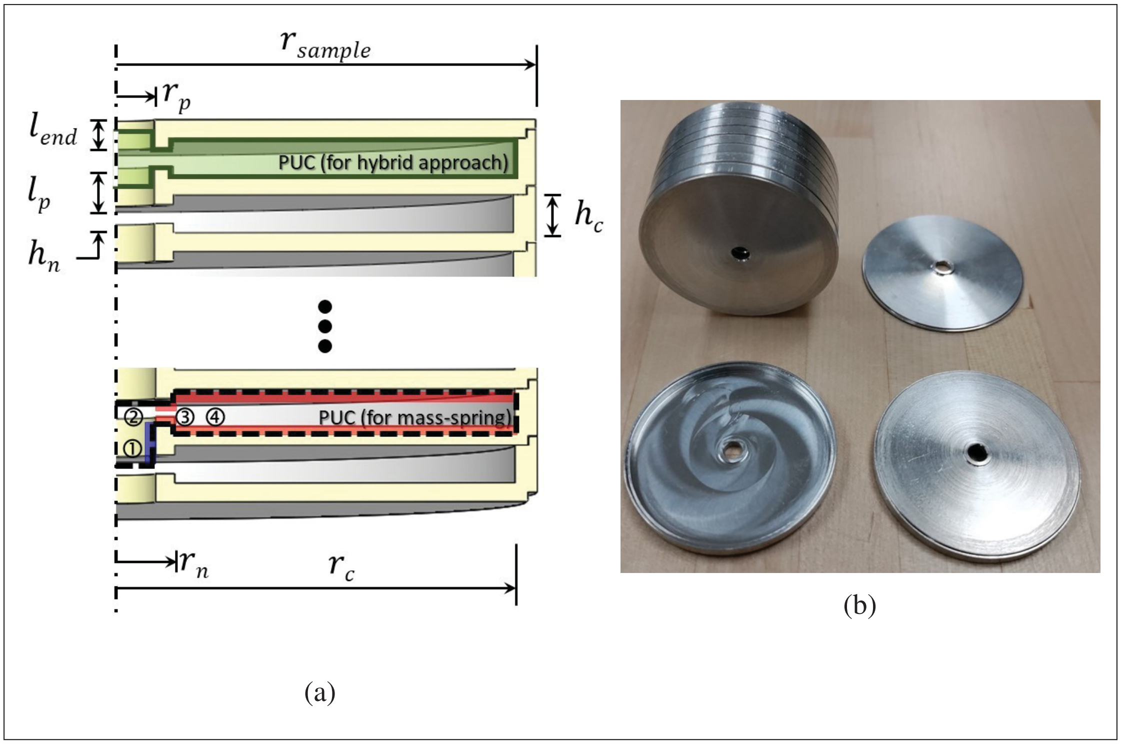

Figure 3.1 (Color online). (a) Schematic of the axisymmetric sectional view. The dashed black line is the contour of the plane defining the fluid of revolution of the PUC for the mass-spring model of section 3.5. The bold green line is the contour of the plane defining the fluid of revolution of the PUC for the hybrid approach of section 3.6.1. The thick colored lines are idealized representations of the acoustic boundary layers where thermal and viscous losses appear in the annular Helmholtz resonator (red) and in the main pore (blue). (b) Photo of the manufactured multi-annular Helmholtz resonators sample

3.4 Annular Hemholtz resonator

An AHR is composed of two thin concentric rings aligned and of different thicknesses, identified as ③ and ④ in figure 3.1(b). The subscript *n* refers to neck and c to cavity. An AHR is supposed to be thin (i.e., small thickness-to-radius ratio h_c/r_c) in a way that only radial propagation is considered. The wave equation for a one-dimensional concentric radial wave is given by (Munjal, 1987)

$$\frac{1}{r}\frac{\partial}{\partial r}\left(r\,\frac{\partial \Psi}{\partial r}\right) - \frac{1}{c^2}\frac{\partial^2 \Psi}{\partial t^2} = 0, \tag{3.1}$$

where r is the radial coordinate, Ψ the acoustic pressure, and c is the sound speed. Each part of the AHR (neck and cavity) is considered as a different media with its own solution of equation (3.1). The air saturating both parts of the AHR has effective fluid properties. These effective properties make it possible to consider the thermal and viscous losses which occur in the acoustic boundary layers along the walls which are perpendicular to the wavefronts in the AHR. As thicknesses h_c and h_n are small, the neck and the cavity are considered as slits. The parameters of the representative slits are given in table 3.2. Also, harmonic regime is assumed, $\Psi(r,t) = p(r)e^{j\omega t}$, with t the time and $j^2 = -1$. The acoustic pressure in the neck ($s = n$) and cavity ($s = c$) can be expressed as

$$p_s(r) = A_s\, J_0(k_s r) + B_s\, Y_0(k_s r) \tag{3.2}$$

where J_m and Y_m are respectively Bessel functions of the first and second kind of order m, A_s and B_s represent the amplitudes of the diverging and converging pressure waves respectively, k_s is the effective wave number of the air in the neck or cavity determined by the JCA model.

Table 3.2 Parameters of the Johnson-Champoux-Allard model for circular pores (main pore) and slits (AHR: neck and cavity). In the table, η is the dynamic viscosity of air, r_p is the radius of the main pore and h_s the thickness of the annular neck ($s = n$) and cavity ($s = c$).

JCA parameter	Units	Circular pore	Slits
Porosity	1	1	1
Tortuosity	1	1	1
Viscous characteristic length	m	r_p	h_s
Thermal characteristic length	m	r_p	h_s
Quasi-static airflow resistivity	$\mathrm{Pa\,s\,m^{-2}}$	$8\frac{\eta}{\phi r_p^2}$	$12\frac{\eta}{\phi h_s^2}$

The radial acoustic velocity is obtained using the one-dimensional Euler linearized equation with cylindrical coordinates,$-\partial p(r,t)/\partial r = \rho \partial v(r,t)/\partial t$ and is equal to

$$v_s(r) = -\frac{j}{Z_s}[A_s\, J_1(k_s r) + B_s\, Y_1(k_s r)], \tag{3.3}$$

where Z_s is the effective characteristic impedance of the air in the neck or cavity determined by the JCA model.

All AHR boundary walls are supposed rigid and perfectly reflective. This imposes the acoustic velocity to be zero at $r = r_c$. Applying this boundary condition for the cavity on equation (3.3) gives

$$B_c = -A_c \frac{J_1(k_c r_c)}{Y_1(k_c r_c)}. \tag{3.4}$$

The surface impedance at the entrance of the annular cavity is determined by substituting equation (3.4) into equations (3.2) and (3.3) at $r = r_n$. This yields

$$Z_{S,c} = \frac{p_c(r_n)}{v_c(r_n)} = jZ_c \frac{J_0(k_c r_n) - \frac{J_1(k_c r_c)}{Y_1(k_c r_c)} Y_0(k_c r_n)}{J_1(k_c r_n) - \frac{J_1(k_c r_c)}{Y_1(k_c r_c)} Y_1(k_c r_n)}. \tag{3.5}$$

The continuity of pressure and flow at the interface between the annular neck and cavity at $r = r_n$ leads to

$$\frac{p_n(r_n)}{S_n v_n(r_n)} = \frac{Z_{S,c}}{S_c}, \tag{3.6}$$

where $S_n = 2\pi r_n h_n$ and $S_c = 2\pi r_n h_c$ are the cylindrical surfaces of the annular neck and cavity at r_n. Substituting equations (3.2) and (3.3) into equation (3.6) gives

$$jZ_n \frac{A_n J_0(k_n r_n) + B_n Y_0(k_n r_n)}{A_n J_1(k_n r_n) + B_n Y_1(k_n r_n)} = \frac{h_n}{h_c Z_{S,c}}. \tag{3.7}$$

By rearranging equation (3.7), the ratio between both amplitudes A_n and B_n can be expressed as

$$\Upsilon = \frac{B_n}{A_n} = \frac{\frac{h_n}{h_c} \frac{Z_{S,c}}{jZ_n} J_1(k_n r_n) - J_0(k_n r_n)}{Y_0(k_n r_n) - \frac{h_n}{h_c} \frac{Z_{S,c}}{jZ_n} Y_1(k_n r_n)}. \tag{3.8}$$

Now, the surface impedance of an AHR (or at the entrance of the annular neck) is obtained from equation (3.2) and equation (3.3). It is given by

$$Z_{S,AHR} = \frac{p_n(r_p)}{v_n(r_p)} = jZ_n\frac{J_0(k_nr_p) + \Upsilon Y_0(k_nr_p)}{J_1(k_nr_p) + \Upsilon Y_1(k_nr_p}). \tag{3.9}$$

$Z_{S,AHR}$ is the input impedance of an AHR seen by the main pore. Subsequently, this impedance will be used in the mass-spring model described in the next section.

3.5 Mass-spring model for a metamaterial

Previous research has shown that periodic DE metamaterials can be modeled using the lumped parameter model (Leclaire *et al.*, 2015; Dupont *et al.*, 2018). The lumped parameter model is generally used with the transfer matrix formulation which gives good agreement with experimental results. However, the transfer matrix method does not allow to give a simple interpretation of the acoustical behavior of a metamaterial, nor to extract analytic formulas of its natural frequencies. For this purpose, the lumped parameter model is employed following a mass-spring analogy. A mass-spring representation of the PUC shown in figure 3.1(a) is depicted in section 3.5.

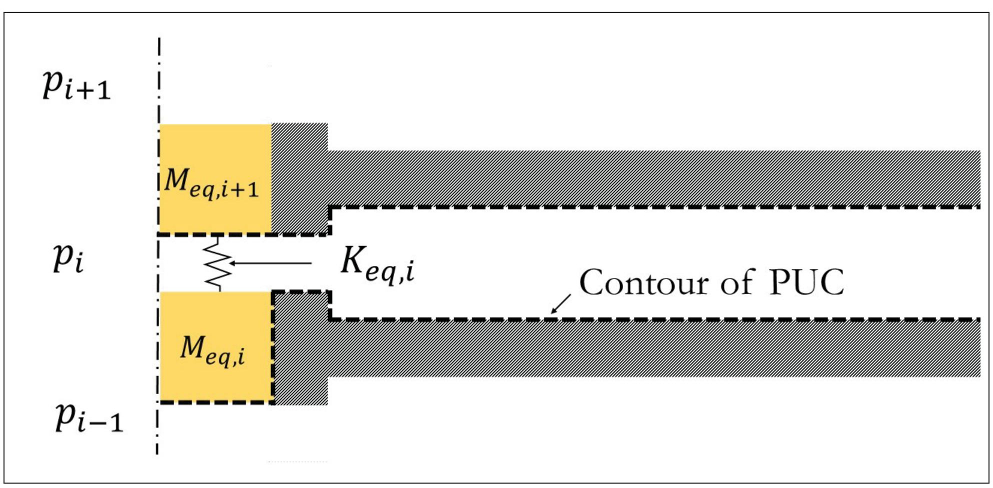

Figure 3.2 (Color online). Mass-spring representation at junction of the PUC shown in figure 3.1(a)

3.5.1 Mass-spring model

3.5.1.1 The lumped model

In a mass-spring analogy, each pore is represented by a corresponding equivalent mass. That is verified if the effective wavelength of a pore is much smaller than its length. To consider viscous losses, the air density is replaced by an effective density of the corresponding pore. The effective density is given by the JCA model for a cylindrical pore with the parameters given in table 3.2. Note that the term "equivalent" refers to a lumped property of the mass-spring system (mass for a pore, stiffness for a cavity), while the term "effective" refers to the properties of the air saturating a component of the metamaterial (i.e.: pore, neck, or cavity). The equivalent mass of the ith pore is

$$M_{eq,i} = \rho_p \, A_p \, l_i, \tag{3.10}$$

where ρ_p is the effective density of the air in the pore, $A_p = \pi r_p^2$ is the pore cross-sectional area, $l_i = l'_p$ for $2 \leq i \leq N$, and$l_i = l'_{end}$ for i=1 and i=$N + 1$. It is worth mentioning that l'_p, respectively l'_{end}, is the corrected length to account for radiation effect on both sides of each inner pore, respectively end pore. From the inner side, an end pore radiates into an AHR cavity, and from the other side it radiates into the exterior medium. For the exterior medium radiation, the length correction is calculated by the method proposed by Karal (1953), l_{Karal}. For the inner side, where a pore radiates into an AHR, the geometry studied is outside the limits of the formulas of length correction given by Karal (1953) and Ingard (1953). In fact, their formulas predict a length correction greater than the distance h_n between two consecutive pores. With this observation, an intuitive and logical approach is that the maximum end correction should not exceed half the distance between two pores. Thus, the author proposes to use the corrected length $l'_p = l_p + h_n$ for the inner pores and $l'_{end} = l_{end} + l_{Karal} + h_n/2$ for the exterior pores. For the geometry described in the previous section and inserted in an impedance tube of the same radius r_{sample} as the metamaterial sample, $l'_p = 3.0$ mm and $l'_{end} = 3.5$ mm.

Applying Newton's second law on the first pore, i=1, the equation of motion is

$$M_{eq,1}\,\frac{\partial^2 x_1}{\partial t^2} = -p_1 A_p + A_p P_1, \tag{3.11}$$

where x_1 is the acoustic displacement relative to the first mass, p_1 is the acoustic pressure at the first junction (identified as ② in figure 3.1(a)), and P_1 is the total acoustic pressure at the input of the metamaterial. Similarly, applying Newton's second law on the inner pores, $2 \leq i \leq N$, the equation of motion is

$$M_{eq,i}\,\frac{\partial^2 x_i}{\partial t^2} = -p_i A_p + p_{i-1} A_p, \tag{3.12}$$

where x_i is the acoustic displacement of mass i, p_i and p_{i-1} the acoustic pressures at junctions i and $i-1$. Finally, applying Newton's second law on the last pore, i=$N+1$, the equation of motion is

$$M_{eq,N+1}\,\frac{\partial^2 x_{N+1}}{\partial t^2} = p_N\, A_p - A_p\, P_{N+1}, \tag{3.13}$$

where P_{N+1} is the total acoustic pressure at the exit of the metamaterial.

To solve the equations of motion, the pressures before and after a junction need to be determined. Inside the junction, the pressure drop is assumed to be constant, and the losses are negligible compared to that of the cavities and pores. The pressure at any junction i can be written as (Dickey & Selamet, 1996)

$$p_i = -\rho_0\, c_0^2\, \frac{\Delta V_J}{V_J}, \tag{3.14}$$

where ρ_0 and c_0 are the adiabatic density and sound speed of the air in the junction,ΔV_J is the variation of the junction volume, and$V_J = A_p\, h_n$ is the junction volume. The variation of volume at junction i can be expressed as

$$\Delta V_J = -x_i\, A_p + \xi_{de,i}\, A_{de} + x_{i+1}\, A_p \quad , \tag{3.15}$$

where x_i and x_{i+1} are the acoustic displacements relative to the upstream and downstream masses connected to junction i, $\xi_{de,i}$ is the radial acoustic displacement at the input of the DE resonator, and $A_{de} = 2\pi r_p\, h_n$ is the common area between the junction and the DE.

Using harmonic dependence, the relation between the acoustic radial velocity and displacement is $v_{de} = j\omega\xi_{de}$. Assuming continuity of pressure at the interface between the junction and the neck of the AHR, the surface impedance at the input of the ith AHR is given by $Z_{S,AHR} = p_i/v_{de,i}$ (all AHRs are identical in the metamaterial). Substituting this result into equation (3.15) and substituting equation (3.15) into equation (3.14) gives the pressure at junction i:

$$p_i = \frac{x_i - x_{i+1}}{\frac{V_J}{\rho_0\ c_0^2} + \frac{A_{de}}{j\omega Z_{S,AHR}}} A_p \quad \forall\, i = 1,\ 2, \ldots N. \tag{3.16}$$

Therefore, the value of p_{i-1} is deduced. It is given by

$$p_{i-1} = \frac{x_{i-1} - x_i}{\frac{V_J}{\rho_0\ c_0^2} + \frac{A_{de}}{j\omega Z_{S,AHR}}} A_p \quad \forall \quad i = 2, \ldots N + 1. \tag{3.17}$$

Using equation (3.16) and equation (3.17), equations (3.11) to (3.13) can be rewritten in a matrix form

$$\left(-\omega^2\, \mathbf{M}_{\text{eq}} + \mathbf{K}_{\text{eq}}\right) \boldsymbol{x} = \boldsymbol{f}, \tag{3.18}$$

where $\boldsymbol{x} = (x_1 \quad x_2 \quad \ldots \ x_{N+1})^{\mathrm{T}}$ is the acoustic displacement vector relative to the masses, $\boldsymbol{f} = (A_p P_1 \ \ 0 \ \ \ldots \ 0 \ \ A_p P_{N+1})^{\mathrm{T}}$ is the force vector, and superscript T refers to the transposed vector. The equivalent mass matrix, $\mathbf{M}_{\text{eq}}$, is diagonal and is written as

$$\mathbf{M}_{\text{eq}} = \begin{bmatrix} M_{eq,1} & & & & 0 \\ & M_{eq,2} & & & \\ & & \ddots & & \\ & & & M_{eq,N} & \\ 0 & & & & M_{eq,N+1} \end{bmatrix}. \tag{3.19}$$

The equivalent spring matrix, $\mathbf{K}_{\text{eq}}$, is tridiagonal and is written as

$$\mathbf{K}_{\text{eq}} = K_{eq} \begin{bmatrix} 1 & -1 & & & 0 \\ -1 & 2 & -1 & & \\ & & \ddots & & \\ & & -1 & 2 & -1 \\ 0 & & & -1 & 1 \end{bmatrix}. \tag{3.20}$$

where K_{eq} is the stiffness of the junction coupled with the AHR given by

$$K_{eq} = \frac{A_p^2}{\frac{V_J}{\rho_0\, c_0^2} + \frac{A_{de}}{j\omega Z_{S,AHR}}}. \tag{3.21}$$

Equation (3.18) is the matrix equation of acoustic motion which relates the acoustic displacements to the external acoustic forces applied to the metamaterial. It can be rewritten in a more compact form as

$$\mathbf{A}\boldsymbol{x} = \boldsymbol{f}, \tag{3.22}$$

where $\mathbf{A}$ is the dynamic stiffness matrix, a combination of the frequency-dependent mass and stiffness matrices of size $N + 1$.

3.5.1.2 Acoustic indicators and global transfer matrix

For a given force, the displacement of the masses can be deduced from equation (3.22). The normal incidence acoustic impedance at the surface of the sample is given by the ratio of the acoustic pressure and velocity. For the harmonic regime under consideration, it is given by $Z_s = P_1/j\phi\omega x_1$, with $\phi = A_p/A_{sample}$ and $A_{sample} = \pi r_{sample}^2$, the cross-section area of the sample. Note here that the metamaterial sample is inserted into a tube of the same diameter (configuration similar to an impedance tube test). From Z_s, the normal incidence reflection coefficient R, incident pressure P_i, and sound absorption coefficient α can be deduced, respectively, from: $R = (Z_s - \rho_0 c_0)/(Z_s + \rho_0 c_0)$, $P_i = P_1/(1 + R)$, and $\alpha = 1 - |R|^2$. If the sample is backed by a rigid and perfectly reflective wall, x_{N+1} must be imposed to zero prior to solving equation (3.22). If the sample is backed by an anechoic termination, the impedance at the rear surface is equal to the characteristic impedance of the transmission fluid, that is $\rho_0\, c_0$. Then the surface impedance at the rear surface of the sample is $P_{N+1}/j\phi\omega x_{N+1} = \rho_0\, c_0$. By continuity, the transmitted pressure is $P_t = P_{N+1} = j\omega\phi\rho_0\, c_0\, x_{N+1}$, and the normal incidence sound transmission loss is $TL = -20\log_{10}(P_t/P_i)$. Another way to compute the acoustic response of the metamaterial is by converting equation (3.22) into a transfer matrix. Equation (3.22) can be modified to link the acoustic pressure and velocity as

$$\mathbf{Z}\boldsymbol{u} = \mathbf{p}, \tag{3.23}$$

where $\mathbf{Z} = \mathbf{A}/(j\omega A_p)$ is the acoustic impedance matrix, $\boldsymbol{u} = \partial\boldsymbol{x}/\partial t = j\omega\boldsymbol{x}$ is the acoustic velocity vector, and $\boldsymbol{p} = (P_1 \quad 0 \quad \ldots \quad 0 \quad P_{N+1})^{\mathrm{T}}$ is the acoustic pressure vector. Second, equation (3.23) is rewritten in a four-pole transfer pressure-velocity matrix formulation. The transfer matrix $\mathbf{T}_{\mathrm{M}}$ of the metamaterial links the upstream acoustic fields to the downstream acoustic fields by the following relation:

$$\begin{bmatrix} p_1 \\ u_1 \end{bmatrix} = \mathbf{T}_{\mathrm{M}} \begin{bmatrix} p_{N+1} \\ u_{N+1} \end{bmatrix}, \tag{3.24}$$

where p_1 and u_1 correspond to the acoustic pressure and velocity at the input pore of the metamaterial, respectively, p_{N+1} and u_{N+1} correspond to the acoustic pressure and velocity at the output pore of the metamaterial. The demonstration of the transition between the two formulations is presented in the appendix I. The transfer matrix of the metamaterial can be written as

$$\mathbf{T}_{\mathrm{M}} = (-1)^{N+1} \begin{bmatrix} \dfrac{\det(\mathbf{Z}_{1:N,1:N})}{\det(\mathbf{Z}_{2:N+1,1:N})} & \dfrac{\det(\mathbf{Z})}{\det(\mathbf{Z}_{2:N+1,1:N}} \\ -\dfrac{\det(\mathbf{Z}_{1:N,2:N+1})}{\det(\mathbf{Z})} + \dfrac{\det(\mathbf{Z}_{1:N,1:N})\det(\mathbf{Z}_{2:N+1,2:N+1})}{\det(\mathbf{Z})\det(\mathbf{Z}_{2:N+1,1:N}} & \dfrac{\det(\mathbf{Z}_{2:N+1,2:N+1})}{\det(Z_{2:N+1,1:N})} \end{bmatrix}, \tag{3.25}$$

where the subscripts on $\mathbf{Z}$ represent submatrix (rows and columns) of $\mathbf{Z}$, and det refers to the matrix determinant. Since the two end pores of the metamaterial open to an outside air medium, the global matrix of the metamaterial sample $\mathbf{T}_{\mathrm{G}}$ is obtained by multiplying $\mathbf{T}_{\mathrm{M}}$ by section change transfer matrices

$$\mathbf{T}_{\mathrm{G}} = \mathbf{T}_{\phi}\ \mathbf{T}_{\mathrm{M}}\ \mathbf{T}_{\phi}^{-1}, \tag{3.26}$$

where

$$\mathbf{T}_{\phi} = \begin{bmatrix} 1 & 0 \\ 0 & \phi \end{bmatrix}, \tag{3.27}$$

with ϕ as defined previously. Here, it is assumed that upstream and downstream exterior air media are identical and of the same lateral dimensions as the metamaterial sample. The normal incidence sound transmission loss (anechoic-backed) and the sound absorption coefficient (hard-backed) of the metamaterial sample can be deduced from the global transfer matrix. They are respectively given by

$$TL = 20\log_{10}\left|\frac{T_{G,11} + T_{G,12}/\rho_0 c_0 + T_{G,21}/\rho_0 c_0 + T_{G,22}}{2}\right| \quad (\text{anechoic} - \text{backed}), \tag{3.28}$$

and

$$\alpha = 1 - \left|\frac{T_{G,11} - T_{G,21}/\rho_0 c_0}{T_{G,11} + T_{G,21}/\rho_0 c_0}\right|^2 \quad (\text{hard} - \text{backed}). \tag{3.29}$$

with $T_{G,ab}$ the elements of the global transfer matrix, where a and b refer to the row and column of $\mathbf{T}_{\mathrm{G}}$.

3.5.2 Dispersion relation

To determine a simple expression for the dispersion relation of our system, we consider this one as a perfect periodic structure. In this case, all the masses in the mass-spring system are identical and given by $M_{eq} = \rho_p A_p h_p$, and the stiffness is given by equation (3.21). The structure is similar to a one-dimensional monatomic chain and the dispersion relation is given by (Fitzpatrick, 2013)

$$\omega^2 = 4\frac{K_{eq}}{M_{eq}}\sin^2\left(\frac{q h_{cell}}{2}\right), \tag{3.30}$$

where q is the wave number and h_{cell} the cell thickness $h_{cell} = l'_p + h_n$.

3.5.3 Natural frequencies – lossless case

One of the interests of the mass-spring analogy is that the natural frequencies and mode shapes can be determined by solving the eigenvalue problem. One of the goals is to predict frequencies at which absorption peaks occur for the hard-backed termination. In this way, displacement of the last mass is imposed to zero, that is $x_{N+1} = 0$.

3.5.3.1 Eigenvalue problem

Since the last mass displacement is zero, the last row and column of the dynamic stiffness matrix $\mathbf{A}$ are eliminated. Previously, the losses were considered in the mass and stiffness matrices. For the estimation of the natural frequencies, the lossless case is considered. All the effective properties are replaced by adiabatic air fluid properties, c_0 and ρ_0, in the calculations of the equivalent mass, equation (3.10), and stiffness,equation (3.21)). In this case, the equivalent mass and stiffness will be identified by $M^0_{eq,i}$ and K^0_{eq}. While $M^0_{eq,i}$ is now real-valued and independent of frequency, K^0_{eq} is real but still depends on frequency due to the Bessel functions. The eigenvalues (natural frequencies) are obtained by solving numerically

$$\det\left(\mathbf{A}^0_{1:N,1:N}\right) = 0. \tag{3.31}$$

where $\mathbf{A}^0_{1:N,1:N}$ is the lossless dynamic stiffness matrix for the hard-backed termination.

3.5.3.2 Expression of the first natural frequency

To obtain a simple formula of the first natural frequency, perfect periodic structure, lossless and low frequency assumptions need to be made. First, the metamaterial is assumed to be perfectly periodic, that is to say that all the equivalent masses are identical (the first mass end correction due to exterior medium radiation are not considered). In this case the wave number for the hard-backed termination can be rewritten as (Fitzpatrick, 2013) $qh_{cell} = \frac{2n-1}{2N+1}\pi$, and all equivalent masses are identical, i.e. $M_{eq,i} \to M_{eq}$. Substituting this wavenumber into equation (3.30) gives the eigen angular frequencies in the perfectly periodic case

$$\omega_n = 2\sqrt{\frac{K_{eq}}{M_{eq}}}\sin\left(\frac{2n-1}{2N+1}\frac{\pi}{2}\right). \tag{3.32}$$

where n is for the nth eigenvalue. Now, neglecting the thermoviscous losses, M_{eq}^0 and K_{eq}^0 can be substituted for M_{eq} and K_{eq} in equation (3.32). Note that $M_{eq}^0 = \rho_0 A_p l'_p$ is real-valued and constant. For its part, the stiffness can be simplified further under the assumption of low frequency development when $kr_c \ll 1$ and $kr_n \ll 1$. The first order Taylor series of Bessel functions for small arguments are (Olver, 1972) $J_0(z) \approx 1$, $Y_0 \approx 2/\pi \ln z$, $J_1(z) \approx z/2$ and $Y_1(z) \approx -(z\pi/2)^{-1}$. With this low frequency assumption, the AHR surface impedance, equation (3.9), simplifies to

$$Z_{S,AHR} \approx 2j\rho_0 c_0^2\left[\omega r_p\left(1-\frac{r_n^2}{r_p^2}+\frac{h_c}{h_n}\frac{r_c^2}{r_p^2}\left(1-\frac{r_c^2}{r_n^2}\right)\right)\right]^{-1}. \tag{3.33}$$

For multi-AHR, perfectly periodic and without thermoviscous losses, equation (3.33) allows the following simplification

$$\sqrt{\frac{K_{eq}}{M_{eq}}} \approx c_0\sqrt{\frac{A_p}{l'_p\left(V_{de}+V_J\right)}}, \tag{3.34}$$

where $V_{de} = \pi r_c^2 h_c - \pi r_n^2 (h_c - h_n) - V_J$ is the volume of an AHR, and $V_J = \pi r_p^2 h_n$. Considering the first natural frequency and enough cell repetitions (N=10 in this study), the sine function of equation (3.32) is approximated by its first order Taylor series $\sin(z) \approx z$. For hard-backed termination, the first natural frequency of a multi-AHR can be approximated by

$$f_1 \approx \frac{c_0}{2(2N+1)}\sqrt{\frac{A_p}{l'_p\left(V_{de}+V_J\right)}}. \tag{3.35}$$

3.6 Validation

To validate the previous developments and highlight certain characteristics, normal incidence sound absorption coefficient and sound transmission loss predicted with the mass-spring model on the multi-AHR described above will be compared with two other approaches: a hybrid numerical-analytical approach and experimental approach. Before proceeding to the validation, these approaches are briefly detailed.

3.6.1 Hybrid numerical-analytical approach

The hybrid numerical-analytical approach is a combination of the finite element method (FEM) and the transfer matrix method (TMM). Its main interest is to explicitly calculate the thermoviscous losses in the acoustic boundary layers, while maintaining a reasonable computing time. This hybrid approach was presented by Kone *et al.* (2021b) for multi-quarter-wavelength annular resonators. Here it is used to study the multi-AHR described above. Firstly, the FEM is used to solve the thermoviscous-acoustic (TVA) [1] problem on a single periodic unit cell of the multi-AHR to extract its four-pole transfer matrix $\mathbf{T}_{PUC}$, see figure 3.1(a). The cell is axisymmetric and is composed of half a pore, a junction with a side-branch AHR, and half a pore. Rigid wall condition is assumed on all material contours. Secondly, the PUC is periodized N times with the TMM by $(\mathbf{T}_{PUC})^N$. On the schematic of figure 3.1(a), one notes that it is necessary to add an extra length to the pores at both extremities of the previously periodized structure. This operation is necessary to take into account the fact that $\frac{l_p}{2} < l_{end}$ in the fabricated sample, and the additional length due to the radiation effect in the exterior medium. The transfer matrix of each of these extra pore lengths is obtained analytically by

$$\mathbf{T}_{end} = \begin{bmatrix} \cos(k_p\delta') & jZ_p\sin(k_p\delta') \\ \frac{j}{Z_p}\sin(k_p\delta') & \cos(k_p\delta') \end{bmatrix}, \tag{3.36}$$

[1] Solving the TVA problem in a geometry with a complex shape, even if it looks like a cylindrical pore or a slit, allows a more accurate evaluation of the thermoviscous losses compared to the assignment of effective air properties calculated by an equivalent fluid model such as the JCA model.

with $\delta = l_p - (h_c - h_n)$ and the corrected associated length is δ'. This length is calculated according to the Karal method (Karal, 1953). For the studied geometry, $\delta' = 2.0$ mm [2]. Thirdly, as for equation (3.26), since the two end pores of the metamaterial open to an outside air medium, the section change transfer matrix of equation (3.27) is used. Consequently, the global matrix of the metamaterial sample for the hybrid approach is given by

$$\mathbf{T}_H = \mathbf{T}_\phi \, \mathbf{T}_{end} \, \left(\mathbf{T}_{PUC}\right)^N \, \mathbf{T}_{end} \mathbf{T}_\phi^{-1}. \tag{3.37}$$

This equation is finally used to compute the normal incidence sound transmission loss (anechoic-backed) and absorption coefficient (hard-backed) with equations (3.28) and (3.29).

In our application of the hybrid approach, the TVA problem was solved with COMSOL Multiphysics 6.0. After validating the FEM model, the CPU time required to solve one converged TVA problem on the studied PUC, at 1500 frequencies from 1 Hz 3000 Hz, was 30 min on a personal computer.

3.6.2 Experimental approach: impedance tube

The transmission loss can experimentally be deduced from equation (3.28), where transfer matrix $\mathbf{T}_{\mathrm{G}}$ is replaced by the measured four-pole transfer matrix. Mecanum impedance tube is used according to the two-cavity three-microphone method (Salissou, Panneton & Doutres, 2012). The third microphone is baffled in the center of the rigid moving end (piston) of the tube. Sound absorption coefficient (hard-backed) can also be deduced from the measured four-pole transfer matrix and equation (3.29). However, due to the high noise attenuation of the metamaterial, the sound absorption coefficient defined by the measured transfer matrix was very noisy. It was preferred to measure directly the sound absorption coefficient (hard-backed) from the two-microphone impedance tube detailed in the standard in ASTM E1050-19 (2019). In this configuration, the sample is backed by a hard termination. The diameter of the tube

[2] This time, according to the method proposed by Karal (Karal, 1953) and the geometry studied, only 1.5 mm is added on the side of the pore connected to the external medium. Indeed, on its other side (inner side), the pore is connected to a pore of the same radius and no length correction is added.

is 44.44 mm and the outside diameter of the tested multi-AHR sample of figure 3.1(a) was manufactured to fit in the tube (both diameters are equals). Petroleum jelly is used around the sample to prevent acoustic leakage. The acoustic excitation is random noise between 115 and 4325 Hz is used as acoustic excitation. Each measurement on a sample is repeated five times. Each time, the internal parts are disassembled and then reassembled randomly. Only the two end sections of length l_{end} are kept at extremities. The experimental result presented in the following comparison is the envelope of all these measurements.

3.6.3 Comparison of the methods

Firstly, the prediction obtained with the developed mass-spring model on the studied multi-AHR is compared with experimental results and the hybrid approach prediction. The comparison is in terms of the normal incidence sound absorption coefficient for the hard-backed termination, and the normal incidence sound transmission loss for the anechoic-backed termination. The results are shown in figure 3.3. The results show a good agreement between the three approaches. For the hybrid approach, the added inertial effect, due to the radiation of an internal pore towards its upstream and downstream AHR cavities, is explicitly taken into account by the numerical calculations of the TVA problem on a PUC. It can be noticed that by substituting the corrected length for the internal pores in the mass-spring model, as presented in section 3.5.1.1, the model predicts a sound absorption coefficient similar to the other two approaches. In figure 3.3, it can be noted that the predictions deviate slightly from each other when the frequency increases. On the one hand, the authors believe that these deviations are due to geometric imperfections of the samples impacting the measurements. Small imperfections are more sensitive as the wavelength is reduced. On the other hand, the thermoviscous losses in the mass-spring model are approximated with the JCA model with parameters for simple canonical pore shapes (cylindrical and slits). While these geometries are, at first order, good idealization of the different parts of the multi-AHR, the real geometries are more complex. Despite these differences, the prediction made with the mass-spring model is rather satisfactory and, a priori, validates the model and the proposed correction for the effective length of the internal pores.

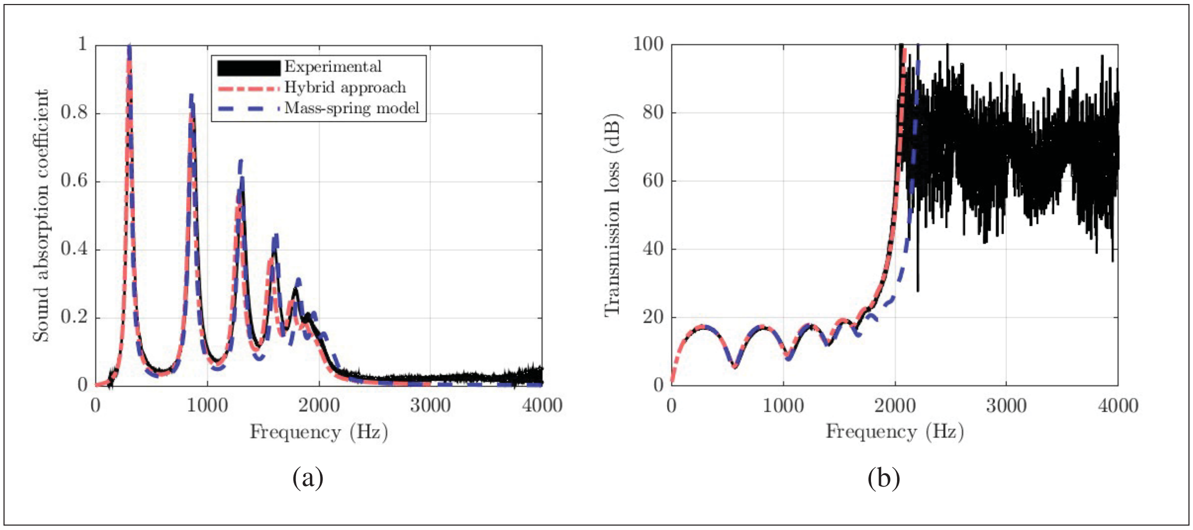

Figure 3.3 (Color online). The normal incidence sound absorption coefficient (hard-backed) and transmission loss (anechoic-backed) of the multi-annular Helmholtz resonators sample. Comparison between experimental approach, hybrid approach, and mass-spring model

In the case of hard-backed termination (absorption problem), figure 3.3(a), the metamaterial presents several peaks of absorption. Absorption peaks are associated with the quarter-wavelength resonances of the metamaterial backed by a rigid termination. This is similar to conventional porous materials. Their position in frequencies depends on the thickness of the metamaterial and its effective properties. For the metamaterial studied, the periodic resonators have the effect of reducing the effective compressibility of the air in the metamaterial (or more precisely that of the air in its central perforation) without modifying its effective density (Leclaire *et al.*, 2015; Dupont *et al.*, 2018). Thus, the effective celerity is reduced and the quarter-wavelength resonances of the metamaterial are shifted towards low frequencies. In the case of anechoic-backed termination (transmission problem), several lobes of transmission loss spaced by troughs are observed, figure 3.3(b). The troughs of the transmission loss are associated with the half-wave resonances of the metamaterial similar to what occurs in conventional porous materials. And the lobes of transmission loss occur at the anti-resonances, quarter-wave profile, of the metamaterial. However, contrary to conventional materials, the metamaterial shows a stopband starting around 2200 Hz where sound cannot propagate inside the metamaterial. The metamaterial becomes almost purely reflective (the absorption tends to zero and the transmission loss increases). Based on the mass-spring model, section 3.7.2 discusses in more detail the complexities of acoustic phenomena in relations to the acoustic resonances of the metamaterial and of its resonators in an extended frequency range. From the previous results, we now focus on the hard backed-termination configuration and absorption peaks. One of the motivations of periodic DE type metamaterials is to have absorption peaks at the lowest possible frequencies and for the lowest total thickness without increasing the volume. Therefore, it is proposed to compare the natural frequencies derived from the mass-spring model, in section 3.5.3, with the resonant frequencies observed on the absorption curves. The first three rows of table 3.3 present the first four resonant frequencies observed on the absorption curves obtained by experiments, hybrid approach and the corrected mass-spring model. Also, table 3.3 presents the natural frequencies obtained by the solution of the eigenvalue problem with the lossless assumption, equation (3.31), the lossless and perfectly periodic assumptions, equation (3.32), and the lossless, perfectly periodic, and low frequency assumptions, equation (3.32) with equation (3.34). For the former two, since the equivalent stiffness in equations (3.31) and (3.32) is frequency dependent, their solutions are obtained numerically. For the last case, equation (3.32) is solved analytically thanks to equation (3.34). Finally, the last row of the table gives the approximation of the first natural frequency obtained by equation (3.35).

Table 3.3 shows that for each peak, the resonant frequencies predicted by the three approaches are very close to each other. They diverge by no more than 2.4 %. Thus, the resonances predicted by the corrected mass-spring model are, a priori, quite satisfactory. These resonances are now used as a reference to validate the different calculations of the natural frequencies. In table 3.3, it can be noted that the numerical solution of the eigenvalue problem, equation (3.31), with the lossless approximation, gives eigenfrequencies slightly higher than the resonant frequencies. The relative errors (values in parentheses) are larger at low frequencies and smaller as the frequency increases. This is logical since the viscous and thermal skin thicknesses decrease with frequency and the losses are lower. When the perfectly periodic assumption is added (fifth row of the table), only a slight increase of 1 or 2 % is observed compared to the previous situation. This was

Table 3.3 Resonant and natural frequencies for the multi-annular Helmholtz resonators sample described in section 3.3. Comparison between the resonant frequencies obtained by the experimental, hybrid and mass-spring approaches, and the natural frequencies obtained by different approximations derived from the mass-spring model. Values in parentheses are relative errors compared to Mass-spring model.

Resonant/natural frequencies (Hz)	**Mode 1**	**Mode 2**	**Mode 3**	**Mode 4**
Experimental approach	306	873	1309	1598
Hybrid approach	301	861	1283	1567
Mass-spring model	301	863	1301	1610
Lossless approximation, equation (3.31)	314 (4%)	887 (3 %)	1333 (2 %)	1646 (2 %)
Lossless and periodic approximation, equation (3.32)	319 (6 %)	899 (4 %)	1345 (3 %)	1656 (3 %)
Lossless, periodic, and low frequency approximations, equations (3.32) and (3.34)	322 (7 %)	958 (11 %)	1572 (21 %)	2152 (34 %)
Formula for first natural frequency, equation (3.35)	322 (7 %)	-	-	-

expected since the difference between the fabricated sample and the perfectly periodic case is small. In fact, the fabricated sample is the periodic sample with additional thickness (additional pore length of 0.5 mm) at both ends. Consequently, the periodic case has a little less mass at its ends, thus increasing the natural frequencies. Now, if the low frequency approximation is added (equation (3.34)), the first natural frequency (sixth row of the table) deviates only by 1 % from the previous situation. However, the deviation largely increases for higher modes (the low frequency approximation is less appropriate as the frequency increases).

A last estimate is given for the first resonance frequency by equation (3.35) assuming lossless, low frequency and perfect periodic system, with linearization of the sine function. This simple formula gives a relatively good approximation of the first resonant. From this formula, it could be noticed that for minimizing the metamaterial first resonant frequency, the volume of the DE, the pore length or number of cells can be increased. On the contrary, the first resonant frequency increases with the pore cross section area.

3.7 Discussion

3.7.1 Band structure – dispersion curve

Equation (3.30) gives the dispersion relation of an infinite periodic one-dimensional monatomic chain, without low frequency approximation. The dispersion curve, or band structure, with or without losses is shown in figure 3.4(a). It should be mentioned that the results presented in figure 3.4 assume that only plane waves propagate upstream, downstream and in the main pore of the axisymmetric metamaterial. In reality, transverse modes could begin to appear from a cutoff frequency above 30 kHz. The results here aim only to study and understand the fundamental behavior of these metamaterials Unlike conventional mono-atomic chain, the

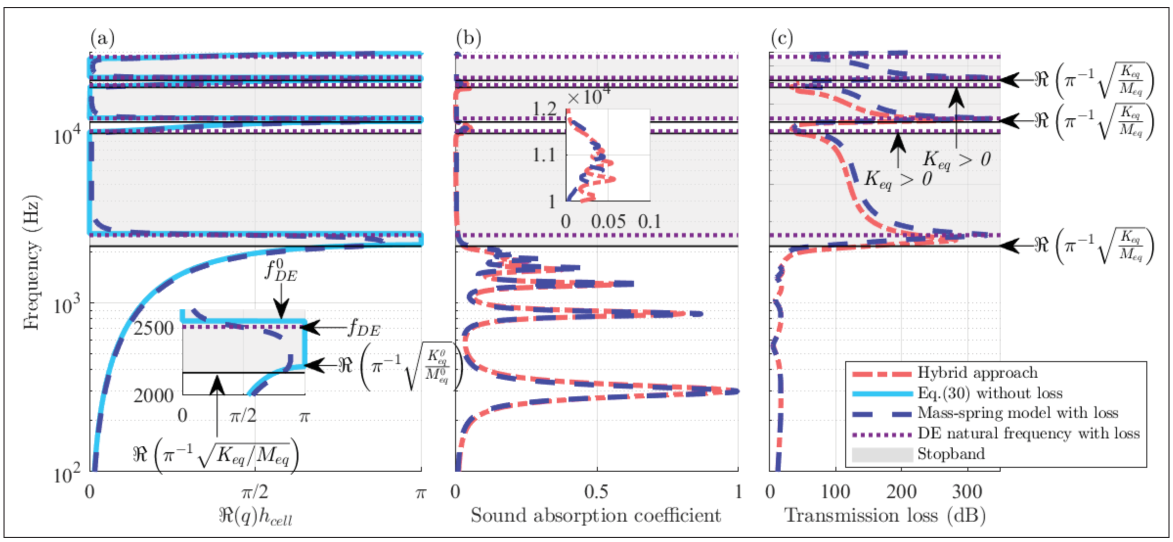

Figure 3.4 (Color online). (a) Dispersion curves obtained by equation (3.30), (b) normal incidence sound absorption coefficient (hard-backed), and (c) normal incidence sound transmission loss (anechoic-backed) for the multi-annular Helmholtz resonators. Stopbands are indicated by grey areas and are delineated by black lines

dispersion curve shows alternating passband and stopband before the cutoff frequency (30 kHz). This is due to the frequency dependence of the stiffness. A stopband appears when no energy is carried by the propagating wave, which is equivalent to the real part of the group velocity being zero (Deymier, 2013). So, a stopband starts each time the real part of the nondimensional wavenumber reaches π, continues when it equals 0 (the real part of the equivalent stiffness becomes negative, for detail see section 3.7.3) and ends when it moves away from 0. The opposite being a passband. In the stopband, the sound does not propagate (lossless case), or slightly (lossy case), inside the metamaterial. In the stopband, the metamaterial is purely (lossless case), or nearly (lossy case), reflective. This yields nearly zero absorption (hard-backed), see figure 3.4(b), and zero transmission (anechoic-backed) (or, basically, infinite sound transmission loss), see figure 3.4(c). For frequencies under the cutoff frequency (30 kHz), three stopbands (2170-10254 Hz, 11762-19063 Hz, and 20721-27808 Hz) are observed, each and linked to a DE resonance.

The phase change in the dispersion curve and the peak of transmission loss in the stopbands are associated to the resonances of the DE, which can be determined by solving numerically $Im\left(Z_{S,AHR}\right) = 0$, equation (3.9). The DE resonances are responsible of the sudden drop of the acoustic wavenumber, figure 3.4(a). The frequencies of the DE resonances f_{DE} differ slightly from the frequencies corresponding to the beginning of the stopbands. The beginning of a stopband depends on the spacing between DE (Bradley, 1991; Sugimoto & Horioka, 1995; Wang & Mak, 2012). Because the spacing is small for the studied geometry, the DE resonances are close to the beginning of the stopbands. For the infinite periodic configuration with losses, the beginning of a stopband is deduced from the numerical resolution of equation (3.30), when $Re\,(q)\,h_{cell} = \pi$, i.e. when $f = Re\left(\frac{1}{\pi}\sqrt{\frac{K_{eq}(f)}{M_{eq}(f)}}\right)$. The zoom in figure 3.4(a) shows that for the lossless case, the start of a stopband beginning clearly at $Re\,(q)\,h_{cell} = \pi$. For the lossy case, the beginning of a stopband appears at a smaller frequency and for a value of $Re\,(q)\,h_{cell}$ less than π. Moreover, the increase in sound transmission loss, figure 3.4(c), starts to increase at a lower frequency than the beginning of a stopband in the lossy case. This is due to two main effects: the finite size of the material and the fact that the end masses are larger due to the end corrections. Anyway, the formula $f = Re\left(\frac{1}{\pi}\sqrt{\frac{K_{eq}(f)}{M_{eq}(f)}}\right)$ gives a good estimation of the beginning of the stopbands.

3.7.2 Modal displacement of masses

The mass-spring model is now used to visualize and analyze the displacements of the masses (i.e., global air displacements of the main pores) in the studied metamaterial for the hard-backed termination. figure 3.5 shows the acoustic displacement mapping of the masses as a function of frequency. The displacement is normalized by the incident displacement. Note that although the mapping is continuous, only displacements at mass positions exist. The masses are at the positions indicated by the horizontal dashed lines, while the vertical solid black lines indicate the beginning and end of a stopband. Figure 3.5(a) shows the mapping when losses are considered, while figure 3.5(b) is in the lossless case – both mappings have similarities. As for it, figure 3.5(c) represents a zoom on the first passband and stopband in the lossless case. In figure 3.5, the vertical lines in yellow are the modal lines. Each corresponds to an eigenfrequency of the metamaterial, the first four eigenfrequencies of which are given in table 3.3. Since the system has N=10 moving masses (hard-backed), 10 modal lines appear in a passband. Similarly, the dark red lines are the nodal lines, where zero displacement occurs. The number of times a modal line is crossed by a nodal line marks the mode number. For example, since only one nodal line (the horizontal one at the rigid termination) intersects the first modal line in the first passband, the first mode is mode 1. Note that the same 10 modes repeat in each passband. This is counter-intuitive compared to a linear mass-spring system or the one-dimensional monatomic chain which will have a finite number of modes equal to the number of degrees-of-freedom. Since a "spring" in the metamaterial has a frequency-dependent stiffness derived from an AHR having multiple natural frequencies, $Im(Z_{S,AHR} = 0)$, the same 10 modes will repeat in each passband. The modal lines associated with these 10 modes are easier to see in the lossless case since the modal and nodal lines are smeared out in the highest passbands in the lossy case.

In figure 3.5(c), it should be noted that when a nodal line intersects a modal line at an exact mass position (a horizontal dashed line), that corresponding mass is stationary and no viscous loss is produced by that mass. On the contrary, when the intersection does not fall exactly at a mass position, that mass will always be in motion and will always produce viscous loss. For example, the tenth mass at 27 mm will always move in the first passband since its position never falls at

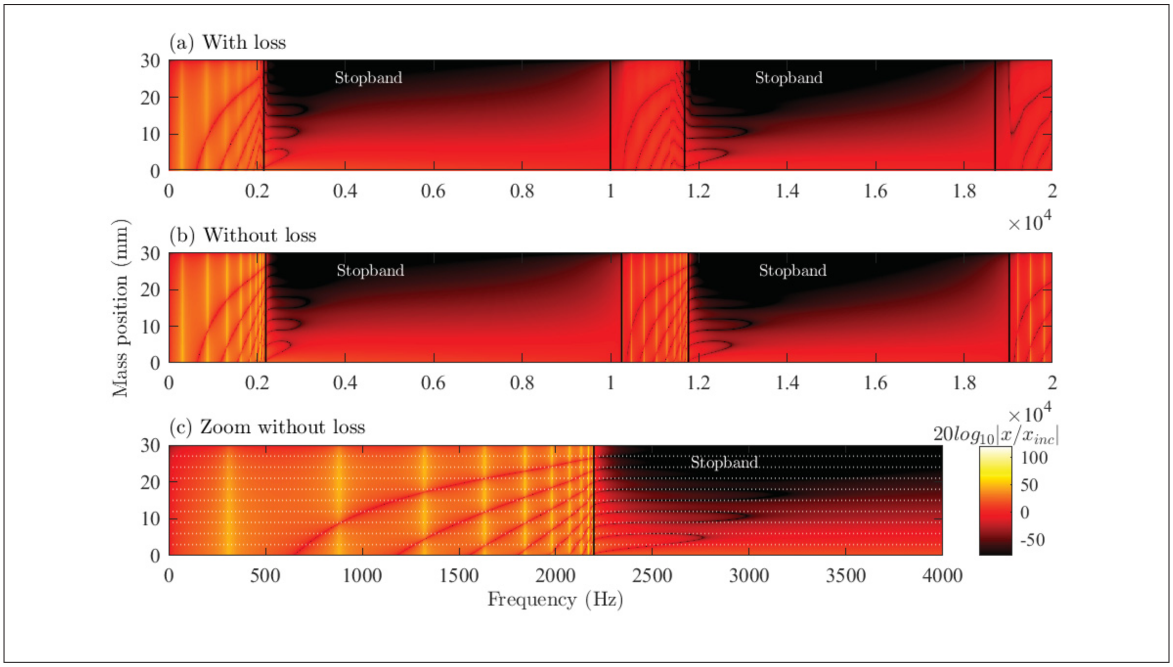

Figure 3.5 (Color online). Displacement mapping of the masses as a function of frequency for the hard-backed termination. Cubic interpolation is used to obtain a continuous mapping. The positions of the masses are indicated by the horizontal dashed lines. The beginning and end of the stopbands are indicated by the vertical black lines

an intersection of a modal and nodal line. The authors believe that this understanding of the position of masses relative to nodal and modal lines could potentially be useful in optimizing the design of these metamaterials by preventing masses from falling close to a nodal line. For now, such optimization remains to be done and is not the purpose of this article.

Figures 3.6 and 3.7 show the modal shapes, in the lossy case, for the first three modes, and the displacement shape in the first stopband for the hard and anechoic backed terminations, respectively. For the hard-backed termination, figure 3.6, the first three mode shapes in the first passband are another visualization of the first three modal lines of figure 3.5(a) (the vertical lines in yellow). The filled areas in the graphs are the envelopes over a time period at the corresponding frequency. The blue dots represent the 11 masses of the mass-spring representation of the metamaterial at an instant corresponding to a maximum amplitude.

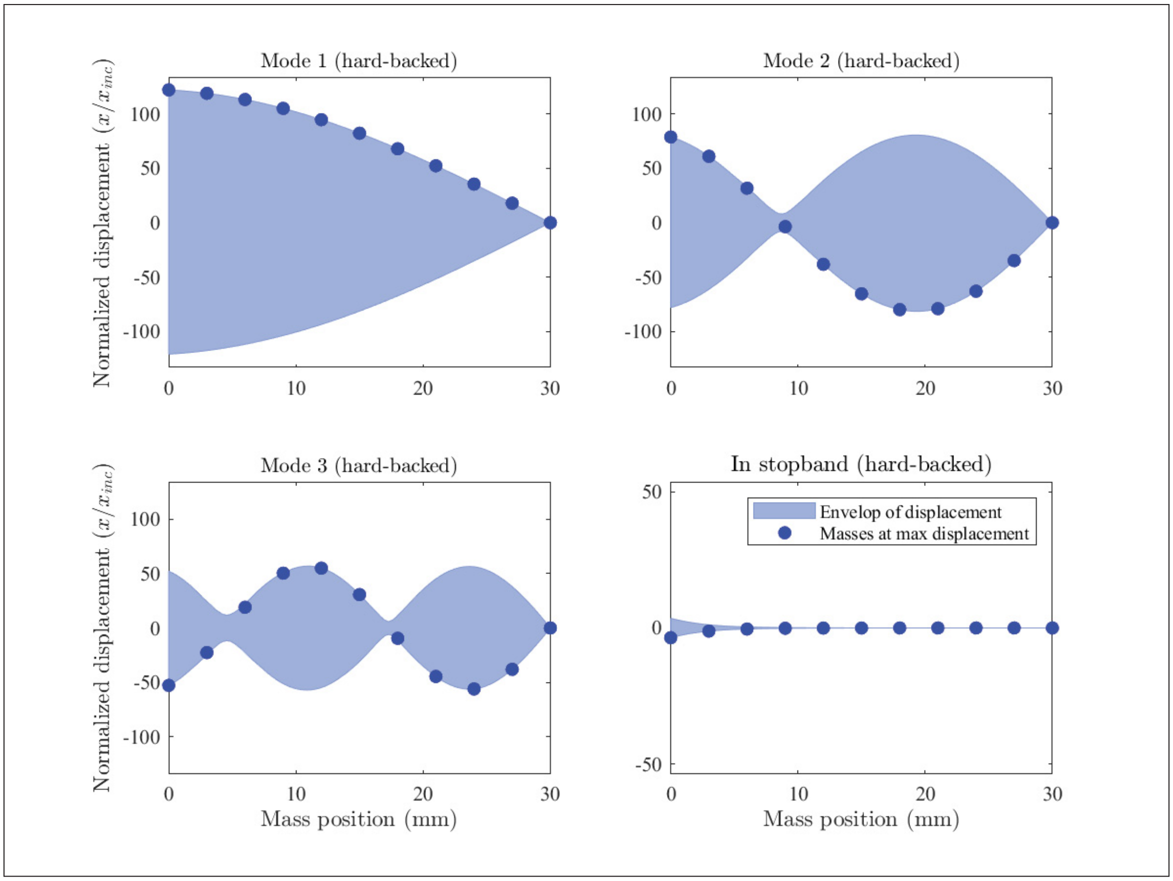

Figure 3.6 (Color online). Mass displacement profile with loss at the first modes and in the stopband for the hard-backed termination

In the hard-backed termination, the last mass is logically always stationary. In figure 3.6, one can recognize that the first mode for the hard-backed termination is the quarter-wave resonance, whereas it is the rigid mode for the anechoic-backed termination. The other mode shapes in the first passband are also those typical of a linear system. Recall that these same mode shapes will repeat in each passband with higher attenuation for higher passbands.

Finally, figures 3.6 and 3.7 show that in a stopband the mass displacement quickly decreased through the material. In this case, the material is almost reflective, and all the sound is mainly reflected by the first mass-spring cell. The insets in figures 3.6 and 3.7, for the "In stopband" case, show the acoustic pressure distribution from the first to third mass. One can note that the pressure at the first mass is nearly twice the amplitude of the incident pressure. This represents

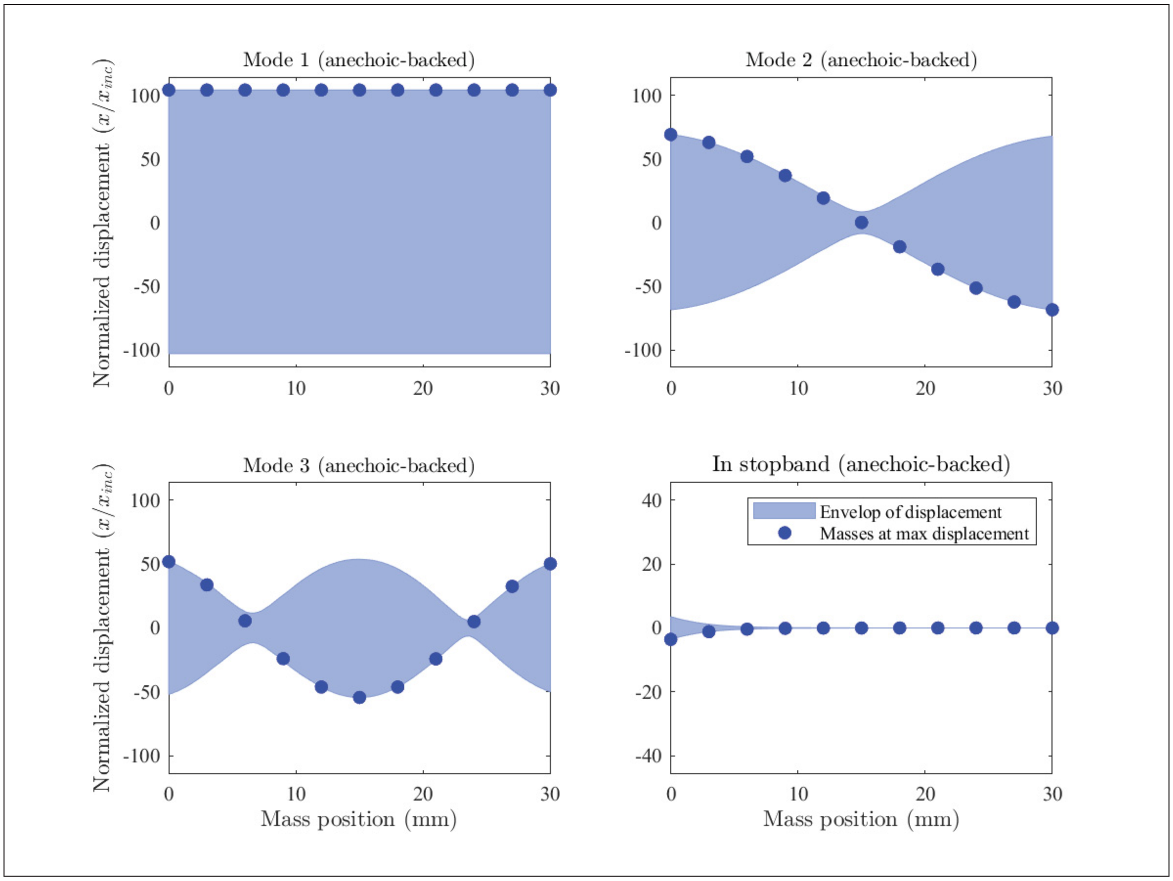

Figure 3.7 (Color online). Mass displacement profile with loss at the first modes and in the stopband for the anechoic-backed termination

the blocked pressure on a hard wall having a reflection coefficient of nearly 1. Note that the acoustic pressure was easily obtained here from the displacements calculated by the mass-spring model by solving Euler's equation with a finite difference scheme. See supplementary materials, section 3.9, for figures of acoustic pressure profiles and animations of mass displacements for the first modes and in the first stopband for the hard and anechoic backed terminations.

3.7.3 Analysis of the equivalent stiffness

As discussed earlier, in a conventional infinite periodic one-dimensional monatomic chain, only one stopband band is present. For a frequency greater than the single occurrence $f = \pi^{-1}\sqrt{K/M}$, the disturbance does not propagate. For our metamaterial, the presence of other passbands is due to the fact that it has several stopbands starting at all occurrences $f = \pi^{-1} \sqrt{K_{eq}(f)/M_{eq}(f)}$. This is because the equivalent stiffness is related to the DE resonances via equation (3.21). At a DE resonance the amplitude of the stiffness exhibits a drop, see figure 3.8(b). Its real part is then equal to zero, see figure 3.8(a), then becomes negative before becoming positive again in the next bandwidth. For each bandwidth, a new problem of N+1 degrees-of-freedom (or N in the case of a hard-backed termination) is redefined with a higher equivalent stiffness leading to the same modes at higher frequencies. The values of K_{eq} increase with the order of the passband. Figure 3.8(b) shows that the stiffness values nearly double from one passband to the next. The fact that the stiffness and the thermo-viscous losses grow with the frequency explains why the maximum absorption or transmission (transmission loss) decreases (increases) with the order of the passband.

Finally, in the first passband, it can be observed that the amplitude of the stiffness is quasi-static at low frequencies and decreases abruptly as the first resonance DE approaches. This decrease in stiffness when approaching the DE resonance explains why the resonances of the metamaterial (absorption or transmission loss peak) are closer to each other with frequency. Near the DE resonance, they overlap.

3.8 Conclusion

A mass-spring model was developed to study metamaterials composed of a compact linear periodic array of thin ring resonators along a main central pore. This resulted in an acoustic equation of motion, where the degrees of freedom are the air motion in each pore segment between the resonators. The resonators were modeled by introducing a surface impedance into the equivalent stiffness matrix of the developed acoustic equation of motion. While the surface impedance can be developed for different types of resonators, this article has developed that of a ring-shaped Helmholtz resonator. From the mass-spring model, a modal analysis of eigenfrequencies and mode shapes was performed, and a formula predicting the first resonance was proposed. The model was used to study the band structure of the metamaterial which shows an infinite succession of passbands and stopbands. In each passband, N resonances

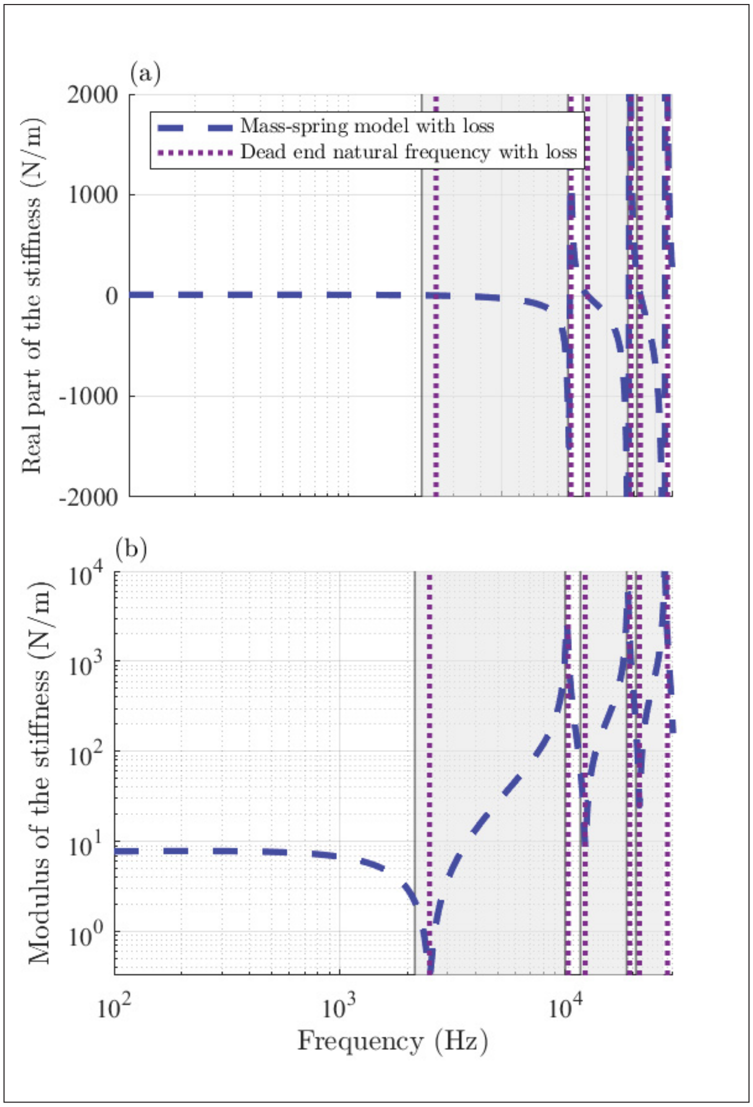

Figure 3.8 (Color online). Real part (a) and modulus (b) of the equivalent stiffness as a function of frequency in the lossy case. Stopbands are indicated by grey areas and are delineated by grey lines

were observed, where N is also the number of masses in the mass-spring model. Unlike a linear mass-spring system of N degrees of freedom, the N-mass metamaterial exhibits an infinite number of degrees of freedom. An original representation of the band structure in terms of cartography of acoustic displacement of masses as a function of frequency has been proposed. This representation made it possible to better understand the acoustic behavior of the metamaterial in relation with the intersections between the nodal lines, the modal lines and the localization of the masses. To validate the model, a prototype of the metamaterial was machined in aluminum. The prototype was tested in an acoustic tube for normal incidence sound absorption and sound transmission loss. A good correlation between the experimental results and the model predictions was obtained.

Acknowlegements

The authors acknowledge the financial support of Natural Sciences and Engineering Research Council (NSERC) [funding reference numbers: RGPIN-2018-06113 and RGPIN-2019-06573].

3.9 Supplementary material

See supplementary material [https://pubs.aip.org/jasa/article-supplement/3061602/zip/530_1_10.0024212.suppl_material/] for figures of acoustic pressure profiles inside the material and animations of mass displacements for the first modes and in the first stopband for the hard and anechoic backed terminations.

Author declarations

Conflict of Interest

The authors state that they have no conflict of interests to disclose.

Data availability

The data that support the findings of this study are available from the corresponding author upon reasonable request.

3.10 Compléments

Dans l'article précédent, un matériau à compressibilité effective augmentée à réseau de résonateurs d'Helmholtz annulaires (*multi-AHR*) a été présenté. Les *multi-AHR* sont comparés avec les matériaux à compressibilité effective augmentée composés d'un réseau de cavités *pancakes* (proposés par Dupont *et al.* (2018)). Les cavités *pancakes* annulaires fonctionnent comme des résonateurs quart-d'onde annulaire (propagation radiale dans les cavités pour les fréquences étudiées). La figure 3.9 montre le coefficient d'absorption mesuré pour différentes ouvertures du col des AHR. Lorsque l'ouverture, h_n/h_c, est égale à 100 %, la largeur du col du AHR est égale à la largeur de la cavité. L'AHR correspond à une cavité *pancake* annulaire. Lorsque l'ouverture des cols des résonateurs d'Helmholtz diminue, la fréquence des pics d'absorption est décalée vers les basses fréquences (effet réactif). Les pics d'absorption en hautes fréquences sont davantage impactés. Le nombre de pics d'absorption est diminué lorsque l'ouverture des cols des résonateurs d'Helmholtz diminue. La majorité des résonances sont regroupées dans la zone d'absorption large bande de fréquence juste avant la bande interdite. L'effet large bande de fréquence est amplifié (augmentation de l'absorption moyenne et largeur de la bande). En effet, la fréquence de la bande interdite est décalée fortement vers les basses fréquences. La résonance d'un résonateur d'Helmholtz annulaire est plus basse que celle d'un résonateur quart-d'onde annulaire, à même volume.

La fréquence du premier pic du coefficient d'absorption diminue légèrement. La fréquence du premier du coefficient d'absorption est de 325 Hz pour h_n/h_c=100 %, 306 Hz pour h_n/h_c=50 % et 292 Hz pour h_n/h_c=20 %. L'amplitude du coefficient d'absorption du premier pic d'absorption est peu impactée, 0.99 pour h_n/h_c=100 %, 0.99 pour h_n/h_c=50 % et 0.97 pour h_n/h_c=20 %. L'amplitude du deuxième pic du coefficient d'absorption est davantage impactée. Les fréquences du premier pic du coefficient d'absorption, les valeurs obtenues par les critères λ_1/e et $\lambda_1/\sqrt[3]{V_{cell}}$ sont rapportées dans le tableau 3.4 pour les différents échantillons. La comparaison entre les matériaux à compressibilité effective augmentée à réseau d'AHR et de cavité *pancake* montre que l'utilisation de AHR permet de décaler les fréquences des pics du coefficient d'absorption vers les basses fréquences sans augmenter le volume du matériau.

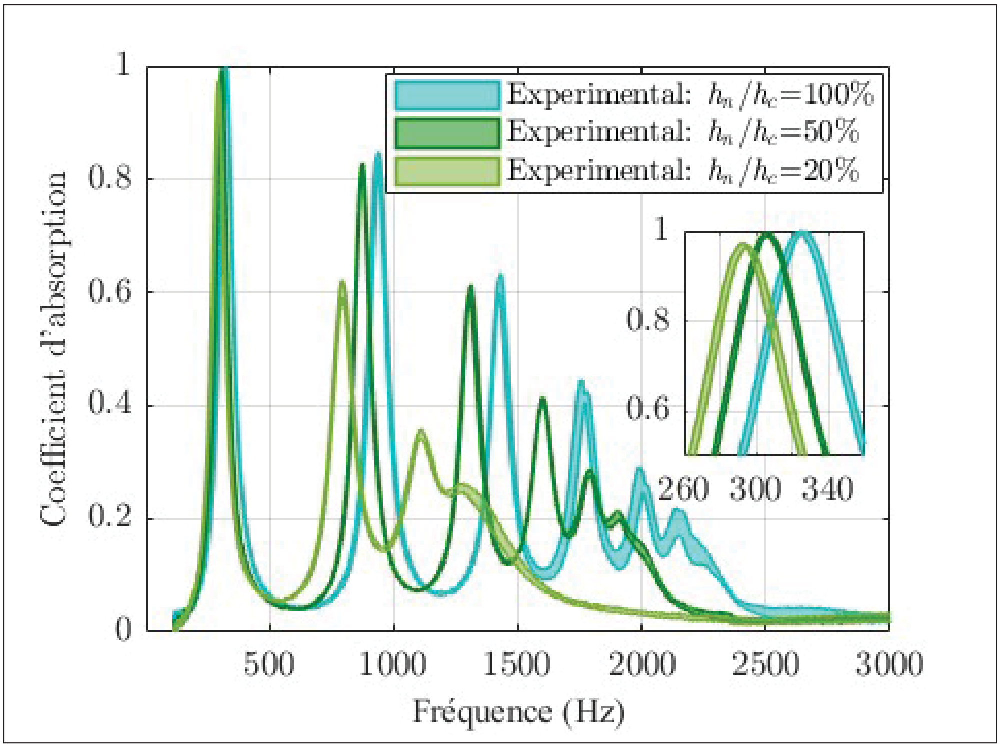

Figure 3.9 Coefficients d'absorption mesurés en tube d'impédance pour des multi-résonateurs d'Helmholtz annulaires (*multi-AHR*) pour différentes ouvertures du col des résonateurs d'Helmholtz annulaires

Tableau 3.4 Comparaison des fréquences du premier pic d'absorption, de différents critères d'efficacité en basse fréquence et des dimensions géométriques (épaisseur e et volume de la cellule élémentaire V_{cell}) pour différentes ouvertures du col des AHR, h_n/h_c

h_n/h_c	f_1 (Hz)	e (mm)	V_{cell} (mm^3)	$\frac{\lambda_1}{e}$ (-)	$\frac{\lambda_1}{\sqrt[3]{V_{cell}}}$ (-)
100 %	327	31	48084	33.8	28.8
50 %	306	31	48084	36.1	30.7
20 %	292	31	48084	37.8	32.2

CHAPITRE 4

INERTIAL EFFECTS ON SINGLE-PERFORATION PLATE RESISTIVITY AT HIGH FLOW RATES : CFD AND EXPERIMENTAL STUDIES

Maël Lopez[1] , Alla Eddine Benchickh Le Hocine[2] , Tenon Charly Kone[3] , Thomas Dupont[1] , Raymond Panneton[2]

[1] Département de Génie Mécanique, École de Technologie Supérieure,
1100 Notre-Dame Ouest, Montréal, Québec, Canada H3C 1K3
[2] CRASH-UdeS, Department of Mechanical Engineering, Université de Sherbrooke,
2500 boul. de l'Université, Sherbrooke, Québec, J1K 2R1, Canada
[3] National Research Council Canada, Flight Research Laboratory,
1200 Montreal Road, Ottawa, Ontario, K1A 0R6, Canada

Article soumis à la revue « Journal of the Acoustical Society of America » en juillet 2024.

4.1 Abstract

This article is interested in viscous and inertial effects on airflow resistivity of periodic arrays of single-perforation plates spaced by thin air cavities. Analyzing this effect would provide better insight into losses within the material, including additional losses due to increasing sound excitation levels. In this way, the material pressure drop is predicted by computational fluid dynamics function (CFD) of the flow rate for corresponding pore Reynolds numbers between 0.3 and 1500. The static airflow resistivity coefficient is determined by the linear part of the pressure drop (viscous effect) and the Forchheimer coefficient from the nonlinear part of the pressure drop (inertial effect). Both coefficients are determined on the entirety of the material (globally) and at the plate levels (locally). Good agreement is observed between CFD predictions and experimental measurements on the whole range of studied Reynolds numbers. By investigated locally the pressure drops, the observations show that the viscous effects are constant through the material. With increasing pore Reynolds number, inertial effects of the first plate dominate over those of the other plates. The consideration of local inertial effect will be a key component in the acoustic modeling of this type of material under high sound excitation levels.

4.2 Introduction

In industrial applications, such as those in aerospace, transportation, and construction sectors, acoustic materials, including metamaterials, are frequently exposed to high sound excitation levels. These extreme conditions can significantly affect their acoustic performance and durability. Acoustic metamaterials, with their engineered structures designed to achieve properties that are not found in conventional acoustic materials, offer promising solutions in this context. These materials generally consist of a compact array of periodic resonators arranged in series (Leclaire *et al.*, 2015; Groby *et al.*, 2015a; Jiménez *et al.*, 2016; Dupont *et al.*, 2018; Lopez, Dupont & Panneton, 2024). In the material proposed by Dupont *et al.* (2018), the periodic resonators are composed of a neck (perforation) coupled with a thin air cavity. The resonator neck restricts the acoustic flow. In acoustic models, the airflow resistivity of the neck is a key characteristic to define the acoustic resistance of the neck (Atalla & Sgard, 2007). Under low acoustic flow rates (or low levels of sound pressure), the airflow resistivity is constant (this parameter is called static airflow resistivity) and it is governed solely by viscous effects following Darcy's law (corresponding here to the linear flow regime). However, at high sound excitation level , inertial effects also come into play alongside viscous effects, and the airflow resistivity is no more constant. It now depends of the flow rate. This defines the nonlinear flow regime. Although similar to the nonlinear response of a micro-perforated plate (MPP) (Laly *et al.*, 2018), the case in question differs due to the presence of a series of successive necks showing strong interactions spaced by thin cavities. Therefore, studies on the nonlinear response of MPP can provide inspiration but cannot be directly applied to this metamaterial.

To account for high sound excitation levels in porous rigid-frame materials, Wilson *et al.* (1988) proposed using the Darcy-Forchheimer's law to define airflow resistivity instead of Darcy's law. In this case, the airflow resistivity is a linear function of the airflow velocities and it is no longer constant. The Forchheimer's coefficient is determined at higher flow velocities. The Darcy-Forchheimer's law is used in acoustic models using an effective value of velocity (McIntosh & Lambert, 1990). Ingård & Labate (1950) investigated the effects of the acoustic circulation and impedance of perforated plate orifices. They showed that increasing sound intensity induces pulsatory effects, such as the formation of jets and vortex rings. The energy of the sound wave is transformed into kinetic energy, which leads to a nonlinear increase in losses as the sound intensity increases. Maa (1994) explained that the acoustic nonlinearity of an orifice is an external phenomenon and proposed a nonlinear acoustic impedance model of the MPP. In his model, the specific nonlinear acoustic resistance is related to the Mach number in the perforation of the MPP divided by the percentage of open area. Further research by Ingard & Ising (1967) involved simultaneous measurements of acoustic pressure and velocity at the perforation, showing that the relationship between acoustic pressure and velocity amplitudes tends to a square law at high velocity amplitudes. They showed that the acoustic resistance of a perforation increases with increasing acoustic velocity, whereas the acoustic impedance of the perforation decreases.

Finally, Laly *et al.* (2018) used an effective fluid model composed of a linear term and a nonlinear term to define the airflow resistivity. This last approach is similar to Darcy-Forchheimer's law of rigid-frame porous materials. The model was validated for several spaced MPPs of different properties (percentage of open area, perforation diameter, plate thickness) at different sound excitation levels.

In previous research on MPP, the cavity thickness behind the panels is relatively large compared to the thickness of the plates. Studies investigating the nonlinear response when a series of perforated plates are closely spaced, as in the metamaterial studied, are rare. Brooke *et al.* (2020) investigated the acoustic and nonlinear responses of the compact periodic array of thin single-perforation plates (SPP) spaced by with thin air cavities proposed by Dupont *et al.* (2018).

In their acoustic model, the high sound excitation levels are considered using the airflow resistivity with Darcy-Forchheimer's law. The Forchheimer coefficient was measured experimentally on the entire material (i.e., on all the SPPs placed in series). The model shows good agreement with acoustic tube impedance measurements at high sound excitation levels. However, the study was limited to SPP having a perforation diameter of 8 mm, and the effect of the number of plates in the SPP was not investigated. Furthermore, most of their investigations on the airflow resistivity were experimental, making the analysis less convenient for acoustic models. Li, Davidson & Peng (2024) have presented a similar analysis on macro-perforated plates. They studied the interaction between parallel perforations on a plate, and how it affects viscous and inertial pressure losses in laminar and turbulent flows.

The present study focuses on the impact of inertial effect on the airflow resistivity of a succession of SPPs space by thin air cavities. The purpose of this paper is to understand this impact under a various number of plates and perforation diameters. It also aims to determine the contribution of each plate to the overall airflow resistivity. After validation with experimental measurements, the research employs a numerical approach using two models of computational fluid dynamics (CFD) (2D-axisymmetric and 3D full-geometry models) to predict the airflow resistivity of the metamaterial, both locally (on each SPP) and globally (on the assembly of all SPPs).

The studied material is described in section 4.3. In section 4.4, the Darcy's and Darcy-Forchheimer's equations are recalled and the experimental and CFD methods are presented. The section 4.5 is organized into three main parts. First, the results of the two CFD models are validated with experimental results. Secondly, the overall pressure drop and the static (Darcy's) and Fochheimer's coefficients are analyzed for various geometries and SPP assemblies. Finally, a local study is proposed to determine the contribution of the different plates.

4.3 Materials

The material studied consists of a compact periodic array of SPPs spaced by thin cavities. Figure 4.1(a) shows a photo of the material sample, which has been made from aluminum. Other details on its fabrication can be found in section 3.3. For a given assembly, all SPPs are identical and have the same perforation diameter d, external diameter D, and thickness h. The spacing between two consecutive SPPs is H. The space between two SPPs forms a thin annular cavity. For the present study, the thicknesses of the SPPs and the annular cavities are set at $h = 1$ mm and $H = 1$ mm, respectively, and the outer diameter is set at $D = 44.44$ mm. The number of successive SPPs will vary from 1 to 16, and the perforation diameter from 1 to 20 mm. A key parameter of the SPP is the percentage of open area (POA) defined by $POA = 100\,(d/D)^2$. In this study, it will vary between 0.05 and 23% due to the variation of d.

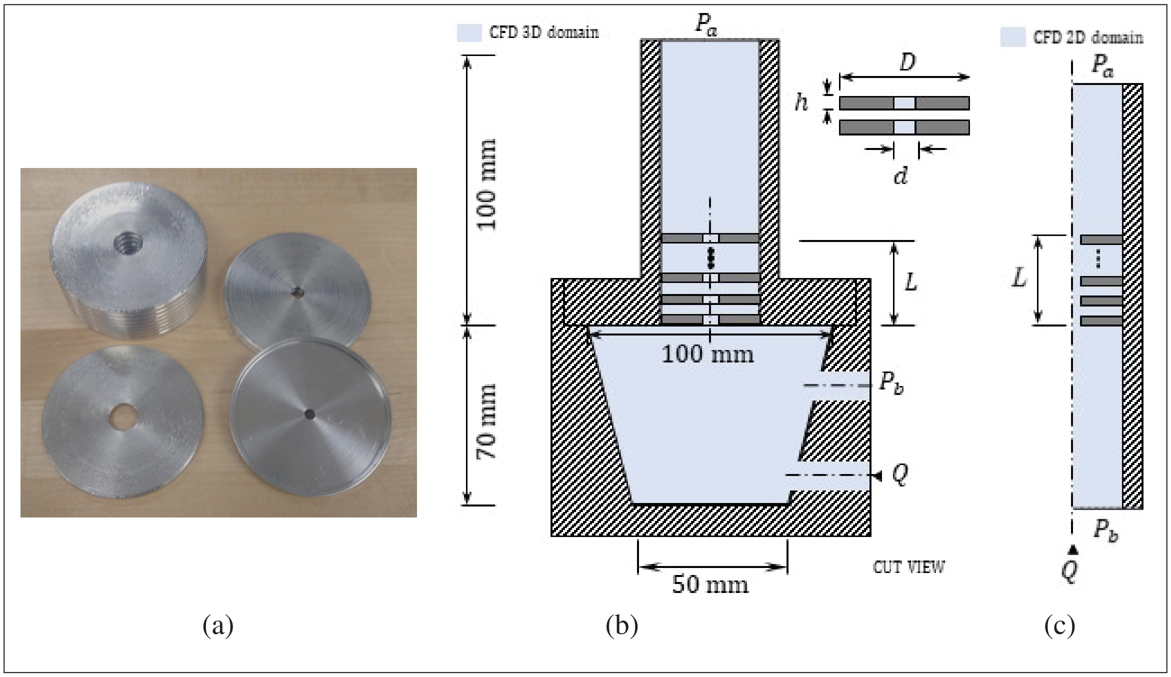

Figure 4.1 (Color online). (a) Photo of the metamaterial studied: succession of single-perforation plates (SPPs). (b) and (c) Three-dimensional (3D) and two-dimensional (2D) axisymmetric representations of the setup and SPPs for airflow resistivity characterization

4.4 Methods

After recalling the modeling approach for airflow resistivity, this section introduces the measurement techniques and numerical simulation methods employed for its characterization.

4.4.1 Modeling method: Darcy and Darcy-Forchheimer's laws

In the field of porous materials, airflow resistivity appears to be a complex function linked to the relationship between the pressure loss and the air flow passing through the material. Mathematically, the airflow resistivity of a porous sample is expressed as follows:(ISO 9053-1, 2018)

$$\sigma = \frac{\Delta P\, A}{Q L} \tag{4.1}$$

where ΔP is the overall pressure difference across the sample, Q the volumetric flow rate passing through the sample, A its cross-section area, and L its thickness.

For a single-perforated sample (SPP or a succession of SPPs) that has a circular perforation, the Reynolds number in the perforation is calculated using the formula $\mathrm{Re}_d = \rho_0 v_p d/\eta$, where ρ_0 represents the air density, $v_p = Q/(\phi A)$ is the velocity in the perforation, $\phi = (d/D)^2$ is the open area (OA), and η is the dynamic viscosity of the fluid saturating the sample. Here, the Reynolds number in the perforation is employed to check if the flow is in the typical laminar range. For practical purposes, the flow is known to be laminar if the Reynolds number is less than 2000. In situations where the Reynolds number Re_d is less than unity ($\mathrm{Re}_d < 1$), the airflow resistivity remains constant, equating to the static airflow resistivity coefficient σ_0. Under low Reynolds numbers, the behavior of the airflow can be accurately described by Darcy's law. According to Darcy's law, the pressure drop ΔP through the sample is a linear function of the velocity imposed in the D=44.44 mm diameter tube, V, and is given by:

$$\frac{\Delta P}{L} = \sigma_0 V. \tag{4.2}$$

For higher Reynolds numbers in the perforation (i.e., $\mathrm{Re}_d > 1$), the relationship between pressure drop and velocity is no longer linear and the airflow resistivity varies with velocity. In this case, the relationship between the pressure drop and the velocity is governed by Darcy-Forchheimer's law, expressed as:

$$\frac{\Delta P}{L} = (\sigma_0 + FV)\, V, \tag{4.3}$$

where F is called here the Forchheimer coefficient. The presence of FV in Darcy-Forchheimer's law indicates the nonlinear dependence of pressure drop on velocity, capturing the impact of inertial forces at higher flow rates. Consequently, from equation (4.1) and equation (4.3), under this nonlinear flow regime, the airflow resistivity can be written as:

$$\sigma = \frac{\Delta P}{VL} = \sigma_0 + FV. \tag{4.4}$$

Determining the Forchheimer coefficient F involves a combination of experimental measurements and/or numerical simulations, ensuring a comprehensive understanding of the airflow dynamics within the porous material or perforated plate system. This dual approach enables researchers to validate and refine their models, enhancing the accuracy of predictions regarding airflow resistivity under varying conditions.

4.4.2 Measuring method: airflow resistivity meter

The material airflow resistivity is measured following the guidelines outlined in the standard ISO 9053-1 (2018). A Mecanum airflow resistivity meter (ARM) is employed for this purpose, with the schematic of the test bench depicted in figure 4.1(b). In the setup, Q denotes the volumetric flow rate at the inlet, while P_b represents the measured pressure upstream of the material. A thin ring is introduced before the material to secure it in the sample holder and petroleum jelly is used to prevent air-leaks. At the exit of the sample holder, the pressure is the atmospheric pressure, denoted as P_a. The overall pressure drop corresponds to $\Delta P = P_b - P_a$ directly given by a differential pressure sensor in the ARM.

To guarantee accuracy and reliability, the measurement on each sample is repeated five times by disassembling and randomly reassembling successive SPPs. The determination of the overall pressure drop involves measuring at various flow rates. The flow is generated by the mass flow controller (MFC) of the ARM. The admissible range of the flow rate is dictated by the MFC capability, the sensitivity of the pressure sensor, and the airflow resistivity of the material. Notably, the measuring range is directly influenced by the perforation diameter d. In fact, for a long circular perforation in a solid cylinder of radius d, the theoretical value (without end effects) of the static airflow resistivity is given by $\sigma_0 = 32\eta/\phi d^2$.

4.4.3 Simulation method: Computational fluid dynamics

In the present study, the computational fluid dynamics (CFD) is used to model the flow inside the ARM in order to predict numerically the pressure drop due to the test sample. Two geometrical models are selected to run the CFD: a 3D model and a 2D-axisymmetric model, see figure 4.1(b) and figure 4.1(c), respectively. The 3D model reproduces the measurement cell of the ARM described earlier. Given that the calculation time for the complete 3D geometry is expected to be extensive, a 2D-axisymmetric simplified model is initially preferred for performing parametric analyses. However, to ensure that the 2D model accurately captures the primary physics of the flow, an initial comparison with the 3D model will be necessary to validate its results. This will be the objective of section 4.5.1.

4.4.3.1 Full geometrical 3D model

The whole ARM has been reproduced numerically, by respecting the different dimensions shown in figure 4.1(b). Calculations are carried out on a single SPP and on the assembly of up to 16 SPPs. The calculations of the flow dynamics inside the ARM for the 16 configurations are performed by a 3D steady-state incompressible RANS solver named SimpleFoam (OpenFoam 6). This solver has been selected for the following reasons: (i) its ability to accurately predict the pressure drop due to the samples; (ii) the steady-state approach is suitable as the objective of the study is to predict the average pressure loss.

A fully second-order scheme is used for the spatial discretization in order to minimize excessive numerical dissipation. The Laplacian and gradient terms are discretized by using a bounded Gauss linear numerical scheme. A linear approach is selected for the interpolation scheme. The SIMPLE (Semi-Implicit-Method for Pressure-Linked Equations) algorithm enables overcoming the pressure-velocity coupling. The generalized geometric-algebraic multi-grid (GAMG) solver with the combined Diagonal incomplete-Cholesky/Gauss Seidel (symmetric) smoother is selected to solve the pressure. The preconditioned bi-conjugate gradient (PBiCG) solver with

Diagonal incomplete-LU (DILU) pre-conditioner is used to solve the rest of the discretized equations.

The boundary conditions of the 3D computational domain are shown in figure 4.1(b). A flow rate condition is imposed at the inlet. The different flow rates are calculated based on the defined Re_d values in the perforation. A pressure outlet is used at the pipe outlet surface where an atmospheric pressure is imposed. An unstructured fine grid mesh is generated by the open-source Salome library. Different views of the mesh are presented in figure figure 4.2(a) Tetrahedral elements have been generated in the whole domain with a refinement around the samples and the pore regions.The minimum and maximum tetrahedral cell sizes are 0.0021 and 0.0005, respectively. A mesh refinement with factor equal to 5 is imposed in the samples and pore regions, with a stretching factor of 1.1.

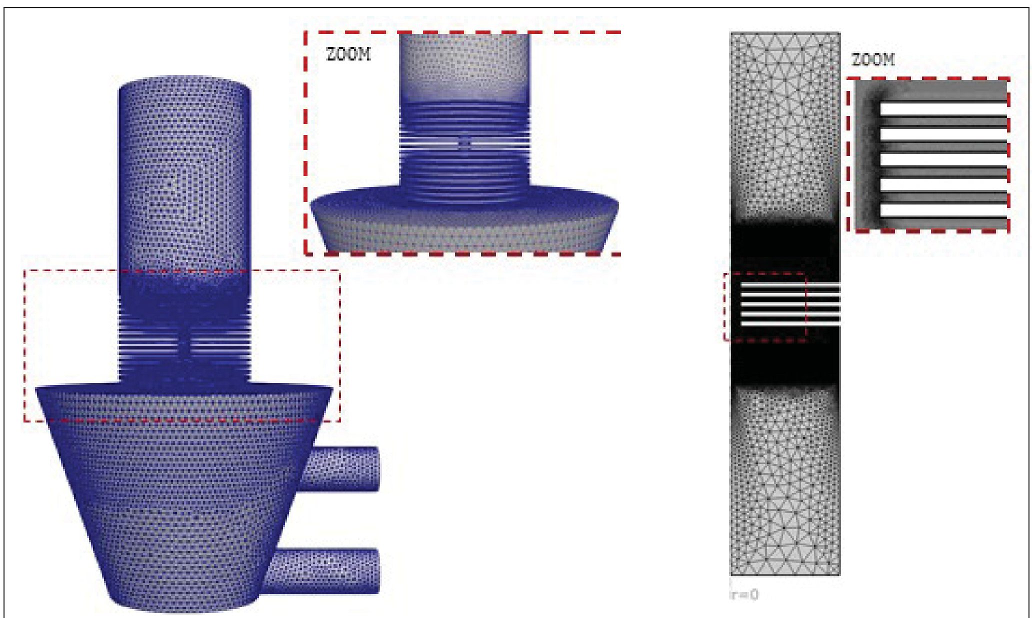

(a) (b)

Figure 4.2 (Colour online.) Views of the mesh distribution sketch of the computational domain of (a) the 3D approach model, and (b) the 2D-axisymmetric model

For all configurations, the CFD process is executed automatically, namely for geometry and mesh generation, calculation, and post-processing. Furthermore, the mesh criteria are kept the same. Convergence is achieved when: (i) the total deviation of the global pressure drop between two subsequent iterations is below 0.1%; (ii) all residuals are lower than 10^{-7}, and (iii) the mass imbalance is lower than 10^{-6}.

4.4.3.2 Simplified 2D-axisymmetric model

A predictive model using COMSOL Multiphysics 5.6 was used to evaluate overall pressure drops at various Reynolds numbers, using the 2D-axisymmetric geometrical model shown in figure 4.2(b). The geometry consisted of three distinct parts: (I) the middle part representing the material under study (1 SPP or a collection of up to 16 SPPs placed in series); (II) an extrusion upstream the middle part, and (III) and extrusion downstream the middle part. Each extrusion is 2.5 times the diameter of the sample (ie, $2.5D$). The simulation was conducted with air at 20°C and atmospheric pressure. Quadratic elements were deployed to discretize the studied domain, employing an extra-fine fluid dynamic element size in the material region, the mesh distribution is shown in figure 4.2(b). For the rest of the domains (extrusions upstream and downstream), the size of the elements was coarse fluid dynamic type. Rigid walls featured a boundary layer mesh with eight layers and a stretching factor of 1.12. The simulation adopted COMSOL's laminar flow approach within the compressible flow (Mach number < 0.3) physical model. Upstream of the tube, fully developed flow rate (Q) boundary conditions were imposed, while fully developed average pressure (P_a) boundary condition was imposed on the downstream tube (output). All solid walls were treated as rigid, adhering to a no-slip boundary condition. The convergence of the solution for each configuration is achieved using the default convergence parameters in COMSOL.

4.5 Results and discussions

The validity of the CFD models is initially established by comparing their results with experimental data. Subsequently, the Forchheimer and static airflow resistivity coefficients of equation (4.3) are derived through regression analysis based on overall pressure drops. Finally, the internal airflow dynamics within the material are investigated. Local variations in the Forchheimer and static airflow resistivity coefficients are deduced from the pressure drop across individual plates. In this study, 'overall' pertains to the flow dynamics across the entirety of the material (entire succession of SPPs), whereas 'locally' describes the flow dynamics specific to individual SPPs within the material. Elsewhere, these overall coefficients for a layered porous medium are named effective coefficients (Lenci, Zeighami & Di Federico, 2022).

4.5.1 Validation

To validate the CFD models, their results were compared with measurements made on four samples. Each sample is a combination of perforation diameter and number of SPPs: (d = 4 mm, N = 5); (d = 4 mm, N = 9); (d = 8 mm, N = 5), and (d = 8 mm, N = 9). Comparisons are made in terms of the pressure drop ΔP versus the Reynolds number. They are shown in figure 4.3.

Considering samples with a diameter of 4 mm, the numerical models and the experimental ones agree fairly well. This is particularly true for Reynolds numbers below 500. The impact of the setup geometry (3D full-geometry model and 2D-axisymmetric geometry) on the overall pressure drops is small. Above this threshold, the difference between the two numerical approaches is minimal, typically around 5 Pa. Remarkably, the pressure drop trends obtained through the 2D-axisymmetric CFD model closely match experimental measurements across all Reynolds numbers. Additionally, it's noteworthy that the computational time required for the full-geometry models is significantly higher. Consequently, for subsequent analyses, the 2D-axisymmetric CFD model is exclusively used for all samples, while the full-geometry model is restricted to samples with a diameter of 4 mm. For the samples with a diameter of d = 8 mm, the overall pressure drops calculated with the 2D-axisymmetric CFD model compare well with measurements as shown in figure 4.3(c) and figure 4.3(d).

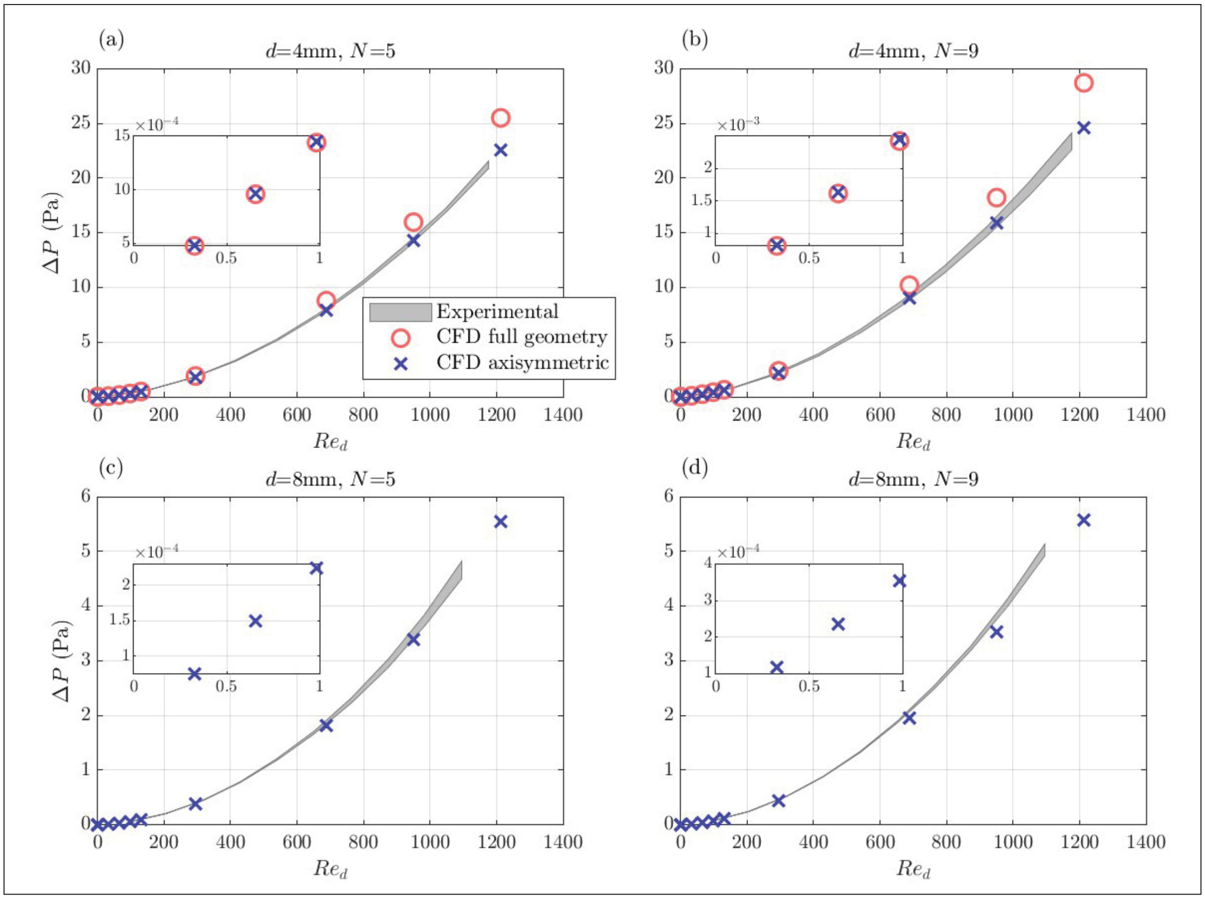

Figure 4.3 (Color online). Overall pressure drops at different Reynolds numbers in the perforation for 2D and 3D numerical models and experimental measurements for four samples. The thickness of the experimental curve represents the dispersion over 5 experimental measurements

The insets in figure 4.3 show the pressure drop at $\mathrm{Re}_d < 1$. At low Reynolds numbers, the pressure drop is not sufficient to be measured experimentally. However, the CFD results show a pressure drop lower than 0.02 Pa and a linear relation between ΔP and Re_d; this follows Darcy's law equation (4.2), where viscous forces dominate over inertial forces. When $\mathrm{Re}_d > 1$, the overall pressure drop tends to increase quadratically with the Reynolds number in the perforation; this is in accordance to Darcy-Forchheimer's law, equation (4.3).

4.5.2 Darcy-Forchheimer coefficients: overall effects

This section addresses the determination and analysis of the two coefficients of Darcy-Forchheimer's quadratic law on the entire sample. These coefficients are used to compare the flow dynamics (i.e., $\Delta P(V)$) at different perforation diameters and number of SPPs. First, the overall methodology for determining the coefficients is described, followed by the extraction and analysis of these coefficients for the various samples.

4.5.2.1 Determination of global coefficients: methodology

In the previous section, it has been observed that the overall pressure drop evolves quadratically with Re_d. According to Darcy-Forchheimer's law equation (4.3), the two coefficients of the quadratic law, F and σ_0, are determined in two successive steps as follows:

1. The static airflow resistivity coefficient, σ_0, is determined when viscous forces dominate, that is at $\mathrm{Re}_d < 1$. For the numerical models, a linear regression is made on the calculated results $\Delta P(V)$, for flow velocities V corresponding to Reynolds numbers less than unity in the perforation. The regression shall pass through the origin, which is a physical constraint to the problem ($\Delta P(0) = 0$ Pa). Following equation (4.2), the slope of the linear regression divided by thickness L gives σ_0 of the SPP (or SPP assembly) of external diameter D. As discussed in section 4.5.1, for the experimental measurements, no data were possible in this linear range. Instead, the stepwise measurement procedure defined in the standard ISO 9053-1 (ISO 9053-1, 2018) is employed with the lowest measurable flow velocities to determine σ_0. A quadratic regression is then made on these measurable data, and an extrapolation to 0 mm/s is done to retrieve the static airflow resistivity.
2. The Forchheimer coefficient, F, is determined in the range where inertial forces dominate. This time, a second-order regression is made on the calculated $\Delta P(V)$ data for laminar flow velocities V corresponding to Re_d between 30 and 1500. Since the linear term σ_0 of the regression is already known, it is imposed in the regression. Consequently, only the Forchheimer coefficient is retrieved from this regression.

4.5.2.2 Results

Figure 4.4(a) presents the overall pressure drop obtained by the axisymmetric CFD model at different flow velocities V. The results of three samples with the same number of SPPs, $N = 5$, with different diameters, $d = 2, 4$ and 8 mm are represented with their corresponding regression curve. The inset shows the data used for the linear regression on a low Reynolds numbers as discussed in the previous methodology section. Each regression has a coefficient of determination R^2 greater than 0.9998. For these samples, extracted static airflow resistivity σ_0 are $7.22{\cdot}10^4$, $5.367{\cdot}10^3$ and $4.16{\cdot}10^2$ Pa.s/m^2, and Forchheimer coefficients, F, are $2.92{\cdot}10^7$, $1.69{\cdot}10^6$ and $1.06{\cdot}10^5$ Pa.s^2/m^3, respectively. From these results, one can observe that σ_0 decreases logically with increasing perforation diameter. A same trend is observed with F. To highlight the last comment, the overall airflow resistivity, equation (4.4), is determined by the overall pressure drops and the velocity V. The overall σ is shown in figure 4.4(b) for the axisymmetric CFD model (same samples than Figure 4.4(a)). The airflow resistivity increases linearly with the pore flow velocities. The slope is associated to the Forchheimer coefficient, F, which is greater the smaller the pore diameter. In the inset, a zoom on a low Reynolds number, i.e., Re_d<1, shows that resistivity is nearly constant. The overall airflow resistivity allows for a similar visualization of the flow dynamics in all three samples as the pressure drops.

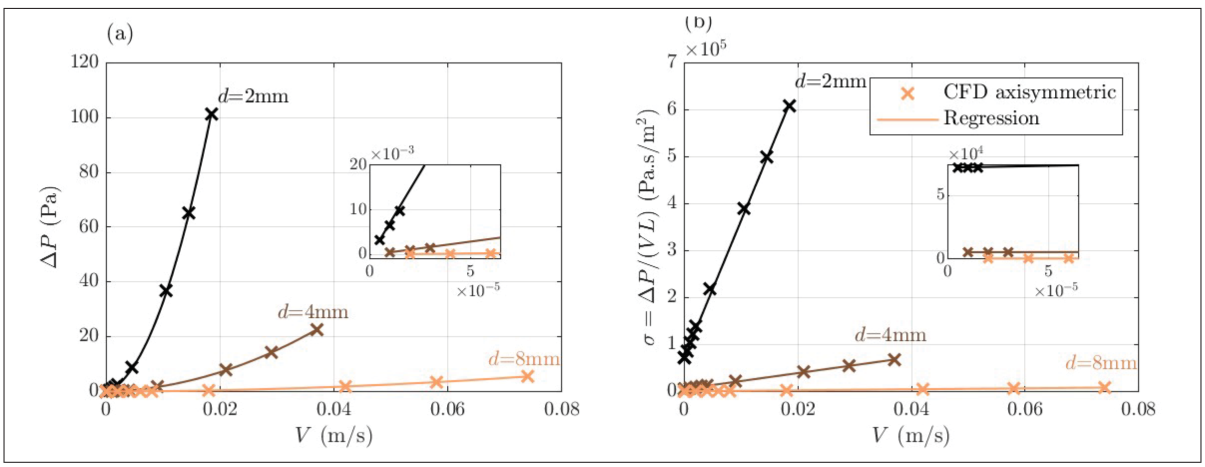

Figure 4.4 (Color online). (a) Overall pressure drop at different pore flow velocities of three samples with different pore diameter and with $N = 5$. (b) Corresponding airflow resistivity

As seen in the previous example on three samples, F and σ_0 characterize accurately ($R^2 > 0.9$) the evolution of the pressure drop and resistivity. Using the methodology of section 4.5.2.1 , the regression coefficients for the data obtained from the two CFD approaches and the experimental approach are now determined for 16 samples with d = 4 mm and N from 1 to 16. Figure 4.5 compares the overall σ_0 and F of the three approaches in function of the number of successive SPPs. The experimental curve represents the regression using the least squares method over all the data. The line and error bars are the mean and standard deviation obtained from five measurements as described in section 4.4.2. The results on figure 4.5 globally show that both σ_0 and F decrease with the number of SPPs. The two CFD approaches agree well with the experiment for the Forchheimer coefficient. However, for the static airflow resistivity, they slightly diverge from measurements for a smaller number of SPPs. As mentioned before in section 4.5.2.1, this is explained by the fact the condition $\mathrm{Re}_d < 1$ was not respected with the ARM setup. Furthermore, the flow contraction and expansion effects have more impact on a thin material. Also, the shape of the perforation impacts the airflow resistivity (Stinson, 1991). Consequently, inaccuracies in the manufacturing of samples (perforation shape and edge chamfer) could have a greater impact on the results for a thin material (especially for a single SPP, thickness of 1 mm). For more than 5 successive SPPs ($N > 5$), the condition $\mathrm{Re}_d < 1$ is still not fulfilled for experimental results. Nevertheless, a good agreement is observed between the three approaches for σ_0. In these cases, the thickness of the assembly is larger, allowing the flow to homogenize (with fewer contributions of end effects). Remarkably, the values of σ_0 of the three approaches tend to the theoretical value for a continuous tube of a circular cross-section (Stinson, 1991). So, a compact array of SPPs (with $N > 5$) has the same overall airflow behavior as a continuous pipe of the same length at low Reynolds numbers in the perforations.

Figures 4.6 (a) and (b) show the static airflow resistivity and Forchheimer coefficient as a function of the percentage of open area and the number of successive SPPs. At a given N, increasing the POA causes σ_0 and F to decrease significantly. Regardless of the POA, σ_0 and F decrease with an increase in the number of SPPs. σ_0 tends towards a constant value as the number of SPPS increases, see figure 4.5. To highlight this last comment, the coefficients in terms of

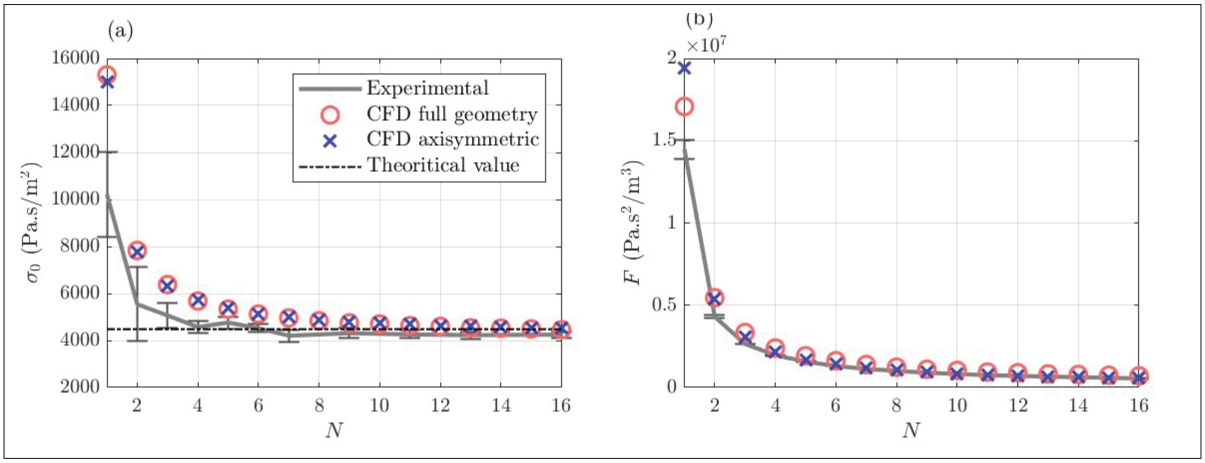

Figure 4.5 (Color online). (a) Overall static airflow resistivity and (b) overall Forchheimer coefficient for different numbers of SPPs with perforation diameter $d = 4$ mm. The standard deviation of the experimental measurements are represented by the error bars

airflow resistance (i.e., σL) are shown in figure 4.6(c) and (d). The static airflow resistance, see figure 4.6(c), unsurprisingly it increases linearly with the addition of SPPs (or indirectly with the thickness). Unlike σ_0, F only decreases as the number of SPPs increases. Figure 4.6(d) shows that $F \times L$ slightly increases without following a linear increase. This observation confirms that F does not tend to a constant value. Strong inertial effects associated with high values of F occurs for the low number of SPPs or thin materials.

The coefficients for the three approaches are given in supplementary materials [1].

4.5.3 Darcy-Forchheimer coefficients: local effects

4.5.3.1 Pressure drop profile

The local pressure drop in each SPP of an assembly was calculated at different Reynolds numbers (Re_d). The results are presented in figure 4.7 for the same four samples as in figure 4.3. Here, the local pressure drop ΔP_l for the i-th SPP of an assembly is the difference between the pressure

[1] See Supplementary materials at [URL will be inserted by AIP] for the overall and local coefficients computed in the present article.

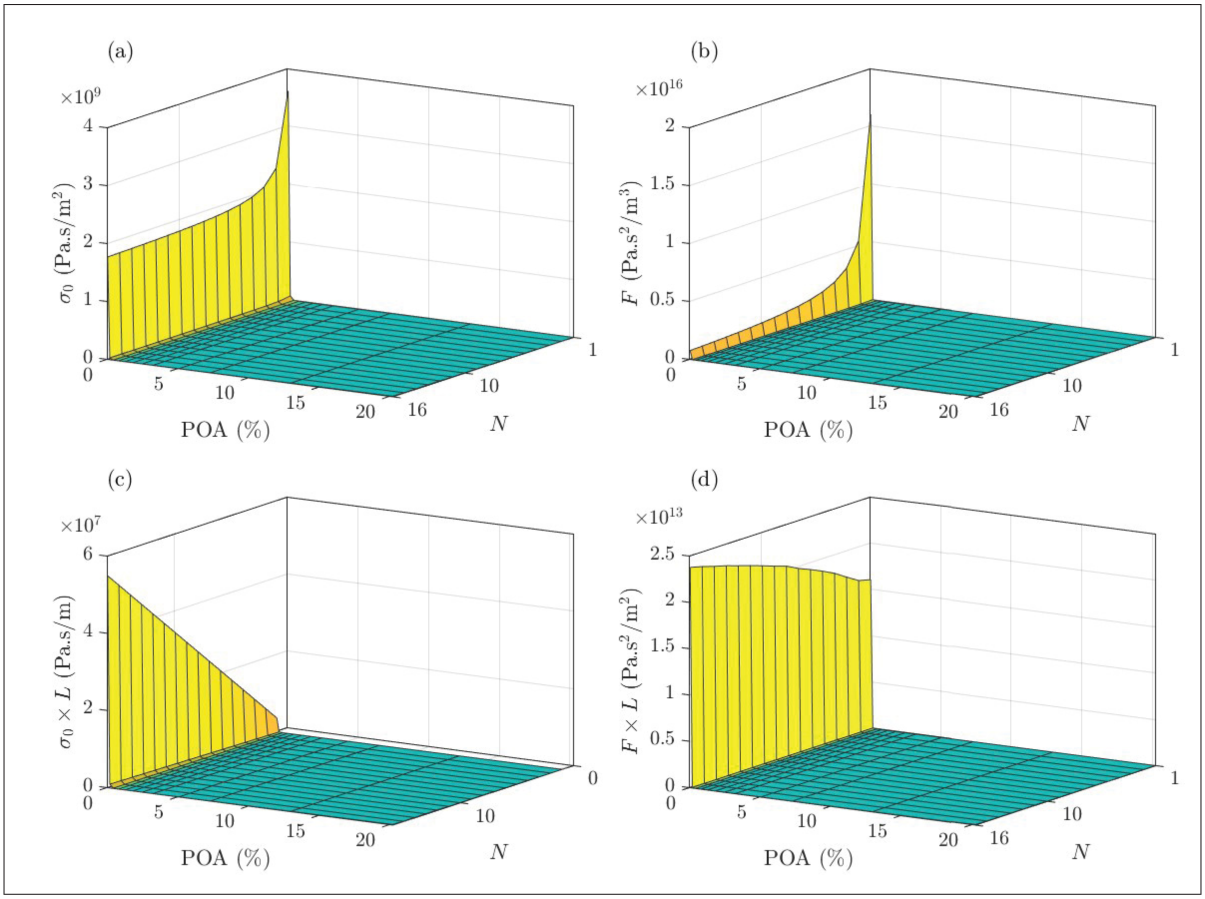

Figure 4.6 (Color online). (a) Overall static airflow resistivity coefficient. (b) Overall Forchheimer coefficient. (c) Overall static airflow resistance coefficient. (d) Overall Forchheimer coefficient multiplied by the thickness. The results are obtained using the numerical model with axisymmetric geometry

upstream and downstream of its perforation. Since the pressure profile is not uniform at the entrance and exit sections of the perforation, an average is taken on each of the sections to evaluate ΔP_l. In figure 4.7, the insets represent the pressure drops at velocities corresponding to $\mathrm{Re}_d < 1$ in the perforation. One can note that at low Re_d the pressure drops are almost constant within the material. All SPPs have the same resistivity. At $\mathrm{Re}_d > 1$, the pressure drop changes with an increase in Reynolds numbers. The pressure drop of the first SPP is much greater than that of the other. The pressure drop decreases in the second plate and may even become negative at high Re_d. Then, it tends to a constant value in the last SPPs. Globally, the profile of the pressure drop with the plate number seems independent of the number of SPPs in the material

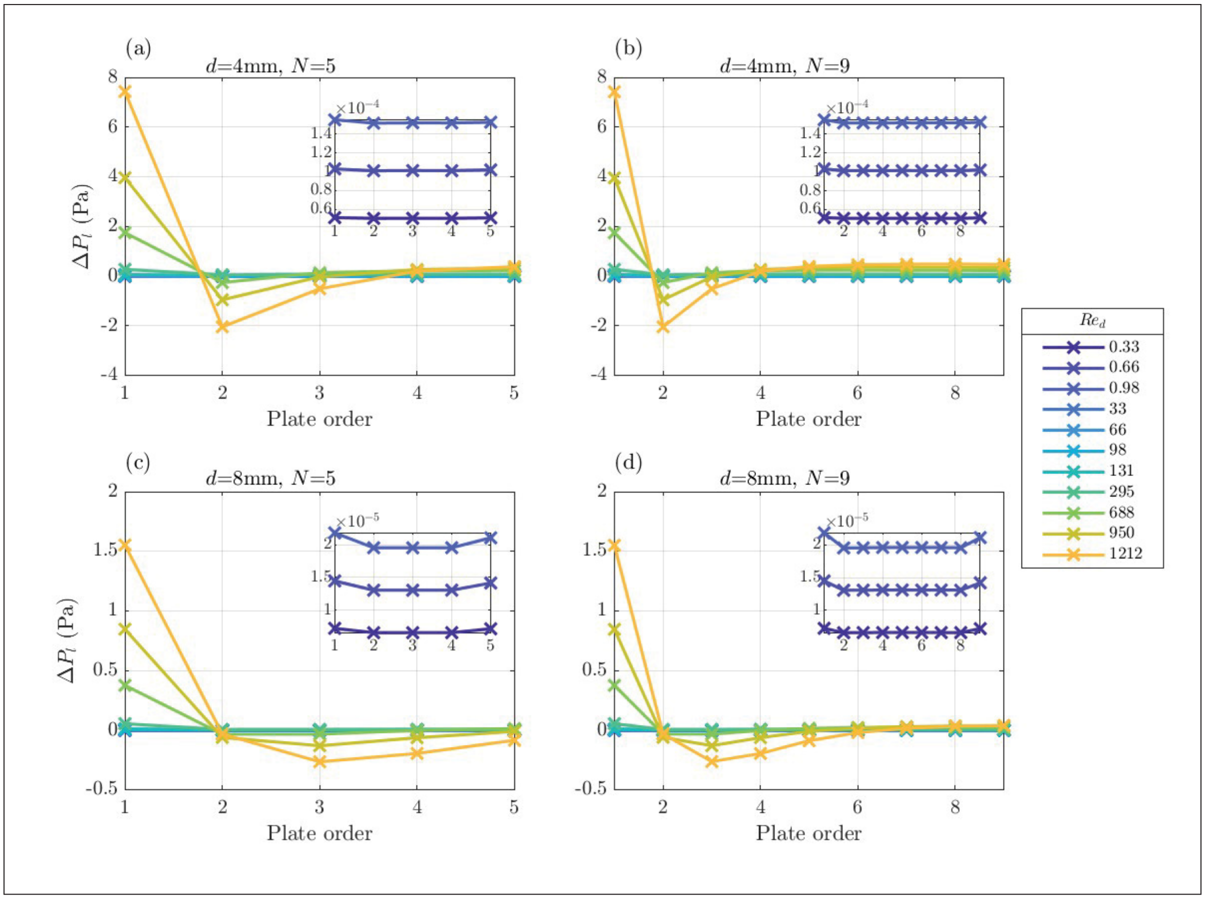

Figure 4.7 (Color online). The pressure drop inside the material for different pore Reynolds numbers. Four samples are presented (a-d)

(e.g., compare Figs 4.7(a) and (b), or (c) and (d)); however, it is reduced with a larger perforation diameter (e.g., compare Figs 4.7(a) and (c), or (b) and (d)).

This analysis of the local pressure drop profile within a series of successive SPPs indicates that the first SPP has the greatest impact on the assembly's pressure drop. Therefore, the first SPP mainly controls the Forchheimer coefficient, effectively controlling the nonlinear dynamics of the airflow.

4.5.3.2 Determination of local coefficients: methodology

The previous analysis of the pressure drop profile showed that the first SPP governs mainly the nonlinear dynamics of the airflow. Consequently, the coefficients of the Darcy-Forchheimer's law are now determined locally on the first SPP. Locally, the pressure drop in the first SPP is given by

$$\Delta P_1 = P_{b,1} - P_{a,1} = \sigma_{0,1} h \phi \bar{v}_p + F_1 h \phi^2 \bar{v}_p^2, \tag{4.5}$$

where $P_{b,1}$ and $P_{a,1}$ are respectively the average pressures on the inlet and outlet sections of the perforation of the first SPP, h is its thickness, and $\sigma_{0,1}$ and F_1 are its static airflow resistivity and Forchheimer coefficient. In the right side of the equation, $\bar{v}_p$ is the average velocity in the perforation ($\phi v_p = V$). It is approximated here by $\bar{v}_p \approx (v_{b,1} + v_{a,1})/2$, where $v_{b,1}$ and $v_{a,1}$ are the average velocities on the inlet and outlet sections of the perforation, respectively. Similarly to the methodology for the overall pressure drop, section 4.5.2.1, the following methodology has been used to determine the first SPP coefficients:

1. $\sigma_{0,1}$ is determined using a linear regression on the $\Delta P_1 \left(\bar{v}_p\right)$ data computed from the axi-symetric CFD model for flow velocities corresponding to $\mathrm{Re}_d < 1$.
2. F_1 is determined by a quadratic regression on the data for flow velocities corresponding to Re_d between 30 and 1500. In this regression, the static term is imposed to $\sigma_{0,1}$ determined in the previous step.

4.5.3.3 Results

The first SPP pressure drops at different flow velocities for samples of $d = 2, 4, 8$ mm and $N = 5$ SPPs are shown in figure 4.8(a). A comparison with figure 4.4(a) shows that the local evolution of $\Delta P_1(V)$ in the first SPP is similar to the global evolution $\Delta P(V)$ of the entire material. The only downside is that, this time, the quadratic regression seems slightly less adapted to the results of the CFD model (see the difference between the regression and the CFD results). This is particularly the case for $d = 2$ mm and $d = 4$ mm. The authors believe this is because locally the nonlinear effects of the flow at the first SPP are much larger than these average effects on the overall assembly. A parallel study by the authors tends to confirm this observation(Benchikh Le Hocine *et al.*, 2023). In fact, in this study it is shown that for a solid cylinder with a single-perforation, the quadratic regression no longer works for $\mathrm{Re}_d > 500$. For these two diameters, the corresponding speeds in the perforation are 3.75 mm/s and 1.88 mm/s, respectively. However, in the present local quadratic regressions, the coefficient of determination R^2, for the three diameters, is greater than 0.95. Keeping this in mind, the quadratic law is assumed to be "adequate" for the Reynolds numbers studied.

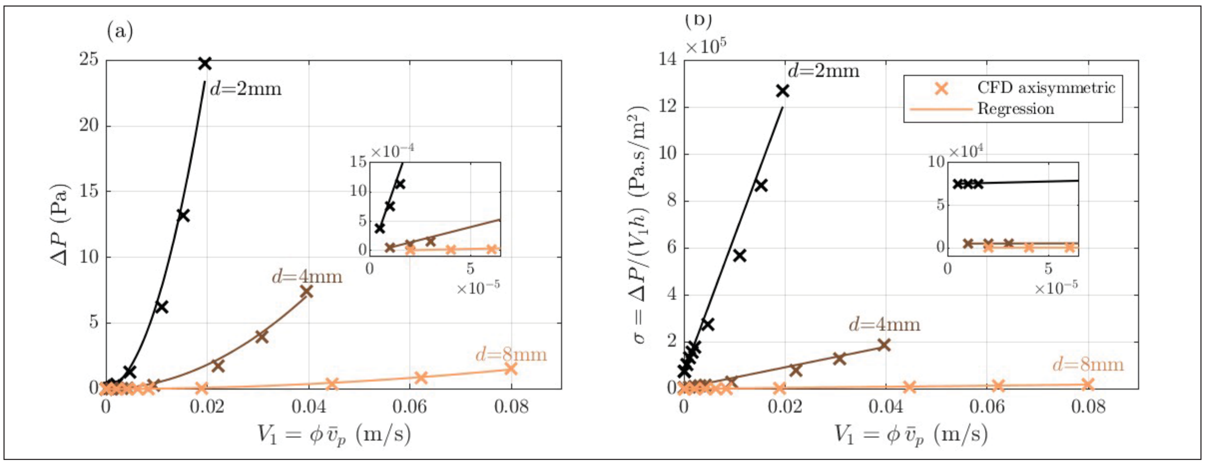

Figure 4.8 (Color online). (a) Local pressure drop of the first SPP at various flow velocities in the perforation for three samples with different perforation diameters, but the same number of SPPs $N = 5$. The lines are the quadratic regressions. (b) Corresponding airflow resistivity

The inset of figure 4.8(a) shows the local pressure drops at $\mathrm{Re}_d < 1$, viscous regime. For viscous and inertial regime, the increase in pressure drops is higher for a small diameter perforation. Figure 4.8(b) shows the first SPP resistivity curves shown in figure 4.8(b). In the same way as for local pressure drops, the evolution of the local airflow resistivity is similar to the evolution overall airflow resistivity, see figure 4.4(b). The slope of the local airflow resistivity is greater the smaller the pore diameter. This will appear clearer in the analysis of the static airflow resistivity $\sigma_{0,1}$ and Forchheimer coefficient F_1 of the first SPP, shown in figure 4.9, for different diameters of perforation and number of SPP N.

In figure 4.9(a), it is observed that $\sigma_{0,1}$ is constant with N. Indeed, at $\mathrm{Re}_d < 1$ the flow is laminar and the pressure drop of the first SPP is independent of the presence of other SPPs. Also, $\sigma_{0,1}$ decreases in $1/d^2$ in function of the POA, and is close to the theoretical value of a circular pipe, that is $32\eta/(\phi\, d^2)$. For $d = 2, 4$ and 8 mm, these values are approximately $7.17{\cdot}10^4$, $4.48{\cdot}10^3$, and $2.80{\cdot}10^3{\cdot}10^2$ Pa·s/m^2.

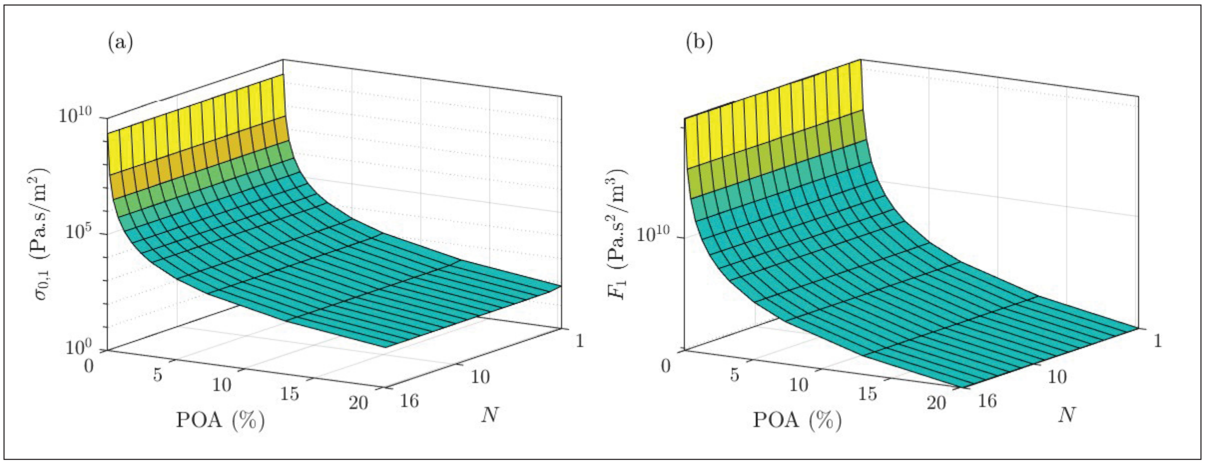

Figure 4.9 (Color online). (a) First plate static airflow resistivity coefficient. (b) First plate Forchheimer coefficient. (a) and (b) are in logarithmic scale along z. The results are obtained using the numerical model with axisymmetric geometry

In figure 4.9(b), similarly to $\sigma_{0,1}$, F_1 is independent of N. This is in agreement with the observations made in figure 4.7. The first SPP pressure drops are identical for samples of the same diameter at the same Re_d. $\sigma_{0,1}$ and F_1 decrease significantly as POA increases (logarithmic scale for the coefficients in figure 4.7).

In this section, we observed that in inertial regime, the pressure drops vary non-uniformly through the material. Inertial effect are dominant at the first plate. Inertial effect of the first plate are independent of the number of SPPs. In view of these observations, a local approach of the airflow resistivity (i.e., using the Forchheimer coefficient of the first SPP) should be preferred to account for acoustic non-linearities in the succession of SPPs spaced by thin air cavities.

4.6 Conclusion

Viscous and inertial effects on the airflow resistivity of periodic array of single-perforation plates have been studied. Two numerical approaches have been used to model the airflow through the material. The geometry of the first one reproduces the experimental airflow resistivity meter and the second is a simplified geometry (2D-axisymmetric). The pressure drops is evaluated at different flow rates on the entirety of the material (globally) and at each plate (locally). The pressure drops follow a quadratic function of the flow velocity imposed, in accordance with Darcy-Forchheimer's law. The coefficients of the quadratic function are determined globally and locally. The impact of the perforation diameter and the number of plates on the coefficients have been investigated. One of the important observations is that at pore Reynolds numbers higher than one (inertial regime), the pressure drops are no more constant. They are maximum for the first plate, drop for the second and are constant for the last plates. Inertial effects dominate for the first plate. Meaning acoustic additional losses due to high sound pressure level will dominate for the first plate. This effect can be taken into account in acoustic models by the Forchheimer coefficient of the first single-perforation plate presented in this article.

Acknowledgments

The authors acknowledge the financial support of Natural Sciences and Engineering Research Council of Canada (NSERC) [funding reference numbers: RGPIN-2018-06113 and RGPIN-2019-06573].

Author declarations

Conflict of Interest

The authors state that they have no conflict of interests to disclose.

Data availability

The data that support the findings of this study are available from the corresponding author upon reasonable request.

CHAPITRE 5

MASS-SPRING MODEL FOR A PERFORATED PERIODIC METAMATERIAL IN LINEAR AND NONLINEAR REGIMES

Maël Lopez[1] , Tenon Charly Kone[2] , Alla Eddine Benchickh Le Hocine[3] , Thomas Dupont[1] , Raymond Panneton[3]

[1] Département de Génie Mécanique, École de Technologie Supérieure,
1100 Notre-Dame Ouest, Montréal, Québec, Canada H3C 1K3
[2] National Research Council Canada, Flight Research Laboratory,
1200 Montreal Road, Ottawa, Ontario, K1A 0R6, Canada
[3] CRASH-UdeS, Department of Mechanical Engineering, Université de Sherbrooke,
2500 boul. de l'Université, Sherbrooke, Québec, J1K 2R1, Canada

Article soumis à la revue « Journal of the Acoustical Society of America » en juillet 2024.

5.1 Abstract

This study is interested in the nonlinear acoustic response of a metamaterial composed of a periodic array of single-perforation plates spaced by thin air cavities. An equivalent mass-spring model is adapted to predict the metamaterial acoustic response under high sound pressure levels. The increase in losses induced by the high level is considered by a quadratic law for the airflow resistivity in effective fluid model. The airflow resistivity coefficients which are included in the mass-spring model are determined from predictions by the computational fluid dynamics method at different flow velocities. The model is validated with impedance tube measurements for samples with different numbers of periodic unit cells and perforation sizes. The results show that the acoustic resistance of the metamaterial increases with increasing sound pressure levels while the reactance is almost unchanged. The absorption peaks at low frequencies are more impacted by high sound pressure levels. A criterion based on the viscous characteristic frequency is proposed to determine the limit of the beginnings of the nonlinear material response. This limit is given by an acoustic Reynolds number, which depends on the frequency and perforation size.

5.2 Introduction

Low-frequency noise control is a challenge for industrial applications where space is limited, such as aerospace. In this field, the acoustic response of materials deviates from the linear regime as the sound intensity increases or in the presence of grazing flow. Understanding the nonlinear acoustic response of materials plays a crucial role in mitigating aircraft engine noise, directing efforts towards designing and improving quieter aircraft. However, dealing with acoustic nonlinearities poses a notable challenge due to the computational complexity required to accurately model nonlinear acoustic phenomena in complex aerospace environments. Developing efficient computational models capable of fast simulations of nonlinear acoustic effects, including interactions with acoustic metamaterials, remains a significant hurdle for researchers and engineers in this field.

Acoustic metamaterials offer promising solutions for addressing low-frequency noise issues in aeronautics. These materials enable improved acoustic performance while requiring smaller thickness and volume compared to conventional materials such as foam and fibrous materials, or side-branch resonators (Groby, Jiménez & Romero-García, 2021).Among acoustic metamaterials, periodic structures with lateral dead-ends (DE) are particularly interesting. While these structures have been extensively studied in the linear regime, (Leclaire *et al.*, 2015; Groby *et al.*, 2015a, 2016; Jiménez *et al.*, 2016, 2017c; Dupont *et al.*, 2018; Romero-García *et al.*, 2020; Kone *et al.*, 2021b; Bezançon *et al.*, 2024; Lopez *et al.*, 2024) only a limited number of studies have addressed their acoustic nonlinearity, primarily due to challenges posed by high sound pressure levels (Brooke *et al.*, 2020) or airflow-induced effects (Aurégan *et al.*, 2016).

To consider high sound pressure levels into rigidly framed fibrous materials, McIntosh & Lambert (1990) have proposed to use the Darcy-Forchheimer's law where the airflow resistivity is a linear function of the airflow velocities instead of Darcy's law, in which resistivity is constant. The Forchheimer coefficient is determined at higher flow velocities, where inertial effects dominate over viscous effects. The Darcy-Forchheimer's law is employed in acoustic models using an effective value of the velocities. Ingard & Ising (1967) have investigated the nonlinear acoustics of an orifice in a perforated plate by simultaneously measuring the acoustic velocity in the orifice and the acoustic pressure. They showed that the relationship between pressure and velocity amplitude is linear at low velocities and approaches a quadratic law at high velocities. They showed that the reactance (the imaginary part of the impedance) decreases slightly as amplitude velocity increases. Maa (1994) explained that the acoustic nonlinearity of an orifice is an external phenomenon and proposed a nonlinear acoustic impedance model for micro-perforated panels (MPP) where the specific nonlinear resistance expression is the Mach number in the perforations divided by the percentage of open area. Laly *et al.* (2018) proposed an equivalent fluid model for MPP backed by cavities with an airflow resistivity approach similar to Darcy-Forchheimer's law for framed fibrous materials. Brooke *et al.* (2020) have considered the sound pressure levels of the metamaterial with periodic DE structure in a similar way to porous materials. They have measured the airflow resistivity on the whole samples to determine the static airflow resistivity and the Forchheimer coefficients. The acoustic model follows an effective fluid approach (Allard & Atalla, 2009b). They implement a resistivity as a linear dependence of velocity in their model following Darcy-Forchheimer's law. For sound pressure levels corresponding to the linear regime, the model agrees well with acoustic measurements at the first resonance, then deviates with increasing frequency. At high sound pressure levels, the validation is only presented for the first resonance frequency with a limited number of measurements.

Based on the work of Brooke *et al.* (2020), this paper aims to go further on the modeling and understanding of the nonlinear acoustic response of periodic DE structure metamaterial to high sound pressure levels. This structure is composed of a compact array of closely spaced single-perforation plates (CS-SPPs). This metamaterial was proposed by Dupont *et al.* (2018) (referred to in their article as "multi-pancake material"). To model the nonlinearities generated by the perforations, the Darcy-Forchheimer's law is used to model the non-constant airflow resistivity in the material at high sound pressure levels. The determination of the static airflow resistivity and the Forchheimer coefficients is based on a previous work presented at a conference by the authors, appendix VII. The present study is interested in the difference on the acoustic response regarding global (on all the material) and local (within the material) effects. The proposed nonlinear acoustic model is an adaptation of an existing equivalent linear mass-spring model chapter 3. The mass-spring model is especially suited to consider the nonlinearity effects associated with the perforations.

The paper is organized as follows. Section 5.3 details the geometry of the studied metamaterial. Then, section 5.4 recalls the basic equations of the mass-spring model, assuming a velocity-independent acoustic response. This section then presents a new adaptation of the model designed for high sound pressure levels, followed by a description of the experimental validation setup. Section 5.5 compares the predictions of the mass-spring model with experimental measurements at different sound pressure levels. Subsequently, the results obtained using two approaches within the model (global resistivity versus local resistivity) are discussed. It then carries out a parametric study analyzing the impact of pore size, number of periodic unit cells, sound pressure levels and linear/nonlinear regimes on the sound absorption coefficients.

5.3 Materials

The studied metamaterial is based on a periodic unit cell (PUC) as shown in figure 5.1(a). The PUC is composed of a pore (labeled 1 on the figure), and a thin cavity: composed of a junction (labeled 2) and a DE annular cavity (labeled 3). The overall metamaterial is formed from a succession of this PUC, i.e., a series of closely spaced single-perforation plates (CS-SPP). In practice, the metamaterial samples are an assembly of machined SPP in aluminum. Figure 5.1(b) shows a picture of a metamaterial sample. A chamfer on each SPP edge is present to minimize acoustic leaks and facilitate their assembly. Each SPP is machined to fit in a 22.22 mm radius impedance tube. For all material configurations studied, the following dimensions are fixed: pore thickness (h_p = 1 mm); cavity thickness (h_c = 1 mm); cavity radius (r_c = 21 mm), and sample radius (r_s = 22.22 mm). Only the following parameters will vary: pore radius (r_p = 1, 2 and 4 mm), and a number of successive PUCs (N = 1 to 15).

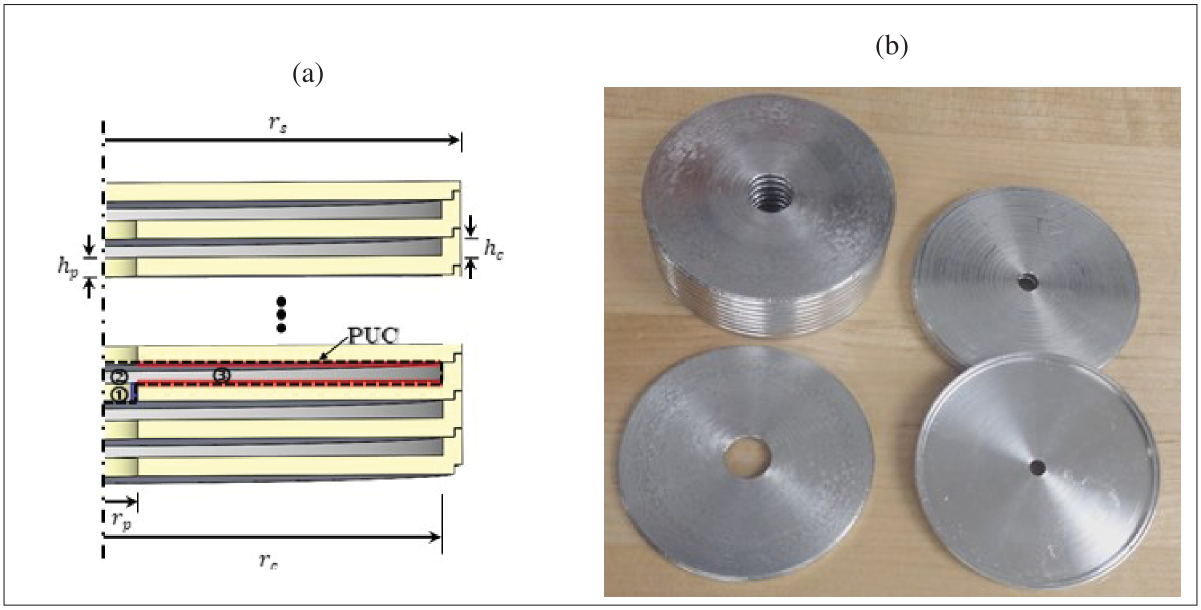

Figure 5.1 (Color online). (a) Metamaterial schematic: closely spaced single-perforation plates (CS-SPP). (b) A picture of a manufactured metamaterial

5.4 Methods

Two methods for characterizing the acoustic properties of the studied metamaterials under high sound pressure levels (SPL) are proposed. The first is an analytical modeling method refers to the "mass-spring analogy for high SPL" developed in this paper. The second is an experimental method that uses an impedance tube at high SPL.

5.4.1 Modeling method

The modeling method employs a mass-spring analogy as described by chapter 3. The prior mass-spring analogy was linear and designed for low SPL in metamaterials featuring periodic DE. This section begins by revisiting the primary equations of the linear mass-spring analogy. Subsequently, the linear model is modified for high SPL situations to develop the nonlinear mass-spring analogy. Lastly, the resolution method of the nonlinear system is outlined.

5.4.1.1 Linear mass-spring analogy

The mass-spring analogy follows a lumped parameter approach. In this model, the pores are modeled with equivalent [1] masses while the cavities (DE cavities and junctions) are modeled by springs. The metamaterial sample under study has small pore dimensions, r_p (1 to 4 mm) and h_p (1 mm), compared to the wavelength and this assumption is always valid within the frequency range studied. The harmonic regime is assumed following convention $e^{j\omega t}$, with t is the time and $j^2 = -1$. Losses are taken into account using Johnson-Champoux-Allard (JCA) effective fluid model (Allard & Atalla, 2009b). In this context, the equivalent mass of the ith pore is given by (equation (3.10)):

$$M_{eq,i} = \rho_{p,i} A_p h'_{p,i}, \tag{5.1}$$

where A_p is the pore cross-section and h'_p is the pore length with the end correction proposed in the original development, see chapter 3. The end correction represents inertial radiation effect. Karal end correction (Karal, 1953) is used for the outer side of the first pore. The pores are spaced by thin cavities (i.e., closely spaced) and the inner end correction of each pore is limited by half of the cavity thickness.

Since the pores are straight circular cylinders, the effective density $\rho_{p,i}$ of the air in the ith pore is expressed in JCA model by: (Allard & Atalla, 2009b)

$$\rho_{p,i} = \rho_0 \left(1 + \frac{\sigma}{j\omega\rho_0}\sqrt{1 + j\frac{\omega}{2\pi f_{cv}}}\right). \tag{5.2}$$

f_{cv} is the viscous characteristic frequency, expressed as:

$$f_{cv} = \frac{1}{2\pi}\frac{\sigma^2 r_p^2}{4\rho_0\,\eta}, \tag{5.3}$$

[1] In this paper the term equivalent refers to a lumped property while the term effective refers to the properties of the air saturating a component of the metamaterial (pore or cavity)

where ρ_0 and η are the density and dynamic viscosity of quiescent air, and ω is the angular frequency. Under low SPL, the airflow resistivity σ in a pore is constant and independent of the acoustic velocity in the pore. It can be given by the theoretical formula of the static airflow resistivity $\sigma_0 = 8\eta/r_p^2$ (Stinson, 1991). The theoretical value is near that obtained by measurements or CFD simulations as discussed in Sec. 5.5.2. It is worth noting that the density remains consistent across all pores since they share the same dimensions. However, we still consider the potential dependence on pore i in equation (5.2), which will be useful for the nonlinear case discussed in the next section.

Since, the cavities are modeled by equivalent springs, and that all the cavities are identical, their equivalent stiffness is given by (equation (3.21)):

$$K_{eq} = \frac{A_p^2}{\frac{V_J}{\rho_0 c_0^2} + \frac{A_{de}}{j\omega Z_{S,de}}}, \tag{5.4}$$

where V_J is the volume of the junction, $A_{de} = 2\pi r_p h_c$ the cross-section area of the DE, and $Z_{S,de}$ is the surface impedance of the DE resonator. For annular thin cavities, this surface impedance is expressed as (Dickey & Selamet, 1996)

$$Z_{S,de} = jZ_{de} \frac{\mathrm{J}_0(k_{de} r_p) + \frac{\mathrm{J}_1(k_{de} r_c)}{\mathrm{Y}_1(k_{de} r_c)} \mathrm{Y}_0(k_{de} r_p)}{\mathrm{J}_1(k_{de} r_p) + \frac{\mathrm{J}_1(k_{de} r_c)}{\mathrm{Y}_1(k_{de} r_c)} \mathrm{Y}_1(k_{de} r_p)}, \tag{5.5}$$

where J_n and Y_n are respectively Bessel functions of first and second kinds, and order n. Z_{de} and k_{de} are respectively the effective characteristic impedance and effective wave number of air in the DE cavities. For the annular DE cavities, the thickness to radius ratio is small. Therefore, the DE cavities are identified as slits in the JCA model.

According to Newton's second law, the matrix form of the equation of motion is given by:

$$\left(-\omega^2 \mathbf{M} + \mathbf{K}\right) \boldsymbol{x} = \boldsymbol{f}, \tag{5.6}$$

where $\boldsymbol{x} = \{x_1, x_2, \ldots x_N\}^{\mathrm{T}}$ is the mass displacement vector (the superscript T refers to the transposition), $\boldsymbol{f} = \{p_t A_p, 0, \ldots 0\}^{\mathrm{T}}$ is the external force vector, and p_t is the total pressure at the input surface of the material. The mass matrix is defined by:

$$\mathbf{M} = \begin{bmatrix} M_{eq,1} & & & 0 \\ & M_{eq,2} & & \\ & & \ddots & \\ 0 & & & M_{eq,N} \end{bmatrix} \tag{5.7}$$

and the stiffness matrix is defined by:

$$\mathbf{K} = K_{eq} \begin{bmatrix} 1 & -1 & & 0 \\ -1 & 2 & \ddots & \\ & \ddots & \ddots & -1 \\ 0 & & -1 & 2 \end{bmatrix}. \tag{5.8}$$

Solving equation (5.6) makes it possible to determine the mass displacement vector $\boldsymbol{x}$ and to deduce the mass velocity vector $\dot{\boldsymbol{x}} = j\omega\boldsymbol{x}$. The normalized surface impedance of the metamaterial is given by:

$$Z_{nS} = \frac{p_t}{V_{in}\rho_0 c_0} = \frac{f_1}{A_p \phi_S \dot{x}_1 \rho_0 c_0} \tag{5.9}$$

where V_{in} is the normal incidence acoustic velocity at the input of the material, c_0 is the sound celerity in air, $\phi_S = r_p^2/r_s^2$ is the open area of the first SPP, and $f_1 = p_t A_p$ and $\dot{x}_1$ are the first term of vectors $\boldsymbol{f}$ and $\dot{\boldsymbol{x}}$, respectively. The normal incidence sound absorption coefficient of the metamaterial backed by a rigid wall is then defined by:

$$\alpha = 1 - \left| \frac{Z_{nS} - 1}{Z_{nS} + 1} \right|^2. \tag{5.10}$$

5.4.1.2 Nonlinear mass-spring analogy

To address the impact of high SPL on the nonlinear response of the metamaterial under study, a non-constant airflow resistivity is taken into account in the pores. This airflow resistivity is modeled following Darcy-Forchheimer's law (Eq. (10) of Wilson *et al.* (1988)). Through the application of Darcy-Forchheimer's law, the airflow resistivity is velocity-dependent and it is determined for each mass (or pore). Formulated in a vector notation, it reads as follows:

$$\boldsymbol{\sigma}(\mathbf{v}_{rms}) = \boldsymbol{\sigma_0}\phi_s + \phi_s^2 \boldsymbol{F} \circ \mathbf{v}_{rms}, \tag{5.11}$$

where $\mathbf{v}_{rms} = \frac{1}{\sqrt{2}}\{|\dot{x}_1| \; \ldots \; |\dot{x}_N|\}^{\mathrm{T}}$ is the vector containing the root mean square values of the mass velocity components. $\boldsymbol{\sigma_0} = \{\sigma_{0,1}, \; \ldots \; \sigma_{0,N}\}^{\mathrm{T}}$ is the vector of the static airflow resistivity coefficients, $\boldsymbol{F} = \{F_1, \; \ldots \; F_N\}^{\mathrm{T}}$ is the vector of the Forchheimer coefficients, and $\circ$ represents the element-wise product or Hadamard's product. These vectors, $\boldsymbol{\sigma_0}$ and $\boldsymbol{F}$, can be obtained from experimental measurements or computational fluid dynamics (CFD), appendix VII. Also, as discussed following equation (5.2), the coefficients of $\boldsymbol{\sigma_0}$ could be deduced from the theoretical formula.In this article, the CFD is used. The coefficients are determined following regressions on the pressure drops across the sample for different flow rates. The link between the flow rate and the velocity in the pores is $Q = \pi r_p^2 \dot{x}$.

In what follows, two CFD approaches will be employed, compared with each other, and evaluated against measurements:

- The first approach, called global approach, involves determining the global static airflow resistivity and the Forchheimer coefficients throughout the geometry. This process involves evaluating the pressure drops before and after the material, followed by the calculation of $\boldsymbol{\sigma_0}$ and $\boldsymbol{F}$ from these pressure drops. The values of the coefficients are supposed constant throughout the material, i.e., $\boldsymbol{\sigma_0} = \sigma_{0,global}\{1, 1, ..., 1\}^{\mathrm{T}}$ and $\boldsymbol{F} = F_{global}\{1, 1, ..., 1\}^{\mathrm{T}}$.
- The second approach, called local approach, is to locally determine the static airflow resistivity and the Forchheimer coefficients of each pore. From this evaluation, we can deduce $\boldsymbol{\sigma_0}$ and $\boldsymbol{F}$. In this approach, $\boldsymbol{\sigma_0} = \{\sigma_{0,1}, \sigma_{0,2}, ..., \sigma_{0,N}\}^{\mathrm{T}}$. If $N \geq 5$ and r_p are the same for all pores,

these coefficients should be very close to each other and to the theoretical value. In this case, the vector could be replaced by $\boldsymbol{\sigma_0} = (8\eta/r_p^2)\{1, 1, ...1\}^{\mathrm{T}}$. In chapter 4, it has been shown that inertial effects (characterized by the Forchheimer coefficient) of the first pore dominate. Consequently, in what follows, we will only consider nonlinear effects on the first pore. In this case, the vector of Forchheimer coefficients simplifies to $\boldsymbol{F} = \{F_1, 0, ...0\}^{\mathrm{T}}$.

According to equation (5.11), the airflow resistivity is dependent on the mass velocity $\dot{\boldsymbol{x}}$. Equation (5.11), when substituted into equation (5.2), transforms the matrix form of the equation of motion (equation (5.6)) into:

$$\left(-\omega^2\mathbf{M}(\mathbf{v}_{rms}) + \mathbf{K}\right)\boldsymbol{x} = \boldsymbol{f}, \tag{5.12}$$

where $\mathbf{M}(\mathbf{v}_{rms})$ is the mass matrix. It depends now on the velocities of the masses $\dot{\boldsymbol{x}}$. In this case, the matrix system is nonlinear, and a simple matrix inversion is not enough to solve equation (5.12). So, equation (5.12) is solved using an iterative scheme. First, the mass velocity vector is assumed to be zero. From this initial velocity vector, the airflow resistivity for each mass is determined. equation (5.12) is solved for this velocity vector, and a new velocity vector is found. The previous steps are repeated with the new velocity vector as input until convergence is achieved, that is the variation of each component of the velocity vector is neglectable. The pseudo-code of the iterative scheme used for an imposed total SPL is given in appendix II.

5.4.2 Experimental method: high SPL level impedance tube

The experimental approach is based on the two-microphone impedance tube method. The Mecanum's high SPL impedance tube is employed. The tube has an inner radius of 22.22 mm, and the microphone spacing is 30 mm. At high SPL, the tube setup, hardware and acquisition system allow noisy-less measurements from 300 to 4300 Hz. Sine-wave excitation is used with iteration processes to ensure that the total SPL at the entrance of the metamaterial is identical for each frequency. The corresponding acoustic pressure is a root mean square value. Measurements were taken up to a total SPL of 140 dB at the material entrance (all SPL are referenced to 20 µPa).

Under low SPL, the results presented in the following give the same results as impedance tube measurements following the standard ASTM E1050-19 (2019). Note that the hard-backed sound absorption coefficient at normal incidence is measured similarly as described in this standard. In this case, the tested metamaterial sample is placed on the hard end of the tube and petroleum jelly is used on its edge to prevent air leakage.

5.5 Results and discussions

5.5.1 Normal sound absorption coefficient of the studied metamaterial

The measured sound absorption coefficients with the experimental impedance tube approach are shown in figure 5.2 for a CS-SPP sample with $r_p = 2$ mm and $N = 11$ at 100, 120 and 140 dB. Each absorption coefficient is represented by an envelope to show the dispersion of the data over 3 measurements. Each measurement consists of mounting/unmounting and reassembling the samples. The studied material configuration has several peaks in the absorption coefficient. They are associated with the acoustic resonances of the material configuration (Dupont *et al.*, 2018; Brooke *et al.*, 2020; Kone *et al.*, 2021b; Lopez *et al.*, 2024). The number of resonances is equal to the number of PUCs, see chapter 3. The resonance frequencies are spaced at low frequencies and become closer as frequency increases. Around 2600 Hz, the absorption coefficient tends to zero. This phenomenon corresponds to the beginning of a stopband, where the sound wave cannot propagate inside the material. This is due to periodic repetition of the annular thin cavities (Dupont *et al.*, 2018; Lopez *et al.*, 2024).

5.5.2 Global approach versus local approach

In figure 5.2, the measured sound absorption coefficients are compared to the predictions obtained from the proposed nonlinear equivalent mass-spring model with the global and local approaches of the Forchheimer coefficient. Figure 5.2(a) shows the predictions with the global approach, where the Forchheimer coefficient is determined by CFD on the overall material configuration as discussed in section 5.4.1.2. In this case $F_{global} = 7.733 \cdot 10^5$ Pa.s^2/m^3 and $\sigma_0 = 4681$ Pa.s/m^2.

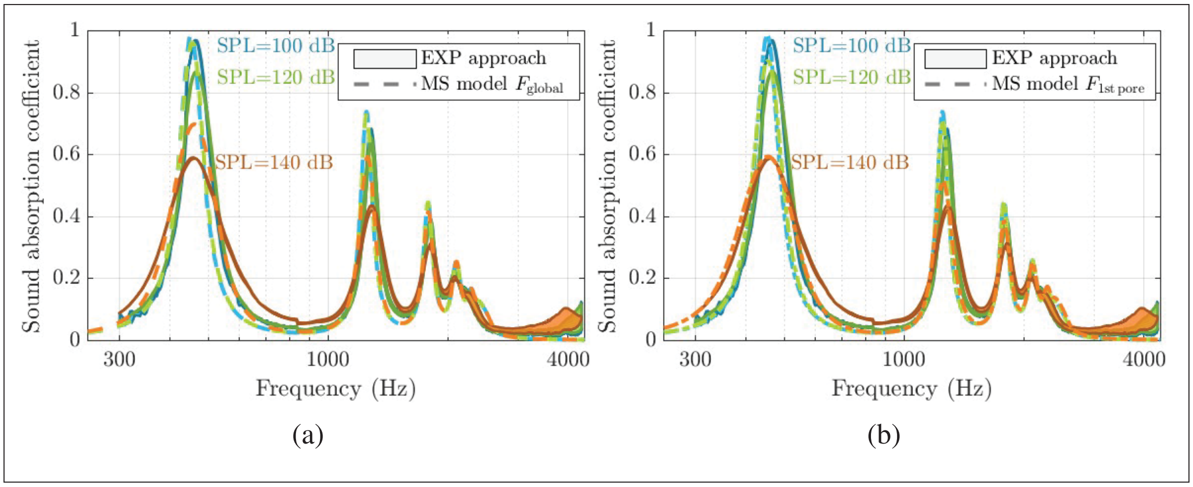

Figure 5.2 (Color online). Normal incidence sound absorption coefficient of CS-SPP ($r_p = 2$ mm, $N = 11$) for the experimental approach and (a) the adapted mass-spring model with the global Forchheimer coefficient, (b) the adapted mass-spring model with the local Forchheimer coefficient of the first pore; for three SPL imposed. The envelope of the experimental results represents the data dispersion over 3 measurements on three samples of the same material configuration

Figure 5.2(b) shows the predictions with the local approach, where the Forchheimer coefficient is only determined by CFD on the first pore. For the other pores, the coefficient is supposed to be zero. In this case, the first-pore Forchheimer coefficient $F_1 = 4.385 \cdot 10^6$ Pa.s^2/m^3 and the resistivity vector
$\boldsymbol{\sigma_0} = \{5119, 5056, 5059, 5062, 5058, 5050, 5060, 5061, 5057, 5058, 5068\}^{\mathrm{T}}$ Pa.s/m^2. As expected, the coefficients are very close to each other and to the theoretical resistivity of 4500 Pa.s/m^2. An average value of 5064 Pa.s/m^2, or the theoretical value, could be used without much difference in the final results.

At SPL of 100 dB, the mass-spring model with the local approach gives identical results to the local approach. Furthermore, these results are in good agreements with experimental measurements, see figure 5.2. Indeed, at this SPL the acoustic response of the metamaterial is linear, the Forchheimer coefficient has no impact on the acoustic response and so on the absorption coefficient.

With increasing SPL, the amplitude of the sound absorption coefficient peaks decreases. The global approach is less precise than the local approach, especially at SPL=140 dB. This is in line with the observation made in appendix VII: the airflow pressure drop profile through CS-SPPs predominates at the first pore [see figure VII-3]Consequently, acoustic nonlinear effects are predominant at the first pore and the local approach seems more appropriated.

At high levels, the results of the mass-spring model with the local approach deviate slightly as frequency increases (second peak and more). The authors think that one possible reason is the fact that the Forchheimer coefficient is determined from steady-state flow conditions. For the acoustic problem, the fluid is at rest with only sound waves generating pulsating flow. Further research on the Forchheimer coefficient determined from a pulsating flow would be interesting.

The previous discussion indicates that the local approach performs better compared to the global approach. Consequently, for the rest of the article, the local approach is used with the nonlinear equivalent mass-spring model.

5.5.3 Robustness and limit

In figure 5.3(a), the predictions of the nonlinear equivalent mass-spring model with the local approach are compared with experimental measurements for three different material configurations. Each material configuration differs in the pore radius r_p and N number of PUC (i.e., for different material configuration thicknesses). The results are presented for the same three SPL, 100, 120 and 140 dB. The characterized values used for the fist-pore Forchheimer coefficient and resistivity vectors of each configuration are given in table 5.1.

Figure 5.3(a) shows the comparison for a configuration with $r_p = 2$ mm and a $N = 2$. The predictions are in good agreement for the three SPL. For the first absorption peak, a same conclusion is obtained for the material configuration with $r_p = 4$ mm and $N = 8$ as shown in figure 5.3(c). However, for the material configuration with $r_p = 1$ mm and $N = 4$, while the same trend is observed as a function of SPL, the predictions show 10% larger coefficients. This material configuration is the one with the highest airflow resistivity as a result of its small pore

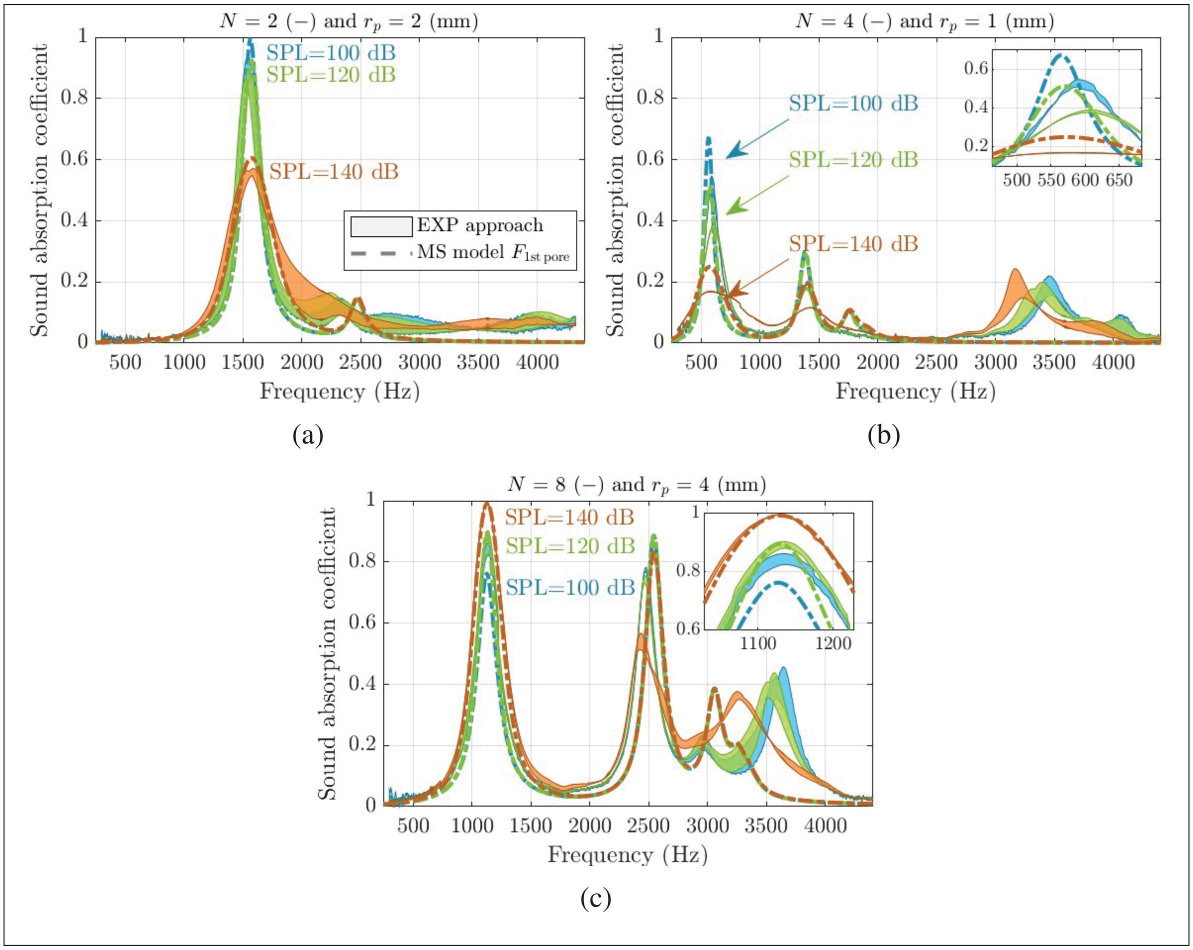

Figure 5.3 (Color online). Normal incidence sound absorption coefficient of CS-SPP (a) $r_p = 2$ mm, $N = 2$, (b) $r_p = 1$ mm, $N = 4$ and (c) $r_p = 4$ mm, $N = 8$. Comparison between the experimental approach and the adapted mass-spring model with the local Forchheimer coefficient for three SPL imposed. The envelope of the experimental results represents the data dispersion over 3 measurements

radius. The authors believe this could be due to the effects of imperfections in pore geometry, which are relatively more significant for smaller pores. In fact, the relative error on the resistivity is equal to $2\delta r_p/r$ with δr_p the uncertainty (or fabrication tolerance) on the pore radius. With a fabrication tolerance of 0.15 mm, the relative errors on the resistivity are 30, 15 and 7.5% for $r_p = 1$, 2, and 4 mm, respectively. A similar impact on the Forchheimer coefficient can also be expected.

Table 5.1 Average local static airflow resistivity coefficient and local Forchheimer coefficient of the first plate from CFD evaluations for the samples in Figs. 5.2 and 5.3

N (-)	r_p (mm)	$\bar{\sigma}_0$ (Pa.s/m^2)	F_1 (Pa.s^2/m^3)
11	2	5064	$4.385 \cdot 10^6$
2	2	5089	$4.365 \cdot 10^6$
4	1	75762	$5.788 \cdot 10^7$
8	4	334	$2.273 \cdot 10^5$

Between 3000 to 4300 Hz, peaks in the absorption coefficient are measured but not predicted. These peaks could be due to elastic vibrations of the frame. In the proposed equivalent mass-spring model, the material frame is supposed to be rigid. In reality, plates can have elastic resonances and modify the acoustic behavior of the material(Dupont *et al.*, 2018). Appendix III presents finite element results on a CS-SPP to validate this hypothesis.

For the different studied material configurations of figures 5.2 and 5.3, the frequency and the sound absorption coefficient of the first peaks are presented in table 5.2. These values were obtained by the experimental approach and the equivalent mass-spring model with the local approach. For the material configurations with r_p = 2 and 4 mm, the relative error of the resonant frequency is less than 3%, and the relative error of the sound absorption coefficient is less than 10%. As mentioned above, the relative errors are higher for the material configuration with a pore radius of r_p = 1 mm.

In conclusion of the robustness and limit section, the comparisons between the proposed nonlinear model results and impedance tube measurements indicate that the model is effective in predicting the nonlinear sound absorption response of CS-SPP metamaterials at high SPL. However, its accuracy diminishes with smaller pore diameters, showing the largest discrepancies with measurements, necessitating further investigation for these cases.

Table 5.2 Frequency and sound absorption coefficient of the first absorption peaks for the experimental approach and the equivalent mass-spring model with local Forchheimer's coefficient approach. The relative errors are shown in brackets. The results are presented for the four metamaterial configurations shown in figures 5.2 and 5.3

			Experimental approach		Mass-spring model	
N (-)	r_p (mm)	SPL (dB)	f_1 (Hz)	α_1 (1)	f_1 (Hz)	α_1 (1)
11	2	100	466	0.97	453 (2.7%)	0.99 (1.9%)
11	2	120	467	0.87	455 (2.6%)	0.90 (4.3%)
11	2	140	459	0.59	455 (1.0%)	0.59 (0.8%)
2	2	100	1548	0.90	1565 (1.1%)	0.99 (10.0%)
2	2	120	1550	0.85	1571 (1.4%)	0.92 (8.2%)
2	2	140	1575	0.56	1575 (0.0%)	0.60 (8.8%)
4	1	100	588	0.53	565 (3.8%)	0.67 (27.5%)
4	1	120	606	0.38	571 (5.8%)	0.51 (34.0%)
4	1	140	573	0.17	573 (0.1%)	0.25 (48.0%)
8	4	100	1136	0.84	1127 (0.8%)	0.76 (9.0%)
8	4	120	1136	0.89	1129 (0.6%)	0.89 (0.9%)
8	4	140	1128	0.99	1129 (0.1%)	0.99 (0.3%)

5.5.4 Impact of sound pressure level

The various results demonstrate that SPL affects the amplitude of the absorption coefficient peaks but has little impact on the acoustic resonance frequency. This last observation is different to MPP backed by thick air cavity, where the resonance frequencies increase with increasing SPL (Maa, 1994; Laly *et al.*, 2018). This increase is explained by the authors as the decrease of the end correction of the pores with the increase in SPL. In the case of thin cavities, the end correction used for MPP with the increase in SPL is no longer suitable. So, repetitions of thin cavities show an interest in achieving low frequency sound absorption at high SPL with no change of the resonance frequencies with SPL (at least for the first resonance).

It should also be noted that for the different material configurations in this study, the frequency of the peak of the absorption coefficient that seems to be induced by vibrations (fluid-structure interactions) is shifted towards low frequencies when the SPL increase. An in-depth study on the subject would be interesting, but this is not the purpose of this article. Especially since the aim of this study is more at low frequencies than at high frequencies.

For the various material configurations, it is observed that the SPL has a stronger impact on the amplitude of the first absorption coefficient peak. A smaller variation is observed for subsequent peaks. In the following paragraphs, we analyze the impact of the SPL on the acoustic response of a CS-SPP metamaterial, first as a function of the number of PUCs and then as a function of the pore radius.

Figure 5.4 shows the mapping of the sound absorption coefficient as a function of frequency and number of PUCs for the three SPL 100, 120 and 140 dB. From this figure, whatever the SPL, it can be noted that: as the number of PUCs increases, the number of absorption coefficient peaks logically increases, their resonance frequency decreases (logical since the thickness of the metamaterial increases with the number of PUCs), and the amplitude of the first peak remains constant. However, as the SPL increases, the amplitude of the absorption peaks decreases and their width at mid-height increases, especially for the first peak (see also figure 5.2).

The variation (increase or decrease) of the absorption peak with the SPL is a point of interest here. For conventional porous material, and also observed for MPP,(Tayong *et al.*, 2010; Laly *et al.*, 2018) the absorption peak can be maximal for a critical acoustic velocity (or critical SPL or critical resistivity). If the critical resistivity is not achieved, increasing it will enhance the

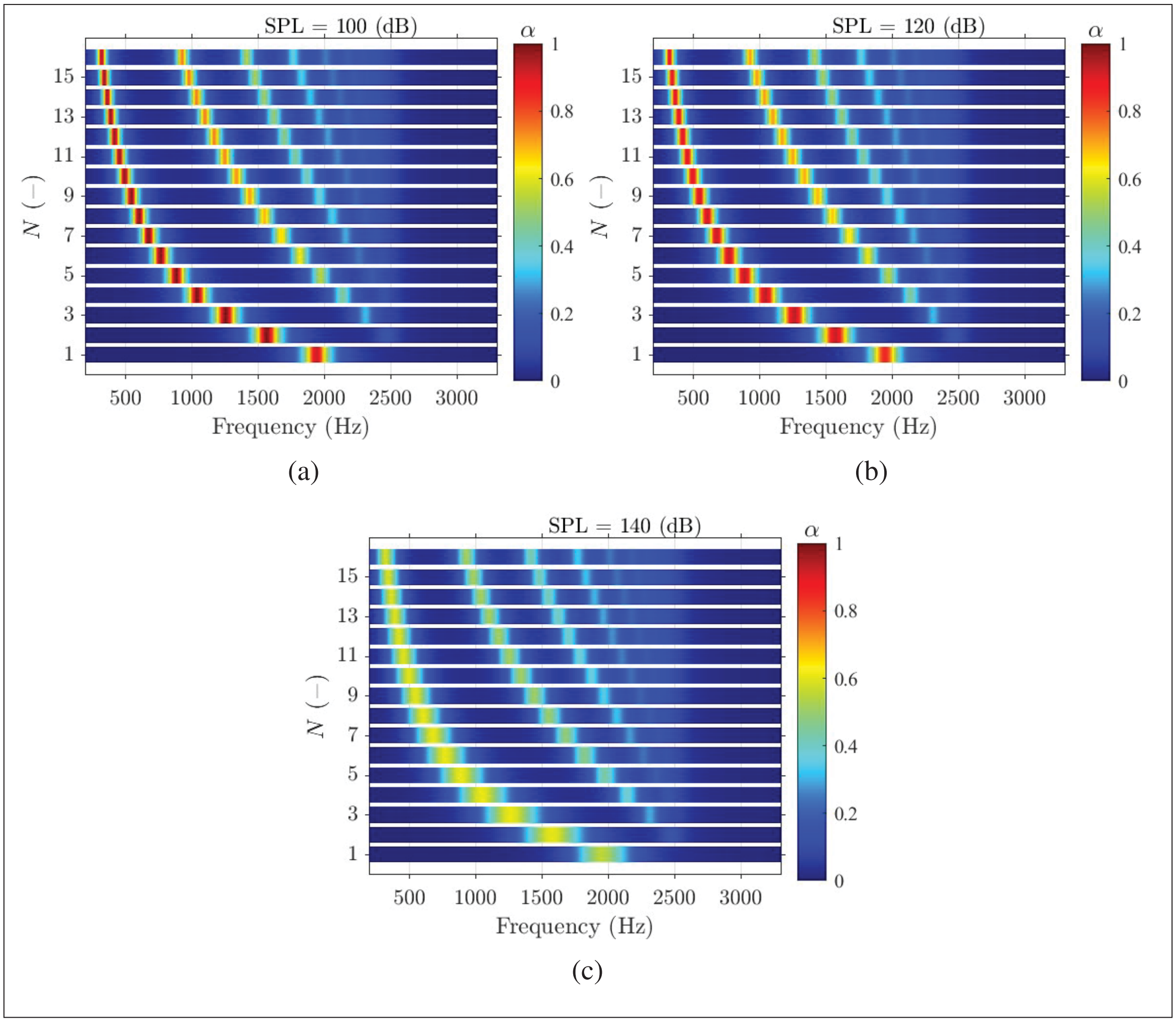

Figure 5.4 (Color online). Normal incidence sound absorption coefficient predicted by the adapted mass-spring model with the local Forchheimer coefficient of the first pore for CS-SPP with $r_p = 2$ mm at three different SPL imposed: (a) 100 dB, (b) 120 dB, and (c) 140 dB. Mapping in function of the frequency and number of PUCs

peak of absorption coefficient. However, if the critical resistivity is exceeded, further increases in resistivity will result in a decrease in the absorption coefficient. As increasing SPL increases the absolute velocity $|\dot{x}|$ in the pores, the resistivity increases according to equation (5.11). Consequently, this indicates that the resistivities in the linear regime for material configurations with $r_p = 1$ and 2 mm (see figures 5.3(a) and 5.3(b)) have already surpassed their critical values, while it has not for material configuration with $r_p = 4$ mm (see figure 5.3(c)).

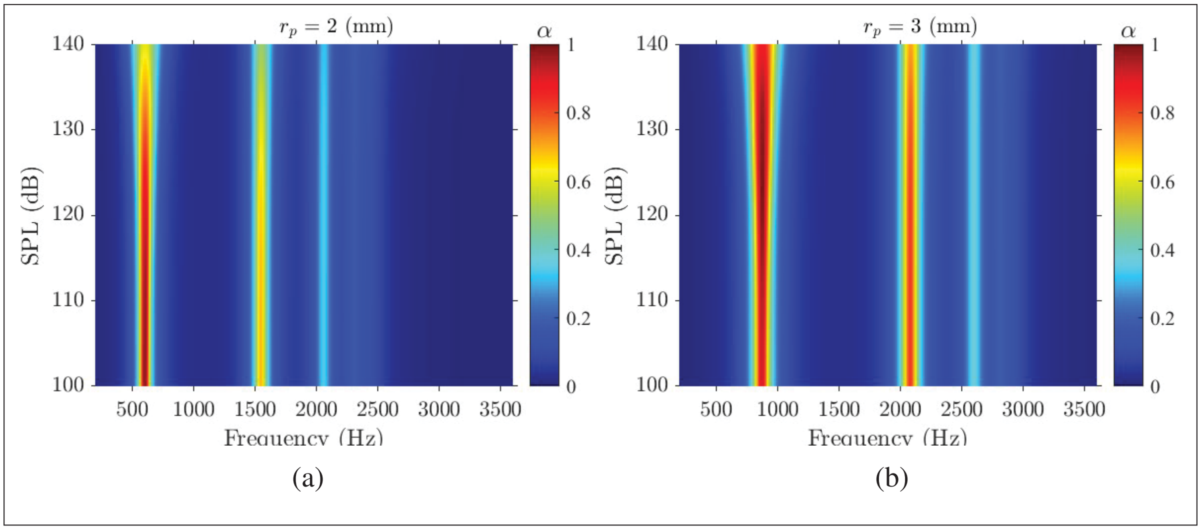

Figure 5.5 (Colour online.) Normalized surface resistance ($\mathrm{Re}(Z_{nS})$) and reactance ($\mathrm{Im}(Z_{nS})$) of the material for two CS-SPP material configurations with the same number of PUCs $N = 8$ and different pore radius: (a) $r_p = 2$ mm and (b) $r_p = 3$ mm

This evolution is also better explained by analyzing the normalized surface impedance Z_{nS} of the materials shown in figure 5.5 for two CS-SPPs with same $N = 8$: (a) $r_p = 2$ mm and (b) $r_p = 3$ mm. The normalized surface impedance of the metamaterial is given by equation (5.9). Its real part is the normalized resistance, and its imaginary part is the normalized reactance. The resistance of the material increases with particle velocity (Ingard & Ising, 1967). The maximum of the peak of the absorption coefficient is obtained at a critical value of velocity or Mach number (Tayong *et al.*, 2010). This occurs when the reactance of the material is zero (corresponding to a resonance), and the resistance of the material matches that of the incident medium, $Z_0 = \rho_0 c_0$. At the first resonance and SPL=100 dB, the normalized resistance is near one for the material configuration $r_p = 2$ mm, see figure 5.5(a). This results in an absorption coefficient close to one at this SPL, see figure 5.6(a). For the material configuration with $r_p = 3$ mm, the normalized resistance is smaller than one at first resonance and SPL=100 dB, see figure 5.5(b). So the absorption coefficient is smaller than one in this case, see figure 5.6(b). In the vicinity of the resonances, the SPL does not have an influence on the normalized reactance for the two material configurations. This is in line with aforementioned comments; the resonance frequencies are not affected by SPL for this metamaterial. At the resonances, the displacements of the masses and their velocities are at their maximum. Consequently, the airflow resistivity is maximal at the resonances equation (5.11), and the normalized resistance increases with SPL. For the material configuration with a pore radius of $r_p = 2$ mm, because the normalized resistance is greater than one at the first resonance and SPL=100 dB, the value of the first peak of the sound absorption coefficient will only decrease with increasing SPL. For the material configuration with $r_p = 3$ mm, the normalized resistance is slightly lower than one at first resonance and SPL=100 dB. Consequently, the value of the first peak of the sound absorption coefficient will increase with increasing SPL, up to a value of one when normalized resistance reaches one, then it will decrease with continuously increasing SPL. From figure 5.5(b), the maximum of the first peak of absorption will occur in this case for an SPL between 120 and 140 dB. This is confirmed by figure 5.6(b).

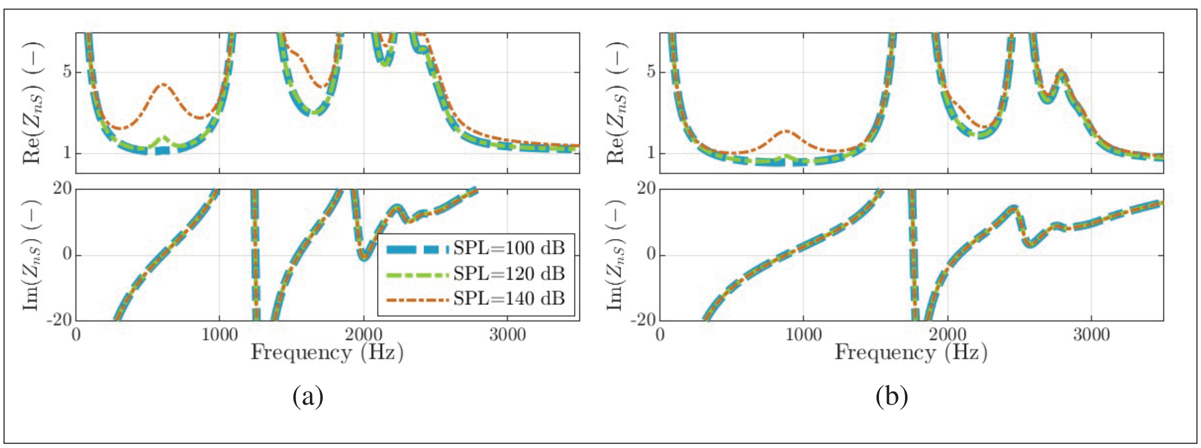

Figure 5.6 (Color online). Normal incidence sound absorption coefficient predicted by the adapted mass-spring model with the local Forchheimer coefficient of the first pore for a CS-SPP with $N = 8$ number of periodic unit cells and different pore radii: (a) $r_p = 2$ mm and (b) $r_p = 3$ mm. Mapping in function of the frequency and SPL

The acoustic response at higher frequencies seem less sensitives to SPL: fewer variations in the acoustic resistance (figure 5.5) and the absorption coefficient (figures 5.4 and 5.6). So, the nonlinear response of the studied metamaterial is frequency dependent. In the proposed approach, nonlinearity is considered only for the first mass (local Forchheimer coefficient), and the first mass velocity depends on the frequency. From the first mass velocity, the Reynolds number of the first pore is determined, $\mathrm{Re}_1 = \rho_0 |\dot{x}_1| 2r_p/\eta$ and shown in figure 5.7(a) for a

CS-SPP with $N = 8$ number of periodic unit cells and a pore radius of $r_p = 2$ mm. The Reynolds number is maximal at a resonance and its value increases with the SPL. At SPL=100 dB, the acoustic response is linear, but the Reynolds number is greater than one for frequencies greater than 29 Hz. For these frequencies, the nonlinear part of the airflow resistivity, $\sigma_{NL} = F|\dot{x}|/\sqrt{2}$, is greater than the static airflow resistivity, σ_0. At Reynolds greater than one, the inertial forces of the flow dominate over the viscous forces. However, this does not necessarily imply that the acoustic response is nonlinear. In fact, under the assumption of a linear acoustic response, the viscous characteristic frequency f_{cv}, given by equation (5.3), does not depend on velocity and is 17 Hz for a circular pore with a radius of $r_p = 2$ mm.

For frequencies above f_{cv}, acoustic losses are no longer controlled by resistivity. As frequency increases, thermal and inertial effects become more important. The rapid oscillation of air molecules in the pores results in friction (converting acoustic energy into heat), and the molecules can no longer keep up with the rapid pressure fluctuations of the sound wave (adding inertia and creating additional energy losses). At these frequencies, the characteristic dimension (here, the pore radius) is the key parameter. By considering a velocity dependence of the acoustic response, the viscous characteristic frequency becomes a function of frequency, as the velocity amplitude is influenced by the frequency-dependent nature of airflow resistivity. This frequency-dependent viscous characteristic frequency $f_{cv}(\sigma(\omega))$ of the first pore is shown in figure 5.7(b) for the CS-SPP. The evolution of $f_{cv}(\sigma(\omega))$ follows that of the Reynolds number of the first pore. At low SPL and low frequencies, $f_{cv}(\sigma(\omega))$ is almost constant and equals to the velocity-independent viscous characteristic frequency calculated with the static airflow resistivity coefficient, that is $f_{cv}(\sigma_0) = 17$ Hz.

Based on the above discussion, figure 5.7(b) can be used to identify when the nonlinear response becomes significant compared to the linear response; this occurs when $f_{cv}(\sigma(\omega))$ exceeds the actual frequency of the analysis, f. f is indicated by the straight line in the graph. For example, it is clear that for SPL=100 dB, the acoustic response is linear for all frequencies. For SPL=120 dB, the nonlinear response is significant only around the first resonance at 603 Hz. For SPL=130 dB, the nonlinear response is significant for all resonances below 3000 Hz. Additionally, the further upward the curve $f_{cv}(\sigma(\omega))$ is from the line f, the greater the nonlinear effect will occur. Which explains why the nonlinear effect is more important for the first resonance frequency than for higher frequencies.

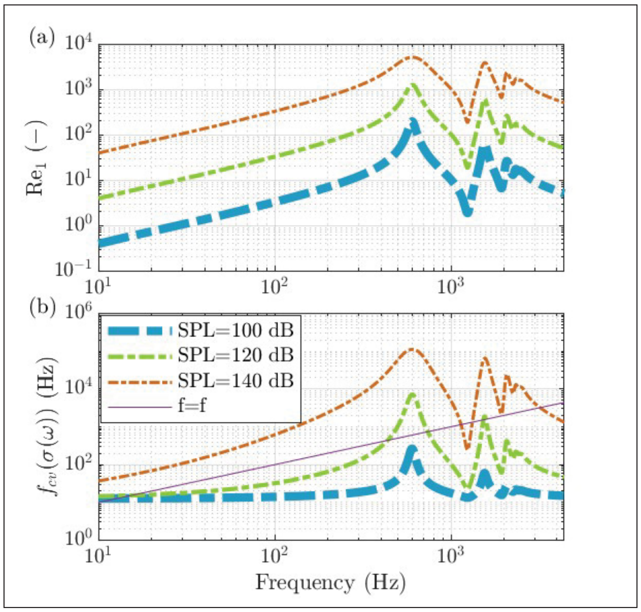

Figure 5.7 (Colour online.) (a) Reynolds number in the first pore and (b) frequency-dependent viscous characteristic frequency $f_{cv}(\sigma(\omega))$ in function of the frequency for CS-SPP with $N = 8$ number of PUCs and pore radius $r_p = 2$ mm

5.6 Conclusion

The acoustic nonlinearity of a metamaterial composed of a periodic array of single-perforation plates spaced by thin air cavities has been studied. A previous mass-spring model is adapted to consider high sound pressure levels. The nonlinearity induced by high sound pressure levels is accounted for by using the Darcy-Forchheimer law for the airflow resistivity of the perforations. The Forchheimer coefficients were determined using a global and local approaches. For the global approach, the coefficients were determined from the airflow resistivity over the entire geometry. The local approach is based on the observation of appendix VII that the inertial forces dominate for the first pore. The mass-spring model predictions with the local approach are closer to the experimental results than with the global approach. The proposed mass-spring model predictions are compared with impedance tube measurements on different samples. The comparisons show that the model is effective in predicting the nonlinear acoustic response of closely spaced single-perforation plates metamaterials at high sound pressure levels. However, the model accuracy decreases with smaller pore diameters at low and high sound pressure levels, a more in-depth study would be interesting for these pore dimensions.

An interest of using closely spaced single-perforation plates instead of micro-perforated panels backed by cavity is that the increase in sound pressure levels has almost no impact on the resonance frequencies.

Parametric study on the pore radii, the number of periodic unit cells and the SPL has been made. The number of periodic unit cells has little impact on the amplitude of the peak of the sound absorption coefficient compared to the variation of pore radius. The amplitude of an absorption peak is maximum when the normalized acoustic reactance is zero and the normalized acoustic resistance tends towards one. The normalized acoustic resistance increases with increasing sound pressure levels. The resistance increase is much higher at the first resonance. The limit between linear regime and nonlinear regime depends on the Reynolds number in the pore and the frequency. It is determined when the viscous characteristic frequency exceed the actual frequency of the analysis.

Acknowledgments

The authors acknowledge the financial support of Natural Sciences and Engineering Research Council of Canada (NSERC) [funding reference numbers: RGPIN-2018-06113 and RGPIN-2019-06573]. The authors thank Clément Cochener for his contribution to the measurement campaign during his internship.

Author declarations

Conflict of Interest

The authors state that they have no conflict of interests to disclose.

Data availability

The data that support the findings of this study are available from the corresponding author upon reasonable request.

CHAPITRE 6

LINEAR AND NONLINEAR RESPONSE OF COMPACT ACOUSTIC BLACK HOLES : PREDICTION AND ANALYSIS BY A MASS-SPRING MODEL

6.1 Avant-propos

Le format de ce chapitre suit celui d'un article. Au moment de la soumission du manuscrit, l'article était en relecture par les co-auteurs pour une soumission prochaine. Différentes personnes ont contribué aux avancées de ce chapitre : Gauthier Bezançonv (ÉTS), Tenon Charly Kone (NRC), Alla Eddine Benchickh Le Hocine (CRASH-UdeS), Olivier Doutres (ÉTS), Thomas Dupont (ÉTS) et Raymond Panneton (CRASH-UdeS).

6.2 Abstract

Acoustic black holes are broadband solutions to sound absorption problems. In their simplest form, they consist of air cavities spaced by perforated plates with a perforation profile decreasing along the thickness of the material. With small perforations and thin cavities, they reduce low-frequency noise with a small thickness relative to the wavelength. This paper focuses on the nonlinear response of compact acoustic black holes when exposed to high sound pressure levels (SPL). A semi-analytical mass-spring model is adapted to predict and understand the effect of increasing SPL on acoustic black holes with thin cavities. Visco-thermal losses from perforations and cavities are taken into account by the Johnson-Champoux-Allard model. The coefficients of the Darcy-Forchheimer's law are determined using Computational Fluid Dynamics (CFD) simulations of airflow. The mass-spring model is used to determine the resonance frequencies and mode shapes of the material function of the SPL. The acoustic responses and sensitivity to SPL of three different types of decreasing perforation profiles are compared. Sensitivity is linked to mode shape, and strongly decreasing pore profiles at the beginning of the material show greater sensitivity to SPL.

6.3 Introduction

Acoustic metamaterials offer efficient solutions for attenuating low-frequency sound, particularly in industrial settings where space constraints necessitate compact designs. A primary objective in this field is the development of metamaterials that achieve broadband sound absorption at low frequencies while minimizing size (thickness and/or volume). However, achieving such performance presents a significant challenge. Acoustic black holes (ABH) also called sonic black hole, present a promising avenue to address this challenge. They draw inspiration from acoustic black holes designed for structural vibrations. The acoustic black hole effect for structural vibrations manifests itself within thin structures by introducing local spatial variations in material or geometric properties, such as plate thickness (Pelat *et al.*, 2020). Transposing this phenomenon to sound waves has received a great deal of research attention (Mironov & Pislyakov, 2002). Recent studies have examined the concept of black hole materials for sound waves (Guasch *et al.*, 2017, 2020; Umnova *et al.*, 2023; Chua *et al.*, 2023; Yu *et al.*, 2023; Li, Xia, Yu, Zhang & Cheng, 2023b; Bravo & Maury, 2023; Serra *et al.*, 2023; Bednarik & Cervenka, 2024; Hruška *et al.*, 2024; Chen *et al.*, 2024; Deng *et al.*, 2024; Peng *et al.*, 2024; Sheng *et al.*, 2024; Zhang *et al.*, 2024). ABHs, in their simplest form, consist of a pseudo-periodic arrangement of air cavities separated by thin perforated plates with decreasing perforation profile. The spatial variation tends to attenuate the amplitude of reflected wave towards zero. Guasch *et al.* (2017) have demonstrated that achieving a reflection coefficient approaching zero requires a considerable number of layers. Moreover, ABHs, even in their simplest forms, exhibit distinctive patterns in the reflection coefficient, characterized by peaks and hollows. As the number of layers increases, the distance between these hollows decreases, indicating a more efficient sound absorption mechanism. Additionally, recent findings by Serra *et al.* (2023) confirm that quadratic [1] decreasing profiles outperform linear ones in open-ended ABH configurations. This observation underlines the importance of careful design to optimize ABH performance. Notably, the peaks of the absorption coefficient, corresponding to the hollows of

[1] Care the equation of the pore profile differs from Guasch *et al.* (2017, 2020); Serra *et al.* (2023), square profiles in the present article correspond to quadratic profile inGuasch *et al.* (2017, 2020); Serra *et al.* (2023) (linear profile is not impacted)

the reflection coefficient, signify resonant modes within ABH structures (Umnova *et al.*, 2023). Furthermore, these resonances exhibit coupling effects, with the first resonances attributed to global resonance (contribution of the whole material) involving the entire material, while the subsequent resonances represent local resonances (contribution of the first part of the material) predominantly affecting the initial portion of the material (Umnova *et al.*, 2023; Bezançon *et al.*, 2024). Umnova *et al.* (2023) and Bezançon *et al.* (2024) have proposed ABH with low frequency sound absorption while maintaining a compact total thickness. In their materials, they have reduced the aperture of the first plate and use thin air cavities. The use of a reduced aperture shifts the beginning zone of effectiveness of ABH towards the lower frequencies.

Acoustic metamaterials, as ABH, can be employed to reduce high intensity noise (Brooke *et al.*, 2020; Zhang *et al.*, 2021; Zhu *et al.*, 2023, 2022). Perforated materials are sensitive to the nature of the excitation. With increasing sound pressure levels (SPL) the relation between the acoustic pressure and the acoustic velocity is no more linear at the orifice (Ingård & Labate, 1950). Increasing sound pressure is responsible for extra losses induced by circulation effects (as the formation of jets and vortex rings) as a result of which the acoustic pressure tends to a quadratic function of the acoustic velocity (Ingard & Ising, 1967). With increasing SPL, the acoustic resistance (the real part of the acoustic impedance) at the orifice is a linear function of the acoustic velocity, and the reactance (the imaginary part of the acoustic impedance) decreases as the acoustic velocity increases. Several models have been proposed to consider the nonlinear response of perforated and micro-perforated plates under high SPL (Maa, 1994; Ingard, 1968; Guess, 1975; Melling, 1973; Cummings & Eversman, 1983; Tayong *et al.*, 2010; Park, 2013; Laly *et al.*, 2018). Laly *et al.* (2018) proposed an effective fluid model where the airflow resistivity becomes a linear function of the acoustic velocity to consider the high SPL. This approach is similar to the way in which high SPL are considered for porous rigid-frame materials. With increasing SPL, the airflow resistivity becomes a linear function of the airflow velocities, following Darcy-Forchheimer's law (Kuntz & Blackstock, 1987; Wilson *et al.*, 1988; McIntosh & Lambert, 1990; Lambert & McIntosh, 1990; Aurégan & Pachebat, 1999; Umnova, Attenborough & Cummings, 2002; Umnova, Attenborough, Standley & Cummings, 2003). The coefficients of the Darcy-Forchheimer's law are determined from pressure drops measurements at high airflow velocities. In the acoustic model, the airflow resistivity is replaced by the effective value of the acoustic velocity. The same approach was applied on a periodic metamaterial to predict the sound absorption at high SPL. The metamaterial geometry is composed of periodic array of thin single-perforation plates spaced by thin air cavities (Brooke *et al.*, 2020) (similar to a ABH with no pore profile variation).

This study aims to model and analyze the effect of high sound pressure levels on ABH. Especially how the acoustic response is affected by the decreasing pore profile under high sound pressure levels. The studied geometry is a ABH with thin cavities. An equivalent mass-spring model (chapter 3) is adapted to the geometry and to consider high SPL. High SPL (up to 145 dB) are considered using the Darcy-Forchheimer's law for the airflow resistivity where the airflow resistivity is a linear function of the velocities at perforations. The mass-spring model is suitable for determining the velocities at perforations, as they correspond to the velocities of the equivalent masses. The coefficients of the Darcy-Forchheimer's law are determined from computational fluid dynamics modeling (CFD). The mass-spring model is used to visualize mode shapes and frequencies of absorption peaks, and how they are influenced by increasing SPL. Also, the mass-spring model is employed to determine the frequency limit between global and local resonances. Finally, the mass-spring model is used to predict and compare the sensitivity to the high SPL of three ABH with different decreasing pore profiles.

The present paper is organized as follows. First the material is described with the studied decreasing profiles in section 6.4. In section 6.5, the equivalent mass-spring model is adapted to analyze the acoustic properties of the ABH and high SPL. Then the method to determine the airflow resistivity coefficients by a computational fluid dynamics model is detailed. The experimental setup is presented in section 6.5. Section 6.6 shows a comparison between the experimental results and the equivalent mass-spring model predictions. The results are discussed in section 6.7.

6.4 Materials

The metamaterial is composed of Pseudo-Periodic Unit Cell (PPUCs). Each PPUC is composed of an air pore linked to a thin air cavity. Figure 6.1(a) shows a schema of the studied metamaterial, highlighting a PPUC. The cross-sections of the perforations (air pores) decrease throughout the thickness of the metamaterial. Three samples with different decreasing pore profiles are investigated. All samples consist of the same number of PPUCs, $N = 15$. The common geometric parameters for each PPUC include: the radius of the first pore $r_{p,1} = 9$ mm, the radius of the last pore $r_{p,N} = 2$ mm, the thickness of the pores $h_p = 1$, the radius of the cavities $r_c = 21$ mm and the radius of the samples $r_s = 22.22$ mm. The variation of the pore radius is governed by the coefficient ϵ, and the radius of a pore i is determined as

$$r_{p,i} = r_{p,1} - \left(r_{p,1} - r_{p,N}\right)\left(\frac{i-1}{N-1}\right)^{\epsilon}. \tag{6.1}$$

Figure 6.1(b) shows a schema of the three decreasing pore profile studied with coefficient ϵ of 0.5, 1 and 2.

A sample with a linearly decreasing pore profile has been manufactured (ϵ=1). A picture of the sample is shown in figure 6.1(c). The sample is an assembly of machined PPUC in aluminum to fit an impedance tube of 44.44 mm diameter. To avoid acoustical leaks, a chamfer is designed at the edge of the PPUCs. Also, petroleum jelly was applied at the PPUCs contact surface and at the surfaces in contact with the impedance tube.

6.5 Methods

6.5.1 Mass-spring model

The equivalent mass-spring model is based on an analogy where the pores are represented by equivalent masses and the cavities by equivalent springs. The present model is adapted from Chapter 3 to consider the variations of the pore sections along the material. The model assumes a harmonic regime with $e^{j\omega t}$ convention, where t is the time and $j^2 = -1$.

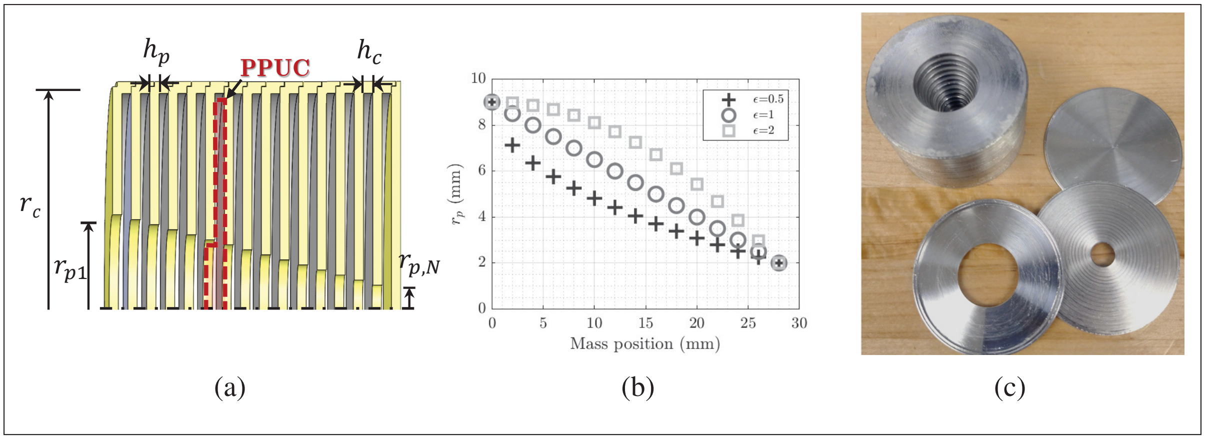

Figure 6.1 (Color online.) (a) Schema of multi-single perforation plates. (b) Evolution of the main pore radius function of the depth for the three ABH decreasing pore profile with coefficient ϵ. (c) A picture of a manufactured material

The viscous losses of the pores are considered using the effective fluid approach. The Johnson-Champoux-Allard (JCA) model (Johnson, Koplik & Dashen, 1987) is used with parameters for a cylindrical pore given in table 6.1. To consider additional losses induced by high sound pressure levels in perforation/pore, the airflow resistivity is a linear function of the acoustic pore velocity, according to Forchheimer's law (Wilson *et al.*, 1988). The airflow resistivity of a pore is defined as:

$$\sigma_i(\dot{x}_i) = \sigma_{0,i}\,\phi_{p,i} + F_i\,\phi_{p,i}^2 \frac{|\dot{x}_i|}{\sqrt{2}}, \tag{6.2}$$

where $\phi_{p,i} = r_{p,i}^2/r_s^2$ is the perforation ratio. $\sigma_{0,i}$ is the static airflow resistivity coefficient and F_i the Forchheimer coefficient of the pore i. These coefficients are determined following the approach described in section 6.5.2. x_i is the acoustic displacement of the pore/mass. $\dot{x}_i$ denotes the derivative of x as a function of time, i.e., the acoustic velocity of the pore.

Assuming that $k_0 h_p << 1$, the equivalent mass of pore is defined as:

$$M_{eq,i}(\dot{x}_i) = \rho_{p,i}(\dot{x}_i) A_{p,i} h'_{p,i}, \tag{6.3}$$

where $\rho_{p,i}$ is the effective density from JCA approach (Johnson *et al.*, 1987). $A_{p,i} = \pi r_{p,i}$ is the pore cross-section and $h'_{p,i}$ is the pore thickness with radiation end correction. The same end

Table 6.1 Parameters of the Johnson-Champoux-Allard (JCA) (Johnson *et al.*, 1987) model for pores i, identified as cylindrical pores, and *pancake* dead-end (DE) resonators, identified as slits

Parameter name	symbol	unit	Pores	DE resonators
Porosity	ϕ	1	1	1
Tortuosity	α_∞	1	1	1
Viscous characteristic length	Λ	m	$r_{p,1}$	h_c
Thermal characteristic length	Λ'	m	$r_{p,1}$	h_c
Aiflrow resistivity	σ	$\mathrm{Pa\,s\,m^{-2}}$	Equation (6.2)	$12\frac{\eta}{\phi h_c^2}$

correction approach is used as in chapter 3. End correction for the exterior medium radiation of the first pore is considered using Karal's formula (Karal, 1953). For the inner pore of the studied geometry, Karal's end correction predicts a length correction higher than the cavity. Intuitively, the pore radiation is limited by the next pore radiation. The inner end correction equals half the thickness of the cavity, see section 3.5 and the work of Bezançon *et al.* (2024).

From the second Newtown's law, the equation of motion of the first pore is

$$-\omega^2 M_{eq,1}(\dot{x}_1)\,\ddot{x}_1 = -A_{p,1}p_1 + A_{p,1}p_t, \tag{6.4}$$

where $\ddot{x}_1$ is the acceleration of the first mass which represent the acoustic acceleration of the air mass in the first pore. p_1 is the acoustic pressure at the first junction. p_t is the imposed total acoustic pressure at the input of the material. Similarly, the equation of motion of an inner pore, $i > 2$, is

$$-\omega^2 M_{eq,i}(\dot{x}_i)\,\ddot{x}_i = -A_{p,i}p_i + A_{p,i-1}p_{i-1}, \tag{6.5}$$

where $\ddot{x}_i$ is the acceleration of the mass ith which represents the acoustic acceleration of the air mass in the ith pore. p_i is the acoustic pressure at the ith junction. The metamaterial is supposed to be rigidly backed, $x_{N+1} = 0$.

The junction is split into two cylinders as shown in figure 6.2. Inside a junction, the pressure is supposed to be constant and the junction volume to be adiabatically compressed (the losses at the junction are negligible compared pore losses). The pressure inside a junction is (Dickey & Selamet, 1996)

$$p_i = -\rho_0 c_0^2 \frac{\Delta V_{J,i}}{V_{J,i}}, \tag{6.6}$$

where ρ_0 is the air density and c_0 is the celerity of the sound in air. $V_{J,i} = A_{p,i} h_c/2 + A_{p,i+1} h_c/2$ is the volume of the junction. $\Delta V_{J,i}$ is the variation of the volume of junction and expressed as:

$$\Delta V_{J,i} = -x_i A_{p,i} + \xi_{de,i} A_{de,i} + x_{i+1} A_{p,i+1}, \tag{6.7}$$

x_i and x_{i+1} are the acoustic displacements of the air masses right before and after the junction i and $\xi_{de,i}$ is the radial displacement at the input of the DE resonator connected to the junction. $A_{de,i} = 2\pi r_{p,i} h_c/2 + 2\pi r_{p,i+1} h_c/2$ is the input DE cross-section. The displacement is assumed to be harmonic, $\dot{x} = j\omega x$ (high sound pressure inside the material results in increasing losses and internal pure tones are not distorted). The surface impedance of the thin annular DE resonator is given by the equation (15) of Dickey & Selamet (1996) and is rewritten here in terms of Bessel functions:

$$Z_{Sde,i} = \frac{p_{de,i}}{j\omega \xi_{de,i}} = j Z_{de} \frac{\mathrm{J}_0(k_{de}\overline{r}_{p,i}) + \frac{\mathrm{J}_1(k_{de} r_c)}{\mathrm{Y}_1(k_{de} r_c)} \mathrm{Y}_0(k_{de}\overline{r}_{p,i})}{\mathrm{J}_1(k_{de}\overline{r}_{p,i}) + \frac{\mathrm{J}_1(k_{de} r_c)}{\mathrm{Y}_1(k_{de} r_c)} \mathrm{Y}_1(k_{de}\overline{r}_{p,i})}, \tag{6.8}$$

where $\overline{r}_{p,i} = (r_{p,i} + r_{p,i+1})/2$ is the mean radius of the pores right before and after a given junction, similarly as Bezançon *et al.* (2024). J_m and Y_m are, respectively, Bessel functions of the first and second kind of order m. Z_{de} is the effective impedance and k_{de} is the effective wave number in the DE resonator given by JCA model with the parameters of slit given in table 6.1.

Combining equations (6.7) and (6.8) into equation (6.6), the pressure at a junction i is

$$p_i = \frac{A_{p,i} x_i - A_{p,i+1} x_{i+1}}{\frac{V_{J,i}}{\rho_0 c_0^2} + \frac{A_{de,i}}{j\omega Z_{Sde,i}}} = \frac{A_{p,i} x_i - A_{p,i+1} x_{i+1}}{\Gamma_i}, \tag{6.9}$$

where Γ_i is the denominator of equation (6.9).

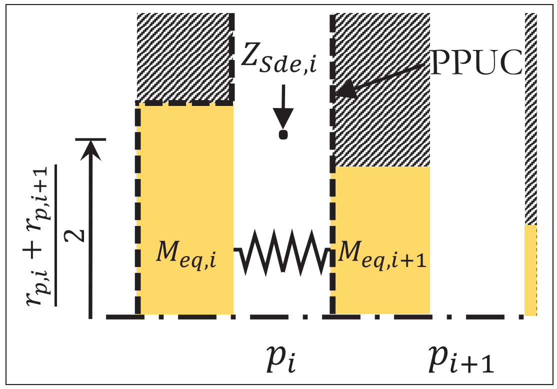

Figure 6.2 (Color online.) Schema at the junction of two consecutive pores and a cavity

Using equation (6.9), equations (6.4) and (6.5) can be rewritten in matrix form:

$$\left(-\omega^2\mathbf{M}(\dot{\boldsymbol{x}}) + \mathbf{K}\right)\boldsymbol{x} = \boldsymbol{f}, \tag{6.10}$$

where $\boldsymbol{f} = (p_t A_p \; 0 \; \dots \; 0)^{\mathrm{T}}$ is the external force vector. The superscript T refers to the vector transposition. p_t is the total acoustic pressure at the material input.

The equivalent mass matrix is diagonal and expressed as:

$$\mathbf{M}(\dot{\boldsymbol{x}}) = \begin{bmatrix} M_{eq,1}(\dot{x}_1) & & & 0 \\ & M_{eq,2}(\dot{x}_2) & & \\ & & \ddots & \\ 0 & & & M_{eq,N}(\dot{x}_N) \end{bmatrix}. \tag{6.11}$$

The equivalent stiffness matrix is tridiagonal and expressed as:

$$\mathbf{K} = \begin{bmatrix} \frac{A_{p,1}^2}{\Gamma_1} & -\frac{A_{p,1}A_{p,2}}{\Gamma_1} & & 0 \\ -\frac{A_{p,1}A_{p,2}}{\Gamma_1} & \frac{A_{p,1}^2}{\Gamma_1}+\frac{A_{p,2}^2}{\Gamma_2} & -\frac{A_{p,2}A_{p,3}}{\Gamma_2} & \\ & & \ddots & \\ 0 & & & \frac{A_{p,N-1}^2}{\Gamma_{N-1}}+\frac{A_{p,N}^2}{\Gamma_N} \end{bmatrix}. \tag{6.12}$$

The acoustic indicators are determined by solving the equations of motions. The normalized surface impedance at the input of the metamaterial is

$$Z_{nS} = \frac{p_t}{\dot{x}_1\rho_0 c_0} = \frac{f_1}{A_{p,1}\phi_S\dot{x}_1\rho_0 c_0} = \frac{j\omega M_{eq,1}}{A_{p,1}\phi_S\rho_0 c_0} + \frac{K_{1,1}}{j\omega A_{p,1}\phi_S\rho_0 c_0} + \frac{K_{1,2}}{j\omega A_{p,1}\phi_S\rho_0 c_0}\frac{x_2}{x_1}. \tag{6.13}$$

Where $\phi_S = A_{p,1}/A_S$ is the open area of the material, A_S is the surface of the material.

The normal incidence sound absorption coefficient is

$$\alpha = 1 - \left|\frac{Z_{nS}-1}{Z_{nS}+1}\right|^2. \tag{6.14}$$

The mass matrix depends on the pore acoustic velocities under high sound pressure conditions. An iterative approach is employed to solve the problem, the iterative approach is detailed in appendix V. The procedure begins by setting the velocities of equivalent masses to zero for the airflow resistivity equation (6.2). Subsequently, the equation of motion equation (6.10)) is solved with the imposed pressure p_t , and new velocities for the equivalent masses are determined. These updated velocities are then used in the airflow resistivity equation equation (6.2). This iterative process continues until convergence is achieved.

6.5.2 Airflow resistivity

The main equations of airflow resistivity are first applied to the geometry under study. Then, the numerical model used to predict airflow dynamic is presented.

6.5.2.1 Darcy-Forchheimer's law

The airflow resistivity of a porous material is expressed as (ISO 9053-1, 2018)

$$\sigma = \frac{\Delta PA}{QL} \tag{6.15}$$

where ΔP is the pressure drop of the before and after the sample, A is the sample cross section, Q is the flow rate and L the sample thickness. In the studied geometry, the cross-section of the plate perforations decreases throughout the thickness of the sample. Viscous and inertial effects on airflow resistivity vary non-uniformly through the sample thickness. In such cases, the overall determination of airflow resistivity across the entire material has its limitations. A local approach to airflow resistivity appears more suitable.

The Reynolds number characterizes the limit between viscous and inertial effects. In a pore i, the Reynolds number is $\mathrm{Re}_{p,i} = \rho_0 V_{in} 2r_{p,i}/(\eta\phi_{p,i})$ where ρ_0 represents the air density, η is the dynamic viscosity and V_{in} is the flow velocity imposed upstream of the ABH. At low flow velocity, corresponding to $\mathrm{Re}_{p,i} < 1$, viscous effects dominate, the relation between the pressure drop and the velocity is given by Darcy 'law predicts and expressed as:

$$\Delta P_i = P_{b,i} - P_{a,i} = h_{p,i}\sigma_{0,i}V_{in} \tag{6.16}$$

where ΔP_i is the pressure drops before and after the pore. $P_{b,i}$ and $P_{a,i}$ are respectively the average pressures on the inlet and outlet sections of the pore.

At higher Pore Reynolds number ($\mathrm{Re}_{p,i} > 1$), the relation between the pressure drop and the flow velocity is no more linear, The local pressure drop of the pore i is determined by Darcy-Forchheimer's law and expressed as:

$$\Delta P_i = P_{b,i} - P_{a,i} = h_{p,i}\sigma_{0,i}V_{in} + h_{p,i}F_{0,i}V_{in}^2 \tag{6.17}$$

From CFD model (see section 6.5.2.2), the pressure drops are evaluated at each plate of the sample for different flow rates. To determine the local static airflow resistivity coefficient, $\sigma_{0,i}$, and local Forchheimer's coefficient, $F_{0,i}$, the following methodology has been used:

- $\sigma_{0,i}$ is determined at each plate using equation (6.16) for low flow velocity corresponding to $\mathrm{Re}_{p,i} < 1$
- F_i is determined at each plate using equation (6.17) for flow velocity corresponding to $\mathrm{Re}_{p,1} > 1$ for the lowest pore Reynolds number (largest radius) up to $\mathrm{Re}_{p,N} = 1400$ (smallest radius).

6.5.2.2 CFD model

The pressure drops are determined from a CFD model using COMSOL Multiphysics 6.1 software at different imposed flow velocities. The geometry is 2D-axisymmetric and consists of the sample under studied with an extrusion of the sample tube upstream and downstream, see figure 6.3. Each extrusion is 5 times the radius of the sample.

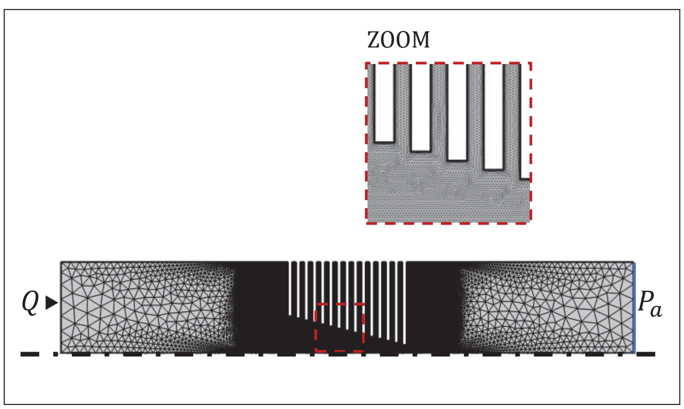

Figure 6.3 (Color online.) Views of the mesh distribution sketch of the computational domain of the CFD model

The simulation was performed under standard conditions of air at 20°C and atmospheric pressure. The domain was discretized using quadratic elements, with an extra-fine mesh employed in the sample region. Rigid walls were meshed with a boundary layer consisting of eight layers and a stretching factor of 1.12. In the upstream and downstream extrusions, coarse fluid dynamic type is used.

The simulation employed COMSOL's laminar flow approach within the compressible flow physical model, applicable since the Mach number was less than 0.3. Upstream of the tube, fully developed flow rate (Q) boundary conditions were applied, while downstream (at the tube output), fully developed average pressure (P_a) boundary conditions were imposed.

6.5.3 High-level impedance tube

The experimental approach is based on the two-microphone impedance tube method using Mecanum's high sound level impedance tube. The sinusoidal wave excitation is employed, with iterative processes ensuring identical total SPL at the input of the metamaterial for each frequency. Experimentally, a total SPL is imposed for each frequency, where the corresponding pressure is a root mean square value. The amplitude of the total acoustic pressure for each frequency is expressed as $p_t = \sqrt{2} \cdot 2 \cdot 10^{-5} 10^{SPL/20}$.

An adapter is used to transition from a 29-mm-diameter tube to a 44.44-mm-diameter tube, suitable for experimental samples. In the adapter, a cone-shaped cross-section is positioned between the sound source and the microphones. The distance between the end of the cone-shaped cross-section and the first microphone exceeds twice the diameter (88.88 mm). Adapter losses are minimal, allowing the source to reach 145 dB at the input of the metamaterial for each frequency.

Under low SPLs, the experimental results using this approach align with impedance tube measurements following ASTM E1050-19 (2019) standard. Measurements were conducted three times at each studied sound pressure level. The samples are described in section 6.4, and the measurements consist of two mixed assembly sets.

6.6 Results

The geometry of interest in the present section is a linearly decreasing pore profile (ϵ =1). Firstly, the pressure drops at the pores, evaluated using the CFD approach, are presented. Based on these pressure drops at various flow rates, the Forchheimer coefficient and the static airflow resistivity coefficient are determined. Secondly, the mass-spring model incorporating the CFD-determined Forchheimer coefficient is compared with experimental impedance tube measurements conducted at different SPLs.

6.6.1 Computational fluid Dynamics results

The figure 6.4(a) shows the local pressure drops at three pore positions (i =1, 3 and 15) for different input flow velocities. At low flow velocities (pore Reynolds number smaller than one), the pressure drops increase linearly with increasing flow velocities. The viscous losses predominate over inertial losses, and the pressure drops follow Darcy's law. In this regime, the airflow resistivity ($\sigma = \Delta P/V$) is independent of the flow velocities for a specific pore. Also, the slop of pressure drops increases with plate position. Indeed, with decreasing pore profile of the geometry, the airflow velocity increases along the profile (this corresponds to flow rate conservation) and generates an increase in local pressure drops.

At high flow velocities (for pore Reynolds number greater than one), the inertial effects dominate. The relation between the pressure drops and the input flow velocity is quadratic, following Darcy-Forchheimer's law.

The local static airflow resistivity and local Forchheimer's coefficients are determined from a quadratic regression over the local pressure drops, see section 6.5.2. The curves of the quadratic regressions are represented by the solid lines in figure 6.4(a). A high prediction is allowed by the regression (smallest R^2 is 0.99778).

Figure 6.4(b) shows the local static airflow resistivity coefficient for the different pore positions. The coefficient increases with pore index i. The regression results from CFD approach are in

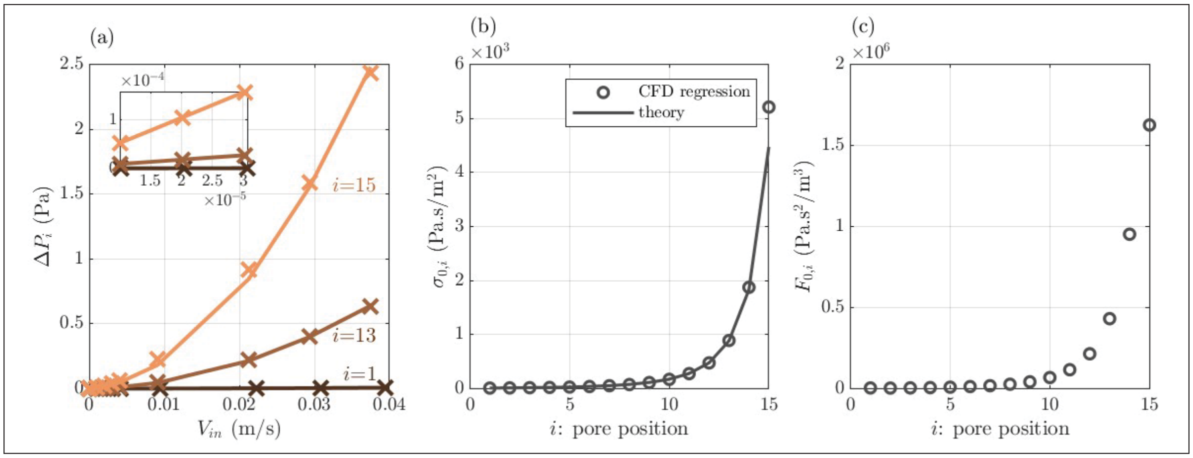

Figure 6.4 (Color online.) (a) Local pressure drops for different input flow velocities at three pore positions: i =1, 3 and 15. The crosses (×) represent the predictions by the computational fluid dynamics approach and the corresponding solid lines (—) the quadratic regressions. The inlet represents the local pressure drops at low flow velocity (Reynolds number smaller than one). (b) Local static airflow resistivity coefficient and (c) local Forchheimer coefficient at the different pore positions. The geometry is a linearly (ϵ = 1) decreasing pore profile

very good agreement with the classic formula of cylinder pore $\sigma_{th} = 8\frac{\eta}{\phi_i r_{p,i}}$ (Stinson, 1991). Figure 6.4(c) shows the local Forchheimer coefficient for the different pore positions. The Forchheimer parameter, and thus the inertial effect, increases along the material profile. All the data of the local static airflow resistivity and the local Forchheimer coefficients are given in appendix IV.

6.6.2 Acoustic results

The comparison between the impedance tube measurements and the mass-spring prediction of the sound absorption coefficient at a low sound pressure (SPL=95 dB) is shown in figure 6.5(a). The model is in pretty good agreements with the measurements especially. Several absorption peaks are observed. For the first and second peaks, the relative error on the amplitude is less than 10 %, and the relative error on the peaks frequencies are less than 1 %. A broad absorption band starts around 1720 Hz (α > 0.5). At the broad absorption band, the difference between the experimental measurements and the model predictions increases. The predictions of the sound absorption coefficient by the mass-spring model are of the same order of magnitude as the measurements. Within this frequency range, differences between theoretical model and experimental measurements are not specific to the mass-spring model. Various reasons have already been raised in previous studies on similar materials as extra losses and vibration of the plates, see chapters 3 and 5 or (Dupont *et al.*, 2018; Brooke *et al.*, 2020; Bezançon *et al.*, 2024). In the experimental setup, acoustic leaks, a manufacturing inaccuracy such as hole shapes and surface roughness, may increase the losses and the absorption coefficient. For example, these extra losses could explain the difference in the hollows of the sound absorption coefficient where the experimental measurements show higher values than the mass-spring model predictions. In addition, vibration effects may affect the sound absorption coefficient. The vibration resonance of a plate can be responsible for additional absorption peak (Hruška *et al.*, 2024). Several resonance frequencies are probably present in our material, one for each perforated plate. Which would explain differences over a wide range of frequencies. Further investigations of the effect of vibrations for the present geometry would be of interest.

The predictions of the mass-spring model with Forchheimer coefficients determined by the CFD approach are compared with experimental measurements with increased SPL figure 6.5(b) SPL=120 dB and figure 6.5(c) SPL=145 dB. The mass-spring model prediction is in good agreement with the experimental measurements, especially for the first two absorption peaks. The comparison between the experimental measurements and the mass-spring model for the first two absorption peaks at the different sound pressure levels is given by table 6.2. The relative error between the two approaches for the first resonance frequency is smaller than 2 %, and 5 % for the absorption coefficient. The relative error is higher at low SPL. This suggests that additional losses are present at low SPL.

At higher frequency (in the broad frequency band area), the measured sound absorption coefficients are on average slightly higher and less oscillations are observed than the mass-spring predictions. Indeed, the results at low and at high SPL were less accurate in this frequency range.

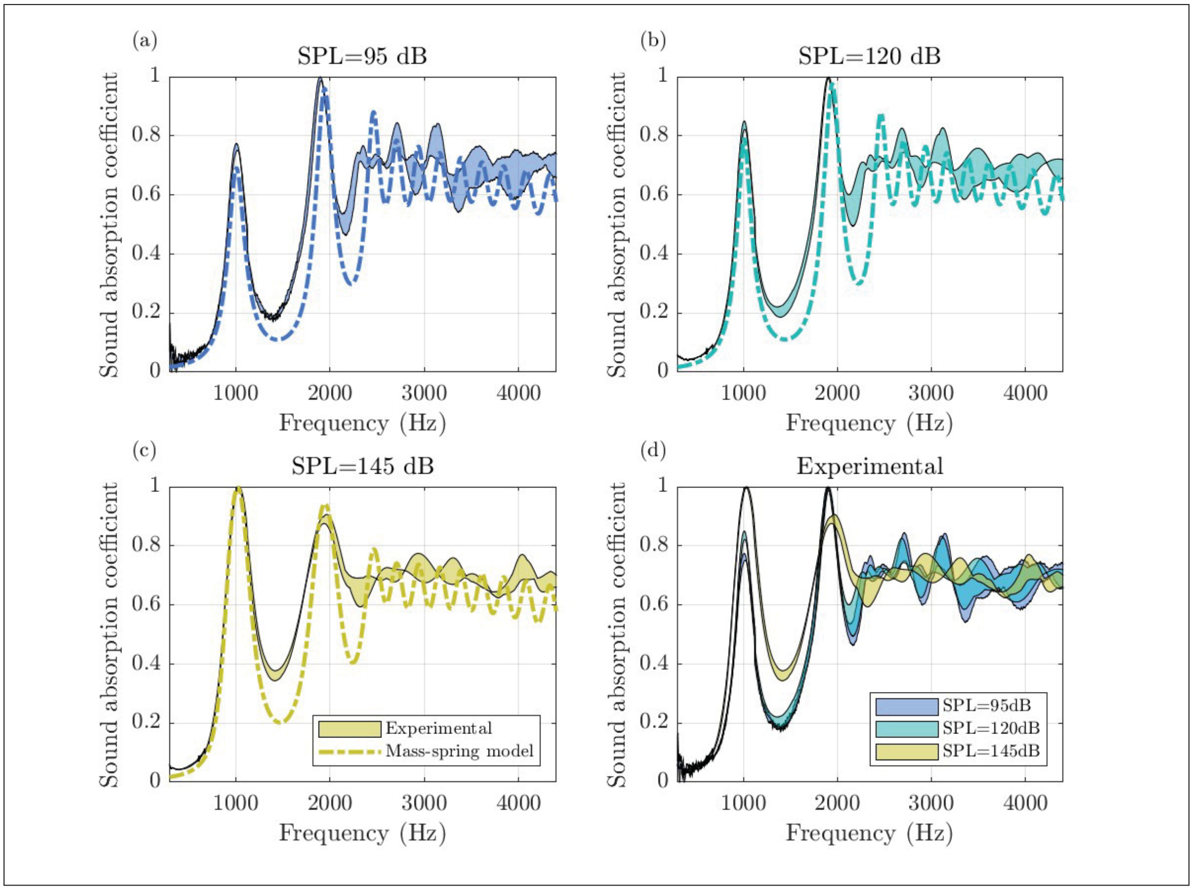

Figure 6.5 (Color online.) Normal incidence sound absorption coefficients. (a-c) Comparison of experimental measurements and mass-spring model predictions at different sound pressure levels. (d) Comparison of sound pressure levels on experimental measurements. The geometry is a linearly (ϵ=1) decreasing pore profile. The thickness of the experimental curves represents the data dispersion over 3 measurements

6.7 Discussion

The mass-spring model is employed to assess the impact of SPL on acoustic indicators such as sound absorption coefficient and normalized acoustic impedance. Sensitivity to SPL is compared across three ABHs with varying pore profiles. Furthermore, the mass-spring model is used to visualize sound propagation. Additionally, the model determines the characteristic frequencies of sound propagation in the ABHs under low SPL conditions. The evolution of mode shapes is then examined as SPL increases. Finally, the last section investigates how changes in mode shapes affect the sensitivity of ABHs to increasing SPL.

Table 6.2 Frequency and sound absorption coefficient of the first absorption peaks for the experimental approach and the mass-spring model with local Forchheimer's parameter approach. The geometry is a linearly (ϵ =1) decreasing pore profile. The relative errors are shown in brackets

	Experimental approach		Mass-spring model	
SPL (dB)	f_{peak1} (Hz)	$\alpha_{peak1}(1)$	f_{peak1} (Hz)	$\alpha_{peak1}(1)$
95	1014	0.76	1009 (0.5%)	0.69 (9.0%)
120	1014	0.83	1010 (0.4%)	0.79 (5.2%)
145	1033	1.00	1023 (1.0%)	1.00 (0.1%)

6.7.1 Impact of high sound pressure levels

A comparison of the measured sound absorption coefficient is presented in figure 6.5(d). The first peaks are particularly sensitive to high SPL. SPL has a reduced impact on the amplitude of high-frequency absorption peaks. With increasing SPL, the amplitude of the first absorption coefficient peak increases while the second peak decreases. Unlike conventional perforated plates, where peak absorption frequencies increase with SPL (as seen in Laly *et al.* (2018)), the present geometry shows consistent peak frequencies. This observation may be attributed to the thin thickness of the cavities ($h_c << r_c$), limiting end pore radiation and vortices size inside the material.

An interesting finding is the slight shift of some absorption peaks of the broad absorption to lower frequencies with increasing SPL, as shown in figure 6.5(d). This contrasts with conventional perforated plates. The authors hypothesize that vibration effects (fluid-structure interaction) could explain this phenomenon, suggesting further investigation, especially under high acoustic excitation amplitudes, would be beneficial. However, such investigations are beyond the scope of the current study, which primarily focuses on the rigid case encountered at first resonances.

Despite these differences, the mass-spring model predicts sound absorption reasonably well when compared to SPL measurements. The model is further used to analyze the acoustic response of various decreasing pore profiles. Figures 6.6(a-c) show the acoustic absorption coefficients as functions of frequency and SPL for three types of decreasing pore profiles. Initially, we examine the linear acoustic response for these profiles at low SPL (SPL=95 dB). Multiple absorption peaks are observed for each profile, corresponding to acoustic resonances where the reactance (imaginary part of the surface impedance) is zero, as shown in figure 6.6(g-i). The resonance frequency of specific modes increases with the parameter ϵ (as annotated in Figures 6.6(g-i)). In the low-frequency approximation of the DE cavities, the first resonance frequencies are influenced by the total volume of the DE cavities (Leclaire *et al.*, 2015). As ϵ increases, the total volume of the cavities decreases, shifting the first resonance frequency to higher values. In the linear regime, the amplitude of the first absorption peak decreases with increasing ϵ (see inset in Figures 6.6(a-c)). At resonance, the reactance is zero, and the absorption coefficient tends toward one as the normalized surface resistance (the real part of the normalized surface impedance) approaches one, see equation (6.13).

At the second resonance, the normalized surface resistance approaches one, resulting in a high amplitude of the absorption coefficient for all three profile types. Higher resonance frequencies are located within the broadband absorption zone. Similar to other studies on ABH (Guasch *et al.*, 2017, 2020; Serra *et al.*, 2023), square[1] decreasing pore profiles exhibit less oscillations in the absorption coefficient and are preferred in the linear regime. For ABH with square decreasing pore profiles, the amplitudes of the absorption coefficient peaks are lower compared to the other profiles in the broadband absorption zone. As frequencies increase, viscous and thermal losses increase, resulting in a normalized surface resistance greater than one and the normalized surface reactance moving away from the zero axis.

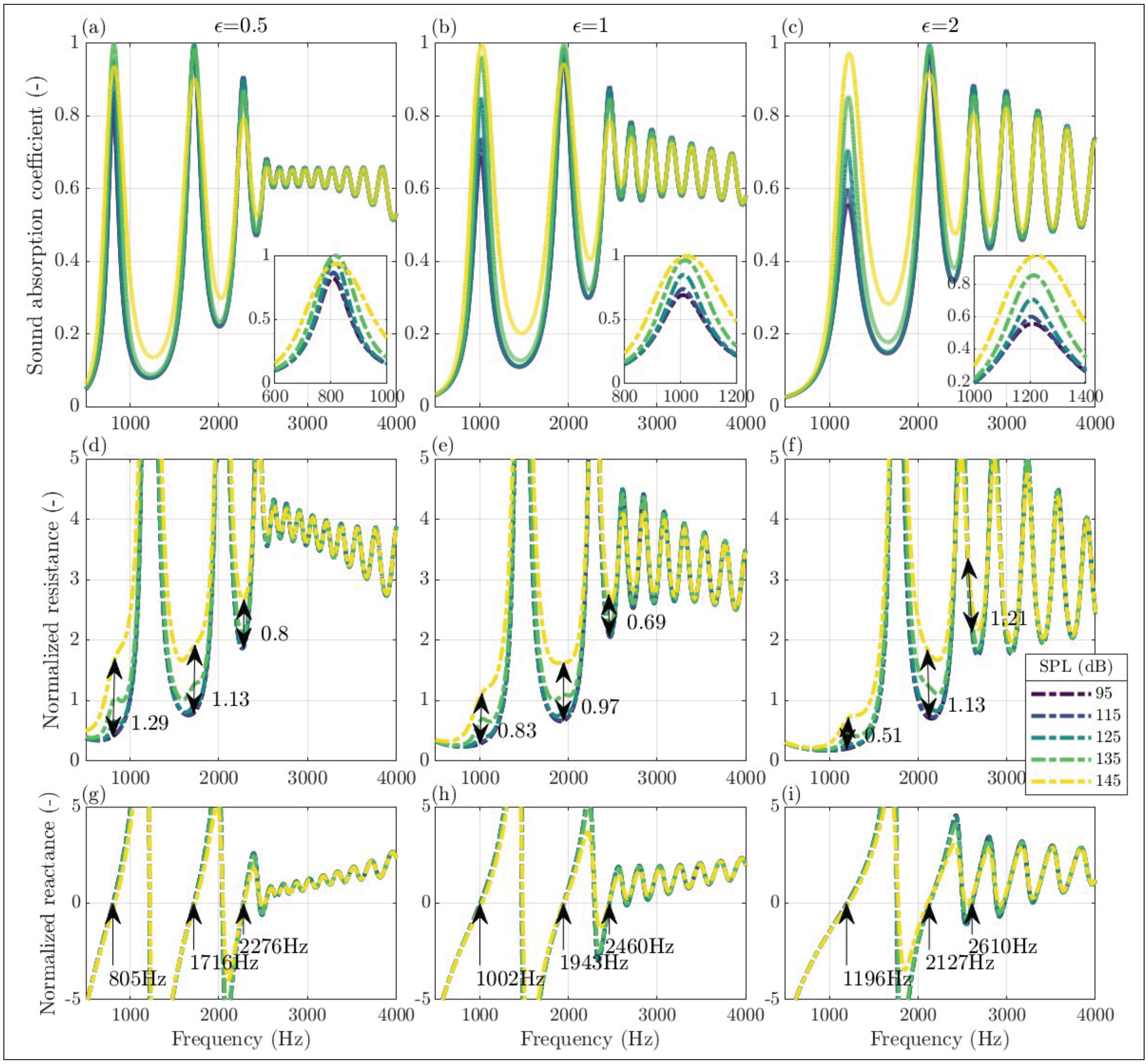

Figure 6.6 (Color online.) (a-c) Mass-spring model predictions of the normal incidence sound absorption coefficients of acoustic black holes with three different decreasing pore profiles (ϵ=0.5, 1 and 2) at different sound pressure levels. (d-f) Normalized surface resistance of acoustic black holes with three decreasing pore profiles same as (a-c) at different sound pressure levels. (g-i) Normalized surface reactance of acoustic black holes with three decreasing pore profiles same as (a-c) at different sound pressure levels

The acoustic behavior of materials under high SPL is now addressed. With increasing SPL, the reactance at resonance remains nearly unchanged for all three types of decreasing pore profile, see Figures 6.6(g-i). This consistency explains why the frequencies of absorption peaks remain constant despite increasing SPL, as shown in Figures 6.6(a-c). Meanwhile, the surface resistance at the resonances increases with the SPL. The increase in normalized surface resistance at resonances is shown in Figures 6.6(d-f) from SPL of 95 dB to 145 dB. For ϵ=0.5, the normalized surface resistance at the first resonance goes to one and continues to increase with SPLs. When the SPL is near 135 dB, the normalized surface resistance approaches one, resulting in a maximum of absorption. At higher SPL, increased losses lead to a decrease in the sound absorption coefficient. Similarly, for ϵ=1, the normalized surface resistance at the first resonance increases until it reaches one at SPL=145 dB, corresponding to increased absorption. Further increases in SPL would reduce absorption. Likewise, for ϵ=2, the absorption coefficient at the first resonance increases as the normalized surface resistance approaches one with increasing SPL. For all the three types of decreasing profiles, the normalized surface resistance at the second resonance approaches one, and continue to increase with increasing SPLs. Consequently, the absorption coefficients reach one then decrease. At higher resonance frequencies, fewer variations in acoustic surface resistance are observed, resulting in fewer changes absorption coefficient with increasing SPL.

For a pseudo-periodic material with a decreasing pore profile, the normalized surface impedance in linear regime allows to determine if the absorption is set to increase or decrease with increasing SPL. However, the material's sensitivity to SPL varies depending on the type of decreasing pore profile, ϵ. And it could not be predicted solely by examining the normalized surface impedance in the linear regime. The material's sensitivity to SPL is represented by the surface impedance of the material. To quantify sensitivity to increases in SPL, the variation in the absorption coefficient should not be considered, as the absorption coefficient depends on whether the normalized surface resistance is near one, see equation (6.13). For example, the sound absorption coefficient variation between 95 dB to 145 dB at the first resonance is 0.23 for ϵ= 0.5, 0.31 for ϵ= 1 and 0.41 for ϵ= 2. Lower values of ϵ show less variation in sound absorption coefficient with SPL, whereas the variation of the normalized surface resistance increases as ϵ decreases, as shown in figure 6.6. As mentioned earlier, the first resonances are more sensitive to the increase in SPL across the different profiles.

6.7.2 Modal displacement of masses

The mass-spring model is employed to analyze the sound propagation (acoustic displacement) inside ABHs. Equation (6.10) allows for determining the displacement of the masses. Firstly, the mass displacement is examined in the linear regime (SPL = 95 dB).

Figure 6.7 shows the acoustic displacement mapping of the masses (air masses in the perforations) as a function of frequency for the different decreasing pore profiles (a-c). The displacement is shown in logarithmic scale and normalized by the incident displacement, x_{in}. In the acoustic displacement mapping of the masses, the yellow vertical lines correspond to modal lines, see section 3.7.2. Similarly, the dark black lines indicate nodal lines, where displacement is zero. For the first mode, all masses vibrate in phases (no nodal points). For the second mode, two groups of masses separated by the nodal point vibrate in phase opposition. Similarly, three antinodes (maximum of mass displacement) and two nodal points are present for the third mode. These modes correspond to global modes/resonances where a mode is along the material (Umnova *et al.*, 2023; Bezançon *et al.*, 2024). Across different pore profiles shown in figure 6.7(a-c), the modes do not occur at the same frequencies: vertical yellow lines move to higher frequency as ϵ increases (see section 6.7.1). The intensity of the yellow lines varies with the different profiles indicating that type of decreasing profile influences the mode shape.

The analysis of global resonances is centered on the first two resonances. The mass displacement at the first resonance is shown in figure 6.8, and at the second resonance in figure 6.9 for the three decreasing pore profiles (ϵ=0.5, 1 and 2). The mass displacement is normalized by the displacement of the first mass (this normalization will be relevant for subsequent analyses in the article). The mode shapes in ABH materials differ from those in periodic DE materials, where the modes are similar to those of equivalent quarter-wavelength resonators, see 3.7.2. In ABHs, the mode shapes vary with different decreasing pore profiles. For the ABHs studied, at the first resonance, the mass displacement starts small at the first mass, increases through the material's thickness, and then decreases. The maximum amplitude of the normalized mass displacement decreases as ϵ increases, and the location of this maximum shifts towards the end of the material.

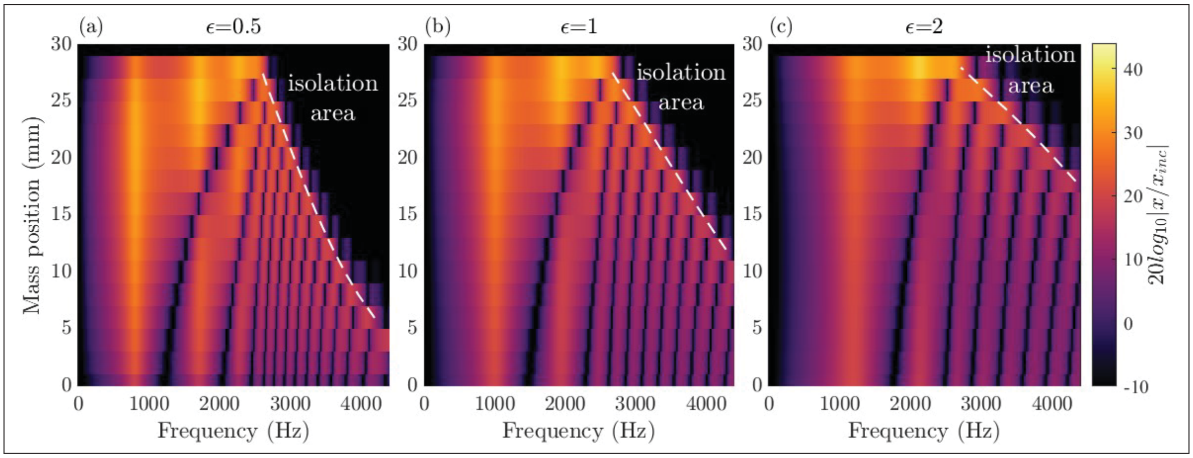

Figure 6.7 (Color online.) Acoustic displacement mapping of the masses as a function of frequency in linear regime (SPL=95 dB) for different decreasing pore profiles ϵ. The material input is located at a mass position of 0 mm. The dashed white line (- - -) is the isolation area beginning

For the first resonance, all masses are in phase with a slight delay due to losses, as shown in figure 6.8(d-f). For the second resonance, as mentioned before, there are antinodes and one nodal point, as shown in figure 6.9(a-c). At the nodal point, the amplitude of the normalized mass displacement is zero, and the phase is $-\pi/2$, as shown in figure 6.9(d-f). In each profile, the amplitude of the normalized mass displacement at the second maximum is higher than at the first maximum. Additionally, the last masses are in opposition phase relative to those at the beginning.

In figure 6.7, around 3000 Hz, a dark area begins, indicating an isolation area with no displacement of the masses. In this area, the acoustic waves do not propagate to the end of the material, behaving as if the material were progressively shorter with increasing frequency. The extent of this isolated area increases with frequency, and the last PPUCs do not contribute within this region. This observation aligns with findings by Bezançon et al. (Bezançon *et al.*, 2024), who compared the acoustic absorption of truncated ABHs. The mass-spring model here provides additional insight into this phenomenon. At frequencies corresponding to the isolation area, modes still exist within the cells where the wave propagates. However, unlike the lower frequency modes, the number of nodal points for each mode does not increase as the mode order increases.

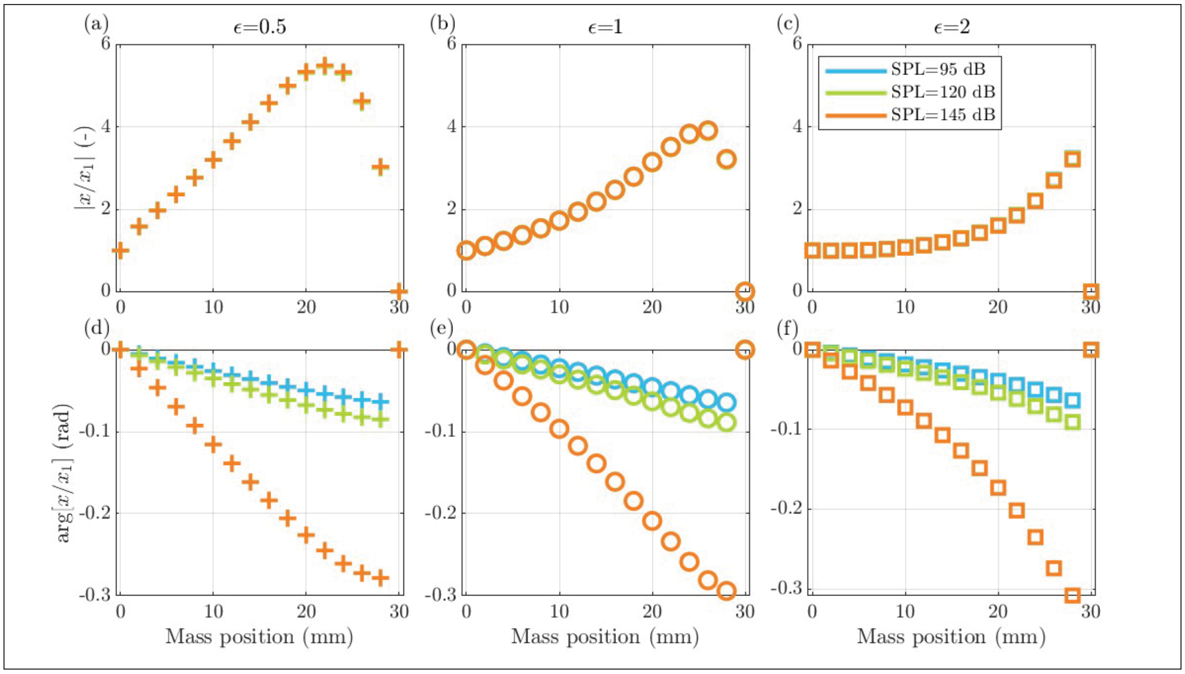

Figure 6.8 (Color online.) Mass displacement profile with loss at the first resonance for different sound pressure levels. The amplitude of mass displacement is shown for different decreasing pore profiles (a-c). The corresponding phases of mass displacement are shown in (d-f). The mass displacement is normalized by the displacement of the first mass

These modes differ from global modes because they only involve the first cells, and are referred to as local modes (Umnova *et al.*, 2023; Bezançon *et al.*, 2024).

Pseudo-periodic DE materials like ABH differ from periodic DE materials in acoustic behavior. In periodic DE materials, band gaps prevent sound wave propagation throughout the material starting from the band gap frequency, see section 3.7.1. In contrast, ABH materials exhibit isolation due to resonances of the PPUC cells (Umnova *et al.*, 2023; Bezançon *et al.*, 2024). The boundary of the isolation area is frequency dependent, showing that beyond a certain frequency, sound waves no longer propagate, extending beyond the frequency range examined (refer to figure 8 of Bezançon *et al.* (2024) for instance). The mass-spring model is employed to identify frequencies that characterize this phenomenon.

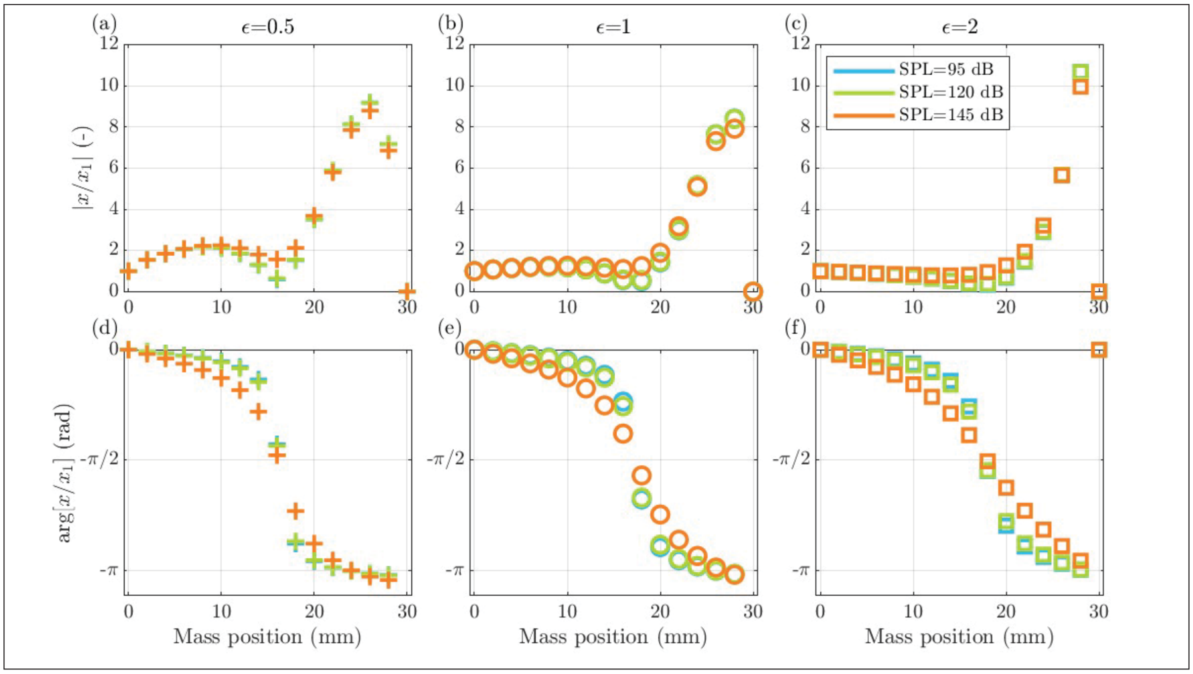

Figure 6.9 (Color online.) Mass displacement profile with loss at the second resonance for different sound pressure levels. The module of mass displacement is shown for different decreasing pore profiles (a-c). The corresponding phases of mass displacement are shown in (d-f). The mass displacement is normalized by the displacement of the first mass

The isolation area begins when the transmission between two consecutive masses is zero, corresponding to (see appendix VI for the detailed development)

$$\omega_{isolation,i} = \mathrm{Re}\left(\sqrt{\frac{K_{i,i} - K_{i,i-1}}{M_{eq,i}}}\right). \tag{6.18}$$

For each group PPUC, the isolation is represented by the dashed white line in figure 6.7. Equation (6.18) allows determining the lower limit of the isolation area. Also, this formula is interesting in two other points. The highest isolation frequency gives the limit before no sound absorption inside the material (higher than the frequency range studied), see for example figure 8 of Bezançon *et al.* (2024). On the other hand, the lowest isolation frequency is the transition frequency between global and local modes. The lowest isolation frequency increases with ϵ and is for ϵ=0.5 $f_{isolation,1}$=2562 Hz, ϵ=1 $f_{isolation,1}$=2606 Hz and ϵ=2 $f_{isolation,1}$=2691 Hz.

6.7.3 Acoustic nonlinear response sensitivity

At low SPL, square[1] decreasing pore profiles are distinguished by the fact that they have fewer oscillations in the sound absorption coefficient, as discussed in section 6.7.1. However, this type of decreasing pore profile is the most sensitive to SPL. The sensitivity to SPL varies significantly among the three decreasing pore profiles studied, particularly at the first resonance. This section specifically focuses on the sensitivity to SPL at the first resonance.

To investigate the material sensitivity to sound pressure, the normalized surface resistance, equation (6.13), is split in two parts. The first part is related to the losses of the first mass. The second part related to the stiffness. The total normalized surface resistance, the part of the surface resistance related to mass and the part of the surface resistance related to stiffness for the first resonance are shown in figure 6.10(a). The results of the three decreasing pore profiles are shown at different SPL. For the different profiles, the total normalized surface resistance is constant at low SPL with the parts of the surface resistance related to mass and stiffness. At low SPL, the stiffness surface resistance part is higher than that of the masses. At low SPL, losses are assumed to be higher for the thin cavities than for the pores of the studied geometry: the viscous and thermal characteristic lengths of the cavities are smaller than those of the pores ($\Lambda_c < \Lambda_p$). With increasing SPL, the total normalized surface resistance increases. The contribution of the stiffness dominates over that of the mass. Viscous mass losses due to high SPL depend on the Forchheimer coefficient and so on the excitation, but have few contributions on the total surface resistance for ABH with thin cavities.

The stiffness contribution depends on two terms, see equation (6.13). Their evolution with increasing SPL for the first resonance is shown in figure 6.10(b) for the three types of profiles. The first term depends on $K_{1,1}$ and is independent of SPL. The second term of the stiffness part depends on $K_{1,2}$ and the ratio between the displacements of the second and first mass. The real part second term of the stiffness part is negative and increases with SPL. The increase is higher for low values of ϵ.

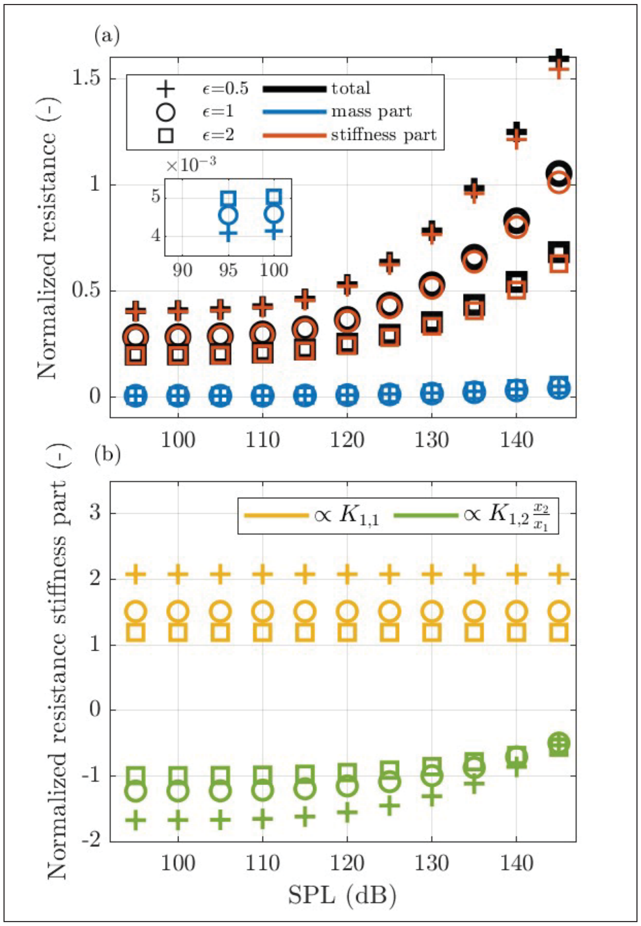

Figure 6.10 (Color online.) Mass-spring model predictions of the normalized surface resistance, equation (6.13), at the first resonance for different sound pressure levels and the three decreasing pore profiles. (a) Total, mass and stiffness parts of the normalized surface resistance (see equation (6.13)). (b) the two terms of the stiffness part of the normalized surface resistance (see equation (6.13))

To explain this difference, the second term of the normalized resistance stiffness part resistance can be rewritten as

$$\mathrm{Re}\left(\frac{K_{1,2}}{j\omega A_{p,1}\phi_S\rho_0c_0}\frac{x_2}{x_1}\right) = \left|\frac{K_{1,2}}{\omega A_{p,1}\phi_S\rho_0c_0}\frac{x_2}{x_1}\right| \cos\left(\arg\left[K_{1,2}\right] + \arg\left[\frac{x_2}{x_1}\right] - \frac{\pi}{2}\right). \tag{6.19}$$

In this equation, the amplitude and on the phase of $K_{1,2}$ is independent of the SPL. But it depends on the amplitude ratio and on the phase between the second and first mass displacements. Figure 6.8 show the normalized mass displacement at the first resonance for different SPL (95 dB, 120 dB and 145 dB) and the three decreasing pore profile (ϵ=0.5, 1 and 2). Figure 6.8 show that the amplitude of the normalized mass displacement of the first mode remains nearly unchanged with increasing SPL. However, the phase increases as SPL increases. High SPL induce additional losses resulting in increased delay within the material in the first resonance. The phase is more impacted for low values of ϵ coefficients, see figure 6.8. Table 6.3 reports the phase difference between the displacements of the second and first masses. For the first resonance of the studied ABH, the phase difference between the displacements of the second and first mass is higher for low values of ϵ, see table 6.3. And profiles with low values of ϵ are more sensitive to SPL increases, see figure 6.10.

Table 6.3 Phrase difference of the displacement of second and first masses for different decreasing pore profiles, ϵ, and sound pressure levels

		$\arg[x_2/x_1] \times 10^{-3}$	
ϵ	SPL (dB)	first resonance	second resonance
0.5	90	-5.3	-24.0
0.5	117.5	-6.5	-25.1
0.5	145	-22.8	-58.9
1	90	-4.5	-22.7
1	117.5	-5.5	-24.1
1	145	-18.4	-57.1
2	90	-3.6	-27.1
2	117.5	-4.3	-29.3
2	145	-13.4	-71.2

Similarly, in the case of the second resonance the amplitude of the normalized mass displacement of the first masses is less affected by the SPL, but the phase difference intensifies, see figure 6.9 . The phase difference is the lowest for the linearly decreasing profile, ϵ=1, see table 6.3. And this decreasing profile presents a fewer impact to SPL increases as shown in figure 6.6(d-f). Therefore, the acoustic nonlinearity that governs the metamaterial response is linked to the phase difference between the displacements of the second and first masses and the stiffness of the first cavity. Profiles with lower values of the phase difference between the displacements of the second and first mass at low sound pressure levels exhibit reduced sensitivity to increases in SPL.

6.8 Conclusion

A mass-spring model has been proposed to study the influence of high sound pressure levels on compact acoustic black holes. The model is in good agreement with experimental impedance tube measurement up to 145 dB, especially at low frequencies. At first resonance, the normalized surface resistance increases with sound pressure levels while the resonance frequencies are almost unchanged. As a result, the amplitude of the first sound absorption peaks changes with sound pressure levels.

The mass-spring model has been used to visualize the propagation of sound inside the acoustic black hole. It shows in a simple way that, as frequency increases, sound does not reach the end of the material (called here isolation area). A formula is derived from the mass-spring model to determine the contour of the isolation zone. This formula is used to determine the frequency boundary between global and local resonances in acoustic black hole.

Three variations of the decreasing pore profile were studied. As is already known, in the linear regime (low sound pressure levels), strongly decreasing pore profiles at the beginning of the material are preferred, as they present fewer oscillations in the absorption coefficient. However, this type of decreasing pore profile is the most sensitive to sound pressure levels in general. The mass-spring model has shown that sensitivity to high sound pressure levels is related to the phase difference of the mass displacement and the stiffness of the first cavity for thin-cavity acoustic black holes. For the profiles studied, a low value of the phase difference between the displacements of the second and first mass reduces sensitivity to sound pressure level increases. In the decreasing pore profiles studied, acoustic black holes with a low decreasing pore profile at the beginning of the material are less affected by the sound pressure levels at the first resonance.

At the second resonance, the linearly decreasing pore profile is the least sensitive to high sound pressure levels. There is less variation in sound pressure levels on absorption at high resonance frequencies.

CONCLUSION ET PERSPECTIVES

7.1 Synthèse du problème de recherche et des objectifs

Cette thèse s'est intéressée au développement et à l'analyse de la réponse de matériaux structurés compacts pour l'absorption acoustique des basses fréquences soumis à des niveaux d'excitation sonore faibles à élevés. De cet objectif principal, trois sous-objectifs sont proposés (voir chapitre 2) :

1. Le premier sous-objectif est l'analyse du comportement et le développement de matériaux structurés périodiques pour le traitement acoustique des basses fréquences dans le domaine linéaire : niveau d'excitation acoustique faible.
2. Le deuxième sous-objectif est la prise en compte et l'analyse du comportement acoustique de matériaux structurés périodiques en régime non-linéaire, c.-à-d. soumis à de forts niveaux d'excitation acoustique, pour le traitement acoustique des basses fréquences.
3. Le troisième sous-objectif porte sur l'analyse du comportement et le développement de matériaux structurés large bande pour des niveaux faibles à élevés avec une application aux trous noirs acoustiques.

Les chapitres 3 à 6 répondent à ces sous-objectifs. La conclusion de cette thèse se poursuit avec une synthèse, les limites des modèles et les perspectives pour chacun des chapitres.

7.2 Analyse des matériaux structurés périodiques en régime linéaire

<u>Synthèse :</u> Un modèle masse-ressort est développé pour étudier un matériau à compressibilité effective augmentée à réseau de résonateurs d'Helmholtz annulaires. Un réseau de résonateurs d'Helmholtz annulaires permet d'atteindre une absorption à des fréquences plus basses qu'un matériau à compressibilité effective augmentée à réseau de résonateurs *pancakes* à même volume.

À partir du modèle masse-ressort, une analyse modale est réalisée. Une expression analytique de la première fréquence de résonance est proposée. Dans la configuration en transmission, le modèle est utilisé pour étudier les bandes interdites et passantes du son dans le métamatériau. Dans chaque bande passante, la résonance correspond au nombre de degrés de liberté c.-à-d. le nombre de cellules pore - cavité.

Une représentation du déplacement acoustique des masses en fonction de la fréquence est proposée. Elle permet de mettre en avant différents phénomènes acoustiques dans le matériau, telles les résonances, bandes interdites et passantes. Le modèle est validé à partir de mesures faites en tube d'impédance sur des prototypes. Une bonne corrélation est obtenue entre les résultats expérimentaux et les prédictions du modèle.

Limites : Dans le modèle masse-ressort, la modélisation acoustique des pores par des masses équivalentes reste valable en approximation à basse fréquence (pore de faible épaisseur et avec un rayon petit devant la longueur d'onde). Pour des pores très longs ou larges, le modèle ne serait plus adapté notamment en moyennes et hautes fréquences. D'un autre côté, dans le cas de faible espacement entre les pores (faible épaisseur de cavité), les épaisseurs de corrections des pores sont limitées à la moitié de l'épaisseur de cavité. Ces épaisseurs de correction constituent une des principales limites du modèle masse-ressort. En effet, lorsque l'espacement des pores augmente, les prédictions du modèle s'écartent des résultats expérimentaux sur la plage de fréquence étudiée (même avec des épaisseurs de corrections du pore principal théoriques).

Perspectives : Les paramètres géométriques pourraient être optimisés pour obtenir une absorption encore plus basse en fréquence et/ou plus large bande. Pour avoir un jeu plus important de paramètres à optimiser, l'influence de la distance entre les pores sur le coefficient d'absorption pourrait par exemple être étudiée. Une étude approfondie du rayonnement acoustique à l'extrémité des pores principaux dans ces matériaux serait intéressante. L'expression d'une correction de l'épaisseur des pores en fonction de l'espacement de deux pores consécutifs serait pertinente.

7.3 Effets inertiels sur la résistivité des matériaux à compressibilité effective augmentée à réseau de résonateurs *pancakes* à des débits élevés

Synthèse : Dans ce chapitre, les effets visqueux et inertiels sur la résistivité de l'écoulement de l'air dans les matériaux à compressibilité effective augmentée à réseau de résonateurs *pancakes* sont étudiés. Deux modèles de dynamique des fluides numériques sont utilisés pour simuler l'écoulement de l'air à travers le matériau. La géométrie de la première approche reproduit le dispositif expérimental et la seconde est une géométrie simplifiée (2D-axisymétrique). Les deux modèles numériques sont en accord avec les mesures réalisées au résistivimètre sur des échantillons comprenant plusieurs plaques perforées (approche globale). Les pertes de charge globales augmentent de façon quadratique avec la vitesse des pores, conformément à la loi de Darcy-Forchheimer. Le coefficient de résistivité statique du flux d'air et le coefficient de Forchheimer sont déterminés à partir des pertes de charge globales. Une étude paramétrique est menée sur le diamètre des pores et le nombre de cellules périodiques élémentaires.

À l'aide du modèle numérique 2D-axisymétrique, les pertes de charge au niveau de chaque pore sont étudiées. Pour un nombre de Reynolds supérieur à un, les pertes de charge ne sont plus constantes, elles sont maximales pour le premier pore, puis sont diminuées pour le second pore et sont constantes pour le reste des pores. Les pertes de charge qui s'effectue dans le premier pore dominent à haut Reynolds. L'étude s'est intéressée par la suite au coefficient de Forchheimer local pour le premier pore pour différents diamètres des pores et nombre de cellules périodiques élémentaires.

Limites : Dans le cas des approches proposées en mécanique des fluides numériques, les écoulements sont considérés comme stationnaires. Les coefficients de Forchheimer et de la résistivité statique au passage de l'air sont donc déterminés pour des écoulements stationnaires. Ces valeurs sont par la suite utilisées en acoustique où les phénomènes sont ondulatoires (oscillation des particules). Les régressions pour déterminer les coefficients sont limitées à l'ordre deux avec R^2>0.85 pour les différentes géométries.

Perspectives : La réalisation d'une étude avec des écoulements pulsés pourrait permettre d'étudier la dépendance des coefficients de la résistivité au passage de l'air statique et de Forchheimer en fonction de la fréquence. Ce qui pourrait améliorer la précision des modèles acoustiques en régime linéaire et non-linéaire. Pour mieux prendre en compte les effets inertiels dans les modèles acoustiques, des régressions à l'ordre trois pour déterminer les coefficients pourraient être appliquées dans le cas de nombres de Reynolds élevés. De plus, l'impact de l'épaisseur des plaques et de la distance entre les plaques reste encore à être étudié.

7.4 Analyse des matériaux structurés périodiques en régime non-linéaire

Synthèse : Dans ce chapitre, la réponse des matériaux à compressibilité effective augmentée à réseau de résonateurs *pancakes* sous des excitations acoustiques de fortes amplitudes est étudiée. Le modèle masse-ressort présenté dans le chapitre 3 est adapté pour les niveaux d'excitation acoustique élevés. Les forts niveaux d'excitation sont pris en compte en utilisant la loi de Darcy-Forchheimer pour la résistivité de l'écoulement d'air des pores. Les coefficients de Forchheimer et de la résistivité au passage de l'air statique sont déterminés selon deux approches. La première approche est globale, les coefficients sont déterminés à partir de la résistivité définie sur l'ensemble de l'échantillon (approche globale). Les coefficients sont ensuite appliqués dans le modèle à l'ensemble des cellules. La seconde approche est locale où les coefficients sont déterminés et appliqués dans le modèle seulement pour le premier pore (voir chapitre 4). Les résultats obtenus avec l'approche locale se rapprochent davantage des résultats expérimentaux en comparaison avec l'approche globale.

De façon similaire aux plaques micro-perforées couplées avec des cavités d'air, la résistance acoustique aux résonances augmente avec le niveau d'excitation acoustique. Sous forts niveaux d'excitation acoustique, ce matériau est intéressant, car sa fréquence de résonance est peu impactée par le niveau d'excitation acoustique.

Une étude paramétrique sur les rayons des pores, le nombre de cellules périodiques élémentaires et le niveau d'excitation acoustique est proposée. Le nombre de cellules périodiques élémentaires est un paramètre moins sensible sur l'amplitude du coefficient d'absorption acoustique en comparaison à l'impact de la variation du rayon des pores. La première résonance est plus sensible aux forts niveaux d'excitation. La limite entre le régime linéaire et non-linéaire dépend du nombre de Reynolds dans le pore et de la fréquence.

Limites : En plus des limites énoncées précédemment pour le modèle masse-ressort, les prédictions du modèle divergent légèrement des mesures en moyennes et hautes fréquences. Les effets de la vibration de la structure du matériau peuvent modifier le comportement acoustique du matériau. Les phénomènes vibratoires sont constatés sur des résultats expérimentaux et ceux issus des calculs par éléments finis. Or, ces effets ne sont pas considérés dans le modèle masse-ressort.

Perspectives : Les effets qui semblent liés à la vibration des plaques pourraient être utilisés pour la réduction du bruit. Le modèle masse-ressort pourrait être adapté pour prendre en compte la vibration des plaques. Par ailleurs, le modèle masse-ressort pourrait facilement être adapté pour étudier le comportement acoustique des matériaux à compressibilité effective augmentée à réseau de résonateurs d'Helmholtz annulaires sous fortes excitations acoustiques. De plus, ces absorbeurs sont successibles d'être utilisés avec des écoulements (ex. : réacteur d'avion). Le modèle masse-ressort pourrait être adapté pour prendre en compte les écoulements rasants.

7.5 Réponse linéaire et non-linéaire de trous noirs acoustiques compacts avec pertes

Synthèse : Un modèle masse-ressort est proposé pour étudier le comportement acoustique de trous noirs acoustiques compacts sous forts niveaux d'excitation acoustiques. Le modèle est validé avec des mesures en tube d'impédance pour des niveaux d'excitations acoustiques pouvant aller jusqu'à 145 dB. À la première résonance, la résistance de surface normalisée augmente avec le niveau d'excitation acoustique tandis que les fréquences de résonance restent quasiment inchangées.

Le modèle masse-ressort est utilisé pour visualiser de façon simple les phénomènes liés à propagation du son dans les trous noirs acoustiques. Lorsque la fréquence augmente, l'onde sonore n'atteint pas l'extrémité du matériau (appelée ici zone de fréquence d'isolation). Une expression analytique est dérivée du modèle masse-ressort pour déterminer les limites de la zone de fréquence d'isolation. Cette expression est utilisée pour déterminer la limite de fréquence entre les résonances globales et locales dans un trou noir acoustique.

Trois profils décroissants des pores sont étudiés. Les profils de pores fortement décroissants au début du matériau sont plus sensibles en général aux forts niveaux d'excitation. Le modèle masse-ressort a montré que la sensibilité aux forts niveaux d'excitation est liée à la différence de phase du déplacement de masse et à la rigidité de la première cavité pour les trous noirs acoustiques à cavité fine (*pancakes*).

Limites : Les prédictions du modèle masse-ressort s'éloignent des mesures expérimentales en moyennes fréquences dans le régime linéaire. Cet écart pourrait être dû à la vibration des plaques qui n'a pas été prise en compte ou à la présence de pertes supplémentaires (liées par exemple à rugosité de surface).

Perspectives : La réalisation de trous noirs acoustiques avec des résonateurs d'Helmholtz annulaires serait intéressante. En effet, les résonateurs d'Helmholtz annulaires permettent d'atteindre une absorption à des fréquences plus basses que les résonateurs quart-d'onde annulaires. Intuitivement, l'ensemble de la zone large bande d'absorption devrait être décalée vers les basses fréquences en utilisant des résonateurs d'Helmholtz annulaires.

APPENDIX I

IMPEDANCE MATRIX TO TRANSFER MATRIX

The passage of the acoustic impedance matrix to the transfer matrix is here demonstrated. The acoustic impedance matrix is defined as $\mathbf{Z}\boldsymbol{u} = \mathbf{p}$, equation (3.23) ($N$+1 by N+1 matrix). Thereafter, the matrix coefficients of $\mathbf{Z}$ are noted z.

The Cramer's rule gives

$$u_k = \frac{\det(\mathbf{Z}_k)}{\det(\mathbf{Z})}, \tag{A I-1}$$

where $\mathbf{Z}_k$ is a square matrix formed by replacing the kth column of $\mathbf{Z}$ by the external pressure acoustic vector $\boldsymbol{p} = (P_1 \;\; 0 \;\; \ldots \;\; 0 \;\; P_{N+1})^t$. The input and output acoustic velocities can be deduced with

$$u_1 = \frac{\det(\mathbf{Z}_1)}{\det(\mathbf{Z})}, \tag{A I-2a}$$

$$u_{N+1} = \frac{\det(\mathbf{Z}_{N+1})}{\det(\mathbf{Z})}, \tag{A I-2b}$$

where

$$\det(\mathbf{Z}_1) = \begin{vmatrix} P_1 & z_{12} & 0 & \cdots & 0 \\ 0 & z_{22} & & & \vdots \\ \vdots & & \ddots & & 0 \\ 0 & & & \ddots & z_{N,N+1} \\ P_{N+1} & 0 & & z_{N+1,N} & z_{N+1,N+1} \end{vmatrix} = \begin{array}{c} P_1 \det\left(\mathbf{Z}_{2:N+1,2:N+1}\right) \\ -(-1)^{N+2} P_{N+1} \det\left(\mathbf{Z}_{1:N,2:N+1}\right) \end{array} \tag{A I-3}$$

and

$$\det\left(\mathbf{Z}_{N+1}\right) = \begin{vmatrix} z_{11} & z_{12} & & 0 & P_1 \\ z_{21} & \ddots & & & 0 \\ 0 & & \ddots & & \vdots \\ \vdots & & & z_{N,N} & 0 \\ 0 & \cdots & 0 & z_{N+1,N} & P_{N+1} \end{vmatrix} = \begin{matrix} (-1)^{N+2} P_1 \det\left(\mathbf{Z}_{2:N+1,1:N}\right) \\ -P_{N+1} \det\left(\mathbf{Z}_{1:N,1:N}\right) \end{matrix}. \qquad \text{(A I-4)}$$

Combining and rearranging equation (A I-2b) and equation (A I-4) leads to

$$P_1 = \frac{P_{N+1} \det\left(\mathbf{Z}_{1:N,1:N}\right) + u_{N+1} \det\left(\mathbf{Z}\right)}{(-1)^{N+2} \det\left(\mathbf{Z}_{2:N+1,1:N}\right)}. \qquad \text{(A I-5)}$$

Combining equation (A I-2a) and equation (A I-3) leads to

$$u_1 = \frac{P_1 \det\left(\mathbf{Z}_{2:N+1,2:N+1}\right) - (-1)^{N+2} P_{N+1} \det\left(\mathbf{Z}_{1:N,2:N+1}\right)}{\det\left(\mathbf{Z}\right)}. \qquad \text{(A I-6)}$$

Replacing P_1 by its expression given by equation (A I-5), u_1 can be rewritten

$$u_1 = \begin{matrix} -P_{N+1} \frac{1}{\det(\mathbf{Z})} \left((-1)^{N+2} \det\left(\mathbf{Z}_{1:N,2:N+1}\right) - \frac{\det\left(\mathbf{Z}_{1:N,1:N}\right) \det\left(\mathbf{Z}_{2:N+1,2:N+1}\right)}{(-1)^{N+2} \det\left(\mathbf{Z}_{2:N+1,1:N}\right)} \right) \\ +u_{N+1} \frac{\det\left(\mathbf{Z}_{2:N+1,2:N+1}\right)}{(-1)^{N+2} \det\left(\mathbf{Z}_{2:N+1,1:N}\right)} \end{matrix}. \qquad \text{(A I-7)}$$

Finally, the transfer matrix is obtained from equation (A I-5) and equation (A I-7)

$$\begin{Bmatrix} P_1 \\ u_1 \end{Bmatrix} = (-1)^{N+1} \begin{bmatrix} \frac{\det\left(\mathbf{Z}_{1:N,1:N}\right)}{\det\left(\mathbf{Z}_{2:N+1,1:N}\right)} & \frac{\det(\mathbf{Z})}{\det\left(\mathbf{Z}_{2:N+1,1:N}\right)} \\ -\frac{\det\left(\mathbf{Z}_{1:N,2:N+1}\right)}{\det(\mathbf{Z})} + \frac{\det\left(\mathbf{Z}_{1:N,1:N}\right) \det\left(\mathbf{Z}_{2:N+1,2:N+1}\right)}{\det(\mathbf{Z}) \det\left(\mathbf{Z}_{2:N+1,1:N}\right)} & \frac{\det\left(\mathbf{Z}_{2:N+1,2:N+1}\right)}{\det\left(\mathbf{Z}_{2:N+1,1:N}\right)} \end{bmatrix} \begin{Bmatrix} P_{N+1} \\ u_{N+1} \end{Bmatrix}. \qquad \text{(A I-8)}$$

APPENDIX II

ITERATIVE PROCEDURE (CHAPTER 5)

Algorithme-A II-1 Pseudo-code of the iteration procedure for solving the nonlinear mass-spring model with an imposed total pressure

Input : p_t is defined
$\boldsymbol{f} \leftarrow \{p_t A_p,\ 0,\ \ldots\ 0\}^{\mathrm{T}}$

for $frequency \leftarrow 1$ ***to*** 4400 ***step*** 2 **do**
  $q \leftarrow 0$ ▹ iteration number
  $\mathbf{v}_{rms}^{q} \leftarrow 0$
  while any$\left(\left|\mathbf{v}_{rms}^{q} - \mathbf{v}_{rms}^{q-1}\right| > 10^{-5}\right)$ **do**
    $\dot{\boldsymbol{x}}^{q} \leftarrow j\omega\left(\mathbf{M}(\dot{\boldsymbol{x}}^{q-1}) + \mathbf{K}\right)^{-1}\boldsymbol{f}$
    $\mathbf{v}_{rms} \leftarrow \frac{1}{\sqrt{2}}\left\{|\dot{x}_1^{q}|,\ \ldots\ |\dot{x}_N^{q}|\right\}^{\mathrm{T}}$
    $q \leftarrow q + 1$
  end while
  $Z_{nS} \leftarrow f_1/(A_p \phi_S \dot{x}_1^{q} \rho_0 c_0)$
  $\alpha \leftarrow 1 - \left|(Z_{nS} - 1)/(Z_{nS} + 1)\right|^2$
end for

APPENDIX III

INTERACTION FLUID-STRUCTURE

To investigate the vibration effects, a simulation using the finite element method (FEM) is performed. The geometry is a virtual three-dimensional impedance tube. COMSOL Multiphysics software is employed. Two finite element simulations are performed. The first considers a rigid frame for the whole material (this complies with the rigid-frame assumption of the developed mass-spring model). The second considers the frame to be elastic. While the first simulation only solves the acoustic problem, the second simultaneously solves the acoustic and elastic problems (fluid-structure coupling). In reality, the sample is made up of several PUCs. The consecutive PUCs touch each other at their chamfer, where petroleum jelly is applied. In this case, in first approximation, one can consider that the acoustic excitation is not sufficient to vibrate the entire structure. Consequently, only the vibrations of the first plate will be considered in the second simulation. On the edge of the plate, simply supported boundary condition is imposed. The elastic properties of the plate are those of our experimental material made in aluminum T06. Thermoviscous acoustic losses in the air saturating the material are considered using the Johnson-Champoux-Allard (JCA) model (similar as the mass-spring model).

After a convergence study, the results of the experimental method and the FEM simulations are shown in figure III-1. The three approaches are in good agreement for frequencies below 3000 Hz. At higher frequencies, the rigid-frame FEM result is similar to the mass-spring model prediction. However, it deviates from the measurements. Considering the vibration of the first plate, the FEM result now shows additional absorption peaks as for the experimental results. Despite the assumptions made for the elastic finite element model, these additional absorption peaks nearly coincide with the experimental measurement around 3500 Hz. These simulations confirm that the absorption peaks at frequencies close to 3500 Hz are due to the vibration of the tested materials.

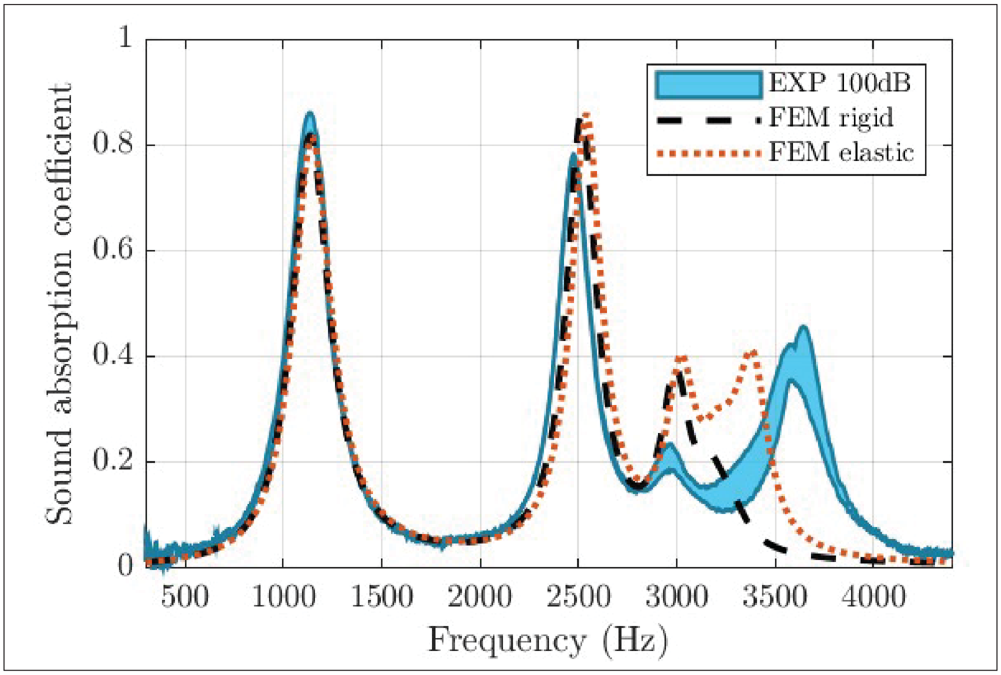

Figure III-1 Normal incidence sound absorption coefficient of CS-SPP with $r_p = 4$ mm and $N = 8$. Comparison between experimental results and FEM results with and without first-plate vibrations. The envelope of the experimental results represents the data dispersion over 3 measurements

APPENDIX IV

LOCAL STATIC AIRFLOW RESISTIVITY AND LOCAL FORCHHEIMER COEFFICIENTS

Table IV-1 Static airflow resistivity coefficient $\sigma_{0,i}$ and coefficient $F_{0,i}$ at the different pore positions for the three decreasing profile studied ϵ

ϵ	perforation index	$\sigma_{0,i}$	$F_{0,i}$
0.5	1	2.80 (R^2 = 0.9993)	7.112e+03 (R^2 = 0.9995)
0.5	2	22.17 (R^2 = 1.0000)	1.228e+04 (R^2 = 0.9994)
0.5	3	40.62 (R^2 = 1.0000)	1.650e+04 (R^2 = 0.9989)
0.5	4	63.49 (R^2 = 1.0000)	2.272e+04 (R^2 = 0.9990)
0.5	5	94.82 (R^2 = 1.0000)	3.153e+04 (R^2 = 0.9991)
0.5	6	137.45 (R^2 = 1.0000)	4.400e+04 (R^2 = 0.9992)
0.5	7	197.59 (R^2 = 1.0000)	6.192e+04 (R^2 = 0.9992)
0.5	8	282.58 (R^2 = 1.0000)	8.789e+04 (R^2 = 0.9992)
0.5	9	404.03 (R^2 = 1.0000)	1.265e+05 (R^2 = 0.9993)
0.5	10	583.81 (R^2 = 1.0000)	1.851e+05 (R^2 = 0.9992)
0.5	11	854.76 (R^2 = 1.0000)	2.764e+05 (R^2 = 0.9992)
0.5	12	1272.16 (R^2 = 1.0000)	4.182e+05 (R^2 = 0.9991)
0.5	13	1927.91 (R^2 = 1.0000)	6.521e+05 (R^2 = 0.9990)
0.5	14	3018.86 (R^2 = 1.0000)	1.037e+06 (R^2 = 0.9989)
0.5	15	5157.65 (R^2 = 1.0000)	1.408e+06 (R^2 = 0.9973)
1.0	1	10.85 (R^2 = 1.0000)	3.979e+03 (R^2 = 0.9999)
1.0	2	13.23 (R^2 = 1.0000)	3.585e+03 (R^2 = 0.9978)
1.0	3	16.64 (R^2 = 1.0000)	4.585e+03 (R^2 = 0.9985)
1.0	4	21.50 (R^2 = 1.0000)	6.244e+03 (R^2 = 0.9989)

ϵ	perforation index	$\sigma_{0,i}$	$F_{0,i}$
1.0	5	28.68 (R^2 = 1.0000)	8.731e+03 (R^2 = 0.9990)
1.0	6	38.57 (R^2 = 1.0000)	1.239e+04 (R^2 = 0.9991)
1.0	7	53.44 (R^2 = 1.0000)	1.801e+04 (R^2 = 0.9992)
1.0	8	75.42 (R^2 = 1.0000)	2.686e+04 (R^2 = 0.9992)
1.0	9	111.85 (R^2 = 1.0000)	4.186e+04 (R^2 = 0.9993)
1.0	10	171.37 (R^2 = 1.0000)	6.805e+04 (R^2 = 0.9993)
1.0	11	277.20 (R^2 = 1.0000)	1.166e+05 (R^2 = 0.9994)
1.0	12	475.95 (R^2 = 1.0000)	2.148e+05 (R^2 = 0.9995)
1.0	13	891.30 (R^2 = 1.0000)	4.316e+05 (R^2 = 0.9996)
1.0	14	1874.69 (R^2 = 1.0000)	9.525e+05 (R^2 = 0.9996)
1.0	15	5210.97 (R^2 = 1.0000)	1.626e+06 (R^2 = 0.9981)
2.0	1	14.67 (R^2 = 1.0000)	3.375e+03 (R^2 = 0.9999)
2.0	2	12.35 (R^2 = 1.0000)	1.145e+03 (R^2 = 0.9954)
2.0	3	12.41 (R^2 = 1.0000)	9.149e+02 (R^2 = 0.9904)
2.0	4	13.19 (R^2 = 1.0000)	1.275e+03 (R^2 = 0.9946)
2.0	5	14.44 (R^2 = 1.0000)	1.999e+03 (R^2 = 0.9976)
2.0	6	16.38 (R^2 = 1.0000)	3.102e+03 (R^2 = 0.9987)
2.0	7	19.29 (R^2 = 1.0000)	4.758e+03 (R^2 = 0.9991)
2.0	8	23.75 (R^2 = 1.0000)	7.393e+03 (R^2 = 0.9992)
2.0	9	31.08 (R^2 = 1.0000)	1.189e+04 (R^2 = 0.9992)
2.0	10	43.53 (R^2 = 1.0000)	2.037e+04 (R^2 = 0.9993)
2.0	11	67.27 (R^2 = 0.9999)	3.821e+04 (R^2 = 0.9994)
2.0	12	119.09 (R^2 = 0.9999)	8.212e+04 (R^2 = 0.9996)
2.0	13	256.45 (R^2 = 0.9998)	2.164e+05 (R^2 = 0.9999)

ϵ	perforation index	$\sigma_{0,i}$	$F_{0,i}$
2.0	14	767.97 (R^2 = 0.9997)	7.777e+05 (R^2 = 0.9999)
2.0	15	5182.93 (R^2 = 1.0000)	2.280e+06 (R^2 = 0.9981)

APPENDIX V

ITERATIVE PROCEDURE (CHAPTER 6)

Algorithme-A V-1 Pseudo-code of the iteration procedure for the mass-spring model to resolve imposed total pressure

```
Input : $p_t$ is defined
$\boldsymbol{f} \leftarrow \{p_t A_{p,1},\ 0,\ \ldots\ 0\}^{\mathrm{T}}$
for $frequency \leftarrow 1$ to 4400 step 2 do
    $q \leftarrow 0$                                        ▹ iteration number
    $\dot{\boldsymbol{x}}^q \leftarrow 0$
    while any$\left(\left|\dot{\boldsymbol{x}}^q - \dot{\boldsymbol{x}}^{q-1}\right| > 10^{-5}\right)$ do
        $\dot{\boldsymbol{x}}^q \leftarrow j\omega \left(\mathbf{M}(\dot{\boldsymbol{x}}^{q-1}) + \mathbf{K}\right)^{-1} \boldsymbol{f}$
        $q \leftarrow q + 1$
    end while
    $Z_{nS} \leftarrow f_1/(A_{p,1}\phi_S \dot{x}_1^q \rho_0 c_0)$
    $\alpha \leftarrow 1 - \left|(Z_{nS} - 1)/(Z_{nS} + 1)\right|^2$
end for
```

APPENDIX VI

TRANSMISSION BETWEEN TWO CONSECUTIVE MASSES

Let us just consider two consecutive masses, the second Newton's law the equation of motion is

$$-\omega^2 M_{eq,i} + K_{i,i-1}x_{i-1} + K_{i,i}x_i = 0, \tag{A VI-1}$$

where $M_{eq,i}$ is defined by equation (6.3) and $K_{a,b}$ is the term in column a and raw b of the stiffness matrix, equation (6.12).

The transmission of the wave between two consecutive masses (isolated of the system) is defined as

$$t = \left|\frac{x_i}{x_{i-1}}\right| = \left|\frac{K_{i,i-1}}{K_{i,i} - \omega^2 M_{eq,i}}\right|. \tag{A VI-2}$$

When the frequency is equal to the PPUC resonance, $\omega_{PPUC,i}$ =Re $\left(\sqrt{\frac{K_{i,i}}{M_{eq,i}}}\right)$, the denominator is equal to zero. A maximum of transmission and a peak of displacement occur at this frequency. The beginning of the isolation area corresponds to transmission coefficient smaller than one. From equation (A VI-2), the isolation area starts at $\omega_{isolation,i}$ =Re $\left(\sqrt{\frac{K_{i,i} \pm K_{i,i-1}}{M_{eq,i}}}\right)$. In equation (6.12) $K_{i,i-1}$ is negative, then $\omega_{isolation,i}$ =Re $\left(\sqrt{\frac{K_{i,i} - K_{i,i-1}}{M_{eq,i}}}\right)$.

ANNEXE VII

HIGH SOUND PRESSURE LEVEL SOUND ABSORPTION IN ACOUSTIC RESONANT METAMATERIALS : ADAPTING A MASS-SPRING MODEL FOR NONLINEAR EFFECT

Maël Lopez[1] , Tenon Charly Kone[2] , Alla Eddine Benchikh Le Hocine[3] , Thomas Dupont[1] , Raymond Panneton[3]

[1] Département de Génie Mécanique, École de Technologie Supérieure, 1100 Notre-Dame Ouest, Montréal, Québec, H3C 1K3, Canada
[2] National Research Council Canada, Flight Research Laboratory 1200 Montreal Road, Ottawa, Ontario, K1A 0R6, Canada
[3] CRASH-UdeS, Department of Mechanical Engineering, Université de Sherbrooke, 2500 boul. de l'Université, Sherbrooke, Québec, J1K 2R1, Canada

Article de conférence « 53rd International Congress & Exposition on Noise Control Engineering ».

1. Abstract

In aerospace, conventional materials as micro-perforated panels backed by cavities are used to absorb sound at high sound pressure levels. These solutions are not optimal at low frequencies compared to resonant acoustic metamaterials, which present an acoustic absorption peak with a wavelength-to-thickness ratio greater than conventional materials, i.e., a ratio $\gg 5$. Acoustic resonant metamaterials are mainly studied at low sound pressure levels (<100 dB). However, they are sensitive to increasing the amplitude of acoustic excitation. The studied metamaterial is composed of a compact array of thin single-perforation panels spaced by thin cylindrical air cavities. In a previous study, a mass-spring model was developed for low sound pressure levels. The perforations are modeled by equivalent masses, whereas cavities by equivalent springs. In the perforations, high values of the acoustic velocity lead to an increase in the acoustic resistance of the material. This effect is considered by the Forchheimer parameter in the mass-spring model. To determine this parameter and to study how it is impacted by the metamaterial geometry, the computational fluid dynamic method is used. The mass-spring model is adapted with a

nonlinear term. The adapted model agrees well with simulations by finite element method at sound pressure levels up to 140 dB.

2. Introduction

In many applications, reducing low frequency noise with a compact solution is a challenge. Conventional sound absorbing material, e.g., porous or Micro-Perforated Panels (MPPs), require thicknesses close to the quarter of the wavelength size to be treated. They are not optimal at low frequencies compared to resonant acoustic metamaterials. Among them periodic arrangement of lateral resonators, dead-end (DE), spaced by air pores (Leclaire *et al.*, 2015; Groby *et al.*, 2015a, 2016; Jiménez *et al.*, 2017c; Dupont *et al.*, 2018; Kone *et al.*, 2021b; Brooke *et al.*, 2020) allow achieving low frequency sound absorption, wavelength-to-thickness smaller than 40. But they are mainly designed for low to medium sound pressure levels. In industrial application as aerospace, sound pressure levels can be high.For MPPs nonlinear effect appear with high sound pressure levels: formation of jet and vortex (Cummings & Eversman, 1983; Cummings, 1984). The acoustic resistance tends to a quadratic law, function of the acoustic velocity (Ingard & Ising, 1967). About periodic DE metamaterial, only one study is interested in the impact of sound pressure levels (Brooke *et al.*, 2020). Brooke *et al.* (2020) have proposed a model to consider high sound pressure levels on a periodic material with DE air cavities spaced by single-perforations. They consider extra losses induced by high sound pressure levels using a Forchheimer's law for the resistivity. To determine the coefficients of the Forchheimer's law, the authors measured the airflow resistivity on the whole material at different flow velocities.

In the present study, we aim to further investigate and model the losses induced by sound pressure levels to predict the sound absorption coefficient. For this purpose an analytical and a numerical models are proposed. The analytical model is an adaptation of a previous mass-spring analogy developed for low-to-medium sound pressure levels to high sound pressure levels. The losses induced by the high sound pressure levels are considered by the Forchheimer law for the resistivity. The coefficients of the Forchheimer law for the first perforation are evaluated by a

Computational Fluid Dynamics (CFD) approach. The numerical model is a virtual impedance tube simulated by a transient Finite Element Method (FEM) .

This proceeding is organized as follows. The studied metamaterial is described in appendix 3. In appendix 4, the adapted mass-spring model for high sound pressure levels is presented with the CFD approach to evaluate the Forchheimer parameter. Then, the impedance tube simulated by the FEM is exposed. In appendix 5, the pressure drops of the proposed metamaterials are presented. The results of the adapted mass-spring model are compared with FEM. Finally, the velocity field at different sound pressure level is deduced from the FEM.

3. Material

The studied material is composed of a compact arrangement of a periodic unit cell (PUC). The PUC is composed of a cylindrical air perforation backed by a thin air cavity. figures VII-1(a) and VII-1(c) show a sectional view and a schema of the material sample. The geometrical parameters of the sample are for the pore radius $r = 2$ mm, the pore thicknesses $h = 1$ mm, the cavity radius $R = 21$ mm, the cavity thicknesses $H = 1$ mm and the number of pores and cavities $N = 7$. The external radius of the sample is $R_s = 22.22$ mm.

4. Methods

4.1 Mass-Spring

The acoustic model presented adapts from the mass-spring model (MS) proposed in chapter 3 to account for high sound pressure levels. In analogy, cylindrical perforations are modelled by equivalent masses while the thin air cavities by equivalent springs. To account for thermal and viscous losses within this framework, the Johnson-Champoux-Allard (JCA) effective fluid approaches (Johnson *et al.*, 1987) is employed. This model allows the calculation of an effective density of a mass, denoted as ρ_i specific to a cylindrical pore and dependent on parameters given in table VII-1. The high sound pressure levels are considered in the resistivity according

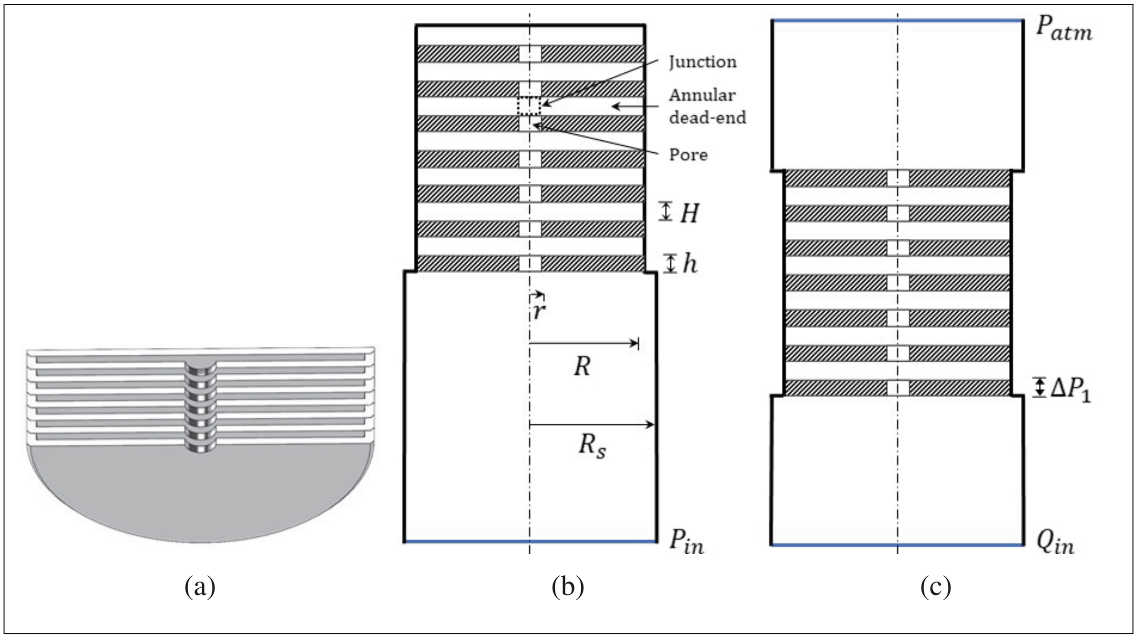

Figure VII-1 ((a)) sectional view of the sample. Asymmetric schema of ((b)) the virtual acoustic impedance tube and ((c)) the airflow resistivity meter.

to Forchheimer's law. The airflow resistivity vector of the equivalent masses are defined as

$$\boldsymbol{\sigma} = \boldsymbol{\sigma}_0 + \boldsymbol{F}\frac{\dot{\boldsymbol{x}}}{\sqrt{2}}, \tag{A VII-1}$$

where $\dot{\boldsymbol{x}}$ are the velocities of the equivalent masses. $\boldsymbol{\sigma_0}$ and $\boldsymbol{F}$ are the quasi-static airflow resistivity coefficients and Forchheimer parameters of the equivalent masses. They are numerically determined using a CFD approach, see appendix 4.2. The equivalent mass matrix of the perforations is

$$\mathbf{M} = \begin{bmatrix} \rho_1(\sigma_1)A_p h'' & & 0 \\ & \ddots & \\ 0 & & \rho_N(\sigma_N)A_p h' \end{bmatrix}, \tag{A VII-2}$$

where $A_p = \pi r^2$ is the cross-sectional area of the perforation. End corrections are used to consider radiation of the pores. The first pore radiates into the exterior medium (exterior side) and a cavity (inner side). The other pores radiate on either side in cavities. The exterior radiation is considered with end correction calculated by Karal's method δ_{Karal} (Karal, 1953). Due to the thin thicknesses of the metamaterial cavities ($H = 1mm$), an inner radiation is limited by the next pore inner radiation. Intuitively, the inner end correction is equal to half of the cavity thickness, see chapter 3. $h'' = h + \delta_{Karal} + H/2$ and $h' = H/2 + h + H/2$ are the correction thicknesses of the pores.

Table VII-1 Johnson-Champoux-Allard effective fluid parameters

JCA parameters	**circular pores**	**slits**
Porosity (1)	1	1
Tortuosity (1)	1	1
Viscous characteristic length (m)	r	H
Thermal characteristic length (m)	r	H
Airflow resistivity($Pa.s/m^2$)	CFD approach (see appendix 4.2)	$\frac{12\eta}{H^2}$

The thin cavities are modelled by equivalent springs. A cavity is composed of an annular dead-end (DE) resonator and a junction, see figure VII-1(c). Due to the thin thickness of the cavity $H << R$ and $H << \lambda$, only radial propagation is considered inside the annular DE resonator, its surface impedance, Z_S, DE, is defined by equation Eq.(15) in Dickey & Selamet (1996). Thermal and viscous losses inside the cavity are considered using JCA effective fluid approach with parameters for a slit pore given in table VII-1.

The equivalent stiffness matrix is (equations (3.20) and (3.21))

$$\mathbf{K} = \frac{A_p^2}{\frac{V_j}{\rho_0 c_0^2} + \frac{A_{de}}{j\omega Z_{S,DE}}} \begin{bmatrix} 1 & -1 & & 0 \\ -1 & 2 & & \\ & & \ddots & -1 \\ 0 & & -1 & 2 \end{bmatrix}, \tag{A VII-3}$$

where $V_j = A_p H$ is the volume of the junction between the perforation and the DE resonator, $A_{de} = 2\pi r H$ is the input cross-section area of the DE cavity, rho_0 is the air density and c_0 is the air celerity.

The equation of motion is

$$(-\omega^2 \mathbf{M} + \mathbf{K})\, \boldsymbol{x} = \boldsymbol{f} \tag{A VII-4}$$

where $\boldsymbol{f} = (p_1 A_p \;\; 0 \ldots 0)^{\mathrm{T}}$ is the vector of the external forces and $\boldsymbol{x} = (x_1 \;\ldots\; x_N)^{\mathrm{T}}$ is the vector of the mass displacements. The superscript T refers to the transposition of the vectors.

By solving equation (A VII-4), the normalized material surface impedance of the rigidly backed sample is

$$Z_{nS} = \frac{f_1}{\rho_0 c_0 A_p \phi_S \dot{x}_1}, \tag{A VII-5}$$

where $\phi_S = A_p/(\pi R_s^2)$ is the surface porosity of the sample.

The reflection coefficient is given by:

$$R = \frac{Z_{nS} - 1}{Z_{nS} + 1}, \tag{A VII-6}$$

and the normal incidence sound absorption coefficient of the rigidly backed sample is

$$\alpha = 1 - |R|^2. \tag{A VII-7}$$

The sound absorption depends on the velocities of the equivalent masses. An iterative procedure is used to determine the sound absorption for incident wave pressure. The iteration procedure is presented in figure VII-2.

4.2 Computational fluid dynamics approach

The quasi-static airflow resistivity and the Forchheimer parameter of the material are determined using a computational fluid dynamics (CFD) methodology, based on the commercial software COMSOL Multiphysics 6.1. The analysis is conducted within a virtual axisymmetric resistivity-meter, illustrated in figure VII-1(b). To simulate conditions accurately, a fully developed flow rate,Q_{in} is imposed as the upstream limit condition at the input of the virtual resistivity-meter. Atmospheric pressure P_{atm} is applied as the downstream boundary condition at the exit. To

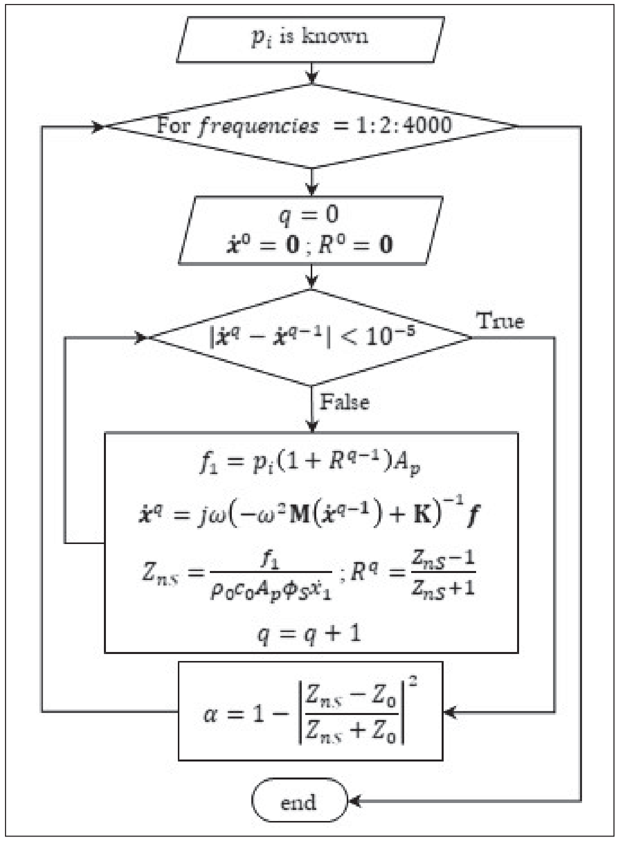

Figure VII-2 Flow chart of the iteration procedure

ensure a fully developed flow both upstream and downstream of the material sample, the distance from the upstream boundary to the material's input, and similarly from the material's exit to the downstream boundary, is set to 2.5 times the diameter of the sample. This configuration allows for the establishment of a controlled flow environment necessary for accurately assessing the material's airflow resistivity and Forchheimer parameter, essential metrics in understanding the flow characteristics through porous or perforated materials. A laminar approach is used to model the flow dynamics in the computational domain.

The pressure drops ΔP_i across various perforations are assessed using a CFD approach at different perforation Reynolds numbers, Re_p. For conditions where $Re_p < 1$, the quasi-static airflow resistivity coefficients are determined through linear regression based on Darcy's law, evaluated at different flow rates Q_{in}. Once the quasi-static airflow resistivity coefficients are established, the Forchheimer parameters are derived from quadratic regressions based on Forchheimer's law. These regressions are applied to the perforation pressure drops calculated at various Q_{in} for Reynolds numbers ranging from 1 to 1300. This approach allows to investigate the sensitivity of the material's airflow resistance to flow conditions and perforation characteristics.

4.3 Numerical validation: high-level virtual impedance tube method

An acoustic finite element (FE) method is used to evaluate the normal sound absorption coefficient of the material. Transient approaches of COMSOL 6.1 software are used to consider the nonlinear losses in the material induced by the increase in incident pressure levels. The geometry is axisymmetric and shown in figure VII-1(c).

The transient thermoviscous acoustic physic with nonlinear thermoviscous acoustics contributions of COMSOL software is used to consider the nonlinear losses inside the material (COMSOL, 2023). A linear discretization (P1-P1-P1) is employed with Galerkin least-squares stabilization. Transient pressure acoustic physic is used for the virtual impedance tube. For both physics, the maximum frequency to resolve for the solver is six times the studied frequency. At the input of impedance tube a plane wave radiation p_in is imposed.

The mesh is refined in the perforations region, where nonlinear losses are predominant. This fine mesh resolution is crucial for accurately capturing the complex interactions and losses within these critical regions.

A parametric study is added to modify the incident pressure amplitude $|p_{in}|$ and the frequency f_0. The time for the solver is set from 0 to $T_{end} = 15T_0$ ($T_0 = 1/f_0$) with a step of $T_0/30$.

The reflection coefficient is evaluated at the tube impedance input from the following equation

$$R = \frac{\int_{T_s}^{T_{end}} (p_t(t) - p_{in}(t))^2 \, dt}{\int_{T_s}^{T_s+XT_0} (p_{in}(t))^2 \, dt} \tag{A VII-8}$$

where p_t is evaluated total pressure, p_{in} is evaluated incident pressure. In the actual study, the amplitude of the total pressure at the input of the impedance tube stabilizes after 5 round trips. T_s is the start time of amplitude stabilization.

5. Results

5.1 Airflow results

The pressure drops determined from the CFD approach for each perforation (each plate) are shown in figure VII-3. figure VII-3 shows the pressure drops at the perforations for flow rates in respect to $Re_p < 1$ figure VII-3(a) and figure VII-3(b) in respect to $Re_p > 1$. At $Re_p < 1$, the pressure drop profile is almost constant with the flow rate (e.g. $Q_in = 4.56310^{-8}(m^3/s)$), see figure VII-3(a). The pressure drops grow linearly with the velocity, and so the flow rate, in accordance to Darcy's law. The quasi-static airflow resistivity coefficients of each perforations are determined using a linear regression on the perforations pressure drops. The values of the quasi-static airflow resistivity coefficients are reported in table VII-2.

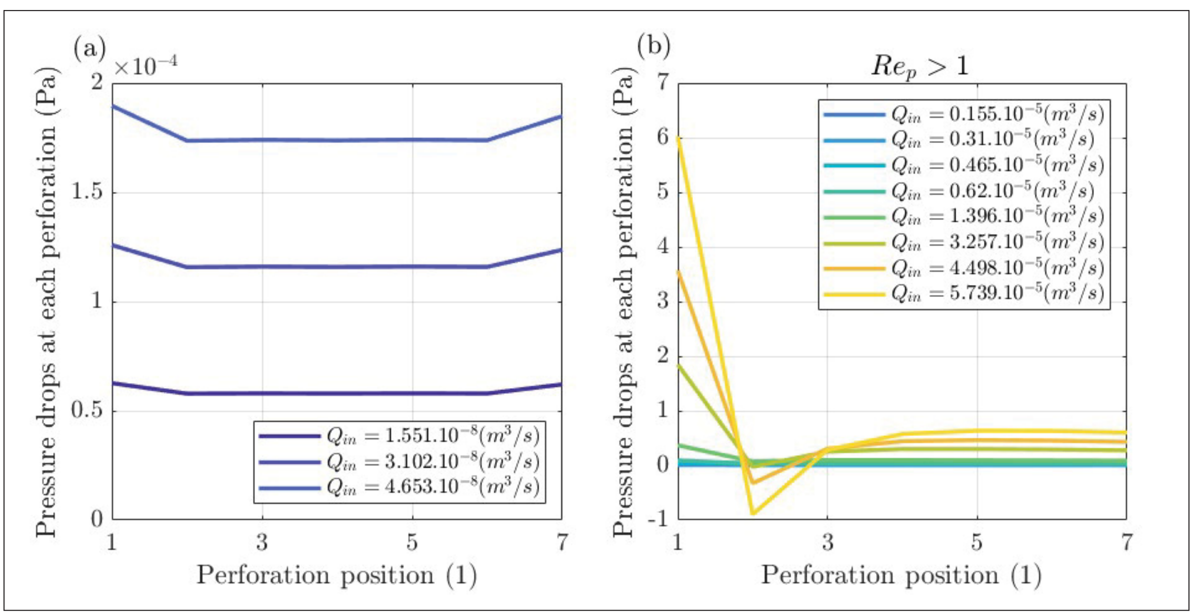

Figure VII-3 Pressure drops at different perforations for different input flow rate Q_{in} in respect of perforation Reynolds number ((a)) smaller than 1 and ((b)) higher than 1.

Table VII-2 Quasi-static airflow resistivity coefficients at the different perforations and first perforation Forchheimer parameter of the studied metamaterial

perforation index i	**1**	**2**	**3**	**4**	**5**	**6**	**7**
$\boldsymbol{\sigma_{0,i}}$ $(Pa/s.m^2)$	50	45	47	46	47	47	46
$\boldsymbol{F_i}$ $(Pa.s^2/m^{-3})$	253	-	-	-	-	-	-

At $Re_p > 1$, the pressure drop profile is no more constant. The first plate pressure drop is the highest. A dip is observed at the second plate for high flow rates. For the last perforations, the profile is nearly constant. The pressure drop of the first plate dominates over the other plates. At this stage, it seems that a strong nonlinear airflow behavior of the first perforation. Resulting in acoustic nonlinear increase of the viscous losses of the first plate and less contribution at other perforations. Inline with this observation, only the Forchheimer parameter of the first plate is determined and reported in table VII-2. As a result, acoustic nonlinearities induced by high sound pressure levels are only considered in the first perforation. equation (A VII-1) is simplified and expressed as

$$\boldsymbol{\sigma} = \left(\sigma_{0,1} + F_1 \frac{\dot{x}_1}{\sqrt{2}},\ \sigma_{0,2},\ \dots\ \sigma_{0,N}\right)^{\mathrm{T}}. \qquad \text{(A VII-9)}$$

5.2 Acoustic results

The comparison of the normal sound absorption coefficient predicts by the acoustic FE approach, and the mass-spring model are shown in figure VII-4. The results are in good agreement for the two approaches for imposed incident sound pressure levels of 100, 120, and 140 dB. At L_{pi} = 100 dB the response is linear, several peaks of sound absorption coefficient are observed. The absorption peaks are associated to metamaterial resonances (Dupont *et al.*, 2018; Brooke *et al.*, 2020). The number of resonances is determined by the number of PUCs. The first resonances are spaced in frequency and the last resonances gather as the frequency increases. Around 2500 Hz, the absorption coefficient drops to zero which is associated to a stopband appearance, see section 3.7.1. No sound propagates inside the material from this frequency, all incoming sound is reflected. For this sample, with increasing sound pressure level, the sound absorption decreases at the resonances, especially for the first metamaterial resonance. The FE results show that the resonant frequency is not impacted by the increase in sound pressure levels. This contrasts with MPPs backed by a cavity, whose resonant frequency increases with sound pressure levels.

When frequency increases, the sound absorption predicted by the mass-spring model deviate a little from the FE approach prediction. The authors think that this difference is due to the fact that the Forchheimer parameter is determined for a steady fluid flow which far from the sinusoidal time variation of the acoustic waves. In this way, it might be more realistic to determine a Forchheimer coefficient with pulsed flow. Further research on this point would be of interest.

One significant advantage of the mass-spring model is its computational efficiency. The model can solve for 2000 frequencies at a given sound pressure level in less than one second. In contrast, the CFD approach requires approximately 4 minutes on a high-performance desktop computer. Meanwhile, the acoustic Finite Element (FE) approach needs around 17 hours to compute 46 frequencies across three different sound pressure levels. This stark contrast in computational time highlights the mass-spring model's suitability for applications requiring rapid assessments.

The FE approach allows for visualizing the acoustic pressure or velocity fields. The acoustic velocity field at the first resonances is shown in figure VII-5 at L_{pi} = 100, 120, and 140 dB. In linear regime the acoustic velocity is maximal at the input of the material, see figure VII-5(a). The acoustic velocity profile of the first resonance through the perforations follows a quarter wavelength profile (see figure 3.6 and the work of Leclaire *et al.* (2015) and Dupont *et al.* (2018). The acoustic velocity is especially high for the first plate. The acoustic velocity grows with increasing sound pressure level figure VII-5 which is similar to MPP (Ingard & Ising, 1967). The quarter wavelength profile is conserved for the three levels. At L_{pi} = 120 dB, it is observed that the boundary layer within the first perforation begins to separate (figure VII-5(b)). Such separation within the perforation can significantly affect the acoustic response of the system, leading to potential nonlinear effects. At a sound pressure level of 140dB, vortex is observed

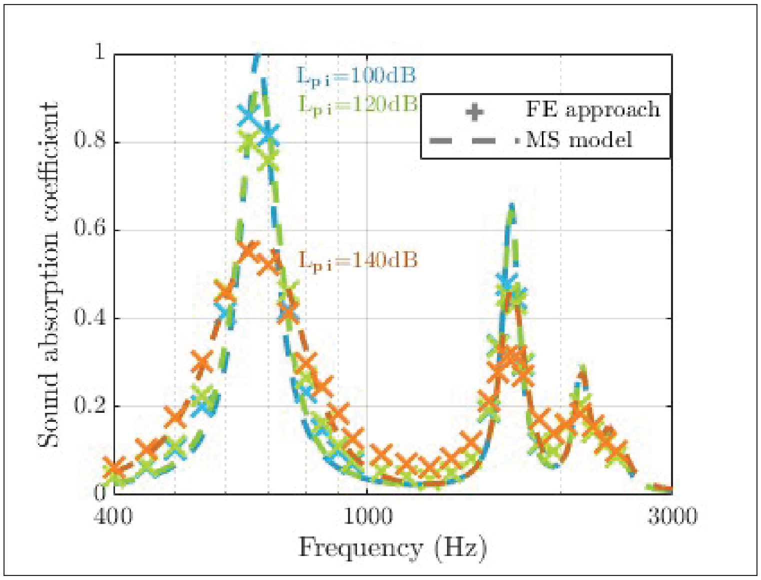

Figure VII-4 Normal incidence sound absorption for different input sound pressure levels.

in the cavities and at the input of the material, as shown in figure VII-5(c). This phenomenon occurs due to the high energy and intensity of the sound waves at such a level. At L_{pi} = 120 and 140 dB, the separation of the boundary layer and the vortex formation lead to an increase of the resistance similarly to MPPs (Ingard & Ising, 1967). They are the highest for the first perforation. These observations support the decision to use a Forchheimer approach that takes into account only the first perforation. At 100 dB, the sound absorption coefficient was maximal, the increase in resistance with increasing sound pressure levels tends to decrease the absorption coefficient as shown in figure VII-4.

6. Conclusion

To consider nonlinearities induced by high sound pressure levels on an acoustic metamaterial response a mass-spring model has been adapted. These nonlinearities are modeled using Forchheimer's law to adjust the resistivity. The pressure drop profile from the computational fluid dynamics approach shows that nonlinearity effect dominates at the input of the material. Therefore, only Forchheimer coefficient of the first perforation is employed. The sound absorption

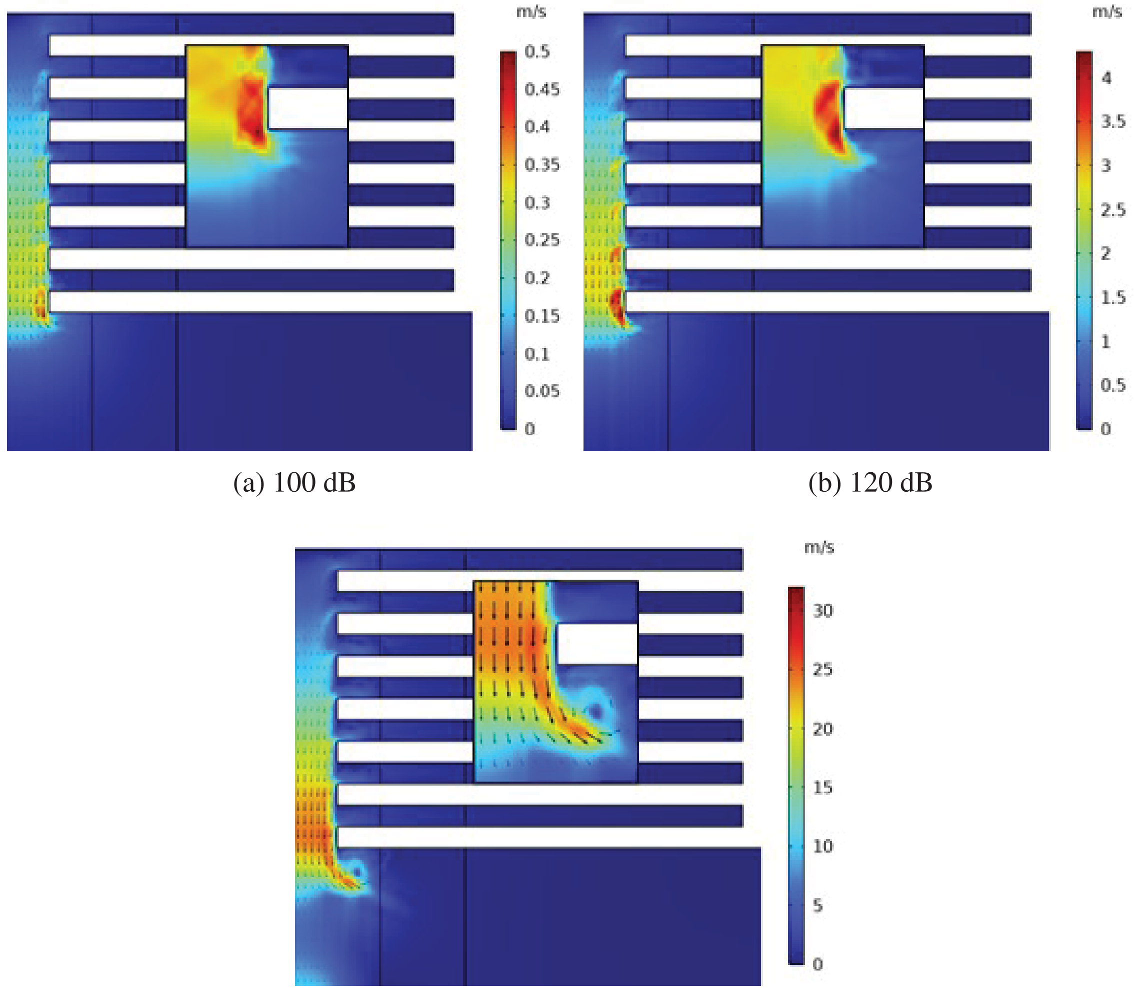

(a) 100 dB

(b) 120 dB

(c) 140 dB

Figure VII-5 Velocity field at the first resonance for an imposed incident pressure level at the beginning of a period. The inlets represent a zoom around the first perforation.

coefficient predicted by the adapted mass-spring model is compared with prediction of finite element simulations at different sound pressure levels. The two methods agree well. In acoustics, the velocity field from the finite element methods shows separation of boundary layers and formation of vortices with increasing sound pressure levels. These phenomena are more developed for the first perforation. These observations support the use of a discrete approach of a Forchheimer law.

Acknowledgements

The authors acknowledge the financial support of Natural Sciences and Engineering Research Council (NSERC) [funding reference numbers: RGPIN-2018-06113 and RGPIN-2019-06573].

BIBLIOGRAPHY

Achilleos, V., Richoux, O. & Theocharis, G. (2016). Coherent perfect absorption induced by the nonlinearity of a Helmholtz resonator. *J. Acoust. Soc. Am.*, 140(1), EL94–EL100. doi: 10.1121/1.4954869.

Al Jahdali, R. & Wu, Y. (2018). Coupled Resonators for Sound Trapping and Absorption. *Sci. Rep.*, 8(1), 13855. doi: 10.1038/s41598-018-32135-5.

Allard, J. & Atalla, N. (2009a). *Propagation of Sound in Porous Media: Modelling Sound Absorbing Materials* (éd. 2). United Kingdom: John Wiley & Sons.

Allard, J. & Atalla, N. (2009b). Sound propagation in porous materials having a rigid frame. Dans *Propagation of Sound in Porous Media: Modelling Sound Absorbing Materials* (éd. 2, pp. 73–109). United Kingdom: John Wiley & Sons.

Ang, L. Y. L., Koh, Y. K. & Lee, H. P. (2018). Plate-type acoustic metamaterial with cavities coupled via an orifice for enhanced sound transmission loss. *Applied Physics Letters*, 112(5), 051903. doi: 10.1063/1.5019602.

Ashcroft, N. W. & Mermin, N. D. (1976). *Solid state physics* (éd. Holt Rinehart and Winston). New York.

ASTM E1050-19. (2019). *Standard Test Method for Impedance and Absorption of Acoustical Materials Using a Tube, Two Microphones and a Digital Frequency Analysis System*. West Conshohocken, PA: American Society for Testing and Materials.

Atalla, N. & Sgard, F. (2007). Modeling of perforated plates and screens using rigid frame porous models. *J. Sound Vib.*, 303(1-2), 195–208. doi: 10.1016/j.jsv.2007.01.012.

Aurégan, Y. & Pachebat, M. (1999). Measurement of the nonlinear behavior of acoustical rigid porous materials. *Physics of Fluids*, 11(6), 1342–1345. doi: 10.1063/1.869999.

Aurégan, Y. (2018). Ultra-thin low frequency perfect sound absorber with high ratio of active area. *Appl. Phys. Lett.*, 113(20), 201904. doi: 10.1063/1.5063504.

Aurégan, Y., Farooqui, M. & Groby, J.-P. (2016). Low frequency sound attenuation in a flow duct using a thin slow sound material. *J. Acoust. Soc. Am.*, 139(5), EL149–EL153. doi: 10.1121/1.4951028.

Bednarik, M. & Cervenka, M. (2024). A sonic black hole of a rectangular cross-section. *Applied Mathematical Modelling*, 125, 529–543. doi: 10.1016/j.apm.2023.09.005.

Benchikh Le Hocine, A. E., Kone, T. C., Lopez, M., Panneton, R., Dupont, T. & Verdière, K. (2023, October). CFD Simulations of the Static Airflow Resistivity of a Perforated Solid: Effects of Size and Flow Velocity. *Canadian Acoustics*, 51(3), 122–123. Repéré à https://jcaa.caa-aca.ca/index.php/jcaa/article/view/4039.

Bezançon, G., Doutres, O., Umnova, O., Leclaire, P. & Dupont, T. (2024). Thin metamaterial using acoustic black hole profiles for broadband sound absorption. *Appl. Acoust.*, 216, 109744. doi: 10.1016/j.apacoust.2023.109744.

Boulvert, J., Cavalieri, T., Costa-Baptista, J., Schwan, L., Romero-García, V., Gabard, G., Fotsing, E. R., Ross, A., Mardjono, J. & Groby, J.-P. (2019). Optimally graded porous material for broadband perfect absorption of sound. *J. Appl. Phys.*, 126(17), 175101. doi: 10.1063/1.5119715.

Boulvert, J., Humbert, T., Romero-García, V., Gabard, G., Fotsing, E. R., Ross, A., Mardjono, J. & Groby, J.-P. (2022). Perfect, broadband, and sub-wavelength absorption with asymmetric absorbers: Realization for duct acoustics with 3D printed porous resonators. *Journal of Sound and Vibration*, 523, 116687. doi: 10.1016/j.jsv.2021.116687.

Bradley, C. E. (1991). *Acoustic Bloch Wave Propagation in a Periodic Waveguide* (Rapport n°ARL-TR-91-19). Repéré le 2020-04-27 à https://apps.dtic.mil/docs/citations/ADA244068.

Bravo, T. & Maury, C. (2023). Broadband sound attenuation and absorption by duct silencers based on the acoustic black hole effect: Simulations and experiments. *Journal of Sound and Vibration*, 561, 117825. doi: 10.1016/j.jsv.2023.117825.

Brooke, D. C., Umnova, O., Leclaire, P. & Dupont, T. (2020). Acoustic metamaterial for low frequency sound absorption in linear and nonlinear regimes. *J. Sound Vib.*, 115585. doi: 10.1016/j.jsv.2020.115585.

Cai, C. & Mak, C. M. (2018). Hybrid noise control in a duct using a periodic dual Helmholtz resonator array. *Appl. Acoust.*, 134, 119–124. doi: 10.1016/j.apacoust.2018.01.015.

Cai, X., Guo, Q., Hu, G. & Yang, J. (2014). Ultrathin low-frequency sound absorbing panels based on coplanar spiral tubes or coplanar Helmholtz resonators. *Appl. Phys. Lett.*, 5.

Chen, Y., Lee, B. & Park, Y.-H. (2020). A Helmholtz Resonator with Spiral Neck for Analyte Concentration Measurement in Low Frequency Range. *Applied Sciences*, 10(11), 3676. doi: 10.3390/app10113676.

Chen, Y., Yu, K., Fu, Q., Zhang, J., Lu, X., Du, X. & Sun, X. (2024). A broadband and low-frequency sound absorber of sonic black holes with multi-layered micro-perforated panels. *Appl. Acoust.*, 217, 109817. doi: 10.1016/j.apacoust.2023.109817.

Chua, J. W., Li, X., Yu, X. & Zhai, W. (2023). Novel slow-sound lattice absorbers based on the sonic black hole. *Composite Structures*, 304, 116434. doi: 10.1016/j.compstruct.2022.116434.

COMSOL. (2023). Nonlinear Slit Resonator. Repéré le 2024-07-02 à https://www.comsol.com/model/nonlinear-slit-resonator-47171.

Cummer, S. A. & Schurig, D. (2007). One path to acoustic cloaking. *New J. Phys.*, 9(3), 45–45. doi: 10.1088/1367-2630/9/3/045.

Cummings, A. (1984). Acoustic nonlinearities and power losses at orifices. *AIAA Journal*, 22(6), 786–792. doi: 10.2514/3.8680.

Cummings, A. & Eversman, W. (1983). High amplitude acoustic transmission through duct terminations: Theory. *Journal of Sound and Vibration*, 91(4), 503–518. doi: 10.1016/0022-460X(83)90829-5.

Deng, J., Guasch, O. & Ghilardi, D. (2024). Solution and analysis of a continuum model of sonic black hole for duct terminations. *Applied Mathematical Modelling*, 129, 191–206. doi: 10.1016/j.apm.2024.01.046.

Deymier, P. A. (2013). Discrete One-Dimensional Phononic and Resonant Crystals. Dans *Acoustic Metamaterials and Phononic Crystals* (pp. 13–19). Springer Series in Solid-State Sciences.

Dickey, N. & Selamet, A. (1996). Helmholtz resonators: one-dimensional limit for small cavity length-to-diameter ratios. *J. Sound Vib.*, 195(3), 512–517. doi: 10.1006/jsvi.1996.0440.

Doria, A. (1995). Control of acoustic vibrations of an enclosure by means of multiple resonators. *J. Sound Vib.*, 181(4), 673–685. doi: 10.1006/jsvi.1995.0165.

Doutres, O., Atalla, N. & Osman, H. (2015). Transfer matrix modeling and experimental validation of cellular porous material with resonant inclusions. *J. Acoust. Soc. Am.*, 137(6), 3502–3513. doi: 10.1121/1.4921027.

Duan, H., Shen, X., Wang, E., Yang, F., Zhang, X. & Yin, Q. (2021). Acoustic multi-layer Helmholtz resonance metamaterials with multiple adjustable absorption peaks. *Appl. Phys. Lett.*, 118(24), 241904. doi: 10.1063/5.0054562.

Duan, M., Yu, C., Xu, Z., Xin, F. & Lu, T. J. (2020). Acoustic impedance regulation of Helmholtz resonators for perfect sound absorption via roughened embedded necks. *Appl. Phys. Lett.*, 117(15), 151904. doi: 10.1063/5.0024804.

Dupont, T., Leclaire, P., Panneton, R. & Umnova, O. (2018). A microstructure material design for low frequency sound absorption. *Appl. Acoust.*, 136, 86–93. doi: 10.1016/j.apacoust.2018.02.016.

Fang, N., Xi, D., Xu, J., Ambati, M., Srituravanich, W., Sun, C. & Zhang, X. (2006). Ultrasonic metamaterials with negative modulus. *Nat. Mater.*, 5(6), 452–456. doi: 10.1038/nmat1644.

Fitzpatrick, R. (2013). Longitudinal standing waves. Dans *Oscillations and waves an introduction* (pp. 69–88). Boca Raton (Fla.): CRC press.

Fok, L. & Zhang, X. (2011). Negative acoustic index metamaterial. *Phys. Rev. B*, 83(21), 214304. doi: 10.1103/PhysRevB.83.214304.

Gao, N., Wu, J., Lu, K. & Zhong, H. (2021). Hybrid composite meta-porous structure for improving and broadening sound absorption. *Mechanical Systems and Signal Processing*, 154, 107504. doi: 10.1016/j.ymssp.2020.107504.

Groby, J.-P., Huang, W., Lardeau, A. & Aurégan, Y. (2015a). The use of slow waves to design simple sound absorbing materials. *J. Appl. Phys.*, 117(12), 124903. doi: 10.1063/1.4915115.

Groby, J.-P., Lagarrigue, C., Brouard, B., Dazel, O., Tournat, V. & Nennig, B. (2015b). Enhancing the absorption properties of acoustic porous plates by periodically embedding Helmholtz resonators. *J. Acoust. Soc. Am.*, 137(1), 273–280. doi: 10.1121/1.4904534.

Groby, J.-P., Pommier, R. & Aurégan, Y. (2016). Use of slow sound to design perfect and broadband passive sound absorbing materials. *J. Acoust. Soc. Am.*, 139(4), 1660–1671. doi: 10.1121/1.4945101.

Groby, J.-P., Jiménez, N. & Romero-García, V. (2021). Acoustic Metamaterial Absorbers. Dans Jiménez, N., Umnova, O. & Groby, J.-P. (Éds.), *Acoustic Waves in Periodic Structures, Metamaterials, and Porous Media: From Fundamentals to Industrial Applications* (vol. 143, pp. 167–183). Cham: Springer International Publishing. doi: 10.1007/978-3-030-84300-7.

Guan, C. & Jiao, Z. (2012). Modeling and Optimal Design of 3 Degrees of Freedom Helmholtz Resonator in Hydraulic System. *Chin. J. Aeronaut.*, 25(5), 776–783. doi: 10.1016/S1000-9361(11)60444-5.

Guasch, O., Arnela, M. & Sánchez-Martín, P. (2017). Transfer matrices to characterize linear and quadratic acoustic black holes in duct terminations. *J. Sound Vib.*, 395, 65–79. doi: 10.1016/j.jsv.2017.02.007.

Guasch, O., Sánchez-Martín, P. & Ghilardi, D. (2020). Application of the transfer matrix approximation for wave propagation in a metafluid representing an acoustic black hole duct termination. *Applied Mathematical Modelling*, 77, 1881–1893. doi: 10.1016/j.apm.2019.09.039.

Guess, A. W. (1975). Calculation of perforated plate liner parameters from specified acoustic resistance and reactance. *Journal of Sound and Vibration*, 40(1), 119–137. doi: 10.1016/S0022-460X(75)80234-3.

Guo, J., Fang, Y., Jiang, Z. & Zhang, X. (2020). Acoustic characterizations of Helmholtz resonators with extended necks and their checkerboard combination for sound absorption. *J. Phys. D: Appl. Phys.*, 53(50), 505504. doi: 10.1088/1361-6463/abb5d8.

Guo, J., Fang, Y., Jiang, Z. & Zhang, X. (2021a). An investigation on noise attenuation by acoustic liner constructed by Helmholtz resonators with extended necks. *J. Acoust. Soc. Am.*, 149(1), 70–81. doi: 10.1121/10.0002990.

Guo, J., Fang, Y., Qu, R., Liu, Q. & Zhang, X. (2021b). An extra-broadband compact sound-absorbing structure composing of double-layer resonator with multiple perforations. *J. Acoust. Soc. Am.*, 12.

Guo, J., Zhang, X., Fang, Y. & Jiang, Z. (2021c). Wideband low-frequency sound absorption by inhomogeneous multi-layer resonators with extended necks. *Composite Structures*, 260, 113538. doi: 10.1016/j.compstruct.2020.113538.

Guo, J., Zhou, T., Fang, Y. & Zhang, X. (2021d). Experimental study on a compact lined circular duct for small-scale propeller noise reduction. *Appl. Acoust.*, 179, 108062. doi: 10.1016/j.apacoust.2021.108062.

Helmholtz, H. v. & Ellis, A. J. (1895). *On the sensations of tone as a physiological basis for the theory of music* (éd. 3). London, New York: Longmans, Green, and Co. Repéré à http://archive.org/details/onsensationsofto00helmrich.

Hruška, V., Groby, J.-P. & Bednařík, M. (2024). Complex frequency analysis and source of losses in rectangular sonic black holes. *Journal of Sound and Vibration*, 571, 118107. doi: 10.1016/j.jsv.2023.118107.

Huang, S., Fang, X., Wang, X., Assouar, B., Cheng, Q. & Li, Y. (2019). Acoustic perfect absorbers via Helmholtz resonators with embedded apertures. *J. Acoust. Soc. Am.*, 145(1), 254–262. doi: 10.1121/1.5087128.

Ingard, U. (1953). On the Theory and Design of Acoustic Resonators. *J. Acoust. Soc. Am.*, 25(6), 1037–1061. doi: 10.1121/1.1907235.

Ingard, U. (1968). Absorption Characteristics of Nonlinear Acoustic Resonators. *J. Acoust. Soc. Am.*, 44(4), 1155–1156. doi: 10.1121/1.1911215.

Ingard, U. & Ising, H. (1967). Acoustic Nonlinearity of an Orifice. *J. Acoust. Soc. Am.*, 42(1), 6–17. doi: 10.1121/1.1910576.

Ingård, U. & Labate, S. (1950). Acoustic Circulation Effects and the Nonlinear Impedance of Orifices. *J. Acoust. Soc. Am.*, 22(2), 211–218. doi: 10.1121/1.1906591.

ISO 9053-1. (2018). *Acoustics — Determination of airflow resistance. Part1: Static airflow method*. Switzerland, Geneva: International Organization for Standardization.

Jiménez, N., Huang, W., Romero-García, V., Pagneux, V. & Groby, J.-P. (2016). Ultra-thin metamaterial for perfect and quasi-omnidirectional sound absorption. *Appl. Phys. Lett.*, 109(12), 121902. doi: 10.1063/1.4962328.

Jiménez, N., Romero-Garcia, V., Pagneux, V. & Groby, J.-P. (2017a). Rainbow-trapping absorbers Broadband, perfect and asymmetric sound absorption by subwavelength panels for transmission problems.pdf. *Sci Rep*, 7(1), 1–12. doi: 10.1038/s41598-017-13706-4.

Jiménez, N., Groby, J.-P., Pagneux, V. & Romero-García, V. (2017b). Iridescent Perfect Absorption in Critically-Coupled Acoustic Metamaterials Using the Transfer Matrix Method. *Applied Sciences*, 7(6), 618. doi: 10.3390/app7060618.

Jiménez, N., Romero-García, V., Pagneux, V. & Groby, J.-P. (2017c). Quasiperfect absorption by subwavelength acoustic panels in transmission using accumulation of resonances due to slow sound. *Phys. Rev. B*, 95(1), 014205. doi: 10.1103/PhysRevB.95.014205.

Jiménez, N., Umnova, O. & Groby, J.-P. (Éds.). (2021). *Acoustic Waves in Periodic Structures, Metamaterials, and Porous Media: From Fundamentals to Industrial Applications*. Cham: Springer International Publishing. doi: 10.1007/978-3-030-84300-7.

Johnson, D. L., Koplik, J. & Dashen, R. (1987). Theory of dynamic permeability and tortuosity in fluid-saturated porous media. *Journal of Fluid Mechanics*, 176, 379–402. doi: 10.1017/S0022112087000727.

Karal, F. C. (1953). The Analogous Acoustical Impedance for Discontinuities and Constrictions of Circular Cross Section. *J. Acoust. Soc. Am.*, 25(2), 327–334. doi: 10.1121/1.1907041.

Kone, T. C., Ghinet, S., Panneton, R., Dupont, T. & Grewal, A. (2021a, August). Multi-tonal low frequency noise control for aircraft cabin using Helmholtz resonator with complex cavity. pp. 13.

Kone, T. C., Lopez, M., Ghinet, S., Dupont, T. & Panneton, R. (2021b). Thermoviscous-acoustic metamaterials to damp acoustic modes in complex shape geometries at low frequencies. *J. Acoust. Soc. Am.*, 150(3), 2272–2281. doi: 10.1121/10.0006441.

Kuntz, H. L. & Blackstock, D. T. (1987). Attenuation of intense sinusoidal waves in air-saturated, bulk porous materials. *J. Acoust. Soc. Am.*, 81(6), 1723–1731. doi: 10.1121/1.394787.

Lagarrigue, C., Groby, J. P., Tournat, V., Dazel, O. & Umnova, O. (2013). Absorption of sound by porous layers with embedded periodic arrays of resonant inclusions. *J. Acoust. Soc. Am.*, 134(6), 4670–4680. doi: 10.1121/1.4824843.

Laly, Z., Atalla, N. & Meslioui, S.-A. (2018). Acoustical modeling of micro-perforated panel at high sound pressure levels using equivalent fluid approach. *J. Sound Vib.*, 427, 134–158. doi: 10.1016/j.jsv.2017.09.011.

Lambert, R. F. & McIntosh, J. D. (1990). Nonlinear wave propagation through rigid porous materials. II: Approximate analytical solutions. *J. Acoust. Soc. Am.*, 88(4), 1950–1959. doi: 10.1121/1.400218.

Langfeldt, F. & Gleine, W. (2019a). Membrane- and plate-type acoustic metamaterials with elastic unit cell edges. *Journal of Sound and Vibration*, 453, 65–86. doi: 10.1016/j.jsv.2019.04.018.

Langfeldt, F. & Gleine, W. (2019b, July). Improved sound transmission loss of glass wool with acoustic metamaterials. pp. 8.

Langfeldt, F. & Gleine, W. (2020). Optimizing the bandwidth of plate-type acoustic metamaterials. *J. Acoust. Soc. Am.*, 148(3), 1304–1314. doi: 10.1121/10.0001925.

Lebel, G., Martin, R. & Dubé, M. (2019). *La perturbation du sommeil et le dérangement associés au bruit environnemental dans la population québécoise en 2014-2015: rapport de surveillance*. Québec, Québec: Bibliothèque et Archives nationales du Québec.

Leblanc, A. & Lavie, A. (2017). Three-dimensional-printed membrane-type acoustic metamaterial for low frequency sound attenuation. *J. Acoust. Soc. Am.*, 141(6), EL538–EL542. doi: 10.1121/1.4984623.

Leclaire, P., Umnova, O., Dupont, T. & Panneton, R. (2015). Acoustical properties of air-saturated porous material with periodically distributed dead-end pores. *J. Acoust. Soc. Am.*, 137(4), 1772–1782. doi: 10.1121/1.4916712.

Lee, S. H., Park, C. M., Seo, Y. M., Wang, Z. G. & Kim, C. K. (2009a). Acoustic metamaterial with negative density. *Physics Letters A*, 373(48), 4464–4469. doi: 10.1016/j.physleta.2009.10.013.

Lee, S. H., Park, C. M., Seo, Y. M., Wang, Z. G. & Kim, C. K. (2009b). Acoustic metamaterial with negative modulus. *J. Phys.: Condens. Matter*, 21(17), 175704. doi: 10.1088/0953-8984/21/17/175704.

Lenci, A., Zeighami, F. & Di Federico, V. (2022). Effective Forchheimer Coefficient for Layered Porous Media. *Transp Porous Med*, 144(2), 459–480. doi: 10.1007/s11242-022-01815-2.

Li, K., Dauchez, N. & Nennig, B. (2023a). A metaporoelastic structure that overcomes the sound insulation weaknesses of single and double panel partitions. *Appl. Acoust.*, 210, 109409. doi: 10.1016/j.apacoust.2023.109409.

Li, S., Davidson, L. & Peng, S.-H. (2024). A pressure-loss model for flow-through round-hole perforated plates of moderate porosity and thickness in laminar and turbulent flow regimes. *International Journal of Heat and Mass Transfer*, 226, 125490. doi: 10.1016/j.ijheatmasstransfer.2024.125490.

Li, S., Xia, J., Yu, X., Zhang, X. & Cheng, L. (2023b). A sonic black hole structure with perforated boundary for slow wave generation. *Journal of Sound and Vibration*, 559, 117781. doi: 10.1016/j.jsv.2023.117781.

Liu, C. R., Wu, J. H., Chen, X. & Ma, F. (2019). A thin low-frequency broadband metasurface with multi-order sound absorption. *J. Phys. D: Appl. Phys.*, 52(10), 105302. doi: 10.1088/1361-6463/aafaa3.

Lopez, M., Dupont, T. & Panneton, R. (2022). A mass-spring analogy for modeling the acoustic behaviour of a metamaterial. *Inter-Noise*, 265(1), 6295–6301. doi: 10.3397/IN_2022_0935.

Lopez, M., Dupont, T. & Panneton, R. (2024). Mass-spring model for acoustic metamaterials consisting of a compact linear periodic array of dead-end resonators. *J. Acoust. Soc. Am.*, 155(1), 530–543. doi: 10.1121/10.0024212.

Lu, Z., Yu, X., Lau, S.-K., Khoo, B. C. & Cui, F. (2020). Membrane-type acoustic metamaterial with eccentric masses for broadband sound isolation. *Appl. Acoust.*, 157, 107003. doi: 10.1016/j.apacoust.2019.107003.

Ma, G., Yang, M., Xiao, S., Yang, Z. & Sheng, P. (2014). Acoustic metasurface with hybrid resonances. *Nat. Mater.*, 13(9), 873–878. doi: 10.1038/nmat3994.

Maa, D. (1994). Microperforated panel at high sound intensity. *INTER-NOISE and NOISE-CON Congress and Conference*, 1994, 1511–1514. Repéré à https://hal.science/hal-04551854/document.

Martin, R., Deshaies, P. & Poulin, M. (2016). *Avis sur une politique québécoise de lutte au bruit environnemental*. Ottawa, Ontario: Bibliothèque et Archives nationales du Québec.

Martínez-Sala, R., Sancho, J., Sánchez, J. V., Gómez, V., Llinares, J. & Meseguer, F. (1995). Sound attenuation by sculpture. *Nature*, 378(6554), 241–241. doi: 10.1038/378241a0.

McIntosh, J. D. & Lambert, R. F. (1990). Nonlinear wave propagation through rigid porous materials. I: Nonlinear parametrization and numerical solutions. *J. Acoust. Soc. Am.*, 88(4), 1939–1949. doi: 10.1121/1.400217.

Mei, J., Ma, G., Yang, M., Yang, Z., Wen, W. & Sheng, P. (2012). Dark acoustic metamaterials as super absorbers for low-frequency sound. *Nat Commun*, 3(1), 756. doi: 10.1038/ncomms1758.

Melling, T. (1973). The acoustic impendance of perforates at medium and high sound pressure levels. *J. Sound Vib.*, 29(1), 1–65. doi: 10.1016/S0022-460X(73)80125-7.

Mercier, J.-F., Marigo, J.-J. & Maurel, A. (2017). Influence of the neck shape for Helmholtz resonators. *J. Acoust. Soc. Am.*, 142(6), 3703–3714. doi: 10.1121/1.5017735.

Merriam-Webster. (2024, June). Definition of META. Repéré le 2024-06-25 à https://www.merriam-webster.com/dictionary/meta.

Mironov, M. A. & Pislyakov, V. V. (2002). One-dimensional acoustic waves in retarding structures with propagation velocity tending to zero. *Acoust. Phys.*, 48(3), 347–352. doi: 10.1134/1.1478121.

Munjal, M. (1987). Propagation of waves in ducts. Dans *Acoustics of ducts and mufflers : with application to exhaust and ventilation system design* (pp. 1–41). New York: John Wiley & Sons.

Nori, M. & Venegas, R. (2017). Sound propagation in porous materials with annular pores. *J. Acoust. Soc. Am.*, 141(6), 4642–4651. doi: 10.1121/1.4986939.

Olver, F. W. J. (1972). Bessel Functions of Integer Order. Dans Abramowitz, M. & Stegun, I. A. (Éds.), *Handbook of Mathematical Functions* (pp. 360). Washington, D.C: United states department of commerce.

Panneton, R. (2023, October). Engineered materials for acoustics: metamaterials, sonic crystals and calculated microstructures. *Canadian Acoustics*, 51(3), 140–141. Repéré à https://jcaa.caa-aca.ca/index.php/jcaa/article/view/4038.

Park, C. M. & Lee, S. H. (2019). Zero-reflection acoustic metamaterial with a negative refractive index. *Sci Rep*, 9(1), 3372. doi: 10.1038/s41598-019-40184-7.

Park, S.-H. (2013). Acoustic properties of micro-perforated panel absorbers backed by Helmholtz resonators for the improvement of low-frequency sound absorption. *Journal of Sound and Vibration*, 332(20), 4895–4911. doi: 10.1016/j.jsv.2013.04.029.

Pelat, A., Gautier, F., Conlon, S. C. & Semperlotti, F. (2020). The acoustic black hole: A review of theory and applications. *J. Sound Vib.*, 476, 115316. doi: 10.1016/j.jsv.2020.115316.

Peng, L., Mao, Q., Wang, H., Lai, L., Shi, Q. & Chen, M. (2024). Enhanced sound absorption with the combined sonic black holes. *Applied Acoustics*, 219, 109932. doi: 10.1016/j.apacoust.2024.109932.

Peng, X., Ji, J. & Jing, Y. (2018). Composite honeycomb metasurface panel for broadband sound absorption. *J. Acoust. Soc. Am.*, 144(4), EL255–EL261. doi: 10.1121/1.5055847.

Pongratz, R. & Redmann, D. (2016). Acoustic liner design for fenestron® noise reduction. Repéré à https://dspace-erf.nlr.nl/server/api/core/bitstreams/78354720-8882-4dbd-987a-10c61203efad/content.

Rayleigh, J. W. S. B. (1896). Theory of resonators. Dans *The Theory Of Sound* (vol. 2, pp. 169–235). New York: Dover publications. Repéré à http://archive.org/details/in.ernet.dli.2015.22520.

Romero-García, V., Jiménez, N., Groby, J.-P., Merkel, A., Tournat, V., Theocharis, G., Richoux, O. & Pagneux, V. (2020). Perfect Absorption in Mirror-Symmetric Acoustic Metascreens. *Phys. Rev. Applied*, 14(5), 054055. doi: 10.1103/PhysRevApplied.14.054055.

Salissou, Y., Panneton, R. & Doutres, O. (2012). Complement to standard method for measuring normal incidence sound transmission loss with three microphones. *J. Acoust. Soc. Am.*, 131, EL216–22. doi: 10.1121/1.3681016.

Seo, Y. M., Park, J. J., Lee, S. H., Park, C. M., Kim, C. K. & Lee, S. H. (2012). Acoustic metamaterial exhibiting four different sign combinations of density and modulus. *J. Appl. Phys.*, 111(2), 023504. doi: 10.1063/1.3676262.

Serra, G., Guasch, O., Arnela, M. & Miralles, D. (2023). Optimization of the profile and distribution of absorption material in sonic black holes. *Mechanical Systems and Signal Processing*, 202, 110707. doi: 10.1016/j.ymssp.2023.110707.

Sheng, H., He, M.-X., Pueh Lee, H. & Ding, Q. (2024). Quasi-periodic sonic black hole with low-frequency acoustic and elastic bandgaps. *Composite Structures*, 337, 118046. doi: 10.1016/j.compstruct.2024.118046.

Simon, F. (2018). Long Elastic Open Neck Acoustic Resonator for low frequency absorption. *J. Sound Vib.*, 421, 1–16. doi: 10.1016/j.jsv.2018.01.044.

Simon, F. & Sebbane, D. (2021). Compact 2DOF liner based on a long elastic open-neck acoustic resonator for low frequency absorption. *noise cont engng j*, 69(1), 1–17. doi: 10.3397/1/37691.

Stinson, M. R. (1991). The propagation of plane sound waves in narrow and wide circular tubes, and generalization to uniform tubes of arbitrary cross-sectional shape. *J. Acoust. Soc. Am.*, 89(2), 550–558. doi: 10.1121/1.400379.

Sugimoto, N. & Horioka, T. (1995). Dispersion characteristics of sound waves in a tunnel with an array of Helmholtz resonators. *J. Acoust. Soc. Am.*, 97(3), 1446–1459. doi: 10.1121/1.412085.

Tayong, R., Dupont, T. & Leclaire, P. (2010). On the variations of acoustic absorption peak with particle velocity in micro-perforated panels at high level of excitation. *J. Acoust. Soc. Am.*, 127(5), 2875–2882. doi: 10.1121/1.3372714.

Umnova, O., Attenborough, K., Standley, E. & Cummings, A. (2003). Behavior of rigid-porous layers at high levels of continuous acoustic excitation: Theory and experiment. *J. Acoust. Soc. Am.*, 114(3), 1346–1356. doi: 10.1121/1.1603236.

Umnova, O., Attenborough, K. & Cummings, A. (2002). High amplitude pulse propagation and reflection from a rigid porous layer. *Noise Control Eng. J.*, 50(6), 204. doi: 10.3397/1.2839692.

Umnova, O., Attenborough, K., Shin, H.-C. & Cummings, A. (2004). Response of multiple rigid porous layers to high levels of continuous acoustic excitation. *J. Acoust. Soc. Am.*, 116(2), 703–712. doi: 10.1121/1.1766051.

Umnova, O., Brooke, D., Leclaire, P. & Dupont, T. (2023). Multiple resonances in lossy acoustic black holes - theory and experiment. *J. Sound Vib.*, 543, 117377. doi: 10.1016/j.jsv.2022.117377.

Wang, X. & Mak, C. M. (2012). Acoustic performance of a duct loaded with identical resonators. *J. Acoust. Soc. Am.*, 131(4), EL316–EL322. doi: 10.1121/1.3691826.

Wilson, D. K., McIntosh, J. D. & Lambert, R. F. (1988). Forchheimer-type nonlinearities for high-intensity propagation of pure tones in air-saturated porous media. *J. Acoust. Soc. Am.*, 84(1), 350–359. doi: 10.1121/1.396937.

Xiao, Y., Wen, J. & Wen, X. (2012). Sound transmission loss of metamaterial-based thin plates with multiple subwavelength arrays of attached resonators. *J. Sound Vib.*, 331(25), 5408–5423. doi: 10.1016/j.jsv.2012.07.016.

Xu, M., Selamet, A. & Kim, H. (2010). Dual Helmholtz resonator. *Appl. Acoust.*, 71(9), 822–829. doi: 10.1016/j.apacoust.2010.04.007.

Yang, Z., Mei, J., Yang, M., Chan, N. H. & Sheng, P. (2008). Membrane-Type Acoustic Metamaterial with Negative Dynamic Mass. *Phys. Rev. Lett.*, 101(20), 204301. doi: 10.1103/PhysRevLett.101.204301.

Yang, Z., Dai, H. M., Chan, N. H., Ma, G. C. & Sheng, P. (2010). Acoustic metamaterial panels for sound attenuation in the 50–1000 Hz regime. *Applied Physics Letters*, 96(4), 041906. doi: 10.1063/1.3299007.

Yu, X., Mi, Y., Zhai, W. & Cheng, L. (2023). Principles of progressive slow-sound and critical coupling condition in broadband sonic black hole absorber. *J. Acoust. Soc. Am.*, 154(5), 2988–3003. doi: 10.1121/10.0021880.

Zhang, C. & Hu, X. (2016). 3D Single-port Labyrinthine Acoustic Metamaterial. *Phys. Rev. Applied*, 6(6), 064025. doi: 10.1103/PhysRevApplied.6.064025. arXiv: 1608.04599.

Zhang, J., Romero-García, V., Theocharis, G., Richoux, O., Achilleos, V. & Frantzeskakis, D. (2021). High-amplitude sound propagation in acoustic transmission-line metamaterial. *Applied Physics Letters*, 118(10), 104102. doi: 10.1063/5.0040702.

Zhang, X., He, N., Cheng, L., Yu, X., Zhang, L. & Hu, F. (2024). Sound absorption in sonic black holes: Wave retarding effect with broadband cavity resonance. *Appl. Acoust.*, 221, 110007. doi: 10.1016/j.apacoust.2024.110007.

Zhao, H., Wang, Y., Wen, J., Lam, Y. W. & Umnova, O. (2018). A slim subwavelength absorber based on coupled microslits. *Appl. Acoust.*, 142, 11–17. doi: 10.1016/j.apacoust.2018.08.004.

Zhu, J., Qu, Y., Gao, H. & Meng, G. (2022). Nonlinear sound absorption of Helmholtz resonators with serrated necks under high-amplitude sound wave excitation. *Journal of Sound and Vibration*, 537, 117197. doi: 10.1016/j.jsv.2022.117197.

Zhu, J., Gao, H., Dai, S., Qu, Y. & Meng, G. (2023). Multilayer structures for high-intensity sound energy absorption in low-frequency range. *International Journal of Mechanical Sciences*, 247, 108197. doi: 10.1016/j.ijmecsci.2023.108197.

Zhu, X.-F., Lau, S.-K., Lu, Z. & Jeon, W. (2019). Broadband low-frequency sound absorption by periodic metamaterial resonators embedded in a porous layer. *J. Sound Vib.*, 461, 114922. doi: 10.1016/j.jsv.2019.114922.

Zieliński, T. G., Opiela, K. C., Dauchez, N., Boutin, T., Galland, M.-A. & Attenborough, K. (2024). Extremely tortuous sound absorbers with labyrinthine channels in non-porous and microporous solid skeletons. *Appl. Acoust.*, 217, 109816. doi: 10.1016/j.apacoust.2023.109816.

Zigoneanu, L., Popa, B.-I. & Cummer, S. A. (2014). Three-dimensional broadband omnidirectional acoustic ground cloak. *Nat. Mater.*, 13(4), 352–355. doi: 10.1038/nmat3901.

Zinn, B. T. (1970). A theoretical study of non-linear damping by helmholtz resonators. *J. Sound Vib.*, 13(3), 347–356. doi: 10.1016/S0022-460X(70)80023-2.